Modelling of Tool Wear and Metal Flow Behaviour in Friction Stir Welding (FSW)

Ahmed Falh Hasan, BSc, MSc

This thesis is submitted to The University of Nottingham for the degree of Doctor of Philosophy

May 2016

Abstract

Friction Stir Welding (FSW) is a solid-state joining process that was invented in 1991; it is particularly useful for joints difficult to make using fusion techniques. Significant advances in FSW have been achieved in terms of process modelling since its inception. However, until now experimental work has remained the primary method of investigating tool wear in FSW.

In this project, two main objectives were set; the first one was to produce a numerical approach that can be used as a useful tool to understand the effect that worn tool geometry has on the material flow and resultant weld quality. The second objective was to provide a modelling methodology for calculating tool wear in FSW based on a CFD model.

Initially, in this study, a validated model of the FSW process was generated using the CFD software FLUENT, with this model then being used to assess in detail the differences in flow behaviour, mechanically affected zone (MAZ) size and strain rate distribution around the tool for both unworn and worn tool geometries. Later, a novel methodology for calculating tool wear in FSW is developed. Here a CFD model is used to predict the deformation of the highly viscous flow around the tool, with additional analysis linking this deformation to tool wear. A validation process was carried out in this study in order to obtain robust results when using this methodology. Once satisfied with the tool wear methodology results, a parametric study considering different tool designs, rotation speeds and traverse speeds was undertaken to predict the wear depth. In this study, three workpiece materials were used which were aluminium 6061, 7020 and AISI 304 stainless steel, while the materials used for the tools used were of H13 steel and tungsten-rhenium carbide (WRe-HfC) with different tool designs.

The study shows that there are significant differences in the flow behaviour around and under the tool when the tool is worn and it shows that the proposed approach is able to predict tool wear associated with high viscous flow around the FSW tool.

With a simple dome shaped tool, the results shows that the tool was worn radially and vertically and insignificant wear was predicted during welding near the pin tip. However, in other regions the wear increased as the weld distance increased. Additionally, from the parametric study that was undertaken for the two tool designs - a dome and a conical shape- the study has found that for both tool designs, wear depth increases with increasing tool rotation speed and traverse speed. It was also shown that, generally, the wear depth was higher for the conical tool design than the dome tool in the pin tip zone. The research concludes that a proposed methodology is able to calculate tool wear associated with high viscous flow around the FSW tool, which could be used as a method for calculating tool wear without the need for experimental trials. The CFD model has provided a good tool for prediction and assessment of the flow differences between un-worn and worn tools, which may be used to give an indication of the weld quality and of tool lifetime. Furthermore, from the results, it can be concluded that this approach is capable of predicting tool wear for different process parameters and tool designs and it is possible to obtain a low wear case by controlling the process parameters.

Acknowledgements

Table of contents

Table of figures

Nomenclature

AS = weld advancing side

FSW = Friction Stir Welding

BM = base metal

rpm = revolutions per minute

$A, \alpha, n, \sigma_R, \beta$, and m = material constants

CEL = Combined Eulerian-Lagrangian

Cp = specific heat at constant pressure

c_1, c_2 = material constants refers to equation 2 - 11

$D.$ = partial slip constant, refers to equation 2 – 7

D_p = mean diameter of the abrasive particle in equation 2-12

$\dfrac{\partial u_j}{\partial x_i}$ = velocity gradient

FEA = Finite Element method

FVM = Finite Volume Method

F_n = Normal force

HAZ = heat affected zone

H_t = pin height

h = wear depth

h_t = height of the flow arm zone, refers to equation 2 -6

i and j = tensor notations equal 1, 2, and 3, which represent the $x, y,$ and z-axes, respectively

k = dimensional Archard wear coefficient

k_{ab} = abrasive wear coefficient

k_{th} = thermal conductivity

L = hydraulic diameter (characteristic linear dimension)

l = weld distance

MAZ = mechanically affected zone

ne = flow behaviour index

P = applied pressure

P_s = power required to cause shear deformation by the tool

P_v = proportion by volume of the reinforced of abrasive particles in equation 2-12

Q_e = activation energy

Q_h = total heat input

Q_s = heat input from the shoulder

q_r = heat flux

R = universal gas constant

RS = weld retreating side

R_i = distance of the calculated point from the tool axis, refers to equation 2.- 1

r = radial position

r_p = tool outer radius

r_p = pin radius

r_s = shoulder radius

S = sliding distance

SEM = scan electron microscope

SWZ = swirl weld zone, refers to Figure 2-5

S_i = cross-sectional tool area

S_o = initial-sectional tool area

$S1$ and $S2$ = Refer to Figure 7

T = temperature

TMAZ = thermo-mechanically affected zone, refers to Figure 2-5

T_m = melting temperature

t = time

t_f = total time

UDF = user define function

u = material velocity in the x-direction

$\boldsymbol{u}$ = velocity vectors for u, v and w velocity components in the x, y and z-directions

u_{mat}, w_{mat} and v_{ma} = material velocity components at the interface in the x, y and z-directions

u_{weld} = welding velocity at the inlet

V = total wear volume

v = material velocity in the y-direction

V_{mat} = material velocity at the interface

V_{tool} = velocity components on the tool surface

V_{slip} = relative interface velocity

W_t = percentage of tool wear

w = material velocity in the z-direction

WN = the weld nugget zone

Z = Zener Holloman parameter

ΔC_{max} = cutting arc, refers to equation 2-12

Δh = wear depth increment

Δt = time increment

ΔS = sliding distance increment

α_t = tool shoulder cone angle

δ = contact state variable

ε_{ij} = shear strain in tensor

$\dot{\bar{\varepsilon}}$ = effective strain rate

θ = angle from the direction of movement of the tool with x-axis

μ = dynamic viscosity

μ_f = friction coefficient

ρ = fluid density

σ_f = flow stress

σ_n = normal stress

τ = shear stress

τ_c = critical shear stress

$\tau_{contact}$ = contact shear stress

$\tau_{friction}$ = frictional shear stress

τ_{yield} = yield shear stress

ω = tool angular rotation speed

Chapter 1 Introduction

1.1 Background

Friction stir welding (FSW) is a solid-state joining process that has many advantages, including the ability to join high strength aluminium alloys, as well as dissimilar metals that are hard to join by conventional fusion techniques [1, 2]. The last two decades have seen significant advances in both tool material and tool design, allowing a wide range of materials to be welded (such as soft aluminium, magnesium alloys, hard carbon-steels or stainless steel), with a range of thicknesses and desired weld quality in terms of a low number of defects and distortion. In addition, joint strengths that can reach those of the base material can be achieved [3]. As the heat input in the process produces temperatures below the melting point, the advantages which are presented above are due to grain refinement in the weld nugget zone (WN) and in addition the lower temperature avoids solidification induced defects in the thermo-mechanically affected zone (MAZ) [4]. The FSW technique has many applications in the aeronautical, automotive and shipping industries [5, 6] and is considered to be energy efficient and environmentally friendly [1].

Fundamentally, this process consists of three main parts, which are the tool, the work-piece(s) and the backing plate; the process is illustrated in Figure 1-1.
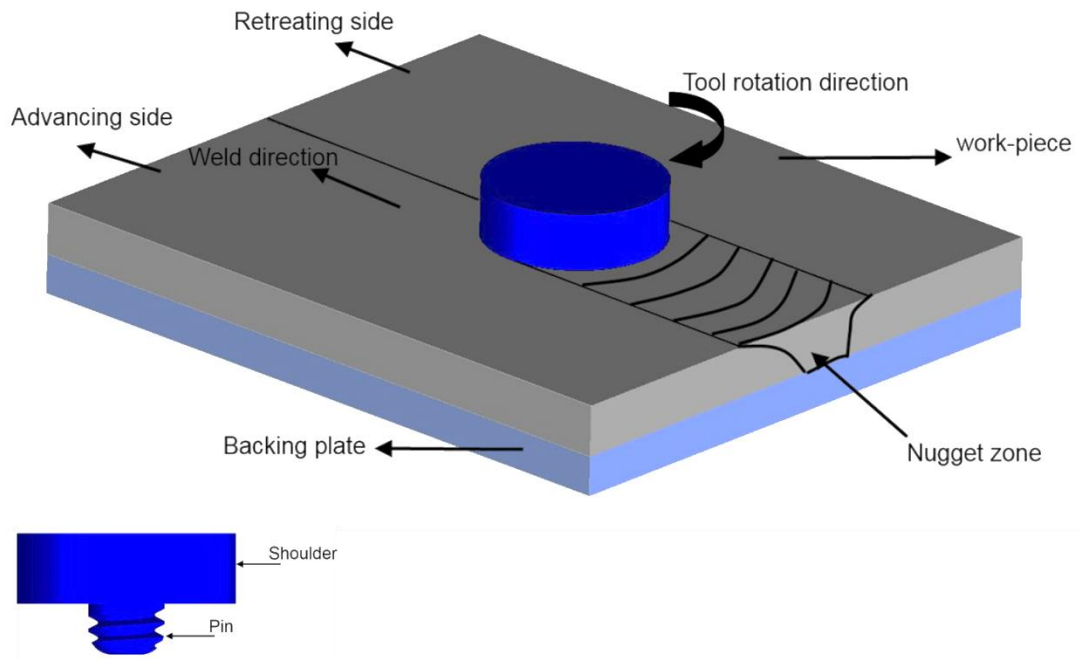
Figure 1-1 Friction stir welding process diagram

The tool has two parts: the shoulder with a large diameter and a pin with a small diameter; mostly, the tools are made from high strength alloys with thermal and mechanical properties higher than the workpiece material, so it is a (relatively) non-consumable part.

Initially, during the process, contact occurs between the rotating tool and the workpiece; frictional heat is generated and is conducted into the body of the workpiece. After that, localized heating caused by the shoulder leads the workpiece to deform plastically [7, 8]. Therefore, the main objective of the tool is to generate heat and to provide plastic deformation in a stirring motion, which results in material movement to form a weld joint from the advancing to the retreating side [3]. The shoulder deforms the plasticised material and consolidates the material behind the pin and concentrates the heat in the weld zone. The workpiece consists of two plates - known as the advancing and retreating sides - and under the shoulder, the welding zone (nugget or stirring zone) forms due to the pin stirring action.

1.2 Motivation and goals

FSW is an extreme plastic deformation process where the flow regime is characterized by solid–state material flow. An analysis of the literature has shown that wear of the tool is very common during the FSW process and that this wear is associated with material flow during the process [9-12]

Although it has been shown that the FSW process has the ability to produce joints in various types of metals, tool integrity issues in terms of tool wear and tool life, seem to be one of the main restrictions for this technique at present, particularly when joining metal matrix composites (MMCs) and steel with a thickness of 6mm and above [15]. While significant advances in FSW tool materials, such as the use of molybdenum-tungsten (Mo-W) alloys, polycrystalline cubic boron nitride (PCBN), cobalt (Co) based alloys and tungsten-rhenium (W–Re) alloys with the addition of hafnium carbide (HfC) [16, 17], have allowed the process to be used for increasingly demanding applications, the wear of FSW tools, which occurs in the form of tool degradation due to wear [18], has remained an issue. Recent developments in FSW have highlighted the fact that, until now, experimental work has remained the primary method of investigating tool wear in FSW.

The characterisation of the microstructure and mechanical properties of the weld zone is a very important technique in determining weld joint quality. However, a numerical technique which has a predictive capability is perhaps more powerful, since it allows the process parameters to be optimized [13, 14]. Much of the literature on FSW has demonstrated different approaches to analysing flow behaviour using numerical models and assessing the tool wear during the process experimentally. However, research concerning the flow behaviour associated with FSW with worn tools has been

limited and mainly covers experimental studies into what happens in terms of the weld root, strain rate and the geometry of the stirring zone after the tool has become worn.

In light of the review of the literature, it can be concluded that there are clearly gaps in understanding the effect of the deformation of the highly viscous flow around the tool on tool wear, and developing a numerical model than can predict the tool wear in FSW.

The study aims to develop a methodology for calculating tool wear in FSW based on a CFD model to predict the effect of the deformation of the highly viscous flow around the tool on tool wear.

This numerical approach should be capable of prediction and comparison of the flow behaviour, the MAZ size and the strain rate distribution around both unworn and worn FSW tools, which may be used to give an indication of the weld quality and of tool lifetime, as well as to provide a guide to assess the flow differences between unworn and worn tools.

The proposed methodology could be used to investigate the effects of process parameters on tool wear and to improve understanding of the effective limits of tool use for welding without the need for experimental trials.

1.3 List of publications

Two papers were published during the study, which are listed below:

1.3.1 Journal paper

[1] Hasan, A., C. Bennett, and P. Shipway, *A numerical comparison of the flow behaviour in Friction Stir Welding (FSW) using unworn and worn tool geometries.* Materials & Design, 2015. **87**: p. 1037-1046.

1.3.2 Conference paper

[1] Hasan, A., C. Bennett, and P. Shipway. *A numerical Methodology for calculating tool wear in Friction Stir Welding*. in *Tribo UK*. 2015. Loughborough University: Loughborough University.

1.4 Thesis structure

Chapter 2 reviews the relevant literature. This chapter includes two main areas that should be covered based on our aims, which focus on material flow in FSW, and tool wear. The tool wear sections include numerical simulation of component geometry changes as a result of wear and tool wear in FSW.

Chapter 3 gives a general overview of fluid flow and describes the applicable governing equations. The concept of solving the fluid dynamics problem numerically using the Computational Fluid Dynamics (CFD) approach is also described. Material constitutive equations and user defined boundary conditions are also outlined in this chapter.

Chapter 4 presents the modelling methodology of the FSW CFD model. This chapter includes the development of a meshing strategy that can be used for further studies. Moreover, as one of the main aspects of this thesis is flow behaviour in the FSW process, the study carried out a validation study for the flow behaviour around a rotating cylinder at different Reynolds number and rotation rates. Also the effect of using strain arte dependent viscosity on the flow behaviour was investigated.

In **Chapter 5,** the study modelled the experimental work of Lorrain et al. [21] in order to determine a strategy to validate the predicted MAZ size and shape. The comparison of the unworn and worn tool geometries in terms of strain rate, flow behaviour, and shape of the weld zones are presented in this chapter.

A methodology for calculating tool wear in FSW based on a CFD model is described in **Chapter 6**, which presents a validation of the experimental results.

Chapter 7 includes a parametric study into the effect of weld parameters on the prediction of tool wear. This includes two parts which are, studying the effects of different rotation rates on the prediction of tool wear, and investigating the flow behaviour for some cases after wear prediction.

In **Chapter 8**, the conclusions and further work were presented, which included the summary of the main finding and suggestion for the future work that can be done to develop this thesis.

Chapter 2 Literature Review

2.1   General FSW modelling

Since the invention of FSW, a large volume of experimental work has been carried out in order to investigate the process and to optimize the process parameters to achieve a sound weld joint for many different materials and material combinations. However, many features, such as material velocity, pressure and temperature distribution, and friction details are extremely difficult to determine experimentally. Therefore, numerical modelling can provide important information regarding the features required for investigating and developing the FSW process. Numerical modelling has covered a wide range of aspects involved in the FSW process including simple heat transfer models, simple flow models and coupled models, which in turn includes coupled thermo-mechanical and thermo-flow models [15, 16].

A large amount of research has been carried out to develop and understand the FSW process; here, the study provides some examples of these modelling techniques, which depend on either the Lagrangian or Eulerian approach. Both approaches require a domain which is discretized using a mesh, in the Lagrangian approach, the domain consists of material nodal points and cells. During analysis, the material points are matched and fixed to the cells, so the mesh deforms with the nodal points and this causes mesh distortion. On the other hand, the Eulerian domain contains cells and spatial nodal points; during the analysis, the nodes remain fixed and the material moves through the mesh, meaning that the mesh and spatial points match [17]. Figure 2-1 represents the Lagrangian and Eulerian approaches. Both approaches are used to

simulate the process and to determine the flow analysis, velocity field, shear stress, thermal history and other features.

Generally, there are three types of process modelling techniques that have been used to investigate and analysis the FSW process, which are solid mechanics models, Computational Fluid Dynamics (CFD) models and analytical models. For the solid mechanics model; a Finite Element method (FEM) is a common approach, while CFD model uses a Finite Volume Method (FVM) as a common approach for the discretization. The FE and CFD models have been used to simulate the FSW process and to understand many features which are difficult to determine experimentally; in addition, the implementation of these models requires a variety of software such as ABAQUS, ANSYS, FLUENT, PROCAST and DEFORM.
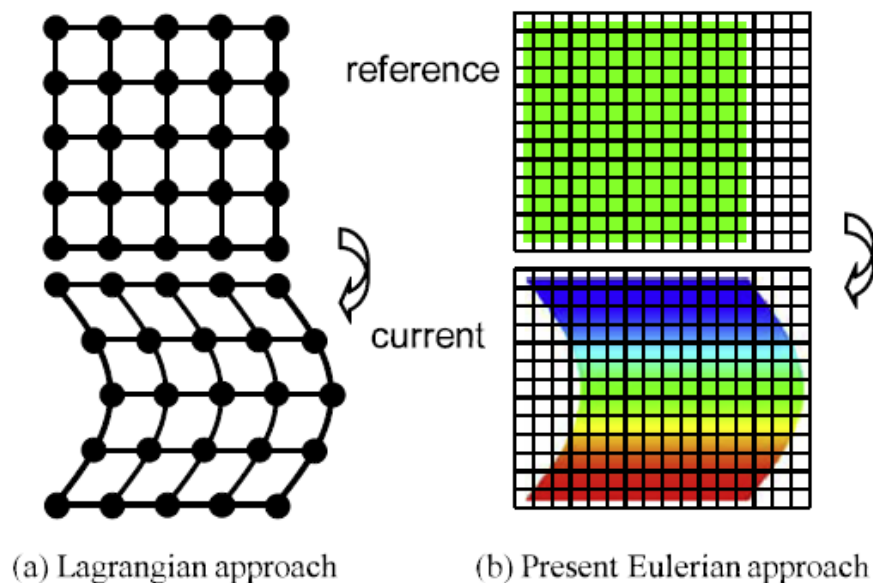
Figure 2-1 The elements and space in both the Lagrangian and Eulerian approaches [18]

One of the early numerical studies was carried out to predict the temperature distribution during the FSW process, using an analytical model, in 2003 by Song and Kovacevic [19]. In their study, control equations were solved numerically and the model described the transient heat transfer during the plunge phase, welding and tool

removal periods. The model considered two heat sources: the first one was frictional heat, which is generated at the shoulder-plate interface, and the second source was heat generated due to plastic deformation of the material in the area surrounding the pin. Frictional heat generation (heat flux rate q_r) was calculated using equation 2-1, thus:

$$q_r = 2\pi\mu_f F_{ni} R_i \omega \qquad\qquad 2\text{-}1$$

where F_{ni} is the normal force applied to the workpiece at each mesh point; μ_f is the friction coefficient; R_i is the distance of the calculated point from the tool axis, and ω is the tool rotation speed (in rev s^{-1}). The results showed that frictional heat generation is the main source of the heat input during the FSW process. It was found that the temperature near the shoulder was close to the melting temperature of the welding material, which was supported by comparison with experimental data.

Chao et al. [7] modelled the heat transfer during FSW using two models. The first one was used to predict the steady state temperature on the tool surface using the ABAQUS FE code. While the second one was used to predict the transient temperature distribution through the thickness of the workpiece utilizing the welding simulation code WELDSIM. WELDSIM was modified for FSW in order to improve the computational efficiency and was used in this study. The workpiece was divided into three layers known as top, mid and bottom. The study did not take into account the radiation between the tool and the plate with the air. The model determined the frictional heat generated between the shoulder and the plate, while the heat generated by plastic work associated with the process was neglected in this study. In this approach, the heat flux rate was calculated based on equation 2-2 below:

$$q_r = \frac{3\,Q_h\,r}{2\,\pi\,r_o{}^3} \quad for\,r \le r_o \qquad\qquad 2\text{-}2$$

where q_r is the heat flux rate; Q_h is the heat flux generated by friction between the tool and the workpiece; r_o is the tool's outer radius, and r is the distance of the calculated

point from the tool axis. The results showed that friction heat is the main source of the heat input to the welding plate and that approximately 95% of the total heat input is to the plate and about 5% is input to the tool surface. These results showed a reasonable agreement with the experimental results of the study.

A numerical approach was carried out by Schmidt et al. [14] to calculate the heat generation in FSW. The analytical model included a slip-stick condition, which, it was argued, could make the model a more realistic representation of the FSW process. The stick condition will occur on the tool surface when the value of the frictional shear stress is higher than the material shear yield stress, in which case the velocity of the interface material has the same value as the velocity of tool surface. On the other hand, the slip condition occurs when the material slipping across the tool surface has a frictional shear stress value of less than that of the material shear yield stress. The study assumed that the heat was generated at the tool–workpiece contact interface; therefore, the calculation was made independently for the shoulder, pin side and pin tip surfaces. In this study, heat generation was calculated using equation 2-3, as below:

$$Q_h = \frac{2}{3}\pi\left(\delta\tau_{yield} + (1-\delta)\mu_f p\right) \times \omega \left(\left(r_s^3 - r_p^3\right)(1 + \tan\alpha_t) + r_p^3 + 3r_p^2 H_p\right) \qquad \text{2-3}$$

where Q_h is total heat generation; δ is the contact state variable; τ_{yield} is the material shear yield stress; ω is the tool angular rotation speed; p is the uniform pressure at the contact interface; μ_f is the friction coefficient; r_s is the tool shoulder radius; r_p is the tool pin radius; H_p is the pin height, and α_t is the tool shoulder cone angle. The results showed that the shoulder surface contributes 86% of the heat generation; while the pin side and pin tip contribute 11% and 3% respectively. The proposed analytical model showed reasonable agreement with the experimental results in term of heat generation.

It is worth mentioning that this analytical model addresses the interface issue and has therefore been used in much of the literature [20-22]; it also provides a good understanding of heat generation mechanisms and calculations in the FSW process.

With regards to the FSW CFD model, an isothermal assumption is normally made for this type of modelling approach as the flow stress value for some aluminium alloys is relatively insensitive across the temperature range from 0.6 to 0.8 of the material melting temperature, as can be seen in some literature (e.g. [13, 22-24]). In addition, some studies have used experimental temperature profiles to construct an approximated thermal field during the simulation, as in the work of Zhang et al. [25]; in both approaches, the solving of the energy equations is neglected during the calculation of the solution. This modelling technique provides the ability to predict the flow behaviour, strain rate distribution, velocity field and pressure distribution on the workpiece and tool surfaces. Details of this modelling technique were demonstrated in (Chapter 2 section 2.2.2).

The two modelling techniques presented above in this section have achieved useful results for the prediction of temperature distribution, heat generation and flow behaviour using mathematical modelling based on solid mechanics or CFD models. In spite of that, some features remain difficult to investigate when using the above techniques. Coupled thermo-mechanical and thermo-flow based models can therefore be used to give a useful insight into the FSW process. A model to simulate FSW was presented by Soundarajan et al. [26] using the ANSYS Finite Element to implement a coupled thermo-mechanical model; temperature dependent material properties (density and thermo-mechanical properties) were considered during the analysis and the maximum temperature was maintained to be less than 528°C, which is the solidus temperature of aluminium alloy 6061 to ensure the simulation was carried out below

melting temperature. The study found that the friction coefficient between the tool and workpiece was considered to be in the range of 0.4 -0.5, dependent on interface temperature. The results showed the ability of the model to predict the stress distribution across the workpiece, and the thermal history for the tool-workpiece during the plunge and tool removal periods. There was a good correlation between the experimental data and predicted temperature.

Sadeghi et al. [27] developed a coupled thermo-mechanical FE model of the FSW process implemented in the DEFORM and ABAQUS codes in 2013. The output results of the DEFORM model was a thermal history in the workpiece, which was fed into the ABAQUS model, due to the fact that this methodology avoids excessive computational time. In this work, the DEFORM model was used to implement a rigid-viscoplastic material behaviour, while the ABAQUS model was used to implement elasto-plastic behaviour in order to obtain residual stress. The study predicted the temperature distribution and longitudinal residual stress along the traverse distance to the workpiece. The predicted results were compared with experimental data for the retreating and advancing sides and showed an acceptable agreement. The work indicated that the developed model can be used as a non-destructive method to predict the residual stress thorough the thickness of the FSW plate.

The CFD code, FLUENT was extended in 2014 by Zhang et al. [28] to simulate the FSW using a coupled thermo-flow based model. The model includes heat generation calculations based on interface conditions and a visco–plastic material model. The study investigated both the thermal history and flow behaviour during a simulation of the welding process. In the study, the velocity profile and material viscosity in a region surrounding the tool were predicted by this model. The study also determined that the shoulder generates heat more that the pin side and pin bottom surface, with the

contribution of the shoulder being about 88% of the total heat input, while the contribution of the pin side was 10.48% and 1.52% for pin bottom surface. The model also provided an understanding of predicted flow and deposition in the zone surrounding the tool surface. The predicted temperature results were validated experimentally and showed a good correlation.

2.2   Material Flow in FSW

FSW is considered a complex process because it depends on frictional behaviour to generate heat in order to produce a solid-state joint. There is a thermal effect, which is generated by the friction between the tool and work-piece, and a mechanical effect from the tool motion, resulting in a stirring action, which produces metal flow resulting in high plastic deformation.

Since 1991, when FSW was invented, many researchers have looked into the complex phenomenon of metal flow under solid-state conditions. Many experimental works have been carried out and several numerical models have been developed to study the flow behaviour and also to optimize the process parameters to enhance the microstructure and joint mechanical properties. Material flow has an effect on the choice of FSW tool material and design, particularly with high strength and high temperature alloys such as steel, nickel and titanium [29, 30].

The flow in FSW is complex due to the interactions of rotational and axial motions of material that occur during the process. According to the literature, the flow regimes in the process can be divided into two directions, which can explain the primary characteristics of the flow as shown in Figure 2-2:

The horizontal plane can be considered the primary plane in which the shear flow of the material is generated. Once the tool rotation is started, the material is wiped from

the advancing side of the plate (AS) in the area where the material is rotated and advanced with the tool translation. In other words, the material under the shoulder zone is subjected to high deformation because of the frictional motion, and moves from the advancing side, producing arc shaped structures. The axial motion of the tool continues along the welding direction, according to the stirring action of the shoulder and pin; therefore, the deformed material will move from the retreating side (RS) to the advancing side in a same direction as the tool rotation direction. The material under the shoulder is subjected to the highest deformation due to the shoulder motion. Then, the flowing material in the vertical plane is pulled down along the weld thickness by the pin from the nugget zone and flows to the weld root (located below the nugget zone, under the end of the pin and contains spoon shaped features) near the bottom; then, it moves upwards into the area beyond the pin. Finally, the deformed material flows up towards the upper part of the workpiece due to the vertical movement of the tool [31].
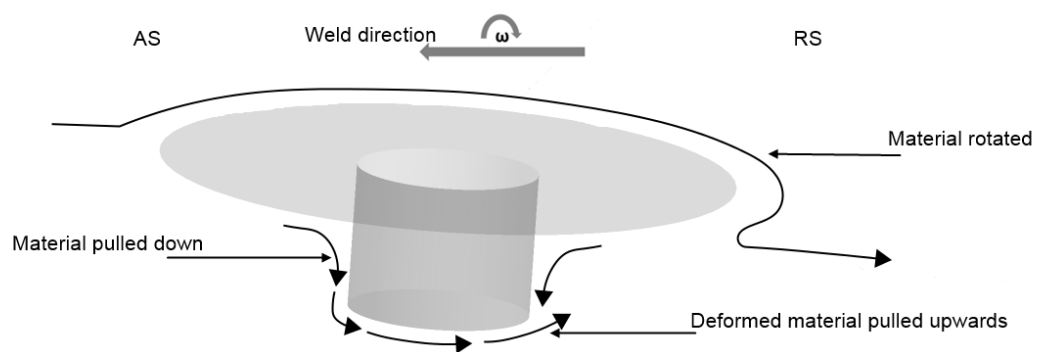
Figure 2-2 A schematic diagram explains the material flow in the FSW process

In the vertical direction, the weld is split into zones, which are the large mixing area or shoulder squeeze area, and the nugget zone which contains onion ring patterns; the

zones are shown in Figure 2-3, and Figure 2-4 depicts the onion ring zone. The gross flow of the weld along the weld centre line is different because it is dependent on heat input, which is related to the process parameters. Therefore, the flow regimes in this area would probably affect the thermal and mechanical properties of the weld joint. The highly deformed material in this plane rotates around the longitudinal axis [31-33]. The metal flow regime through the weld thickness is identified by spiral or vortex patterns. Then, it seems to flow along the weld line with tool rotation. The combination of the stirring action due to the tool rotation and the extrusion of the deformed material around the pin causes a circulation in the vertical plane.
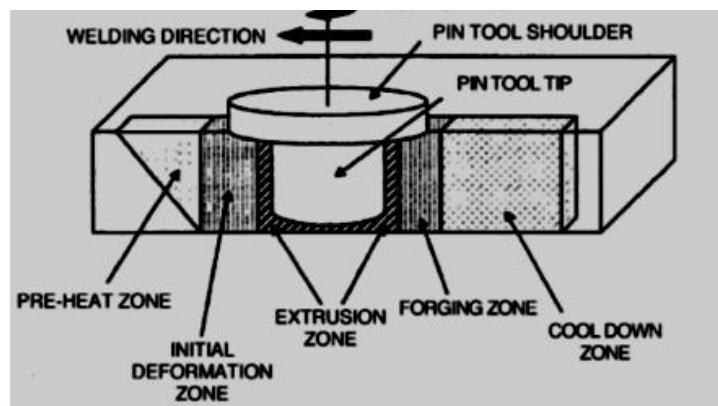
Figure 2-3 Processing zones in FSW and material flow patterns [3]
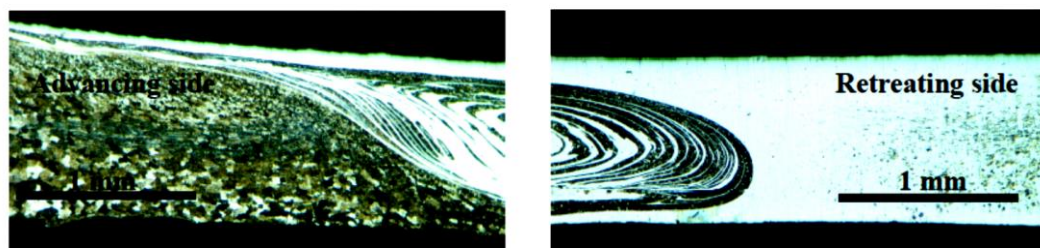
Figure 2-4 Onion ring zone (Nugget zone) in the FSW Process [34]

According to Attallah et al. [35], there are five conventional working zones during the process, which are the preheat zone, the initial deformation zone, the extrusion zone, the forging zone and the post heat/cool down zone as shown in Figure 2-3. Essentially,

these zones form due to tool rotation and traversing along the weld line and they form from the zone which abuts the shoulder edge; where, the frictional heat is generated and material deforms plastically due to tool movement. Several microstructurally distinct zones form in relation to the tool stirring action and in the area surrounding the tool; the schematic of those zones can be seen in Figure 2-5.
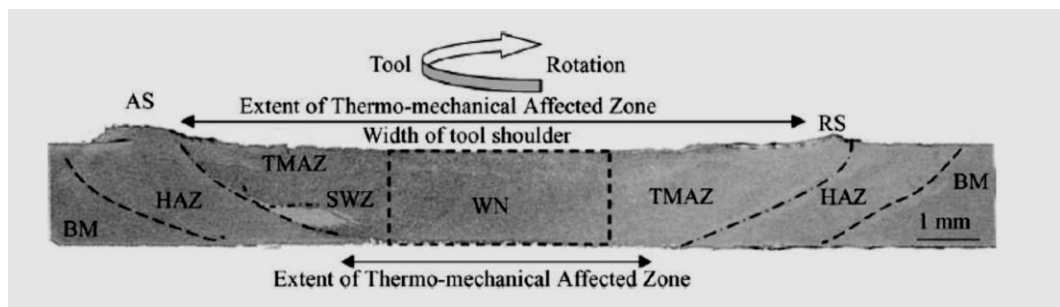
Figure 2-5 FSW microstructural zones according to Attala for AA2095 Al-alloy[35]

Different microstructures form during the FSW process which are fundamentally related to the main microstructure zones formed through the process, namely, the nugget zone (WN), the Mechanical Affected Zone (MAZ) (Note that in Figure 2-5 dented as TMAZ), the Heat Affected Zone (HAZ). The WN zone is located close to the tool and experiences highly plastic deformation and heat-induced microstructural changes result in a fine grained microstructure. The MAZ is between the HAZ and the nugget zone [36, 37]; one of the features of MAZ is that it experiences slight plastic deformation and heat-induced microstructural changes. The last zone is HAZ; the main feature of this zone is that it does not undergo plastic deformation, but is subjected to the thermal cycle that occurs during the process [38]. The grain structure in this zone is similar to base metal grains, which means dynamic recrystallization does not occur and grain growth is reduced [39]. However, only dissolution of the strengthening precipitation of the secondary phases can be seen there; particularly for the aluminium alloys [40].

2.2.1 Experimental Material Flow Visualization

Various techniques have been used to investigate the material flow during the FSW process, and the majority of this work has focused on aluminium alloys. In this section, it can be seen that different techniques, such as the use of steel shot tracers, plasticine material, dissimilar joints, copper foil and the stop action technique have been utilized to track the metal flow during the FSW process. The majority of these studies used microstructural investigation techniques to observe the material flow patterns during the process.

One of the earliest trials to investigate the material flow in the FSW process was carried out by Colligan [41], who used steel shot tracer material. The results of this technique revealed that the material rotated with the shoulder at least one full rotation, then extruded under the pin, with the material flowing upward behind the pin. The material was stirred on the top surface before being pulled down by the threads and the extrusion could be considered the main factor for metal translation. It also showed how the extrusion of the material on the retreating side around the pin is driven upwards in the process as it advances around the pin. However, in the study, the tracer material used was insufficient to provide useful visualization of the vertical motion of the flow. Material flow visualization and dynamic re-crystallization phenomena that occur during the FSW process were observed along the weld line by Li et al. [42]. Metallographic examination was used to investigate the FSW mixing and flow patterns, while Transmission Electron Microscopy (TEM) was used to reveal the interaction of the alloy and homogeneous material at the weld centre. According to the metal flow visualization, the study indicated that there was a complex flow which appeared to move in a spiral-like motion. The work indicated that good mechanical

properties with good microstructure in the upper, nugget and bottom zones along the pin axis could be achieved by using FSW; it also revealed that a soft region occurred in the bottom zone, which should be removed by controlling the process parameters to enhance the metal flow there.

A marker insert technique was used by Seidel et al. [31] to visualize the material flow in the FSW. The marker material used in the process was made from AA5454-H32 alloy and was embedded in line with the FSW tool on the faying surface. Faying surface is one of the plate surfaces that are in contact at a joint of the weld. The microstructure and the material flow were investigated by metallographic examination. In addition, the mechanism of the material movement on the advance and return sides was determined by the study. The flow pattern was not symmetric around the weld centre line and it appeared that the material was transported to the zone just behind the original position. On the horizontal plane, the primary flow circulated along the longitudinal axis of the weld. However, the study was limited in terms of reconstructing the actual flow path of the material. Moreover, the study concluded that the relationship between weld pitch; which is defined as the ratio between the FSW tool travel speed; and rotational speed of the tool; and weld energy was inversely proportional and this caused an increase in the movement of marker material from the weld bottom retreating side to the upper side.

Guerra et al. [33] and Dickerson et al. [43] investigated the flow pattern during friction stir welding. The work used copper foil and copper strips of 0.1mm thickness, which were sited on the faying surface of the lap joint. The investigation showed a significant vertical flow mixing in the weld, which was generated by the vortex motion due to pin threads movement. The study showed a similar behaviour in flow pattern to that

described in the work of Seidel et al. [31] and Colligan [41] in terms of the weld zone along the pin axis having a helical motion of flow on the vertical plane.

In a study by Liechty [44], different colours of plasticine were placed along the weld joint by a hydraulic press within a 15mm thickness to visualize the material flow in the FSW. The observation of the marker materials showed that a small amount on the advancing side moved forwards with the tool motion in the weld direction, while a larger proportion of the material moved backwards by approximately a 1 pin diameter. This behaviour of the material flow on the horizontal plane showed agreement with Seidel et al. [31] and Guerra et al. [33] findings. Another interesting point from the study was that, at a low traverse rate, a low rotation speed showed a low mixing rate in the flow of the metal. In contrast, high values of rotation speed and traverse rate caused removal of the material under the shoulder away from the weld surface.

A tin plate of 0.05mm thickness was used in an experimental study for tracking the material flow in FSW by Hamilton et al. [45]. They showed how the weld nugget zone was formed by surface material from the retreating side. The material flow pattern on the retreating side of the weld is shown in Figure 2-6, which demonstrates how the material moves in the opposite direction to the material from the advancing side, while Figure 2-7 illustrates how the nugget zone forms from surface material in the area located under the shoulder, which is extruded from the retreating side to form the nugget zone, which has high plastic deformation. The observations of this study were consistent with those noted by Seidel et al.[31] and Guerra et al.[33].
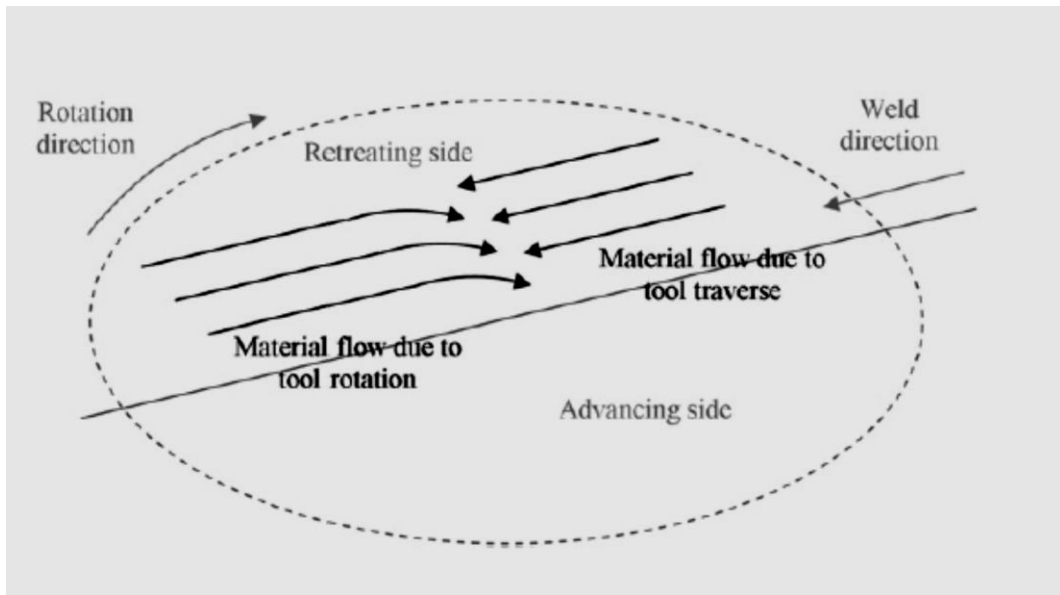
Figure 2-6 Material flow pattern on the retreating side of the weld [45]
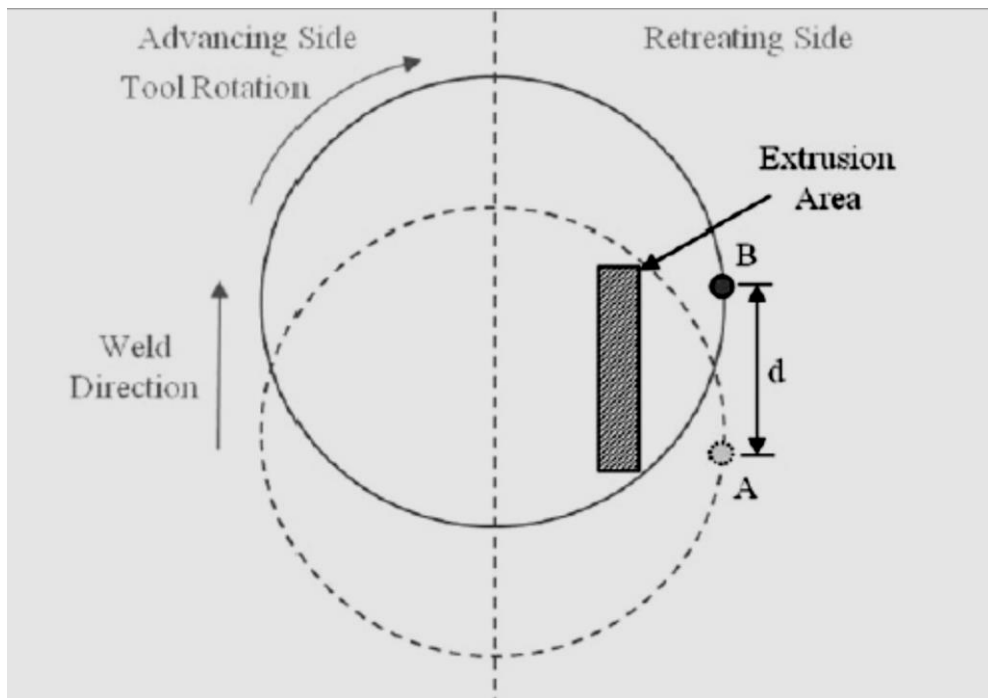
Figure 2-7 Tool advance and extrusion area per revolution.[45]

The "Freeze" technique could be considered one of the most important methods in the study of metal flow in FSW, and is carried out by breaking the tool pin of the FSW process during the welding with the pin embedded in the workpiece. This is accomplished by continuing the welding process until the failure occurs, at which point

the rotation of the pin will stop. This technique was used to study the flow behaviour and formation of the nugget zone in FSW by Chen et al. [32]. A better understanding was gained about the nugget zone is formed than was possible in previous literature, such as in the work of Dickerson et al. [43] and Hamilton et al. [45]; thus, the phenomenon of metal flow presented in the previous literature is similar to the observations of this work in terms of how the material is swept from the advancing side to the retreating side and vertical flow of the material around the tool.

2.2.2 Numerical Material Flow Visualization

Over the past few years, metal flow visualization has been examined by various studies using either FE or CFD models. The effect of process parameters on the FSW was modelled using two approaches by Reynolds et al. [46]. The first was a thermal model to calculate the temperature profile. The input parameters of the first model were input power (which is input torque multiplied by the tool rotational speed), thermo-physical material properties and tool geometry, and heat flux was applied through the application of equation 2-1. The second approach was a 2-D CFD model. The result of the first model showed that welding energy is inversely proportional to welding speed, which is sensitive to the weld pitch, except at low welding speeds. The study argued that the increase in the weld power and welding speed could give high peak temperatures in a short time. On the weld advancing side for both cases, the results of the second model showed that the flow bifurcated outside the tool diameter when the rotation rate was low, while a bifurcation of the flow occurred very close to the tool diameter in case of high rotation rate. From the study, the second model gave a physical understanding of the x-axis force (drag force) behaviour, which was based on observations of the streamline metal flow. However, due to the 2D nature of the flow model, it could not give any details about defects caused by lack of penetration or on

the volume of material which is transferred to the retreating side, as well as how this is replaced by the moved volume with tool transition and flow bifurcation around the pin.

A stick condition at the FSW tool surface was implemented by Colegrove et al. [13, 47] and Aljoaba et al. [48] who examined the metal flow in FSW using different tool geometries. Coupled thermo-flow based models and isothermal flow analyses were performed with 2D and 3D CFD models using the commercial code FLUENT. This work described the flow of the metal through the use of streamlines and velocity vectors and predicted that workpiece material would be swept from the advancing side to the retreating side of the pin before flowing vertically down near the surface of the pin until it reached the weld root, whereupon it would flow upwards towards the upper part of the workpiece behind the pin. In addition, the stick condition was also used recently by Kim et al. [17] and Ji et al. [24] when they examined the metal flow in FSW using 3D CFD models. Their findings in terms of flow patterns are in agreement with those seen in the experimental literature of Seidel et al. [31], Colligan [41] and Dickerson et al. [43]. Moreover, the study predicted the values of the welding torque, the traversing force of the weld, strain rate and thermal profile.

While these models provided useful insight in terms of material flow, the models were limited to qualitative prediction of the size of the deformed zone based on a region provided by a limiting value of strain rate, which may be the reason for the over-prediction of the deformed zone in these works. Another important point when considering these works was that the contact interface between the material and the tool was only considered as a sticking condition, which may again lead to an over-prediction of the deformed zone due to the likely presence of slip on some areas of the tool. In addition, mesh quality was a drawback of these studies, leading to the

suggestion that further development is needed to avoid any numerical error which could occur during the simulation.

To address the issue of slip- stick conditions on tool surface, Colegrove et al. [47] developed a novel approach by considering the partial slip conditions on tool surface. The study specified two values of the shear stress as a shear limit and predicted the value of the shear stress on the tool surface through the use of a UDF for this model. The CFD model was implemented in the commercial code FLUENT. The study compared the flow behaviour around different tool designs. The study showed that slip is more likely to occur during the FSW process and material stick and slip regions were determined through the model. The study provided a useful understanding of the tool- material interface and this approach could be used to avoid the over prediction of the power required for the welding process.

Zhang et al. [49] examined the flow behaviour on the retreating side and advancing side in the FSW process. A 2D model was developed in order to understand the mechanism of FSW. The FEA model was created in the ABAQUS software and a slip –stick condition was implemented using equation 2-4, which was used as an upper limit for the value of shear stress. This was to provide less shear friction than shear yield, leading to a slip condition at the interface between the tool and welded material.

$$\tau_c = \frac{\sigma_{yield}}{\sqrt{3}} \qquad\qquad 2\text{-}4$$

where, τ_c is the critical shear stress and σ_{yield} is the yield strength of the material. The study showed that the material on the retreating side never rotates with the pin, while on the advancing side the welded material forms a fluidized bed (this term refers to a zone near the tool surface where significant plastic deformation occurs) around the tool and separates after a few revolutions. The model was compared with the results of Reynolds et al. [46] and Deng et al. [50], which were mentioned in the paper, and

these results were validated in terms of equivalent plastic strain distribution and flow behaviour. However, the validation results could have been presented graphically on the paper to add further support. Although the study provided useful insight in terms of material flow and strain rate distribution in the weld zone, it was limited in providing a realistic slip model because it considered a constant value for the critical shear stress. The strain rate distribution during FSW was addressed by Buffa et al. [51] through the simulation of the FSW using the DEFORM-3D finite element software including a visco-plastic material model. The study examined both conical and cylindrical tools with different dimensions in order to optimize the tool geometry with different process parameters in an attempt to increase the size of the nugget zone whilst simultaneously producing uniform grain size refinement within this region and a more uniform temperature distribution and flow through the thickness. The results showed that as the pin surface area increases, a larger MAZ could be obtained with an increase in the material circulation around the pin. The study also demonstrated that the increase in the pin surface area provides a more uniform distribution of parameters such as temperature and strain rate through the thickness of the workpiece, both of which have been shown to be favourable for obtaining higher joint strength. In spite of the informative results presented in this work, the model was limited in its consideration of the condition of the contact interface and quantitative validation for the size of the deformed zone.

Nandan et al. [20] used experimental work and an analytical model to study the heat transfer and viscous plastic flow of a mild steel plate joined by FSW. A 3D-model was implemented to solve the equations of conservation of mass, energy, and momentum. The calculation of the non-Newtonian viscosity of mild steel flow was based on temperature and strain rate dependent flow stress. The results from the numerical

model showed that near the tool, a high plastic flow occurred and the main mechanism of the heat transfer was convection. It also illustrated how the fluid flows on the retreating side with highly viscous plastic flow close to the surface; this flow behaviour was similar to that documented during the experimental observations by Seidel et al. [31]. The model provided good insight in terms of material flow, viscosity and strain rate distribution in the weld zone. Moreover, the study provided useful information about the fractional slip and friction coefficient between the tool and workpiece. The main limitations of the study were computing and validating the size of the weld zone. 3D and 2D axisymmetric FSW models were developed by Colegrove et al. [52] using the ANSYS FLUENT CFD software. The models aimed to predict temperature of the weld by examining the thermal properties and flow behaviour of the hard and soft alloys at different rotation speeds. The model also took into account the stick-slip condition at the tool shoulder interface, which was implemented by specifying the velocity at the shoulder, which was set to equal pin velocity at the junction between pin and shoulder and then linearly decreased to zero at the periphery. A value of 5 mm s^{-1} was chosen as an indication of the plastic deformation limit. The results of the study showed agreement with the experimental study in terms of the flow deformation of the rotating material under the shoulder near the tool surface; for the hard alloy, the study indicated some local deformation at a high rotation rate. The localisation of the flow was a consequence of the material properties that were used in the model. High rotation speeds caused more localisation of the flow due to using an Empirical Softening Regime between solidus and melting temperature which was arbitrarily set to 50°C for each. This resulted in a smaller deformation region. Thus, there was a correlation between the macro-section experimental results and the flow, visualised in terms of the velocity profile, that was predicted by the model. Figure 2-8 shows that the

simulation results agreed with experiential in prediction of the smaller area of deformation at a lower rotation speed (400 rpm); this area is located under the shoulder when using the slip boundary condition.
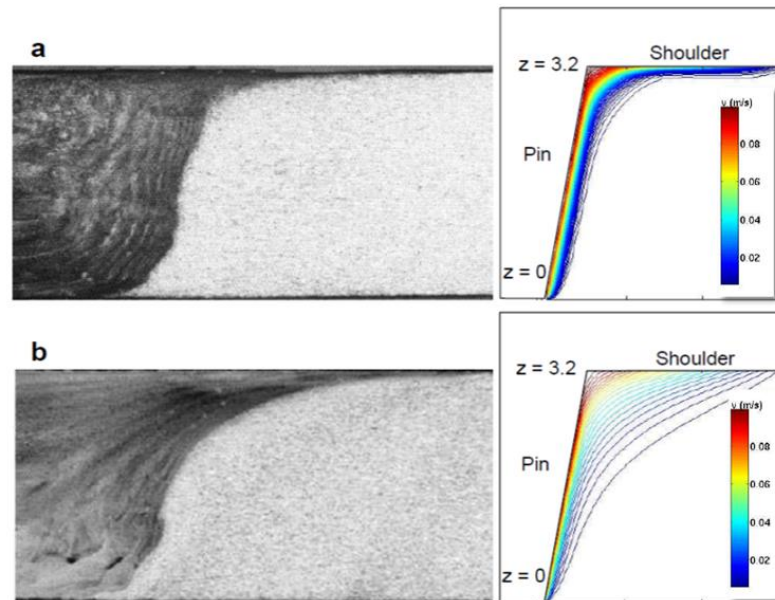
Figure 2-8 Experimental weld micro-section with simulation flow diagram at (a) 1600 rpm and (b) 400 rpm rotation speeds and 0.2 m/min welding speed for 2014 Al alloy.

Finally, it is clear that the novel modelling technique presented in the study provided a good understanding for material deformation at different welding speeds in the weld zone. However, it was limited to providing qualitative assessment in terms of predictions for the size of the deformed zone, and the slip model needed further development to determine it as a function of the tool radius and welding parameters. Geuerdoux and Fourment [53] developed an FE model to calculate the temperature development and to monitor the flow behaviour during the process using threaded and unthreaded tools. This approach was implemented with the FORGE 3 FE software. The study assumed the contact condition between the tool and workpiece simply as a 'foot print', meaning that the shoulder was only just in contact with the plate. Additionally, it is worth mentioning that, in this study, different friction coefficients

were considered. The developed approach showed agreement with the experimental results in terms of shape of MAZ, as shown in Figure 2-9, which illustrates the extension of MAZ on both sides of the shoulder and downward along and underneath the pin, which was also presented numerically; in addition, the figure also shows the MAZ experimentally and numerically at 5.4s in terms of equivalent strain rate. However, the study indicated some limitations related to the friction contact parameters; the author argues these difficulties are due to a high strain rate and temperature gradient near the interface between the tool shoulder and the plate.
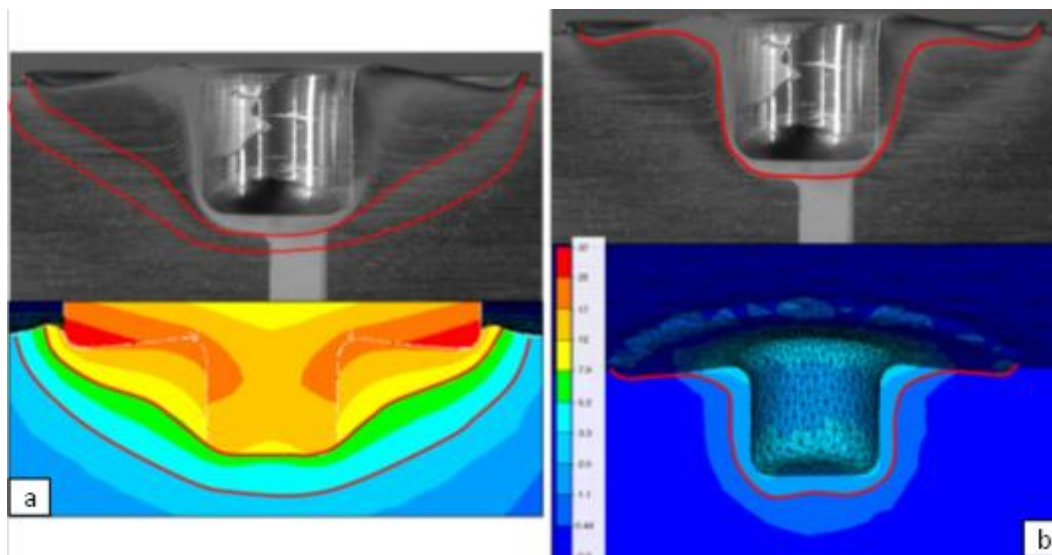
Figure 2-9 Experimental observation and numerical study: (a) shape of thermal zone and simulation temperature profile, (b) observation of MAZ with simulated equivalent strain Geuerdoux and Fourment [53]

A 3D finite element model of material flow and temperature distribution in FSW of an Aluminium alloy was developed by Santiago et al. [54] to predict the temperature distribution and flow of the material. A slip-stick condition was considered in this work. In addition, it was assumed that the whole tool surface had uniform relative slip of 50% with the interface material. The results of the flow behaviour that were reported in this work were consistent with previous observations presented in the above

sections. The shape of the weld zone was calculated using the model by plotting the iso-surface velocity at values of 3 mm s^{-1}, 5 mm s^{-1} and 20 mm s^{-1} respectively, as shown in Figure 2-10. From the figure it can be seen that at a velocity value of 3 mm s^{-1} and 5 mm s^{-1}, the deformed zone was larger on the retreating side than on the advancing side, whereas at a at velocity value of 20 mm s^{-1}, the predicted deformed zone was symmetrical about the pin axis.
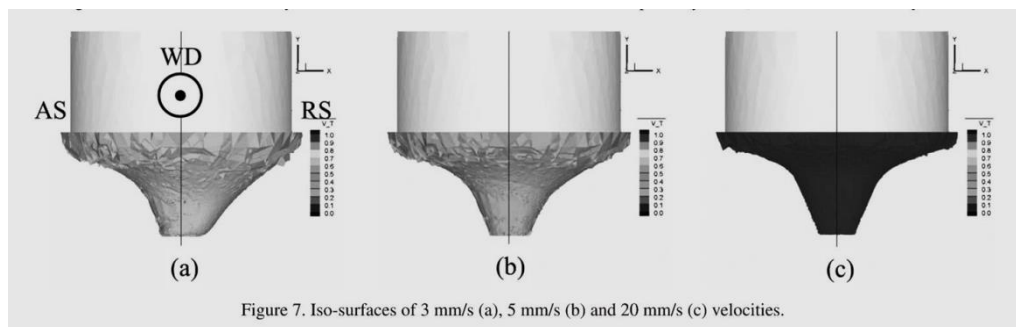
Figure 7. Iso-surfaces of 3 mm/s (a), 5 mm/s (b) and 20 mm/s (c) velocities.

Figure 2-10 Iso-surface of the velocity at (a) 3mm s^{-1}, (b) 5mm s^{-1}, and (c) 20mm s^{-1} [54].

While the works by Guerdoux and Fourment [53] and Santiago et al. [54] produced many interesting results, little has been achieved in terms of slip condition and quantitative validation of the deformed zone, which needs further investigation.

A new Combined Eulerian-Lagrangian (CEL) fully-coupled thermo-mechanical model of the FSW process was produced by Grujicic et al. [55] wherein a finite element model was defined in the ABAQUS software. The effect of the process parameters on the material flow in the workpiece, such as weld pitch, tool tilt angle and the pin diameter, were examined. It is worth noting that this model considered the slip-stick condition at the interface between the tool and workpiece; it was assumed that this condition was limited by prescribing the value of shear friction at the interface, when the shear friction is larger than the material shear strength, sticking occurs; otherwise, slip will occur. The simulation results revealed that the highest attainment of marker material dispersion was at the lowest value of the weld pitch. It was argued

that at a constant traverse speed, increasing the tool rotation speed would increase the heat input in to the workpiece, which softens the material for stirring. The study also showed that increasing the tool pin size could extend the marker material stirring at the welding line. This modelling approach, however, provided only limited details for the contact interface, and the study findings were not validated by the experimental data.

Jacquin et al. [56] developed a 2D axisymmetric thermo-mechanical model, which was proposed by a previous study [57]. The model was implemented in the ABAQUS software in order to investigate the flow behaviour and a partial sliding condition was considered in this study. The study determined the sliding velocity through use of equation 2-5 .

$$V_{slip} = V_{tool} - V_{mat} \qquad\qquad 2\text{-}5$$

where V_{slip} is the sliding velocity, V_{tool} tool rotational velocity and V_{mat} is the surface velocity which was calculated based on equation 2-6:

$$V_{mat} = \frac{h_t \sqrt{3}\, \dot{\bar{\varepsilon}}_m}{r_m} \qquad\qquad 2\text{-}6$$

where h_t is the height of the flow arm zone (which was defined as the zone for the torsion velocity field; and h_t value was determined in the model); $\dot{\bar{\varepsilon}}_m$ is the mean strain rate and r_m is the tool mean radius and takes the following form: $\left(r_s - \frac{r_p}{2}\right)$ where, r_s is the shoulder radius and r_p is the pin radius. V_{mat} was found by iteration on the model and started with an initial value of 0.1 from the tool rotation velocity.

The circumferential velocity field, with and without tool rotation, is given in Figure 2-11, which shows the influence of the circulation intensity on the flow lines; this field results in asymmetry between the advancing and retreating sides of the weld.
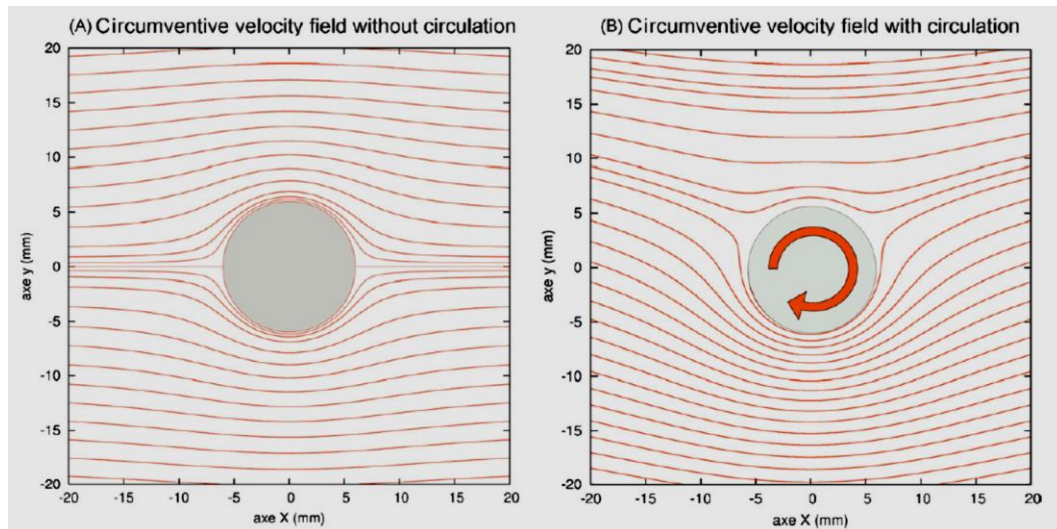
Figure 2-11 Influence of the rotation intensity on the flow lines [56]

A direct correlation between the tool rotation velocity and sliding ratio was shown, while the sliding ratio decreased at the zone beside the tool area that has a low temperature. The work emphasized the sliding ratio control of the metal flow in order to minimize the thermo-mechanical loading on the tool. The authors argued that when the sliding ratio has a high value, this would lead to an amount of the material under the shoulder being removed, or local melting which causes welding instability. However, if the value is small, it could cause a high degree of sticking on the metal flow, and then the torque value would increase for the tool, leading to tool failure [56]. While a 2D axisymmetric model cannot be used to represent the details of the whole process, a 3D model provides a more realistic representation for the FSW process in terms of the weld zone shape and size; thus, this can be considered the main drawback of this approach.

Over two decades, many numerical simulations have been implemented to develop the FSW process; however, many difficulties have arisen, such as welding different materials, high levels of deformation generated during the process, and mesh distortion. Most of the models have used Lagrangian or Eulerian approaches, or a

combination of the two. However, some studies used a meshless approach to solve some of the difficulties of mesh technique. A novel approach has been developed by Pan et al. [58] to simulate the material flow and the mechanism of material mixing. This new approach used Smooth Particle Hydrodynamics (SPH), which is a meshless technique. A 3D SPH model for FSW was implemented to study a non-Newtonian flow and to indicate the growth of the microstructure for that particular alloy. The study took into account the stick-slip condition that occurs between the material being welded and the tool, to avoid over prediction of heat generation when a no-slip condition is imposed. A partial slip constant D was included in the flow stress σ_f equation (equation 2-7) and the value of D took a value of 0.1, thus:

$$\sigma_f = D\sigma_R \sinh^{-1}\left[\left(\frac{Z}{\beta}\right)^{1/m}\right] \qquad 2\text{-}7$$

where, σ_R , β and m were the material constant and Z was the Zener–Hollomon parameter; details of these equations can be found in [58]. This work examined the effect of the traverse speed and tool rotation speed on temperature evolution, material tracking and the distribution of the grain size; the results of material tracking can be seen in Figure 2-12. The model results were compared with the results of Darras et al. [59] qualitatively. Their study had some limitations in terms of metallurgical and texture evolution, and they suggested including hyper elastic-viscoplasticity properties with the SPH model to address this. In addition, one of the most common limitations of using SPH is computational limitations in terms of memory size and CPU time [60].
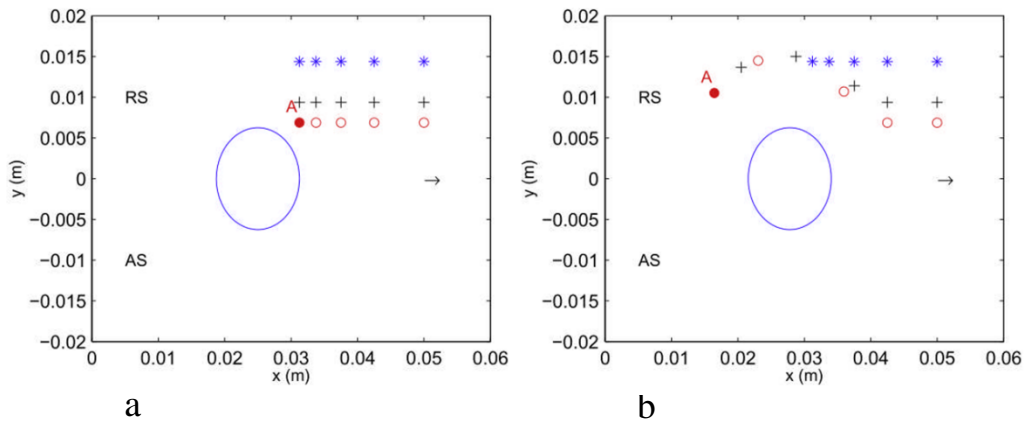
Figure 2-12 Material flow on the surface of the retreating side (RS): (a) t = 0s and (b) t = 0.9s [58]

2.2.3 Final remarks on flow behaviour

Visualization of the flow behaviour in FSW have been extensively studied experimentally and numerically. Regarding the experimental approach, different techniques have been utilized to track the metal flow during the FSW process, such as steel shot tracer [41], marker insert technique [31], copper foil [33] or copper strip [43], tin plated [45] and freeze technique [32]. These studies described the flow behaviour of the metal and showed that workpiece material is swept from the advancing side to the retreating side of the pin, before flowing vertically down near the surface of the pin until it reaches the weld root, whereupon it flows upwards towards the upper part of the workpiece behind the pin. Microstructural investigation techniques have also been used to observe the material flow patterns during the process; the results gained from these efforts have provided a better understanding of flow patterns during the process. However, all the studies reviewed so far were done using experimental methods which are costly in nature and can be easily replaced by numerical methods provided that all the historical experimental data is available. Indeed, this can be considered the main drawback of these studies, which can prove costly from an economic perspective.

Many important features during the FSW process could not be captured and it is difficult to understand the physics of the process and many phenomena by experimental study alone. There are many numerical studies which have been established and reviewed in this chapter, including some where empirical data has been included for validation and verification. Insight gained from these studies can be used to develop a model that can provide a better understanding of features that cannot be studied experimentally in order to develop the FSW process.

As can be seen in this review, some of the numerical studies considered the stick condition at the contact interface between the material and the tool [23, 24, 46, 48, 61], while others considered the partial slip condition by assuming a constant critical shear stress [49], constant velocity value at the shoulder - as in the work of [52] - and uniform relative slipping [54]. A further development has provided a good understanding of the stick-slip approach [20, 56, 58]. It is clear that these studies have provided a good insight in terms of material flow and temperature distribution; furthermore, they have shown reasonable agreement when compared against experimental works. However, the bulk of the literature concerning the numerical modelling of the FSW process has demonstrated over-prediction of the temperature, power input and the size of the MAZ when comparing the results of simulations with experimental observations, and little detail was provided on the effects on the weld root area.

It can be concluded that using partial stick-slip condition on the tool surface reduces the heat input and avoids material melting at the interface between the tool and workpiece, and for this reason material deformation under the shoulder will be reduced.

2.3 Tool wear

Tool wear plays a significant role in the economy of many machining processes. Wear is a complex phenomenon as it is related to the mechanical or chemical properties of the tool and work-piece material.

The tool wear can be calculated simply by considering the wear rate (volume loss per unit distance) of the material combination. Tool life can be defined as the period of working time of the tool before failure or the presence of any defects on the surface of the product [62].

To understand tool wear in the FSW process, this study will start by providing a theoretical background on wear phenomena in general. Then, published literature on tool wear in some machining processes and the FSW process will be discussed. The aim of this section therefore, is to outline current understanding of wear mechanisms and tool wear assessment methods to provide a basis for the modelling of tool wear in the FSW process.

2.3.1 Wear

Wear in materials can be defined as the material removed from a surface due to relative motion such as a rolling or sliding under contact conditions. Depending on the industrial application, this phenomenon can be considered desirable or undesirable; for instance, in polishing and machining, 'wear' is desirable. However, in other applications such as cams, seals, bearings, gears, drills or other machining tools, wear is considered undesirable [63].

There is always some mechanical element to a wear process, although the process may also involve chemical changes of material, with these chemical changes influencing both the rates and mechanisms of materials removal [63].

There are five main types of wear [64, 65]:

- Adhesive wear

- Abrasive wear

- Surface fatigue wear

- Corrosive wear

- Diffusion wear

In the next section, the details of adhesive and abrasive wear will be discussed as these are relevant to the FSW process [66-69].

2.3.1.1 Adhesive wear

Adhesive wear occurs when two flat surfaces make contact with each other at the interface asperities, where bonding between the asperities takes place due to adhesion. During sliding, a breaking of the asperity junctions occurs and this could lead to loose wear particles or transfer of material from one surface to the mating surface. Another possible cause of wear particles is the repeated loading and unloading process, causing fractures in the contact area. Figure 2-13 illustrates schematically the process of adhesive wear. This type of wear is commonly described by the Archard equation, which is presented in equation 2-8, thus:

$$V = k\,W\,S \qquad\qquad 2\text{-}8$$

where V is the total wear volume; k is the dimensional Archard wear coefficient, which is dependent on the material and surface cleanliness; W is the applied load and S is the sliding distance.
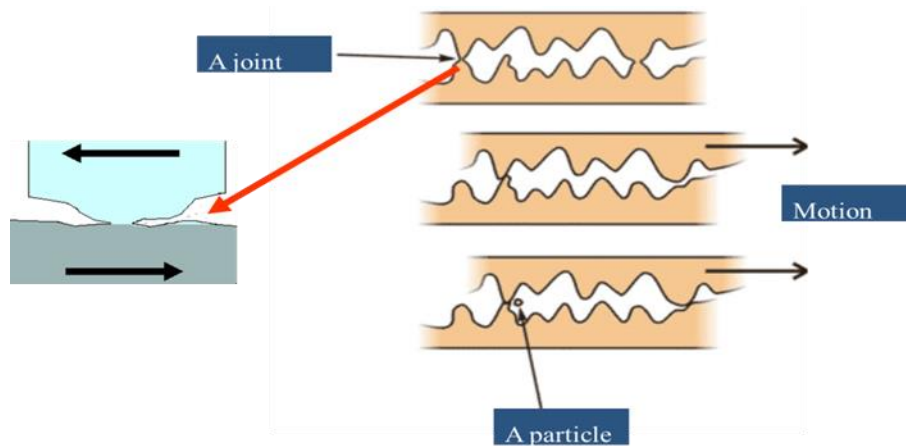
Figure 2-13 Two surfaces in intimate contact with each other during sliding, represents adhesive wear

[70]

The most common manifestation of adhesive wear is when fragments of material from one surface material can be seen on the other surface and the rate of wear is gradual [71].

2.3.1.2 Abrasive wear

Abrasive wear takes place when a hard, rough surface slides on a soft surface or when a surface of low hardness is ploughed by a hard body under relative motion. Plastic deformation could be the primary factor for material loss. Rabinowicz [71] outlined a simple way to model the abrasive wear by assuming a conical shape for the abrasive particle as shown in Figure 2-14, and assumed that all the material displaced was removed; in this case, the volume loss due to abrasive wear is expressed by equation 2-9.

$$V = k_{ab}WS \qquad\qquad 2\text{-}9$$

The similarity in form with the Archard wear equation (equation 2-8) should be noted. It has been determined that the abrasive wear coefficient k_{ab} is typically between 10^{-4} to 10^{-1}; this range depends on the material parameters and contact conditions [64].
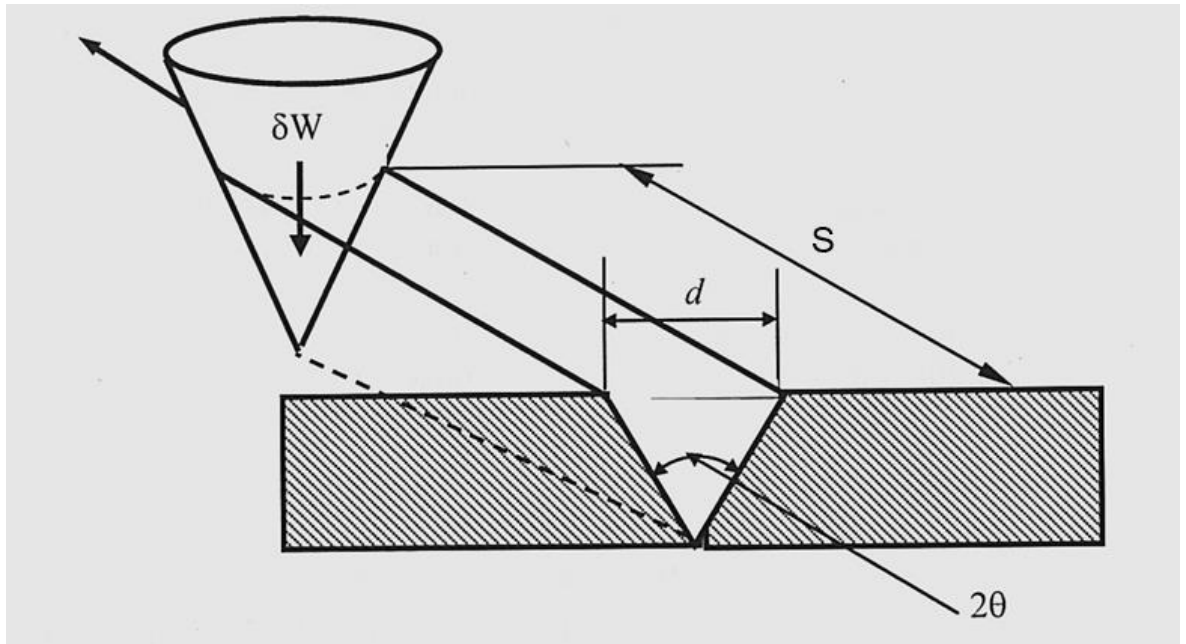
Figure 2-14 Schematic diagram representing the abrasive wear process [64].

Figure 2-15 shows the wear rate as a function of particle size for the abrasive wear of copper using SiC paper at different sliding speeds. The wear rate is higher at low sliding speeds as, when the velocity is increased, the strain rate of the deformed material increases; in metallic systems, the yield stress tends to increase under higher strain rates leading to a reduced rate of wear. This type of wear can also be affected by surface roughness and the hardness of the body contacting the workpiece due to adhesion. During sliding, a breaking of the asperity junctions will occur, which could lead to loose wear particles or detachment of fragments from one surface to the mating surface at the point of contact.
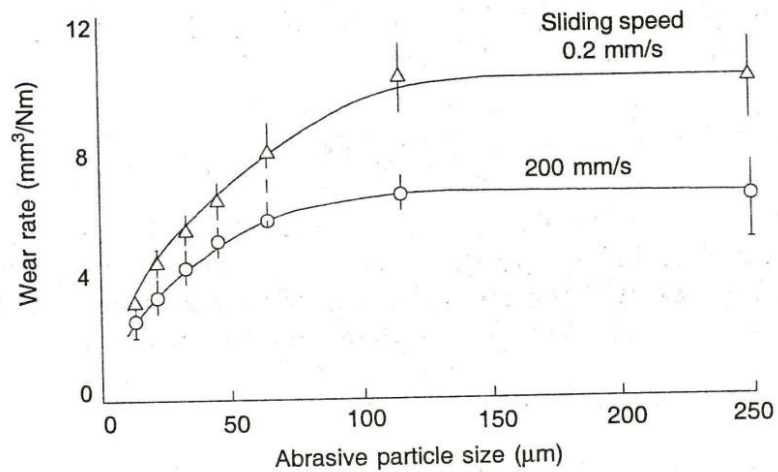
Figure 2-15 Wear rate of copper, subjected to two–body abrasion by SiC abrasive paper, as a function

of abrasive particle size at two different sliding velocities [63].

This type of wear can be recognised by the grooves ploughed out by the harder material

and by a rapid rate of wear [72].

2.3.2 Numerical simulation of component geometry changes as a result of wear

Over the years, many researchers have shown interest in the field of wear phenomena and prediction of the wear in different processes, such as sliding wear in two-body contact and machining processes. They have carried out numerous simulations and numerical approaches to illuminate this field of study. Their findings and suggestions are presented here.

In complex industrial contexts, both the rate and spatial distribution of wear in a contact can be affected by the geometrical changes associated with any wear that has occurred up to that point in time. Moreover, the material properties themselves may be dependent upon the preceding history of the contact (for example, due to frictional heating of the contact). In such complex and interdependent systems, simulation can provide important information regarding these quantities required for the investigation of wear phenomena and tool wear; therefore, research has been carried out on the simulation of wear in different engineering applications utilizing Finite Element (FE) analysis. A number of workers [73] have used finite-element based methods to develop a time-marching model of wear, where wear at any instant is dependent upon changes that have taken place in previous steps [74], [75].

In a very different field, Ding et al. [10] studied the fretting wear of high strength steels for aeroengine applications in a cylinder-on-flat configuration. A time-marching FE model, implemented in ABAQUS, was used to predict the contact pressure and slip distribution for different fretting cycles. Fretting wear was calculated based on a modified Archard equation, as given by equation 2-10 and the position of the interface

nodal coordinates were adjusted accordingly to revise the FE model geometry, thus simulating wear; a flow chart of the model is shown in. Figure 2-16.

$$\Delta h = k\, p\, \Delta S \qquad\qquad 2\text{-}10$$

where Δh is wear depth increment; k is a dimensional Archard wear coefficient; p is contact pressure, and ΔS is sliding distance (discrete time increments of particular time at an average velocity value); this equation allows us to determine the local wear depth for a given position.
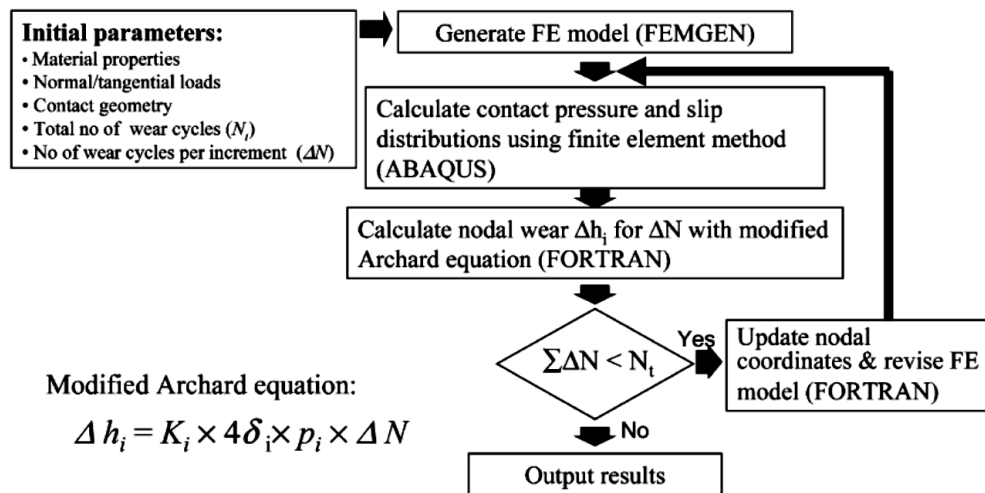
Figure 2-16 Simulation of fretting wear [73]

In the same field of study, a wear simulation algorithm was presented by Cruzado et al. [76] to estimate fretting wear scars in thin steel wires; using the same methodology as that used by Ding et al. [73]. The validation of the study against the experiments showed a 10% error; it also demonstrated a good predication for the wear scar, volume and dimensions.

Nurnberg et al. [74] proposed a model used to simulate the wear in metal forming tools; again using the same methodology as that used by Ding et al. [73]. However, the study used the wear software REDSY to calculate the tool wear and this modified

methodology enables the consideration of an individual value of wear coefficient at each location. The outcome of this study was that, at each location, the loading history is considered along with an independent wear coefficient.

More recently, Thepsonthi and Ozel [77] developed a 3D-FE model to investigate the tool wear in a micro-end milling process for Ti-6Al-4V alloy. Their visco-plastic metal deformation model used the DEFORM 3-D software to simulate the milling process. The rate of volume loss was calculated on the tool per unit area, including surface temperature on the tool model. The calculation was made based on equation 2-11:

$$\frac{dW}{dt} = c_1 \, \sigma_n \, V_{slip} \, e^{-c_2/T} \qquad\qquad 2\text{-}11$$

where $\frac{dW}{dt}$ is the wear rate; T is the interface temperature; σ_n is the normal stress and relative interface velocity V_{slip} on the tool surfaces, while c_1 and c_2 are material-dependent constants. The model provided an insight into tool wear in the milling process, and reasonable agreement with the experimental results was found in this study. It is clear that this approach is different from other approaches that have been used to predict wear because it considers tool surface temperature as another factor which affects the wear calculation.

Up to date, studies relating to the tool wear modelling in FSW have been relatively few; a study by Gant et al. [78] considered the FSW of L80 steel plate using a cylindrical commercially pure tungsten (CPW) tool. They developed a 2D axisymmetric model using the ABAQUS FEA software to predict the tool deformation during the process and the results were compared with experimental data. The study suggested that the mechanical properties of the tool material, such as yield strength at 1000°C are important factors affecting tool mushrooming. The experimental results from the study showed that wear amounts to a material loss of 7% of the original volume after a 305 mm weld length. The model successfully predicted the plastic

deformation in terms of tool shortening, while radial change was poorly predicted at the region between pin-tip and pin-mid. This is because at this region, wear is the dominant mechanism as opposed to deformation in the form of tool mushrooming and this model does not include the calculation of material removal. The study concluded that plastic deformation and wear were the main causes of CPW FSW tool degradation. Prater et al.[79] predicted the amount of wear in FSW tool when welding metal matrix composite. The study developed an equation based on rotating plug model which was developed previously by Nunes et al. [80], this model predicted the width of the rotating shear layer zone surrounding the tool. Details of this model can be found elsewhere [80]. In this study the percent volume loss *Pct wear* was calculated according to equation 2-12 and the results were compared with experimental data.

$$Pct\ wear = \frac{5 D_p \Delta C_{max}\ P_v\ \omega\ S}{24\ r_p\ u_{weld}} \qquad 2\text{-}12$$

where, P_v is proportion by volume of the reinforced of abrasive particles with mean diameter D_p and ω, S r_p and u_{weld} represent the rotation rate, distance welded, and weld velocity, respectively. The volumetric wear rate in this study was calculated according to the span of the cutting arc ΔC_{max} , which is predicted based on plug model. The ΔC_{max} term can be defined as a region of shear zone surrounding the tool where abrasion wear can occur. The model provided useful information relating to the process parameters, particle size of the abrasion material and the percentage of the reinforcement particles. The study considered 27 samples for the validation and the average difference between model and experiment was 24% with the maximum difference being 66%. The results of the model showed that when the radius of the abrasion particle is more than the thickness of the rotating shear layer, there is a high

probability of particle contact with tool surface which could cause wear on the tool. The authors outlined the main drawback of the model where the tool shape evolution, thermal effect, tool material properties and using different tool designs could further enhance the outcome the model.

2.3.3 Experimental investigation of tool wear in FSW

Experimentally, there are some methods which have been used to assess tool wear in the FSW process, the most common of which is the photographic technique, which assesses the change in tool volume using image-processing to compare a standard image of the tool (unworn) with an image of the tool after a specific length of time being welded. The work of Prado et al. [10], Shindo, Rivera and Murr [81] and Prater and Strauss [82] measured the wear of FSW tools by assessing the change in tool shape using this technique when welding an aluminium-matrix composite. They showed that tool rotational speed and weld traverse speed are the most important factors that contribute to wear and so-called "self-optimization" of the tool shape [10]. It is important to note that the term "self-optimization" of the tool is a term used by [10] and in fact usually a worn tool performs less well than a new one. These studies also compared the microstructure and hardness of welds created with the worn and unworn tools and revealed a homogenous metal flow and uniform grain size in the stirring zone for the "self-optimized" pin (It should be noted that despite this the optimised tool does not perform the weld as satisfactorily as the original tool design). The authors demonstrated that the presence of this homogenous microstructure and the low wear rate of a self-optimized pin could be related to the reduction of turbulent flow around the pin during the process after self-optimization; moreover, it was shown that a self-optimized tool generated thinner flow layers, compared to the unworn tool, leading to a more uniform flow. An empirical equation was derived by Prater and Strauss [82] which indicated that tool wear could be estimated by using the weld parameters in equation 2-13:

$$W_t = 0.584l - 1.038u_{weld} + 0.009\omega - 6.028 \qquad \text{2-13}$$

where W_t is the percentage of total tool wear; l is the weld distance in inches; u_{weld} is the traverse speed, and ω is the rotation speed.

In the same field of study, the effect of reinforcement particle size on tool wear in FSW of an aluminium-matrix composite was investigated by Prate et al. [83]. The results of the study revealed that tool wear increased by increasing the size of the reinforcement particle diameter.

While the works of Prado et al. [10], Shindo, Rivera and Murr [81] and Prater and Strauss [82] considered the wear of the tool during the FSW process, their main focus was on the wear phenomenon rather than the resulting effect on the material flow and the shape and size of the weld zone. While they did investigate the hardness profile of the weld carried out with the worn tool, it was limited to measurements taken from the mid thickness of the welded plate and little detail was provided on the effects on the weld root area.

Thompson [30] and Michael [67] used digital profilometry, in the form of a laser scanner that provided a 2D tool profile, to characterize the tool dimensions before and after each weld. The study assessed the wear rate when welding steel and observed the reduction in the tool length and area. They identified the tool degradation mechanism and investigated changes in the tool's microstructure. The study by Thompson [30] revealed that abrasive wear, intergranular failure and twining were the main mechanisms of tool degradation.

In contrast , the study by Michael [67] revealed that material was lost at the pin-tip and in the pin-shoulder intersection; moreover, a rolling pattern, smeared material and groove regions were observed in the tool images. Abrasive wear was also observed in the tool images and occurred at tapered pin and pin-shoulder intersection, which can be seen in Figure 2-17 and Figure 2-18 respectively. Therefore, the author argued that

the presence of abrasion and abrasive wear lead to tool degradation. It was also demonstrated that whole grains were lost from the tool, which could have been because of the intergranular attack. However, it should be noted that the hardness profile of the weld zone was not investigated, with the work limited to determining the shape and size of the weld zone.
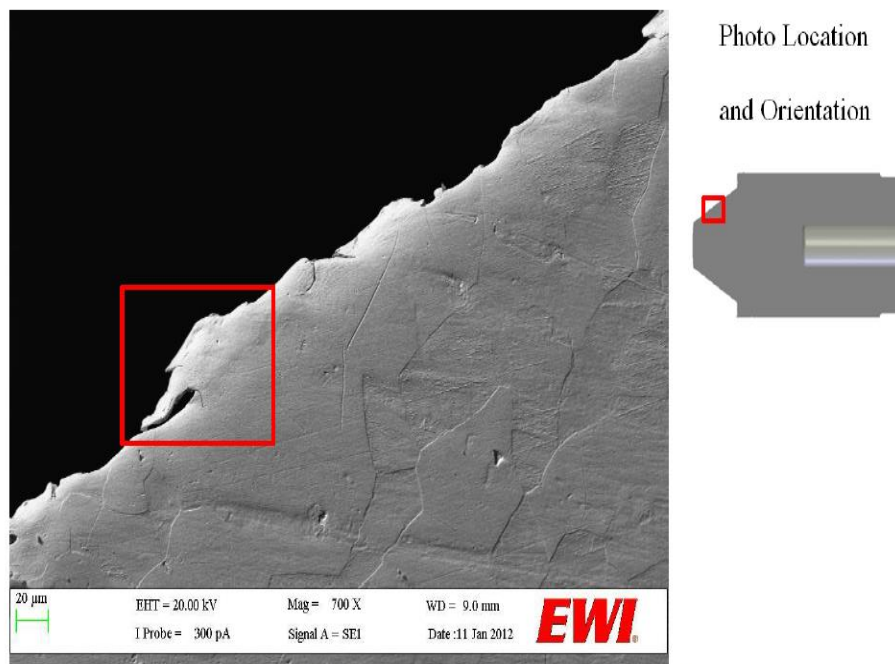
Figure 2-17 SEM photo of taper pin shows smeared material, suggesting abrasive wear [67]
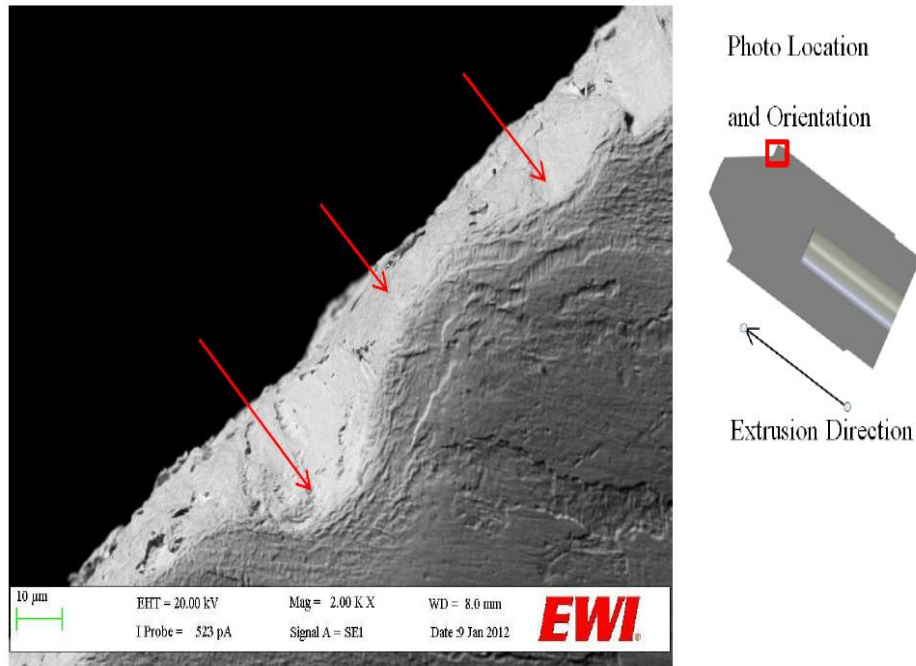
Figure 2-18 SEM photo of the shoulder shows a rolling pattern, suggesting abrasive wear [67]

Three types of FSW tools were examined by Buffa et al. [84] to join a 3 mm Ti-6Al-4V plate using a conical pin. They investigated 300, 700 and 1000 rpm rotation speeds and a 35 mm min^{-1} traverse speed. The experimental study examined tool wear until tool failure. For the all tools types, the highest value of the tool life was observed at a rotation speed of 700 rpm, and tool damage was observed in the first millimetre of welding and in the final stage of the plunge step. The authors mention the fact that tool wear could seriously affect the soundness of the obtained joints; however, they did not provide details to show this effect. The authors suggested that the wear of tools should be considered with particular focus on numerical modelling.

The work by Miyazawa et al. [85] examined the durability of FSW tool used to weld 304 stainless steel plates after different welding distances. The degree of tool wear was evaluated by the area reduction rate, after the tool wear was measured, using equation 2-14:

$$\text{Area reduction rate} = \left[\left(\frac{S_i - S_o}{S_o}\right) \times 100\right] \qquad \text{2-14}$$

where S_i is the cross-sectional tool area and S_o is the initial cross-sectional tool area. The results showed a ~20 % tool reduction with a weld distance of 10×10^3 mm at 22.2 rev s^{-1}, while wear of less than 10 % was achieved at 18 rev s^{-1}. Moreover, defects were observed above 20×10^3 mm weld distance with a reduction in the weld zone size. The study concluded that a reduction in the tool volume caused a decrease in the stirring action and changes in heat input.

A 3D white light scanning technique was utilized to investigate tool wear when welding AISI 304 stainless steel by Siddiquee and Pandey [86]. The study examined different shoulder diameters, welding speed and rotation speed, each at three values. They observed the highest wear volume when using the highest welding speed and the lowest tool rotation speed, while the largest single factor affecting tool wear was the shoulder diameter. The results also revealed the formation of a cup shape on the pin's bottom surface, and a groove formation at the pin shoulder interface. Material diffusion from the base metal to the tool surface was observed through the tool micrograph section as a result of diffusion wear occurring at the pin shoulder intersection. Diffusion wear occurs as a result of atoms moving from the tool to the workpiece material due to the presence of high temperature [65]. The results of the total tool wear volume showed that wear volume was reduced at the lowest values of the tool rotation and traverse speeds. The study also explained that the cause of the formation of a cup shape on the pin's bottom face was due to diffusion, and adhesion wear. The study further argued that the occurrence of adhesion on the pin's bottom face could be due to low heat input, which could cause an irregular flow of material past the tool in that particular position. Nevertheless, the study did not provide any evidence for this hypothesis in terms of heat input and flow behaviour.

Studies relating to the weld zone characteristics when using worn tools have been relatively few. Wang et al. [87] investigated the tool wear mechanism and weld zone characteristics of titanium alloy plates joined by FSW. Three conical tools were used to perform the weld each made from a different material. Tool wear was assessed by utilizing a photographic technique and the wear mechanism was determined through optical microscope images of the cross-section of the three tools. The results of the appearance of the tools at different welding distances showed that a significant change in the tool shape was observed in some tools, while no noticeable change after the entire weld length for the other tools, as presented in Figure 2-19. From the study, it was observed that some tools suffered from rapid fracture and chipping, plastic deformation and adhesion wear in different tool locations, as shown in Figure 2-20.
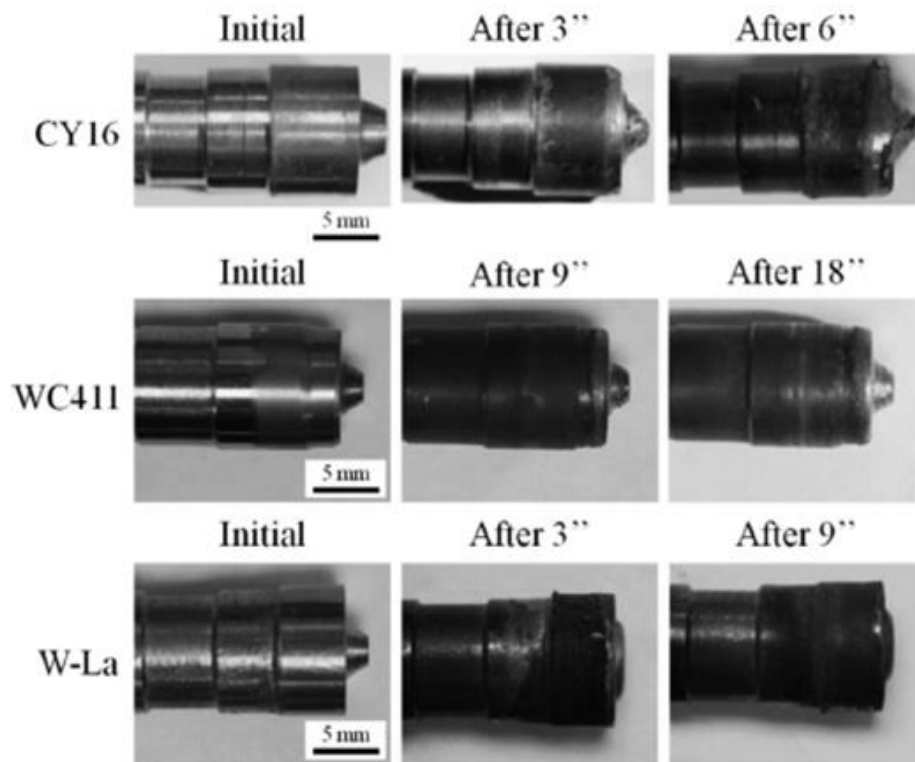
Figure 2-19 Tool geometries at different welding lengths. Note that the total length of accumulative welds is different for the three different tools (length in inches) [87].
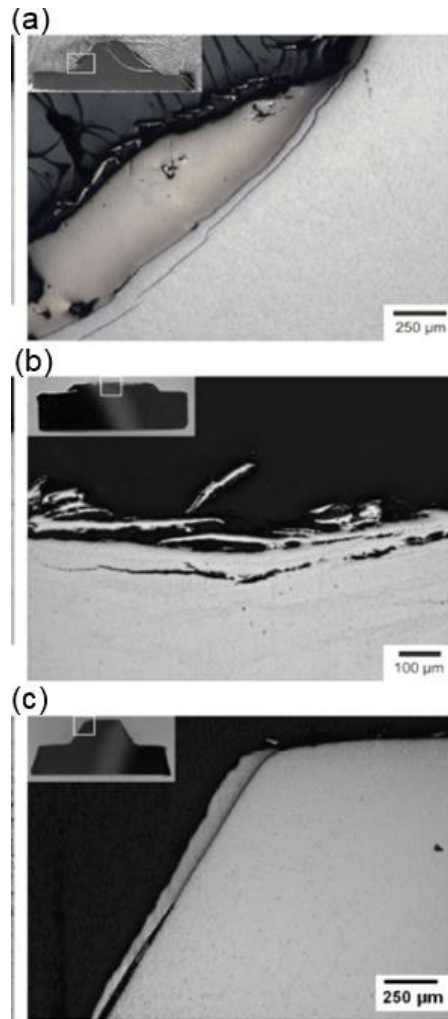
Figure 2-20 Cross-section images of (a) CY16, (b) W–La, and (c) WC411 tools were taken by optical microscopy graphs [87].

The study revealed that WC-Co alloy tools suffer from adhesion layers which are layers formed due to the chemical reaction between the workpiece material and tool material because of WC decarburization. This leads to the formation of irregular boundary layers, which might be pulled from the tool surface and incorporated into the material being welded. Furthermore, the results of the MAZ, seen in Figure 2-21, reveal that in all welds, defects were observed, and a basin-shape nugget was noticed under the shoulder area. The FSW nugget zone is classified into two types which are basin-shaped or elliptical shaped; the basin-shaped nugget is wider near the top than the bottom and forms at a low tool rotation speed [23]. This is attributed to high plastic

deformation and frictional heating at the tool shoulder and lack of vertical movement of the material and lower heat input near the pin tip and weld root. From Figure 2-21 it can be seen that the weld zones are different with different material types. The author argued that this is due to tool degradation after weld distance as shown in Figure 2-19. Therefore, the tools that experienced no significant change in their shape produced an enhancement in the weld zone in terms of weld penetration and nugget width.
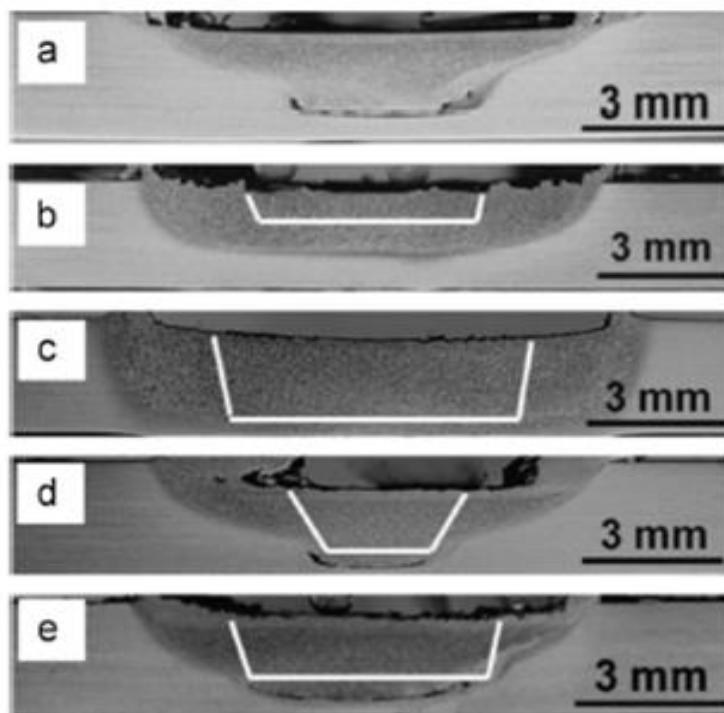
Figure 2-21 Weld zone cross-section images after FSW with a tool rotation rate of 1000 rpm and traverse speed of 50mm per minute using (a) CY16, (b) W–La, (c) W–La-L, (d) WC411 and (e) WC411-L tools [87].

2.3.4 Final remarks on tool wear

Tool wear phenomena in different processes have been extensively studied to seek to develop understanding relating to the wear mechanisms which operate and the assessment methods used to quantify wear. Several researchers have addressed the problems of wear that occur in different industrial applications. Research in the area of prediction of wear using simulation approaches has shown reasonable agreement when validated against experiential studies. The research findings of a number of researchers [73], [76] and [88] demonstrated the ability of FEA to determine the locations of contact points and pressure in order to calculate the wear depth using a modified Archard wear equation.

The presented works successfully assess tool wear in the FSW process. Moreover, the results gained from these efforts have provided a better understanding of the wear mechanism, such as the self-optimization phenomena [10], abrasion wear and intergranular wear [67], diffusion wear, and adhesion wear [86]. Furthermore, Buffa et al. [84], Siddiquee and Pandey [86] and Wang et al. [87] concluded that tool wear in FSW leads to a decreasing in the stirring action and causes much lower heat input into weld zone, which could cause an irregular flow of material past the tool and a lack of vertical movement of the welding material through the plate thickness. Additionally, Prado et al. [89] , Miyazawa et al. [85] and Prate et al. documented that tool rotation speed, weld traverse speed, weld distance and the reinforcement particle diameter are the factors which results in an increased wear in the FSW tool.

It has been shown that the FSW process has the ability to produce joints in various types of metals, however, tool degradation due to wear has remained an issue for this technique at present, particularly when joining metal matrix composites (MMCs), steel

with a thickness of 6mm and above and titanium alloy [10, 87, 90]. The main reason for this is either the welding material which is typically harder than tool material, or the formation of new phases of metal carbide at welding temperature causing erosion and chemical reaction with the tool material.

All the studies reviewed so far, however, suffer from the fact that experimental methods need dimensional measurement, device calibration and machine set up to perform the weld and to assess the tool wear. Indeed, all of these limitations would be costly from an economic perspective. Therefore, it is important to develop a numerical methodology that can be used to improve understanding of the effective limits of tool use for welding, considering the specific weld parameters and component geometry being welded without the need for experimental trials.

2.4   Summary and knowledge gaps

It is the intention of this thesis to produce a validated model of the FSW process using the CFD software FLUENT, with this model then being used to assess the detail of the differences in the flow behaviour, mechanically affected zone (MAZ) size and strain rate distribution around the tool for both unworn and worn tool geometries, which have not been investigated before. This modelling approach can therefore be used to improve understanding of the effective limits of tool life for welding, with a specific outcome of being able to predict and interpret the behaviour when using specific weld parameters and component geometry without the need for experimental trials.

An analysis of the literature has shown that wear of the tool is very common during the FSW process, and that this wear is associated with the material flow during the process [91]. Moreover, the pressure generated due to material flow is an important factor contributing to tool wear in the process.

As presented in this research, until now, experimental work has remained the primary method of investigating tool wear in the FSW. It has also shown that flow pattern differences in FSW with worn tool needs further investigation in order to determine the tool life that can produce sound welds.

In this chapter, a review has been made of several relevant aspects of tool wear in the FSW process. It can be seen that there is still a lack of understanding into the effect of the deformation of the highly viscous flow around the tool on tool wear, and an appropriate modelling methodology that can be used to predict tool wear in the FSW process.

Computational fluid dynamics (CFD) is a technique that can provide valuable insight in to the flow behaviour during the FSW process; therefore, it has been utilized in this study to assess differences in the flow behaviour around and under the tool when the tool is worn. This modelling approach can therefore be used to improve understanding of the effective limits of tool life for welding, without the need for experimental trials.

In light of this review, a methodology for calculating tool wear in FSW based upon a CFD model is presented in this study by predicting the effect of the deformation of the highly viscous flow around the tool on tool wear. This modelling approach could be used to improve understanding of the effective limits of tool use for welding, considering the specific weld parameters and component geometry being welded without the need for experimental trials.

Chapter 3 Numerical techniques

This chapter gives a general overview of fluid flow and describes the applicable governing equations. The concept of solving the fluid dynamics problem numerically using the Computational Fluid Dynamics (CFD) approach is also described. The nature of the problem solved in this work requires some extra capability on top of the standard CFD functions, in the form of material constitutive equations and user defined boundary conditions, these were formulated and implemented in the commercial software (ANSYS-Fluent) as User Defined Functions (UDF), as outlined in this chapter.

3.1   General fluid flow background

A fluid is a substance which has the ability to flow without fixed shape and which deforms continuously when shear stress is applied [92]. Fluid flow can be generally classified as steady/unsteady, viscous/inviscid, compressible/incompressible, uniform/non-uniform and laminar/turbulent flow. A brief explanation of these classifications is given below [93]:

- Steady and unsteady flow: a flow is regarded as a steady flow if the flow fields or properties do not change with time at specified locations in the stream of the flow. In reality, there is always some form of change, but where there is little significant fluctuation, the flow is considered a steady flow. An unsteady flow is also called a transient flow, whose properties vary with time. Most practical flows exhibit some transient characteristics.

- Viscous and inviscid flow: viscous flow is the real flow, in which the fluid particle has a continuous steady motion and the value of the viscosity is considered; however, if the fluid viscosity is ignored, this means the pressure forces have a larger effect than the shear forces. This is known as an inviscid flow, and it is considered an ideal fluid.

- Compressible and incompressible flow: compressibility in flow assumptions is based on the idea that a fixed mass of fluid can occupy different volume under different pressures. A compressible fluid can be made to occupy a smaller volume at high pressure and can also expand to occupy a larger volume at reduced pressure. The fluid density changes with the changing pressure for compressible flows, whereas incompressible flows have constant densities.

- Uniform and non-uniform flow: if the velocity vectors of the flow are the same in their direction and magnitude for any instant of time and at each point. This is called a uniform flow, and vice versa.

- Laminar and turbulent flow: in a laminar flow, fluid particle velocity has a constant value at any particular point in time, and the fluid parcels have no severe change in their direction with regular and smooth behaviour; otherwise, the flow is known as turbulent, in which case, for example, some properties such as pressure and velocity undergo rapid variation in space and time.

3.1.1 The Reynolds number

Reynolds number (Re) is a dimensionless parameter, and it also represents the balance between flow forces, which are inertia and viscous forces, as given in equation 3-1 [94].

$$Re = \frac{uL\rho}{\mu} = \frac{inertia\ forces}{viscus\ forces} \qquad\qquad 3\text{-}1$$

where $\textbf{\textit{u}}$ is a characteristic velocity (flow speed); L is the characteristic dimension a; ρ is the density, and μ is the dynamic viscosity.

Re can be used to give an indication of the different flow regimes (laminar or turbulent) in the same flow situation, and it can also help to predict flow patterns for the particular flow regime in different situations [95].

Furthermore, Re has different ranges, which can differ on a case by case basis; for example, the Re range value used to indicate the range of the laminar to turbulent, in-pipe flow is different from that used for an open channel or flow around a cylinder. Here, the study gives an example of the Re value of the flow around a circular cylinder because, in this thesis, it was assumed that the flow in FSW is similar to the flow around a circular cylinder. Noack [96] determined that the range of the laminar regime is Re < 160, while for the transient it is 160 > Re < 260, and for the turbulent it is Re > 260.

3.1.2 Newton's law of fluid dynamics

"Isaac Newton (1642-1727) proposed that for parallel motion of streamlines in a moving fluid, the shear stress transmitted across the fluid in a direction perpendicular to the flow is proportional to the rate of change of velocity, (velocity gradient)"[97]. Fundamentally, Newton's law of fluid dynamics is a law which explains flow behaviour under shear stress. The common form of the Newtonian fluid law is given by equation 3-2, which shows the stress-strain relationship:

$$\tau_{ij} \ = \ 2\mu \, \varepsilon_{ij} \ = \ \mu \left(\frac{\partial u_i}{\partial x_j} + \frac{\partial u_j}{\partial x_i} \right)^{ne} \qquad\qquad 3\text{-}2$$

where τ is the shear stress; i and j equal 1, 2, and 3, which represent the x, y, and z-axes, respectively; $\frac{\partial u_j}{\partial x_i}$ is the velocity gradient; ne is the flow behaviour index ($ne = 1$

for Newtonian flow), and ε_{ij} is the shear strain in tensor form, which can be written as equation 3-3 [97, 98].

$$\dot{\varepsilon}_{ij} = \begin{pmatrix} \varepsilon_{xx} & \varepsilon_{xy} & \varepsilon_{xz} \\ \varepsilon_{yx} & \varepsilon_{yy} & \varepsilon_{yz} \\ \varepsilon_{zx} & \varepsilon_{zy} & \varepsilon_{zz} \end{pmatrix} = \frac{1}{2} \frac{\partial u_i}{\partial x_j} + \frac{\partial u_j}{\partial x_i} \qquad\qquad 3\text{-}3$$

According to this law, shear stress has an effect on fluid behaviour; if the fluid has a constant μ, there will be a linear relationship between the shear stress and velocity gradient and the fluid can be classified as Newtonian while if the μ of the fluid varies under stress, it is known as a Non-Newtonian fluid, meaning that the fluid does not obey Newton's law.

3.1.3 Fluid flow governing equations

In this thesis, assumptions were made in order to model the Friction Stir Welding process; it was assumed that there was a steady state behaviour during the simulation, incompressible flow and that the fluid was a non-Newtonian fluid. These assumptions have been considered previously by Colegrove and Shercliff [13], Nandan et al. [20], as well as by Arora [99] when modelling the FSW process. Thus, the fluid flow governing equations are given in equations 3-4 to 3-6, which represent the continuity, momentum, and energy equations as described below [98]

- The continuity equation 3-4 is a statement of conservation of mass, which can also be defined as the rate of mass change equal to mass inflow rate minus the mass outflow rate; note that this is for an incompressible single phase flow because the fluid density is constant; thus, the equation below is used for this assumption:

$$\nabla \cdot \boldsymbol{u} = 0 \qquad\qquad 3\text{-}4$$

  where ∇ is shorthand for $\frac{\partial}{\partial x} + \frac{\partial}{\partial y} + \frac{\partial}{\partial z}$

while u is the velocity vectors for u, v and w velocity components in in the x, y and z-directions.

- The momentum equation 3-5 is a statement of Newton's Second Law of motion. This equation links the value of viscous stress and the effect of pressure on fluid particles; it can be described by the rate of change of momentum equivalent to the sum of forces on fluid particles.

$$\rho \boldsymbol{u}. \nabla \boldsymbol{u} = -\nabla p + \nabla. \tau \qquad 3\text{-}5$$

where p is the pressure and τ is shear stress tensor, which is given by equation 3-2.

- The steady state energy equation 3-6 represents the energy of heat transfer in the fluid and the effect of this energy on the fluid. It therefore represents the First law of thermodynamics. The energy change rate of fluid particles is equal to the heat addition rate plus the work done rate of the fluid particle.

$$\rho C_p \nabla(u_{weld} T) = \nabla(k\nabla T) + q_{(r)} \qquad 3\text{-}6$$

where C_p is the specific heat capacity; k is the thermal conductivity; T is the temperature in K; $q_{(r)}$ is the rate of heat input per unit of volume generated by the mechanical work between the tool and workpiece (in FSW), and u_{weld} is the free-stream velocity [100].

3.2 Computational fluid dynamics (CFD)

CFD is a computer-based simulation technique which has the capability of analysing many phenomena related to fluid flow, heat transfer, and the reaction of chemical processing, which is considered a useful tool for solving fluid flow problems by solving the fluid flow equations; with this solution, the value of flow variables such as pressure and velocity can be determined [94]. With increasing demand for efficiency and performance improvement in the industrial sector, several commercial CFD

software packages have been developed to solve fluid problems; ANSYS FLUENT is among the most popular software used to solve the CFD problems and is used in this thesis [94, 101].

With this code, the solution is produced through three sequential steps: the first one is known as pre-processing; in this step, the fluid domain (geometry of the fluid flow situation) is set; then the mesh is constructed, which means the domain is divided into small control volumes or cells. After that, the model is selected; in this part, the fluid phase(s) and flow regime are defined and then the desired fluid properties for the solution are specified. Finally, the appropriate boundary conditions, which can represent the physical model, are defined. The second step is the solution step; in this step, the fluid flow governing equation is solved. This step is detailed in the next section (numerical method).

The last main step is the post-processing; in this step, the results of the fluid analysis can be displayed in a graph, in which vectors and contours represent the velocity and pressure and other properties of any fluid flow [101].

3.2.1 Numerical method

In order to solve any CFD problem, there are many numerical available methods for discretising the flow equations and solution algorithm; details of these have been widely presented and described in many books and open source solvers [98, 102].

The term discretisation can be defined as transferring the continuous problem of the fluid or model equations to another form which can be implemented using a computer; thus, this method can make a numerical approximation of the partial differential equations of the fluid problem. Most commercial CFD codes utilize the Finite Volume Method (FVM) as a discretization technique; this method is based on the fact that the

fluid governing equations can be written in the formula of a conservation law. The detail of this method can be found in [98].

An iterative method is used to solve the problem, and solving can be done in a steady or unsteady state. Using an iterative method, an initial estimated value is normally taken for the solution variables to start solving the equations; after that, a more accurate approximation is produced and the solution is updated with the new approximation value until convergence is reached. A solution is converged when the successive terms in the iterations do not change significantly.

ANSYS FLUENT includes two kinds of algorithms, also called solvers, which are a Pressure-Based Solver and Density-Based Solver. Both of these types of solvers solve the governing equation (Momentum, Mass and Energy), although the main difference between these approaches is the way that they are used to solve these equations simultaneously or sequentially [102]; an explanation of how the each solver works is illustrated graphically in Figure 3-1.
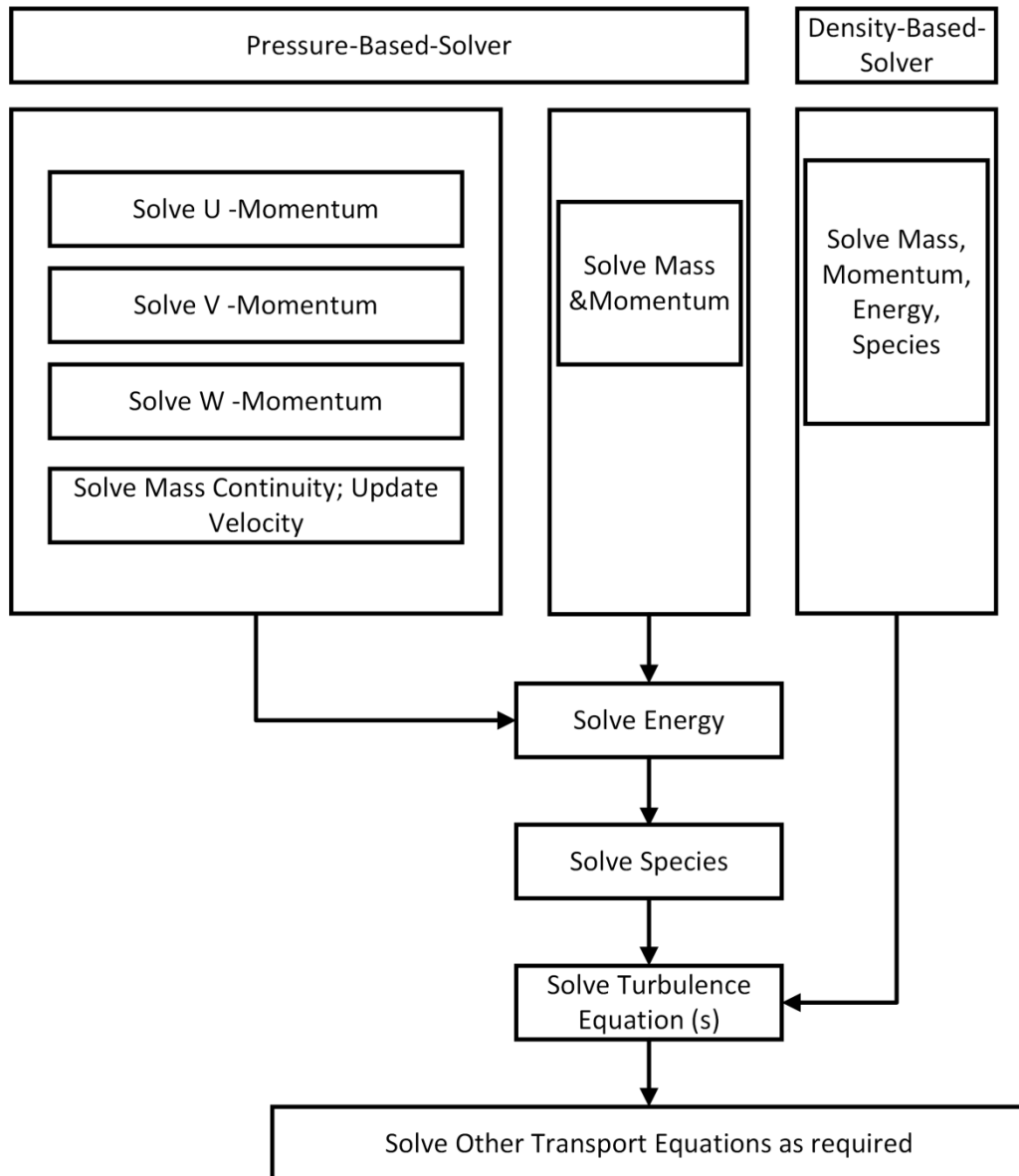
Figure 3-1 FLUENT solvers [102]

A Pressure-Based Solver can handle a wide range of incompressible and compressible flow regimes; it is therefore preferred to solve most single phase flow problems [102]. On the other hand, a Density-Based Solver is applicable for high speed compressible flow, even with combustion, a hypersonic flow model and a multiphase flow model. For incompressible flow calculations with a low Reynolds number, use of a Pressure-Based Solver is recommended, such as that considered in this work.

3.3 Constitutive equations

A common equation used to define the flow stress for the hot working and high plastic deformation of metals is the constitutive equation initially proposed by Zener and Selloors and then modified by Sheppard and Jackson [103] when they determined the material constant of the hot extrusion process by compression and torsion tests as a way of predicting the flow stress. In these equations, the flow stress of the metal, σ_f, is a function of the process parameters, and also of the parameters which were established from the experimental studies, known as the Zener-Holloman parameter Z. According to equation 3-7, the flow stress is a function of the temperature T and strain rate [103, 104]

$$\sigma_f = \frac{1}{\alpha} \, sinh^{-1}\left[\left(\frac{Z}{A}\right)^{\frac{1}{n}}\right] \qquad\qquad 3\text{-}7$$

$$Z = \dot{\bar{\varepsilon}} \, exp\left(\frac{Q_e}{RT}\right) \qquad\qquad 3\text{-}8$$

where A, α, and n are material constants; Q_e is activation energy; R is the gas constant, and $\dot{\bar{\varepsilon}}$ is the effective strain rate.

FSW can be considered a hot deformation process and the interaction between the flow stress and material strain rate is important; to account for this, a constitutive equation has been used to represent the material. In this case, equations 3-7 and 3-8 can be used to calculate the flow stress, the Zener-Hollomon parameter, and subsequently material viscosity through the use of equation 3-9 [13, 105].

$$\mu = \frac{\sigma_f}{3\dot{\bar{\varepsilon}}} \qquad\qquad 3\text{-}9$$

It is necessary to note that the strain rate can be computed at any point from the velocity field in the fluid domain through the use of equation 3-3 [106]; thus, the effective strain rate can also be calculated by using equation 3-10 [13, 106]:

$$\dot{\bar{\varepsilon}} = \sum \left[\frac{2}{3} \left(\dot{\varepsilon}_{ij}{}^2 \right) \right]^{\frac{1}{2}} \qquad\qquad 3\text{-}10$$

3.4   User defined function (UDF)

A UDF is a macro that includes formulae that are not part of ANSYS FLUENT. This macro is "loaded" into ANSYS FLUENT to get some features that are appropriate for particular problems. Fundamentally, the UDF file includes functions and macros which are compiled and then linked to the FLUENT solver. The main advantage of using a UDF is its ability to enhance the ANSYS FLUENT standard features, and therefore the UDF can be used to define the material properties, modify the boundary conditions, initialize the solution, and also modify the post-processing features of FLUENT [107].

The viscosity of the material is considered one of the most important properties which should be specified in ANSYS FLUENT [107]. Because the value of the dynamic viscosity of the material is not constant and is a function of the temperature and strain rate, this property has been specified by the UDF. In this current work, the UDF includes the formulations - presented in equations 3-7, 3-8 and 3-9 - to calculate the Zener-Hollomon parameter, the flow stress, and subsequently material viscosity; the UDF is presented in Appendix 1and 4.

Chapter 4 Modelling methodology

4.1 Introduction

In this chapter the modelling methodology of the FSW based on the commercial CFD software FLUENT model that was used for the studies in this thesis is detailed, including the development of a meshing strategy. As one of the aspects of this work is flow behaviour in the FSW process, a validation study for the flow behaviour around a rotating cylinder at different rotation rates with a Reynolds number value of 0.01 was carried out. The outcomes from this chapter were used for the validation of the size and shape of the Mechanically Affected Zone (MAZ) in FSW and the prediction of the tool wear presented in the next chapters.

4.2 Assumptions

In this work, 3D models were used with an incompressible fluid flow using a viscous laminar flow model, as the value of Reynolds number (Re) is less than 160 [96], typically around 10^{-6}. A steady state solution method was used for these models, since the study considered constant conditions (essentially the study assumed the simulation was in a steady state period of the process). A total of five models were implemented in this thesis; three of them were used for modelling the aluminium alloys 6061-T6 and 7020 and solved isothermally, whereas the fourth and fifth models were used for modelling the welding of 304 stainless steel and were non-isothermal models which included heat generation.

A double precision option was used for the modelling due to the significantly different length scales of the geometry; this option provides greater accuracy for the nodal coordinates during the calculation and reduces convergence errors [107].

4.3 Geometry

The geometry of the computational domain of the model that was used for the mesh study was a rectangular cuboid and had the following dimensions: 320 mm length, 160 mm width, and 9.53 mm thick. The diameter of the pin was 8 mm, with a shoulder diameter of 25.4 mm and 6.35 mm tool length; it was placed in the first half of the domain as shown in Figure 4-1. The tool dimensions were selected according to the work of Rai et al. [90], while the distances to the inlet, outlet, and sides of the domain from the tool centre were defined as 5d, 15d, and 10d respectively; where d is the pin diameter; these distances were used based on the work of Zdrawkvich et al. [108].
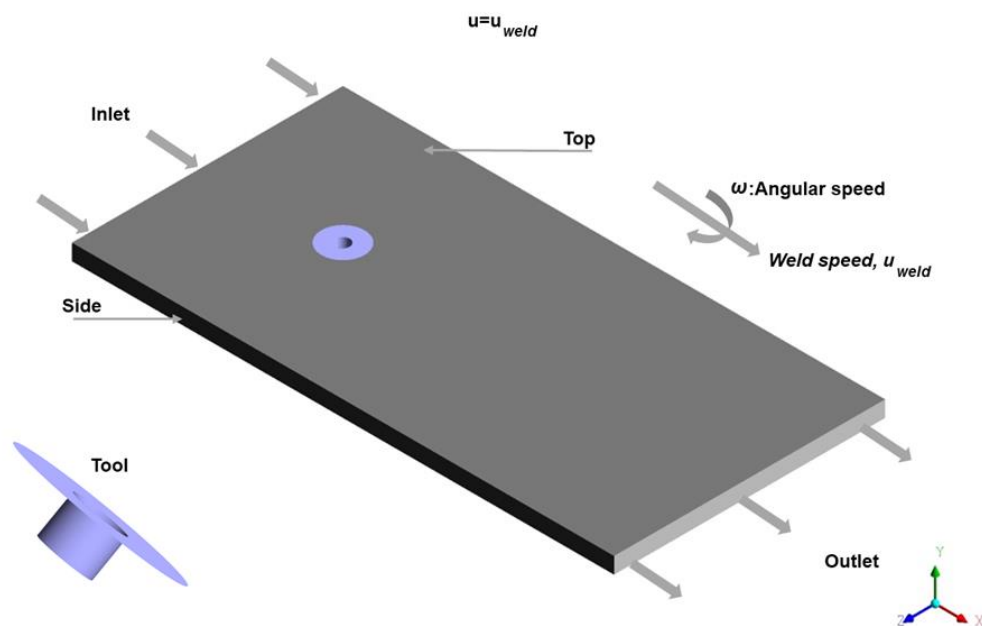
Figure 4-1 Computational domain and boundary conditions

4.4 Boundary conditions

The boundary conditions can have a significant effect on the results of CFD models. In order to ensure that the physical situation is well represented and that the model produces accurate results, the boundary conditions need to be specified correctly for the domain shown in Figure 4-1. The inlet flow condition was defined as:

$$u = u_{weld} , \qquad v = 0, \qquad w = 0 \qquad\qquad 4\text{-}1$$

where $u, v,$ and w are the magnitude of the velocities in the x, y and z directions respectively; u_{weld} is the welding velocity at the inlet, which took different values based on the welding parameters for which the model was constructed. The outlet boundary was a pressure outlet with a zero static (gauge) pressure value to ensure no reverse flow and both sides and the upper and lower surfaces of the domain were defined as free slip walls (the shear stress value was equal to zero).

4.4.1 Tool boundary conditions

It is clear that the interface between the tool and the workpiece is a crucial aspect in the numerical modelling of the FSW process; it has been suggested by Schmidt et al. [14] that material at the interface can reach the solidus temperature and that a thin layer of molten material may be generated adjacent to the tool surface, which can have an effect on the shear stress of the material in this region.

Generally, the Coulomb friction law can be used to represent the contact between surfaces and it is widely used to calculate the value of the shear stress as shown below:

$$\tau_{contact} = \tau_{friction} = \mu_f p \qquad\qquad 4\text{-}2$$

where $\tau_{contact}$, is the contact shear stress, $\tau_{friction}$ is the frictional shear stress, $p,$ is the contact pressure and μ_f is the friction coefficient. Clearly, this law is valid for the case of the motion of two rigid bodies in contact even if they slide or stick, however, if this law is applied in the FSW processes to calculate the shear friction between the

tool and the workpiece, the behaviour of material flow in the shear layer next to the pin surface is normally neglected. To address this, Schmidt, Hattel and Wert [14] developed a numerical approach to address the interface issue in FSW. They specified three conditions that could occur at the interface of the FSW process, and included a contact state variable, δ, to account for this, defined as:

$$\delta = \frac{V_{mat}}{V_{tool}} \qquad\qquad 4\text{-}3$$

where δ is the ratio between the material interface velocity, V_{mat}, and the tool velocity, V_{tool} which is defined as the velocity components on the surface of the tool (position dependent tool velocity of ωr) [15]. They proposed that the conditions at the contact interface were based on the interaction between the contact and material shear yield stress τ_{yield}, defined as follows:

$$\tau_{yield} = \frac{\sigma_{yield}}{\sqrt{3}} \qquad\qquad 4\text{-}4$$

The three conditions that they proposed were:

1. Sliding behaviour: This condition occurs when $\delta = 0$, which means the velocity of the material at the interface is zero; for this case, the shear yield stress (τ_{yield}) is more than $\tau_{contact}$ and there is no flow of interface material.

2. Stick behaviour: Here the velocity of the tool equals the interface material velocity where they are in contact, or $\delta = 1$. The interface material rotates at a velocity equal to the tool rotation speed and for this case the value of $\tau_{contact}$ is more than τ_{yield} leading to high plastic deformation at the interface.

3. Stick-sliding behaviour: In this particular case, δ will be between 0 and 1, leading to a partial sticking-sliding condition. The interface velocity is less than the tool velocity, and in this case the value of $\tau_{contact}$ equals τ_{yield}. Neto and Neto [15] and Schmidt and Hattel [14] documented that stick-sliding behaviour is

more likely to occur in the FSW process and they argued that differences in the relative velocity at different angular locations on the tool surface will lead to some parts of the interface layer being under a stick condition and some parts will be in the partial slip regime.

Nandan et al. [20] and Arora et al. [21] specified the velocity components on the tool surface in terms of the tool angular translation velocities; these components define the material velocity at the tool interface for u_{mat}, w_{mat} as shown in equations 4-5 and 4-6, which also include the δ term to specify the contact condition; while $v_{mat} = 0$:

$$u_{mat} = (1 - \delta)(\omega r \sin \theta - u_{weld}) \qquad\qquad 4\text{-}5$$

$$w_{mat} = (1 - \delta)(\omega r \cos \theta) \qquad\qquad 4\text{-}6$$

where ω is the tool rotation speed, θ is angle from the direction of movement of the tool with the x-axis, and the value of r lies in the range $r_p < r < r_s$. They also modified the relationship derived from the data in the work of Deng, Lovell and Tagavi [109] in cross-wedge rolling to develop the following relationship for the slip as a function of tool radius and welding parameters:

$$\delta = 0.2 + 0.6 \times \left(1 - exp\left(\delta_o \; \frac{\omega}{\omega_o} \; \frac{r}{r_s}\right)\right) \qquad\qquad 4\text{-}7$$

where the variable δ_0 is a constant and was determined by Arora et al. [21] to have a value of 3 and $\left(\frac{\omega}{\omega_0}\right)$ is the ratio between the rotational speed and a reference speed, ω_o.

In the current research, material velocity components at the tool interface (equations 4-5 and 4-6) have been specified using a user defined function (UDF), given in Appendix 2; and these were implemented as a boundary condition for the models in

Chapters 5, 6 and 7. A constant value of 0.07 was used for δ; this assumption was made based on the work of Chen et al. [32] where they determined the value of δ experimentally based on the estimation of the pin travel distance after one revolution and the location of the flow front of each of the deformed layers around the pin.

4.4.2 Thermal model

In chapters 6 and 7, 304 stainless steel was used as a welding material. It is well known that this material is very sensitive to temperature and strain rate [110] and that the variation of temperature through the plate thickness has a significant effect on the pressure and velocity in the weld zone [111]; therefore, it is important to implement a heat generation model in the FSW model for this application. The tool in the FSW process is the source of heat generation; and it has been determined that frictional heat generation and plastic deformation are the main mechanisms of heat generation [7, 8, 112]. Initially, during the process, contact occurs between the rotating tool and the workpiece, heat is generated and is conducted into the workpiece. After that, localized heating caused by the shoulder leads the workpiece to deform plastically [7, 8]. The shoulder generates more heat than the pin, with the contribution of the heat generated by the pin being less than 15 % of the total heat input [14]; therefore, in the current work, it was assumed that the heat input came from the shoulder only. Hamilton et al. [112] and Selvaraj [8] proposed that the power required to cause shear deformation by the tool in the FSW is converted to the heat and it is given by equation 4-8:

$$P_s = \frac{2\pi}{3}\,\tau\omega\left(r_s{}^3 - r_p{}^3\right) \qquad\qquad 4\text{-}8$$

where r_s is the maximum shoulder radius, r_p is the pin radius, τ is shear stress and ω is tool rotation speed. The expression (τ) is the material shear stress or flow stress (σ_f), as determined by the study of Nandan et al. [20] shown in equation 4-9.

$$\tau = 3\dot{\bar{\varepsilon}}\mu \qquad\qquad 4\text{-}9$$

In the current study, a steady-state thermal model was implemented and the temperature in the domain was calculated. Moreover, it was assumed that all of the power input (equation 4-8) in the FSW process (the power required to cause shear deformation by the tool during the process) is converted to heat; therefore, the total heat input Q, was equal to the power input in the process [8], so in this case $Q_s = P_s$, where Q_s is the heat input from the shoulder.

The value of the shear stress is directly proportional to the value of the strain rate and material viscosity; Nandan et al. [113] documented that no significant plastic deformation occurs below a viscosity of 4×10^6 Pa s for 304 stainless steel.

Selvaraj [8] used this values of viscosity to determine the critical value of shear stress (τ_c) using equation 4-9 leading to a value of 15×10^6 Pa, and a corresponding temperature of 1038 $^\circ$C, approximately 0.7 of the melting temperature (T_m). Therefore, it can be said that when the temperature in the FSW process is less than 0.7 T_m, the flow stress of the material is high enough for the plastic deformation to be insignificant. However, when temperature is greater than 0.7 T_m, the flow stress value decreases; leading to plastic deformation.

Zhu and Chao [114] experimentally determined the value of Q_h from the measured torque during the FSW of stainless steel 304 to be in the range 1760 to 2240 W. This range has been further confirmed numerically by Zhu and Chao [114] and Selvaraj [8]. In this study, equation 4-8 was used to calculate Q_s based on the value of $\tau = 15 \times 10^6$ Pa and was determined to be 2227 W. The value of Q_s is acceptable when compared with the studies of Zhu and Chao [114] and Selvaraj [8] in terms of rotation speed and tool radius.

In order to implement the heat generation, it is necessary to use the rate of heat input to the workpiece (heat flux q_r); q_r was defined by Chao et al. [115], which was the first study to simulate heat generation in the FSW process. The heat flux (q_r) is given by equation 4-10:

$$q_r = \frac{3 \, Q_h \, r}{2 \, \pi \, \left(r_s{}^3 - r_p{}^3\right)} \qquad 4\text{-}10$$

where r_s is the shoulder radius and r_p is the pin radius. It is clear from equation 4-10 that q_r increases with increasing tool radius; which means that during the welding process, the highest temperature is expected to be within the tool shoulder . The heat flux, equation 4-10, is applied as a boundary condition in the shoulder region by using a UDF (the details of this UDF are given in Appendix 3).

In addition, a convection thermal boundary condition was applied on the extents of the domain. It was assumed that the top and side surfaces have free air convection with a value of 15 W m^{-2} K^{-1} as a heat transfer coefficient [8], while the bottom surface was assumed to be in contact with the backing plate (note that the backing plate was not modelled in this study). The heat transfer coefficient of this surface took a value of 300 W m^{-2} K^{-1}, an assumption that has been made previously by other researchers [8, 116]. It is worth mentioning that in this study, the steady-state thermal model was implemented and the temperature throughout the domain was calculated.

4.5 Solver

The SIMPLE (Semi-Implicit Method for Pressure-Linked Equation) pressure-velocity coupling algorithm was used for this study, since it has been used to solve the incompressible flow problem, pressure gradient term, and viscosity term effectively [117]. For spatial discretization, a least squares cell-based approach was chosen to determine the solution gradients of the variables in the cell with standard pressure and

second order upwinding for the momentum that provides a more accurate and stable solution.

4.6   Convergence criteria

In order to assess convergence of the steady-state solution, the monitor check for absolute convergence criteria was turned off for all models, in order to make sure that the solution is converged in the area of interest (around the tool). The velocity value at two points was monitored throughout the solution until the change in the velocity was less than 0.05 % per iteration. The first point was located in the upstream near the tool; which is the interest area where the high velocity gradient occurs and the second point was in the free stream before the outlet to ensure that no reverse flow occurs during the simulation. To avoid divergence in the solution, the cases were initially run without tool rotation until convergence, and then the tool rotation speed was gradually increased until it reached the specific value of each model. It is important to ensure for each tool rotation speed that the convergence criteria were met before increasing.

4.7   Mesh development

A mesh can be defined as a discrete representation of the domain, which represents the model case [118]. The mesh or grid consists of many cells, and there are different types of cells as given in Figure 4-2, and they are different by their shapes and number of nodes. Hexahedral cells have eight nodes with six quadrilateral faces, while tetrahedral cells have four nodes with four faces. On the other hand, prism cells (wedge) have six nodes with five faces. Hexahedral cells can provide better solution accuracy and a superior rate of convergence as opposed to tetrahedral cells in the case where the flow and cell directions are aligned [101, 119]. Due to the fact that tetrahedral cells depend

on a linear shape function (calculated by the gradient at the cell centre) for the control volume during the solution, there could be some problems at the wall with neighbouring cells. Therefore, prism cells can more efficiently capture the shear gradient near the wall surface, recirculating flow for the boundary layer area, and achieve good convergence [120, 121].

Generally, three types of grids are available in the ANSYS software which are structured grid, unstructured grid and hybrid grid. In a simple definition for these grids, a hexahedral mesh refers to a structured grid, in which the cells and nodes are placed regularly, while when they are placed in an irregular manner the grid is known as unstructured and it normally has tetrahedral cells.

triangle   quadrilateral

2D Elements

tetrahedron   hexahedron

pyramid   prism/wedge

3D Elements
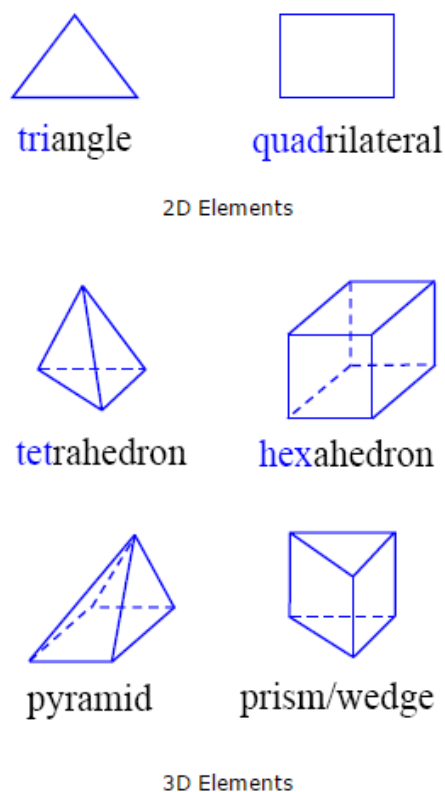
Figure 4-2 Cell shapes [121]

A hybrid grid is a combination between hexahedral cells which are generated by blocking techniques, for the simple part of the domain, with tetrahedral or tetrahedral

and prism cells for the complicated part of the domain, which are merged using a non-conformal interface. A non-conformal interface is used to join two mismatching cell zones with a different number of nodes or mesh topologies and permit the cell zones to be easily connected to each other by passing fluxes from one mesh to another [122]. Generally, it is used to produce one interior zone in the fluid domain [102]. It is important to make the cell size at the interface nearly equal for the two types of cell to reduce the numerical error. In addition, the interface should be set away from the region of interest to minimise the gradient of the mass flow in that area [121].

A hexahedral mesh can better capturing the flow features because in hexahedral grids the predominate flow direction is aligned with the grid nodes [119]; however, it is difficult to generate a hexahedral mesh for complex geometry; particularly for the FSW tool such as a threaded tool with a concave shoulder, and tilted at an angle. Santiago et al. [54] and Fourment and Guerdoux [25] have used tetrahedral cells to model the FSW process with a complex tool design. The use of a tetrahedral mesh throughout the domain results in a large number of cells, leading to an increased computational time. Therefore, a hybrid mesh can be used to generate mesh for the complex geometry with less number of cells for the same solution. It is worth noting that the advantage of using hybrid grids for complex geometry was highlighted in the ICEM User Manual [121] and Zitzmann et al. [123].

It has been documented that the accuracy and efficiency of the CFD solution depends on the mesh quality [101]. As this work aims to provide additional insight into the behaviour of the material around the unworn and worn tool and to predict tool wear associated with highly viscous flow around the FSW tool, an unstructured grid with tetrahedral cells, and which contains a prism layer near the sharp edge of the complicated geometry, can be used to compute the shear gradient and recirculating

viscous flow near the boundary layer. In this study, the hexahedral mesh was used as a reference solution, using a simple geometry, for the development of a hybrid mesh. The aim of this is to examine the solution efficiency and accuracy to determine the errors introduced when using a hybrid mesh for the study of complex tool designs. All cases were run on a High Performance Computing (HPC) facility using a single 8-core (Intel Sandybridge 2.6 GHz) machine with 16 GB of memory.

4.7.1 Structural hexahedral mesh study

4.7.1.1 Model description

In this study, a steady state 3D flow model of the FSW process was produced using the commercial CFD software FLUENT. This model was used to extract velocity values at particular positions in order to conduct a mesh independence study. It is solved isothermally, as used by Colegrove et al. [47] and Ji et al. [24] previously; this assumption was made as the flow stress of aluminium alloy 6061-T6 is relatively insensitive across the temperature range from 0.6 to $0.8T_m$ experienced in the welding process. The model assumptions, boundary conditions of the workpiece, solver and convergence criteria were defined based on the details included in the previous sections of this chapter. A stick condition [24, 47] has been applied on the tool surface to simplify the model for this case.

4.7.1.2 Mesh

The ICEM software was used to generate the structured HEXA-QUADRATIC mesh, and the aspect ratio of the cells around the tool was kept less than 7 for the all cells. The geometry was split into nine blocks and an O-Grid was used in the block of the tool (pin and shoulder) to get a good quality of mesh around the tool using biases. This type of mesh is flexible and was therefore used in this study to generate a very fine mesh with low cell distortion around the tool. Figure 4-3 shows the meshing blocks,

with edge numbers; and Figure 4-4 shows the mesh construction around the tool, while Table 4-1 detials the five cases of the mesh (grids) which were used in the study.
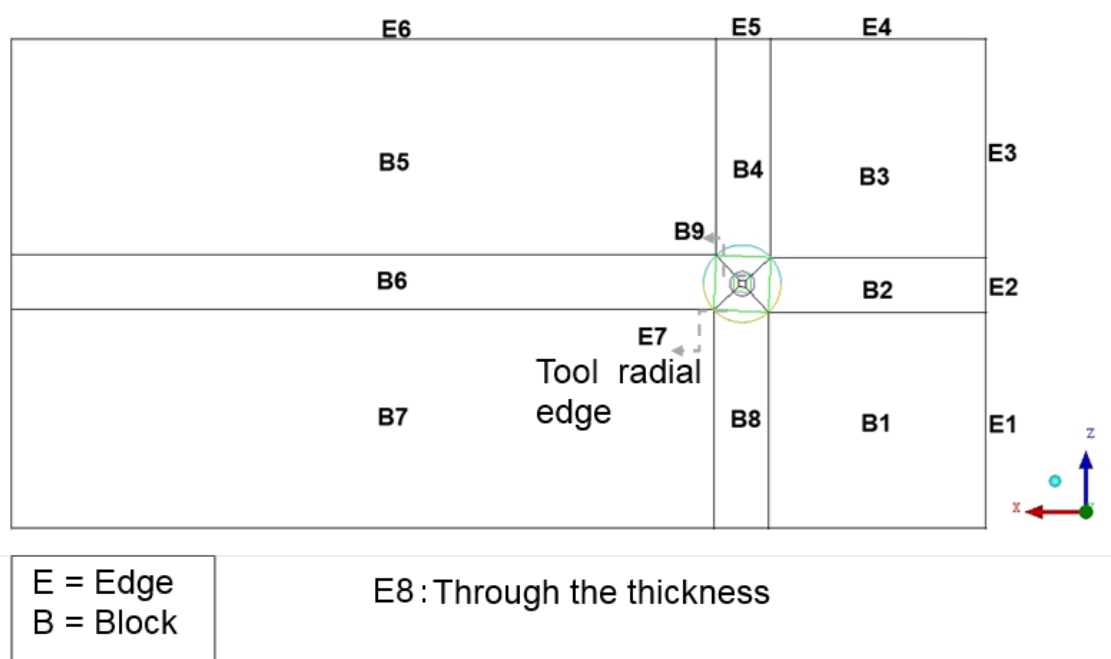
Figure 4-3 FSW model domain blocking strategy
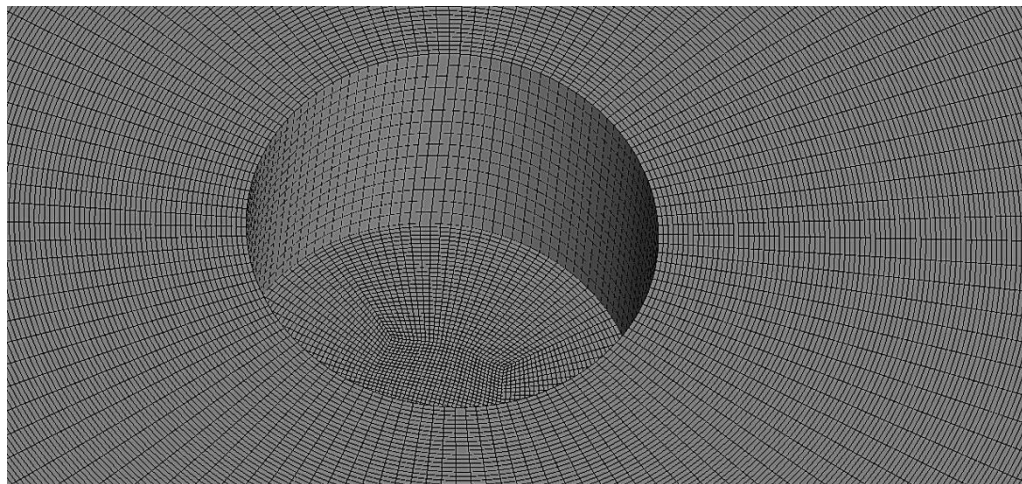
Figure 4-4 Hexahedral mesh shape at the tool surface

Table 4-1 Hexahedral mesh grids used in the study

Grid name	Block 9 cell size (mm)	Number of nodes on edge (key to edges in Figure 4-3 FSW model domain blocking strategy)								Total number of cells
		E1	E2	E3	E4	E5	E6	E7	E8	
Hexa 0.4	0.4	60	16	60	40	16	90	23	12	40308
Hexa 0.2	0.2	60	16	60	40	16	90	45	12	290847
Hexa 0.1	0.1	120	32	120	80	32	90	90	24	1623796
Hexa 0.05	0.05	120	32	120	80	32	90	90 *	24	1623796
Hexa 0.025	0.025	120	32	120	80	32	90	90 **	24	1623796
* Biased; exponential with spacing 0.05 ** Biased; exponential with spacing 0.025										

4.7.1.3 Material properties

The material used in the simulation was aluminium alloy 6061–T6, the material properties and the process parameters are presented in Table 4-2 and Table 4-3.

Table 4-2 Aluminium alloy 6061-T6 material properties Nandan et al. [105]

Material property	Value
Density, ρ	2700 Kg m^{-3}
A, material constant	8.863×10^6 s^{-1}
α, material constant	0.045×10^6 Pa^{-1}
n, material constant	3.55
Activation energy, Q_e	145×10^3 J mol^{-1}
Gas constant, R	8.314 J K^{-1} mol^{-1}

Table 4-3 Mesh study process parameters.

Weld parameter	Value
Inlet velocity, u_{weld}	3.39 mm s^{-1}
Tool Rotation speed, ω	770 rpm
Temperature (0.8 T_m)	684 K

4.7.1.4 Results

The instability of the velocity value and velocity gradient of the viscous flow near the boundary layer (in the area away from the pin surface) have been reported by Mittal et al. [124], Thinbo et al. [124] and Colegrove et al. [13]. Therefore, in this study, the velocity profile was investigated along a radial line at an angular position of 45° as shown in Figure 4-5. This was used to indicate the free stream area on the horizontal plane at 0 mm on the y-axis; where (0, 0, 0) was located at pin tip.
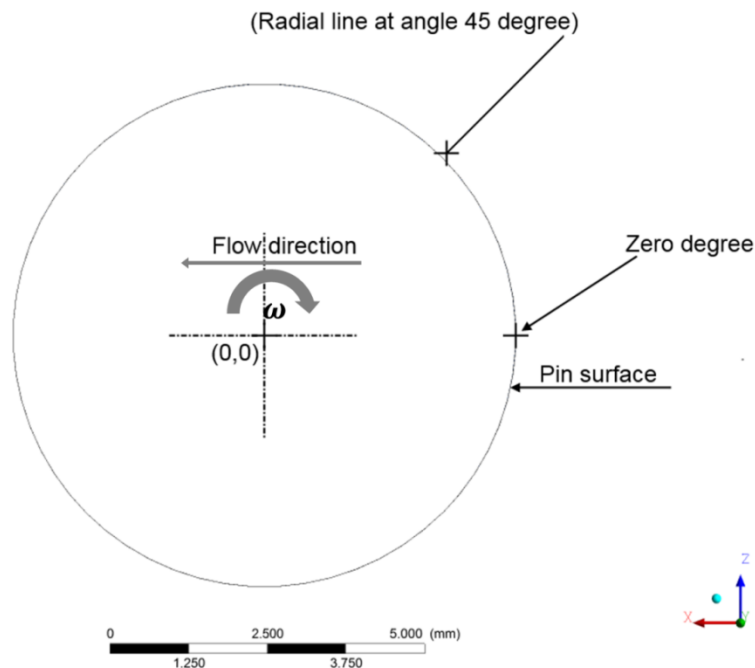
Figure 4-5 Radial line at angle position of 45° used for data analysis
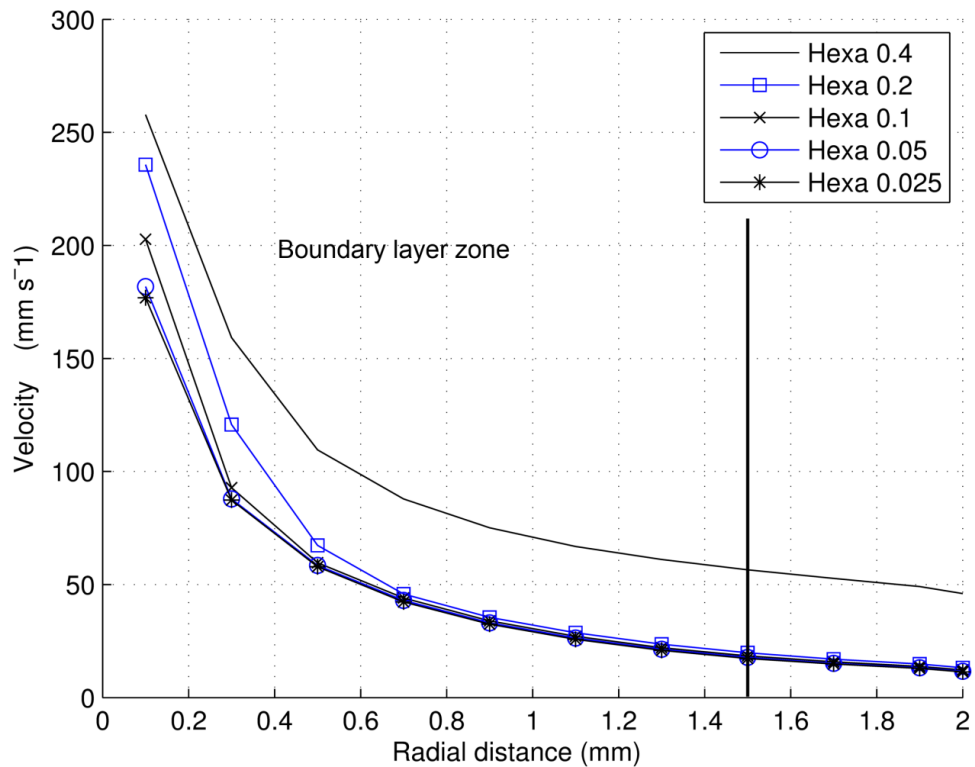
Figure 4-6 Velocity profile with the radial distance away from the tool surface at an angle of 45^{o,} for

the hexahedral grids

The results of the velocity value along that radial line are shown in Figure 4-6 to

determine which cell size provided a grid independent solution for the velocity profile.

This figure shows the relationships between velocity values with radial distance from

the pin surface at 45° as presented in Figure 4-5. It is clear that the results of the mesh

with radial cell sizes of 0.2, 0.1, 0.05, and 0.025 mm have no significant changes in

the free stream region, which is indicated at 1.5 mm away from the pin surface,

whereas up to this distance the velocity gradient was not identical for the different

types of mesh. The effect of the inconsistency in the flow behaviour can be seen near

the boundary layer; the maximum percentage difference between the Hexa 0.05 and

Hexa 0.025 grids was less than 6 %, while the other grids have more than 16%

difference with Hexa 0.025. Therefore, in this study Hexa 0.05 was used as a reference

converge solution for modelling the FSW with the simple tool design. Moreover, velocity streamlines were plotted in order to show the flow behaviour for the hexahedral mesh around the tool, as shown in Figure 4-7 and it is consistent with what has been reported in the literature [105].
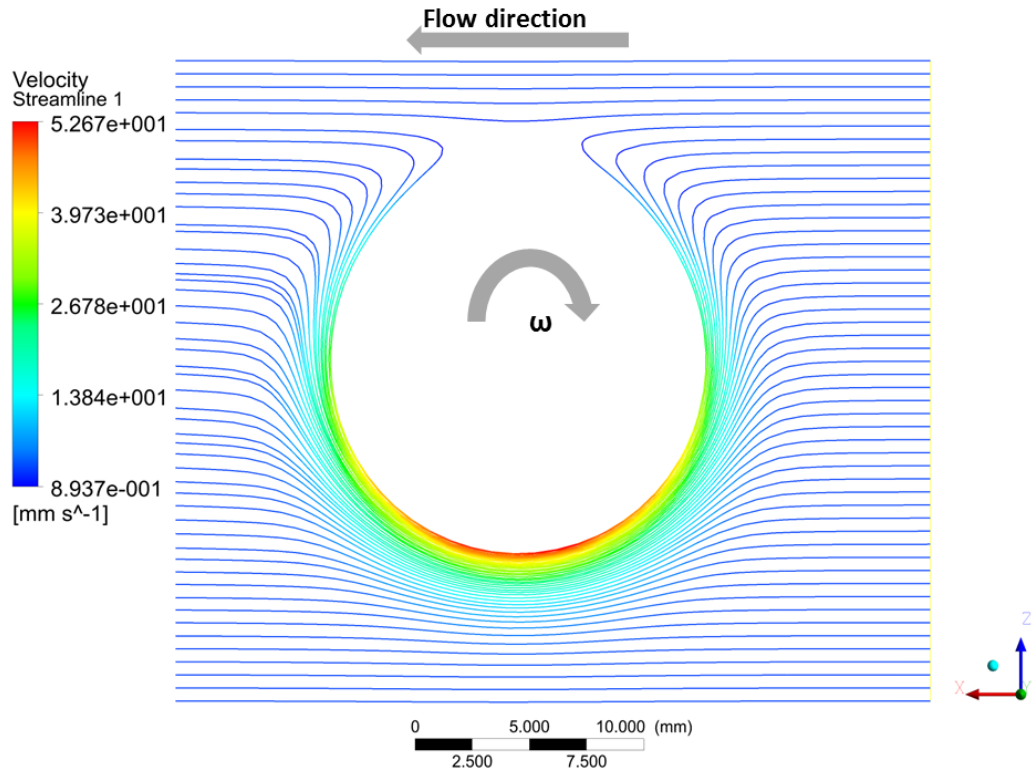
Figure 4-7 Velocity streamlines on the x-z plane at the tool midpoint (y = 3.175 mm), for grid Hexa 0.05

4.7.2 Hybrid mesh study

In this study, the development of a hybrid mesh strategy was undertaken to determine appropriate tetrahedral cell size and developing the this mesh by including prism layers for the CFD modelling of the FSW process using complex tool geometry.

To conduct a hybrid mesh study, the geometry, boundary conditions, material properties, solution control and methodology were the same as that used in the structured mesh study in section 4.6.1. The ICEM software was used to generate the hybrid mesh. Ideally, it is important to refine the mesh in the area of interest, which is mostly the plastic deformation area (zone around the tool) so that many cells are generated in that particular area.

4.7.2.1 Mesh

In order to generate the hybrid mesh, three hybrid grids were considered, as given in Table 4-4, and velocity profile was investigated along radial line from the pin surface as shown in Figure 4-5, in order to determine appropriate tetrahedral cell for the hybrid mesh which provided a converged solution for the velocity profile and then the results were compared with the converged hexahedral mesh profile (Hexa 0.05). This was followed by developing the hybrid mesh by investigated the use of prism cell layers in terms of the velocity profile as used in tetrahedral cells. Finally, the velocity magnitudes at two points close to the base of the pin were used to confirm the mesh convergence.

It is important to split the geometry into nine blocks, as shown in Figure 4-3. All blocks were meshed using hexahedral cells, except the middle block which was the surrounding the tool (B9). ICEM was used to generate the mesh with an aspect ratio of less than six for the hexahedral cells. The middle block was meshed separately by

using tetrahedral cells and the study kept the mesh quality value for this block more than 0.4 as recommended by the ICEM User Manual [121]. With regard to mesh quality, it is a method that examines mesh characteristics which give an indication for the accuracy and efficiency of a simulations based on the solution of fluid flow governing equations [125]. There are three main criteria for determining the mesh quality which are skewness (equiangular skew), smoothness (change in cell size) and aspect ratio (ration between longest to shortest edge of the cell) [121].

Table 4-4 Hybrid mesh grids used in the study

Grid number	Block 9 tetrahedral cell size (mm)	Number of nodes on edge (key to edges in Figure 4-3 FSW model domain blocking strategy)							
		E1	E2	E3	E4	E5	E6	E7	Total number of cells
Tetra 0.6	0.6	60	75	60	60	75	90	10	604269
Tetra 0.4	0.4	60	75	60	60	75	90	10	1205193
Tetra 0.2	0.2	60	75	60	60	75	90	10	8584393

Similar to the hexahedral mesh study, velocity streamlines were plotted in order to show the flow behaviour for the hybrid mesh around the tool, as shown in Figure 4-8, and it is consistent with what has been produced by the using hexahedral mesh.
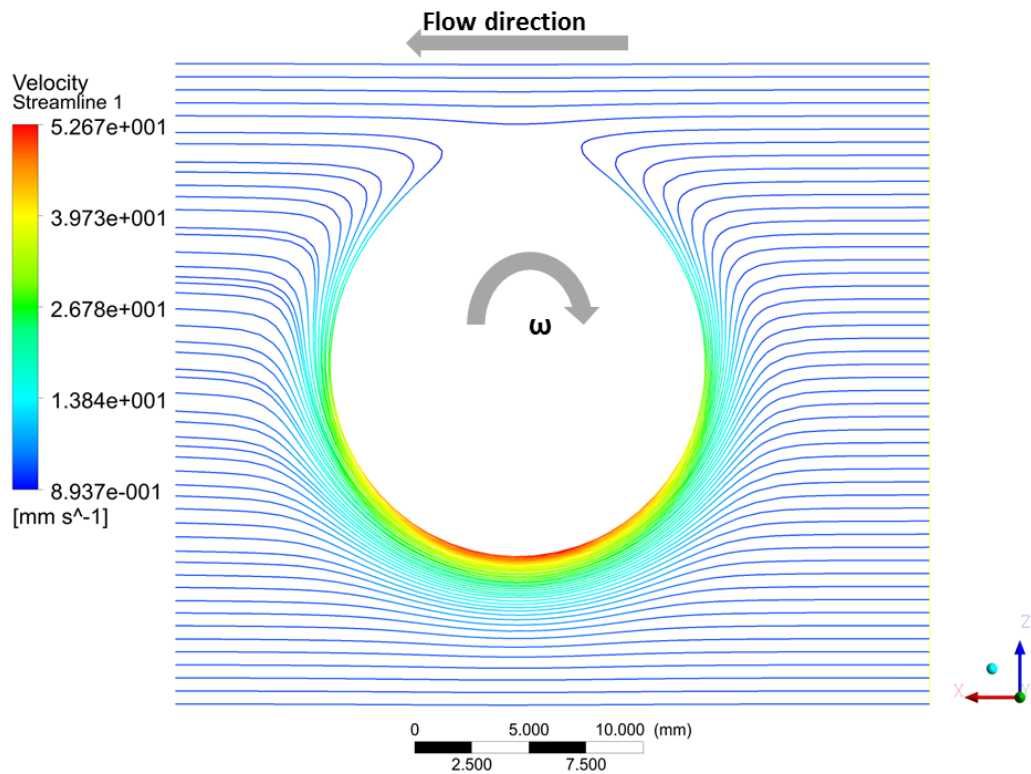
Figure 4-8 Velocity streamlines on the x-z plane at the tool midpoint (y = 3.175 mm), for grid Tetra

0.4

4.7.2.2 Tetrahedral mesh study results

Figure 4-9 shows the velocity behaviour for the three tetrahedral grids detailed in Table

4-4 along a radial line at the same 45° angle (Figure 4-5); the profile for the mesh

independent solution using a hexahedral mesh is also shown for comparison. The

results revealed similar behaviour to the hexahedral mesh study in terms of

inconsistency of the flow near the boundary layer. It can be seen that near the tool

surface (below 0.5 mm radial distance); the maximum percentage difference between

the Hexa 0.05 and grids Tetra 0.6,Tet 0.4 and Tetra 0.2 were 63%, 27% and 9%

respectively.

It is apparent that at the radial distance after 0.2 mm and above there is no significant difference can be seen between grid Tetra 0.4 and grid Tetra 0.2. Additionally, grid Tet 0.2 had more than 8 million cells, while grid Tet 0.4 had ~1.2 million cells, highlighting that this mesh can be further improved by including prism layers, which can maintain a reasonable accuracy in predicting the velocity gradient near the tool surface. Thus, it can be said that the grid Tetra 0.4 is better than the grid Tetra 0.2 in terms of number of cells and this mesh size can be used for future studies.

Also from the graph, at the radial distance between 0.5 to 0.9 mm, the lines of tetrahedral meshes are converging on the under-predicted solution, with reference to Hexa 0.05. It can be argued this behaviour of under prediction is due to fact that the unstructured grid algorithm is automatic which gives misalignment of the grid cells [126]. It has also been documented that the concept of numerical solutions obtained on hexahedral grids is different from tetrahedral grids because in tetrahedral grids the predominant flow direction is not aligned with the grid nodes [101, 127].
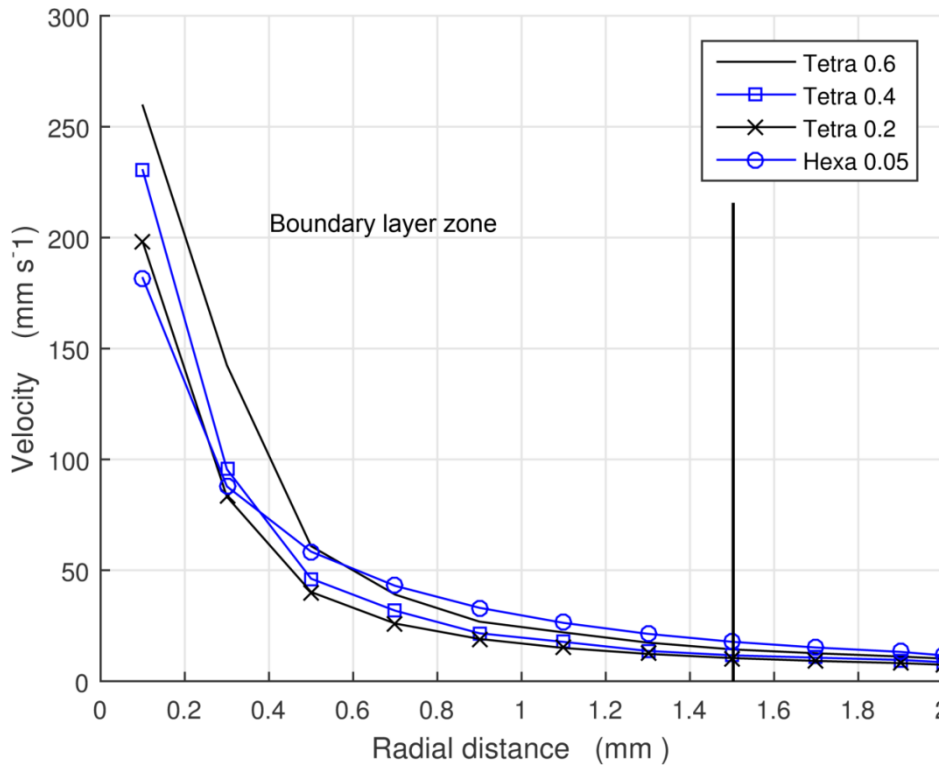
Figure 4-9 Velocity profile with the radial distance away from the tool surface at an angle of 45° for
the tetrahedral grids and a converged hexahedral grid.

4.7.2.3 Results with inclusion of prism layers

In the previous section, it was determined that the Tetra 0.4 grid had a lower number of cells to capture the velocity profile and further improvement is needed to maintain the accuracy near the tool surface; possibly inclusion of prism cells can be used to achieve that. Thus, in this section, the effect of prism cell edge length and height of the prism layer were examined in terms of the velocity profile. The study investigated the use of three prism cells, which were 6 prism layers with 0.05 mm prism height, 12 prism layers with 0.05 mm prism height and 12 prism layers with 0.025 mm prism height. All prism cells had edge length of 0.4 mm on the tool surface for block 9 in Figure 4-3. Figure 4-10 shows the shape of the prism layers used in the simulation work; this technique will be used to mesh more complicated tool design that will be used for further studies in this thesis.
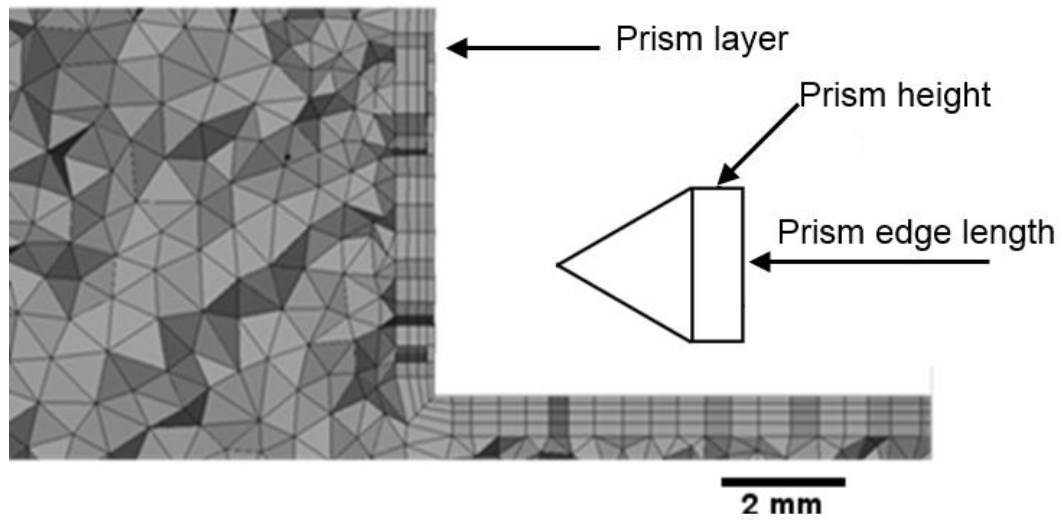
Figure 4-10 Mesh detail with prism layers for block 9 at the tool surface; (Note that the graph represents half the tool).

Figure 4-11 shows the results using three prism cells, which were 6 prism layers with 0.05 mm, 12 prism layers with 0.05 mm and 12 prism layers with 0.025 mm and the velocity profile at an angle of 45° at radial distance that given in Figure 4-5 was extracted. The profile for the converged hexahedral mesh is also shown for comparison in order to show the advantage of using prism cells and to indicate whether including prism layer would give similar results to those of the hexahedral mesh.

It appears that near the tool surface grid, including prism layers significantly increased the accuracy at the tool surface when compared with pure tetrahedral cell (Tet 0.4 in Figure 4-9) with reference to Hexa 0.05. The results of this figure also show that no significant difference can be seen when using different prism height or number of layers and the lines seem to be identical, except 12 prism layers with 0.025 mm which showed a difference of less than 7.5% at a radial position of 0.1 mm. It is important to mention that using additional layers can be problematic with complex geometries in terms of mesh construction, therefore, it is concluded that 6 prism layers with 0.05 mm can be used for future studies and will be referred to as "Prism 0.4" thereafter. It can

be also concluded that prism layers significantly increased the accuracy at the tool surface when compared with pure tetrahedral cells, which is an important region for predicting tool wear in Chapter 6. However, it can be seen that there is still an under predication of less than 30% with reference to Hex 0.05 at a radial distance between 0.5 to 0.9 mm due to use of tetrahedral cells.
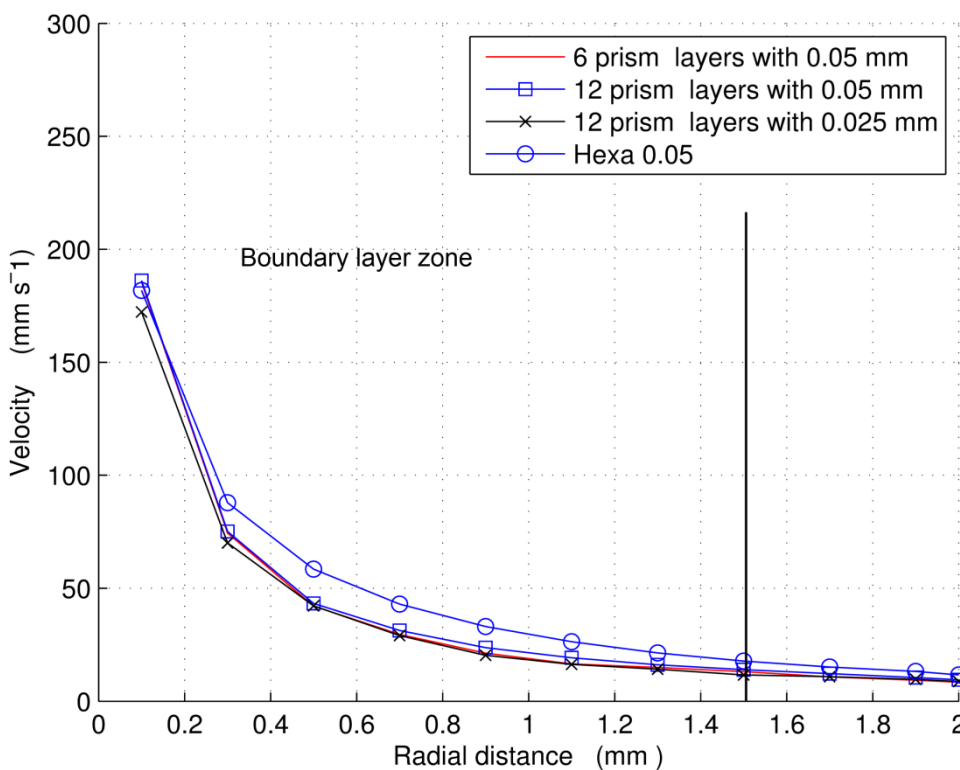
Figure 4-11 Velocity profile with radial distance from the tool surface at an angle of 45º using different prism layers and Hexa 0.05length and size

The velocity magnitude at two points close to the base of the pin were used to confirm the mesh convergence. These points are shown in Figure 4-12, point 1 (p1) was at an angle of 45° which is located in the upstream region, while point 2 (p2) was at an angle of 225° which is located in the downstream region. Those points were located at pin tip (y = 0 mm) and at 0.1 mm in the radial direction away from the pin surface. At the monitoring points chosen, the flow has a combination of rotation, separation, and flow

in the vertical direction (material flows down from the top surface to underneath the tool) and therefore, can be described as very complex flow [33] and is a good confirmation of the conclusions of the mesh independent study.
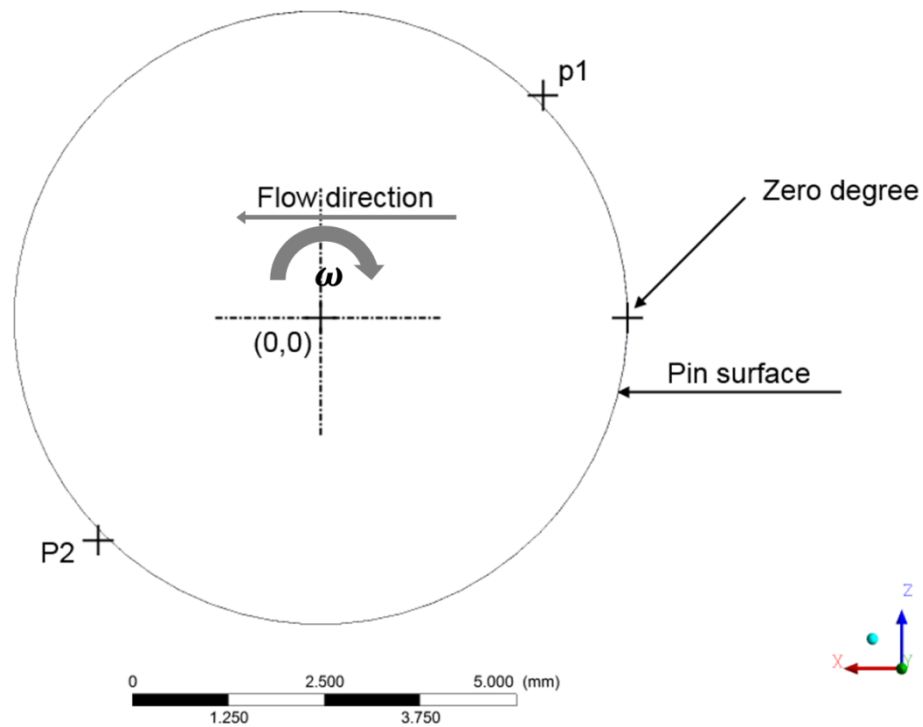
Figure 4-12 Angles used for computation at pin tip (y = 0 mm) and located at 0.1 mm in the radial direction from the pin surface

Figure 4-13 shows the relationship between 1/cell size and the value of velocity at p1 and p2; the hexahedral cells with a different cell size for the block (B9) are compared with the with the pure tetrahedral mesh (Tetra 0.4) and the hybrid mesh, Prism 0.4 that includes prism layers (6 layers of 0.05 mm). For the hexahedral mesh (Hexa), it is clear that by refining the mesh, the difference in the results between a cell size of 0.05 mm and 0.025 mm is less than 2% for the both points. In contrast, the results of the mesh including the prism layers show differences compared to the finest mesh (Hexa) of less than 3%. The mesh including the prism layers also brings a significant improvement over the pure tetrahedral mesh with the equivalent size, the difference in the results between Prism 0.4 and Tetra 0.4 is 23% referenced to Hexa 0.05.
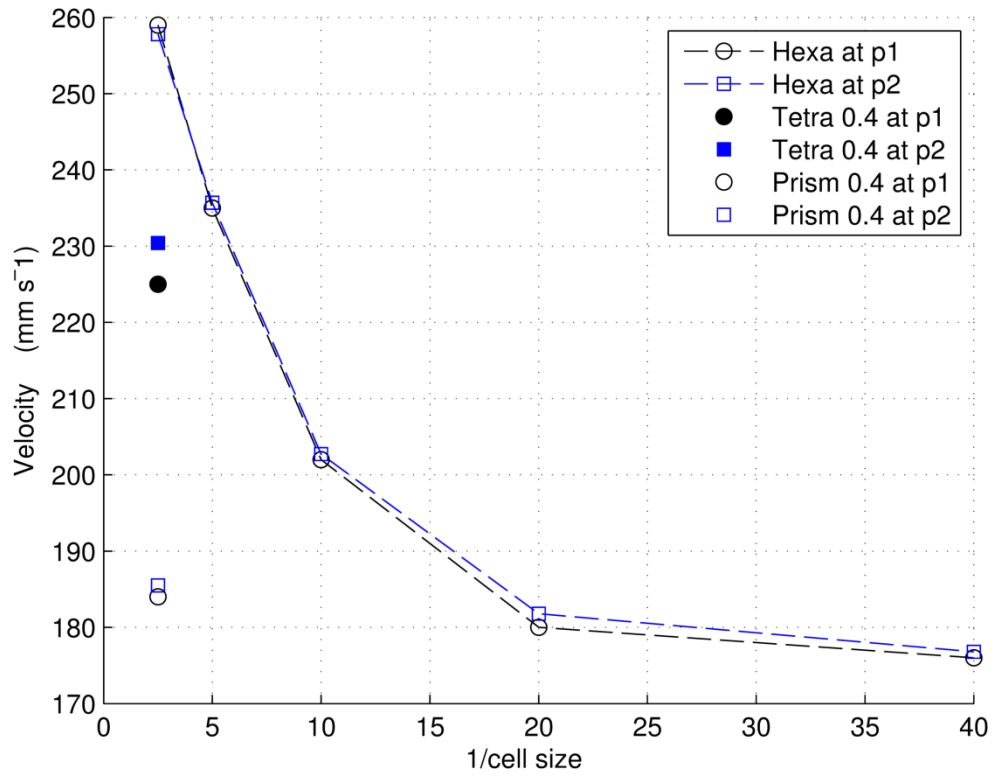
Figure 4-13 Mesh sensitivity study showing the variation in the total velocity at points 1 and 2 against 1/cell size and the effect of the inclusion of the prism layer at the tool surface and pure tetrahedral cell size of 0.4 mm.

4.8 Flow behaviour validation

In this section, the work starts with a replication of the analysis by Stojkovic et al. [128] to validate the flow behaviour in FSW model. Fundamentally FSW can be described as flow around a rotating cylinder, so we have incompressible non-Newtonian fluid rotating with a particular angular speed. In order to understand the effect of the rotation rate at Reynolds number, Re, value of 0.01 on the flow, and to make sure that the model is implemented correctly. The study will compare the streamlines of the flow of water in the work of Stojkovic with aluminium alloy 6061-T6 at the same Re number and rotation rate, and then the study will be carried out using the UDF to calculate the material viscosity to examine the effect of the viscous term on the streamline behaviour for the same cases.

4.8.1 Model details

Stojkovic et al. [128], Sanjay and Kumar [129] and Champmartin et al. [130] have documented that the flow around a circular cylinder is a function of the Re number and rotation rates α_r, which is the ratio of the cylinder rotational speed to the oncoming flow velocity (inlet velocity). Equations 4-11 and 4-12 define the two terms Re number and α_r:

$$Re = \frac{u_{inlet}D\rho}{\mu} = \frac{Inertia\ force}{Viscouse\ force} \qquad\qquad 4\text{-}11$$

$$\alpha_r = \frac{D\ \omega}{2u_{inlet}} \qquad\qquad 4\text{-}12$$

where, u_{inlet} is the inlet velocity at the inlet boundary, D is the diameter of the cylinder, μ is the dynamic viscosity, ρ is the material density and ω is the rotating speed of the cylinder.

A 3D model with incompressible fluid flowing at Re numbers of 0.01 and rotation rates of α_r = 0, 1and 3 were produced using the commercial CFD software FLUENT. The study considered these values of Re number and α_r, which were implemented in a steady state viscous laminar flow model and was solved isothermally. The study considered aluminium alloy 6061-T6 with the material properties presented in Table 4-2 , and viscosity was calculated using the UDF as a function of the strain rate and flow stress [105] (the details of this UDF are given in Appendix 1). The computational domain geometry of the work was a rectangular cuboid and had the following dimensions: 1×10^3 mm length, 0.5×10^3 mm width, and 4 mm thick. The cylinder had a diameter of 8 mm and a length of 4 mm; it was placed in the first half of the plate, towards the inlet. The model dimensions were selected according to the work of Stojkovic et al. [128]. The study used the same mesh, solver convergence and boundary conditions as those used in the structured mesh study in this chapter, a stick condition was applied on the cylinder surface and the rotation was in the clockwise direction.

4.8.2 Model validation

4.8.2.1 Flow behaviour at $\alpha_r = 0$

The case of Re number (0.01) at α_r = 0 were run and the flow behaviour was investigated by plotting the streamlines, as shown Figure 4-14; the simulation results of aluminium alloy 6061-T6 using a constant value of viscosity showed a good correlation when they were compared with the work of Stojkovic, presented in Figure 4-15. For the case of Re = 0.01 the viscous term in the Re number equation (equation 4-11) has an impact on the fluid motion, which means the material viscosity controls

the flow behaviour. The symmetrical flow can be seen and it is the characteristic of flow with this Re number value. This flow behaviour is known as creeping flow in which viscous transport and convective transport are predominant factors [128]. Furthermore, a viscosity was investigated for this case of Re = 0.01 and ($\alpha_r = 0$) and it was found that the viscosity retained a constant value of 1.78×10^5 Pa s.
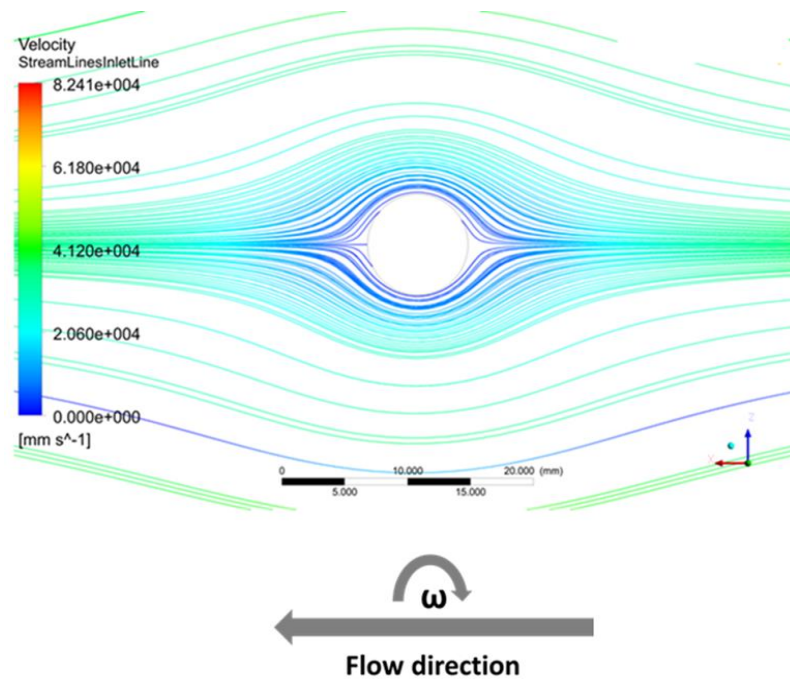
Figure 4-14 Re = 0.01 with fixed cylinder ($\alpha_r = 0$); constant value of viscosity value (=1.78×10^5 Pa s)
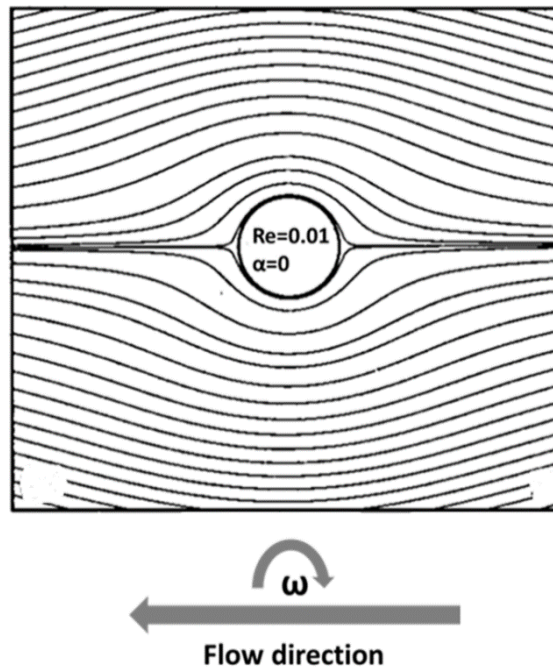
Figure 4-15 Streamline for Re = 0.01 at $\alpha_r = 0$ from Stojkovic et al. [128])

4.8.2.2 Flow behaviour at Re = 0.01 with $\alpha_r = 1$ and 3

The streamlines shown in Figure 4-16 a and Figure 4-16 b show a different behaviour from those predicted in the case of $\alpha_r = 0$ (fixed cylinder).

At $\alpha_r = 1$ an egg-shaped flow region formed, and the flow behaviour was different from the symmetry behaviour that was observed at $\alpha_r = 0$. At $\alpha_r = 3$ the angular velocity increased, and the egg-shaped region around the cylinder was enlarged compared to the case of $\alpha_r = 1$, due to the fact that the lift force is a linear function of the rotation rate [128]. For the case of $\alpha_r = 1$ the peak velocity was 8.24×10^4 mm s^{-1}, while for case of $\alpha_r = 3$ the peak velocity was 2.47×10^5 mm s^{-1}. If we compare the results of the fixed and rotating cylinder, it can be seen that at the leading edge of the cylinder the stagnation point in the upstream part moves in the direction of the cylinder rotation. Furthermore, when the rotation rate increases, the density of the streamlines also increase near the cylinder surface. In addition, our study used the work of Stojkovic et

al [128] to verify the CFD model because it has a wide range of Re and α_r with a better representation for the streamlines. The simulation results of aluminium alloy 6061-T6 using a constant value of viscosity showed good prediction for the flow field behaviour when they were compared with the work of Stojkovic shown in Figure 4-17 in terms of egg-shaped region around the cylinder at different rotation rate. The bulk flow field features obtained by Stojkovic are also seen in the CFD model. There are small local differences, notably at the top of the "egg" region and these are likely due to the fact that the current work was done on a 3D mesh compared to Stojkovic's 2D mesh and also the mesh density was higher in the current case.
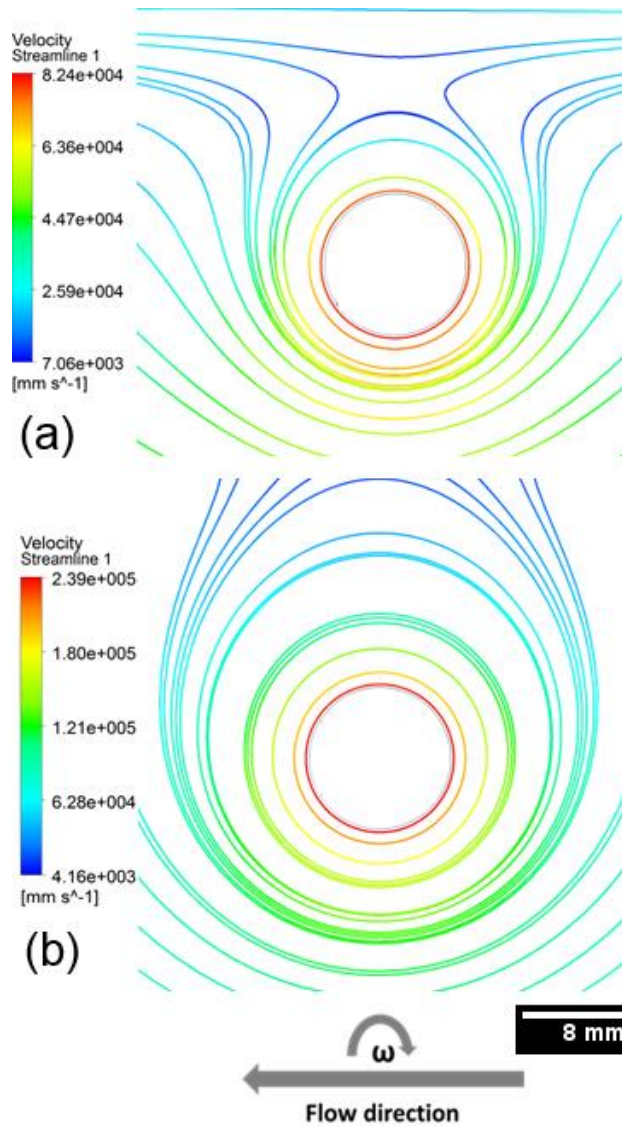
Figure 4-16 (a)- Re = 0.01 $\alpha_r = 1$, (b)- $\alpha_r = 3$ with constant value of viscosity value (=1.78×10^5 Pa s)
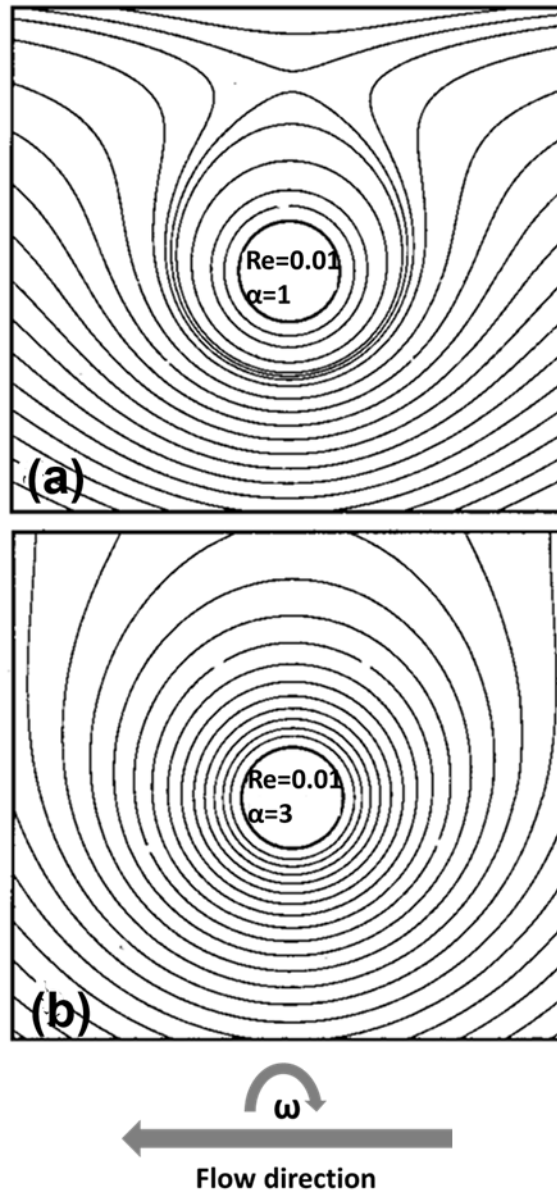
Figure 4-17 Streamlines for (a)-Re = 0.01 at α_r = 1 and (b)- Re = 0.01 at α_r = 3 (from Stojkovic et al.

[128])

4.8.3 The effect of using strain rate dependent viscosity on the flow behaviour

The streamlines shown in Figure 4-18, with $\alpha_r = 0$ and Re = 0.01, demonstrate that when using the UDF, the order of magnitude of the velocity around the cylinder and on both sides in the wall direction is higher than that presented in Figure 4-14 when a fixed value of material viscosity was used and took a value of was 8.24×10^4mm s^{-1}. However, the symmetry behaviour of the flow around the cylinder for UDF material viscosity is the same behaviour as that seen when using the constant viscosity value. The region of plastic deformation around the rotating cylinder can be seen in Figure 4-20 a and Figure 4-20 b, with the UDF material viscosity. From the examination of the streamlines, the egg-shaped region for the cases of $\alpha_r = 1$ and 3 decreased significantly when compared to Figure 4-16. The flow of the material occurs due to cylinder rotation and is directly proportional to the circumferential velocity. It can also be seen that the flow bifurcates outside the cylinder diameter when $\alpha_r = 1$, whereas, a bifurcation of the flow occurred very close to the cylinder diameter in case of $\alpha_r = 3$, consistent with what has been reported by Reynolds et al. [46]. It can be argued this behaviour of flow bifurcation at $\alpha_r = 3$ is due to the increase in the lift force with increasing rotation rate and the effect of the axial flow decreases when rotation rate increases. Flow around a circular cylinder (fixed or rotated) produces two force, which are drag (in-line force) and lift (cross-flow force) on the cylinder [131, 132]. In Figure 4-19, the viscosity is not constant and it is a function of the strain rate. It is clear that by increasing the velocity on the both side of the cylinder, there is a reduction in the viscosity in that region. In case of Re 0, $\alpha = 1$, there is are a reduction in the viscosity value in area surrounding the cylinder where a high velocity gradient occurs as can be

seen in Figure 4-21; which is the area of plastic deformation. It can be noticed how the implementation of the UDF caused a significant change in the viscosity contour when it is compared with a constant value of viscosity.
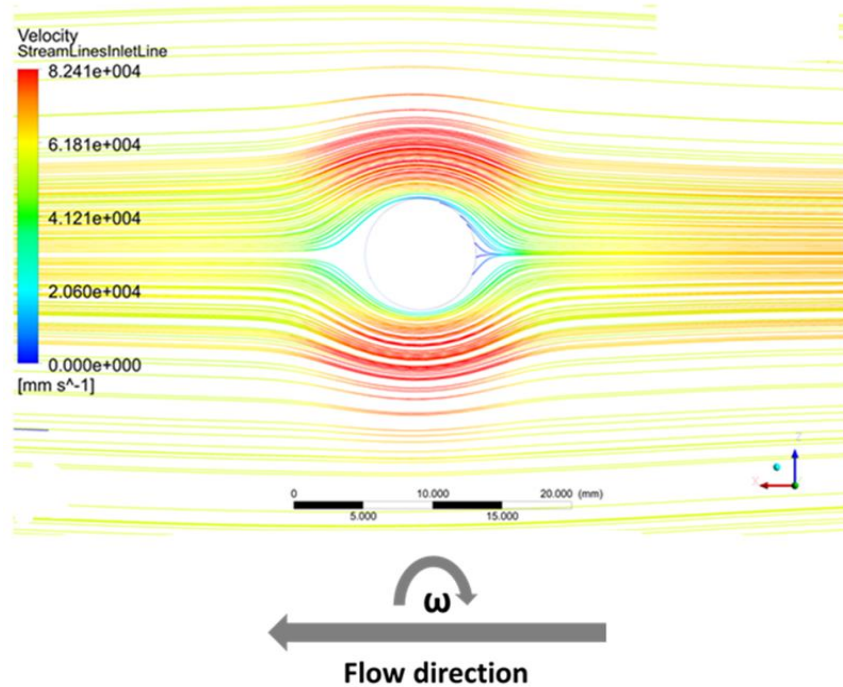
Figure 4-18 Streamlines for -Re = 0.01 fixed cylinder ($\alpha_r = 0$) with UDF
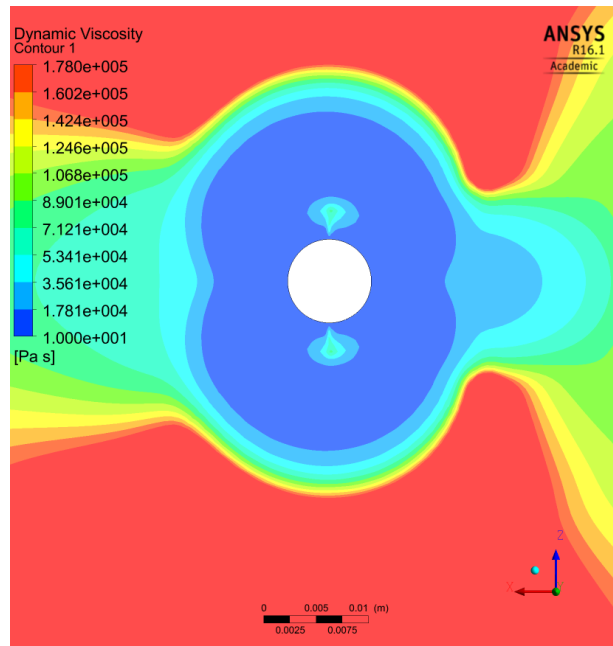
Figure 4-19 Viscosity contour for Re = 0.01 fixed cylinder ($\alpha_r = 0$) with UDF
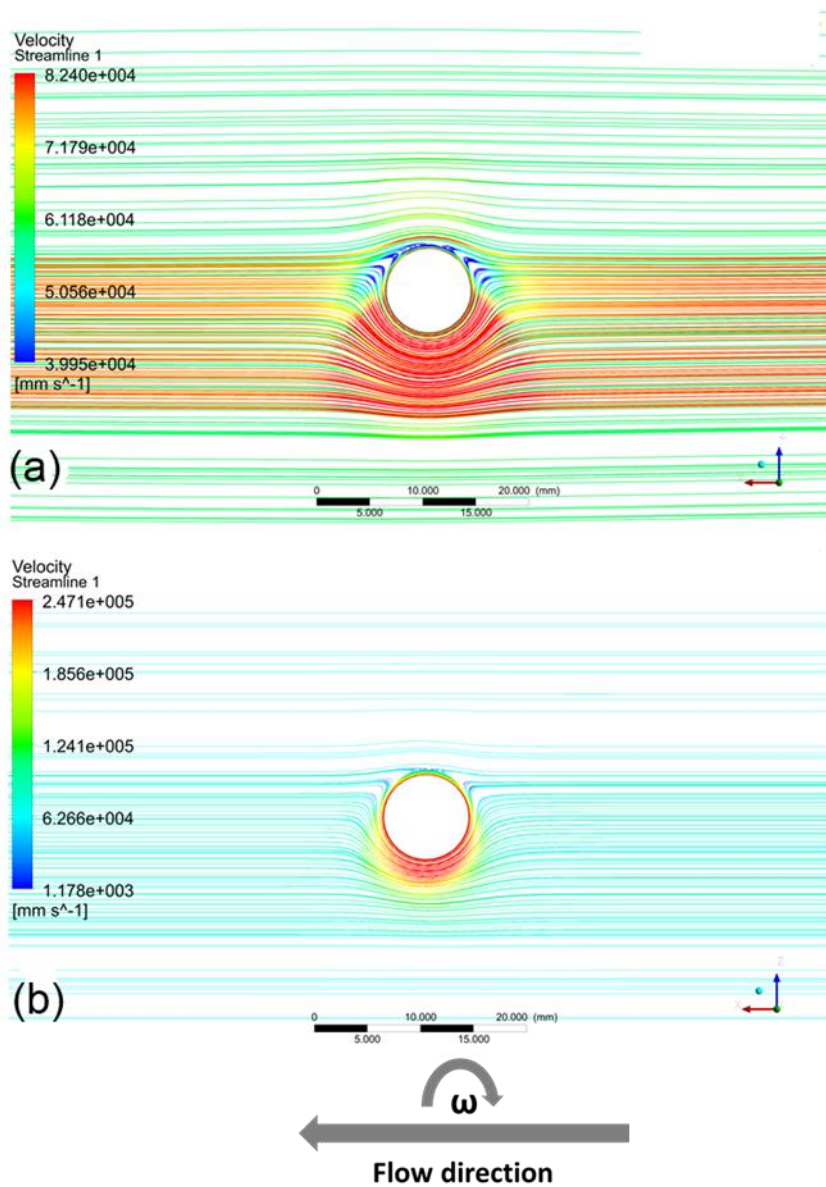
Figure 4-20 Streamlines for Re = 0.01, at (a)- $\alpha_r = 1$ and (b)- $\alpha_r = 3$ with UDF
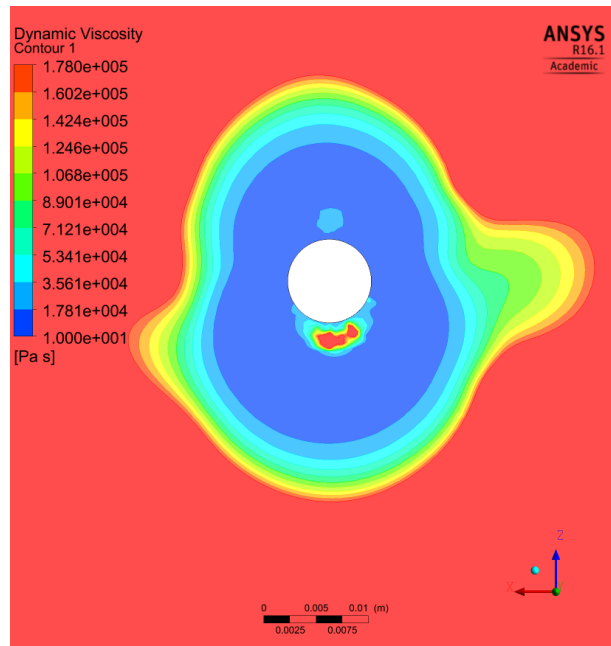
Figure 4-21 Viscosity contour for Re = 0.01, at α_r = 1 with UDF

4.9 Discussion

It is important to note that FSW has a very complex flow, and at the monitoring points chosen for the mesh study, the flow is a combination of rotation, separation, and incoming flow in the vertical direction (material flows down from the top surface to underneath the tool) [33]. It is noteworthy that the tetrahedral mesh (Tetra 0.4) had a significant difference when it compared with one that includes prism layers, highlighting that mesh with the prism layers is better because it can maintain a reasonable level of accuracy in predicting the velocity near the pin of the tool and at the boundary layer when compared with the mesh independent solution hexahedral mesh. Therefore, this mesh strategy can be used for further studies.

The results of the flow behaviour validation showed that for the cases of Re = 0.01, with constant material viscosity value; the symmetrical flow can be seen. Sanjay and Kumar [124] and Stojkovic et al. [128] concluded that creeping flow dominates the behaviour of the flow in these circumstances. Creeping flow is a term used to describe the flow when the viscous force plays a significant role in the Re equation [128]. Figure 4-18shows that the symmetry behaviour of the flow around the cylinder for UDF material viscosity is the same behaviour as that seen in the constant viscosity value. There is a significant difference in the velocity magnitude when using the UDF material viscosity for the case of Re 0.01. It can be argued that the reason for the increase in the velocity magnitude is due to the fact that incoming flow passes the cylinder at the stagnation point which has a zero velocity value, and then the flow bifurcates around both sides of the cylinder causing a notable increase in the velocity. This behaviour leads to an increase in the strain rate also at the both side of the cylinder

[133]. The viscosity of the material reduced as a result of the increasing strain rate where the relationship between these two parameters is inversely proportional [48]. During the rotation of the cylinder, one side of it moves with a velocity value higher from the free stream velocity; it moves with the wall of the cylinder velocity because there is a pressure difference on one side, which changes the symmetry behaviour. The lift force is a linear function to the rotation rate because the pressure distribution and the drag force are not affected by α_r [128]. Therefore, an egg-shaped flow region around the cylinder formed, which was enlarged when α_r increased. It can explain this due to the fact that the lift force is a linear function of the rotation rate.

When using the UDF material viscosity for the cases of $\alpha_r = 1$ and 3, the egg-shaped region decreased significantly. It can be argued that the plastic deformation of the material occurs due to cylinder rotation and is directly proportional to the circumferential velocity. By using a non-Newtonian viscosity, which is a function of the local strain rate, in the region surrounding the rotating cylinder with high strain rate there is a reduction in the material viscosity, which is the area of plastic deformation. In that region, the deformed material moves from one side to another side in the same direction of the tool rotation direction. This behaviour has been reported by Nandan et al. [13] and Cho et al. [134] when they modelled FSW.

4.10 Conclusions

As stated in the introduction, a goal of this chapter was to establish guidelines for simulation of FSW using the CFD model. Structured and hybrid grids were utilised to determine the best mesh quality and the study examined the advantages of using prism cells near the tool surface to capture the flow behaviour near the boundary layer. In addition, the flow behaviour around cylinder with different values of Reynold's number and rotation rate were studied in order to validate the flow behaviour in FSW modelling.

From the study, several conclusions can be drawn:

- The results of the mesh study showed that a hybrid mesh could be better in achieving the best solution for the FSW process and for modelling complex tool geometry.

- Flow in the boundary layer is a crucial issue therefore a grid with a prism layer has been shown to be a powerful technique for solving this issue.

- The streamlines of the aluminium alloy 6061-T6 flow showed good agreement with the literature at the same rotating rate and Re number.

- At high strain rate (near the rotating tool) there is a reduction in the viscosity, which is the area of the plastic deformation.

In the next chapters, the knowledge gained from this study will be used to study the flow behaviour for the unworn and worn tool design and to calculate the tool wear in the FSW process.

Chapter 5 Mechanically Affected Zone (MAZ) validation and flow comparison

5.1 Introduction

Much of the literature on FSW has demonstrated different approaches for analysing the flow behaviour using experimental methods and numerical models as presented in chapter 2. However, research concerning the flow behaviour associated with FSW with worn tools has been limited and mainly covers experimental studies into what happens in terms of the weld root, strain rate and the geometry of the stirring zone after the tool has become worn (or self-optimized). In this chapter, validated flow models of the FSW process have been produced using the ANSYS FLUENT-CFD code in order to enable the prediction and comparison of the flow behaviour and the Mechanically Affected Zone (MAZ) size around both unworn and worn tools. Two models are presentenced in this chapter; model 1 was used for the MAZ validation, whereas model 2 was used to compare the flow behaviour around unworn and worn tools.

5.2 Models description

Two models were created based on the methodology that was established in chapter 4 in terms of assumption, workpiece boundary conditions, solver, convergence and mesh. They were solved isothermally , was done by Colegrove and Shercliff [135] previously; the isothermal assumption was made as the flow stress is relatively insensitive across the temperature range between 0.6 to $0.8T_m$. Additionally, Naidu [136] reported differences in the welding temperature through the thickness of the plate

to be less than 10 °C for the welding of Al7050 alloy. Moreover, the study developed the models by including the slip-stick condition described in chapter 4. For both models, a slip-stick condition has been implemented on the tool shoulder through the application of equations 4-5 and 4-6, whilst a stick condition has been applied on the pin surface; this combination of boundary conditions for the tool is widely used in the literature [14, 137] and so is adopted here. In this chapter the study used Al-7020 as the welding material for both models, and the material properties are presented in Table 5-1.

Table 5-1: Al-7020 material properties [105, 138]

Material property	Value
ρ, density	2700 kg m^{-3}
α, material constant	0.038 MPa $^{-1}$
A, material constant	7.86 x10^6 s^{-1}
n, material constant	5.37
Q_e, activation energy	232.56 kJ mol^{-1}
Temperature (0.65 T_m)	578.5 K

5.3   Validation the size of the MAZ

5.3.1 Geometry of model 1

The computational domain of model 1 was a rectangular cuboid 200 mm long, 100 mm wide and 0.4 mm thick. The diameter of the pin was 5 mm (a smooth cylinder) with a concave shoulder (2.5°) with a diameter of 13 mm.

5.3.2 Validation procedure

To confidently use Computational Fluid Dynamics (CFD) results for investigating the FSW process, the CFD model has to be correctly defined and a thorough validation has to be achieved. It is known that the stirring action caused by the tool rotation produces the characteristic shape of the MAZ [139] and that at a distance away from the tool surface, there is a lack of plastic deformation. Kim et al. [140] reported that a lack of plastic flow occurred during compression testing of Al 7050 at viscosities in the range 10^5 to 10^6 Pa s. Based on the constitutive equations used for Al 7020 in this work, calculations show that at a strain rate less than 50 s^{-1} at temperatures between 0.6-0.8 T_m, the viscosity ranges from 10^6 to 10^7 Pa s, showing consistency with the work of Nandan [141]. Therefore it is possible to determine the shape and size of the MAZ at the region where no significant flow occurs by using an iso-viscosity surface (cut-off viscosity), an approach consistent with the work of Nassar and Khraisheh [142].

To refine the value of viscosity that could be used to determine the MAZ, the experimental work of Lorrain, Favier, Zahrouni and Lawrjaniec [143] was modelled and the size of the MAZ was extracted from the model using an iso-viscosity surface to define the limit of the plastic flow. A number of different values of viscosity were

evaluated to define the limit of the MAZ and the error for each value was calculated compared to the experimental MAZ values. Based on these results, a value of viscosity was determined for this material from the four experimental cases that could be used for further work in this material.

Four lines were used, shown in Figure 5-1 , to compare the MAZ width; these lines were located on the base of the plate (L_r), and 1, 2 and 3 mm from the base of the plate for L_1, L_2 and L_3 respectively. Table 5-2 presents the process parameters and the MAZ size at the different locations that were used to validate the model. A plane was set perpendicular to the welding direction across the tool in the z-direction to calculate the size.
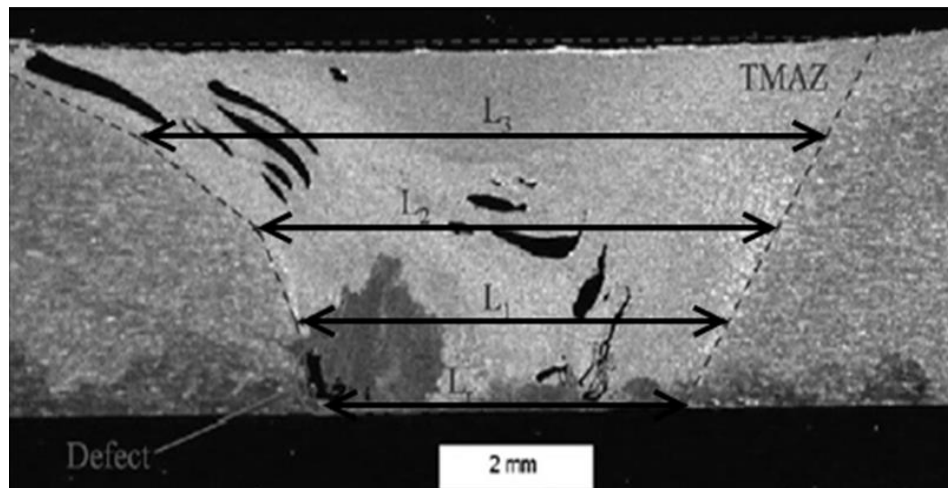
Figure 5-1: Weld zone measurement locations for validation data [143]

Table 5-2: Weld parameters and measured values of the weld zone (in mm) used for the valiation

Case	u_{weld} [mm s^{-1}]	ω [rpm]	L_r [mm]	L_1 [mm]	L_2 [mm]	L_3 [mm]
1	1.66	300	4.8	5.5	6.5	8.6
2	1.66	600	4.8	6.5	7.5	10.4
3	8.33	600	5	5.6	8.1	10.8
4	15	900	5.2	6.4	7.4	9.1

Each line was set in the same location as in the experimental work to maintain consistency in the results. Four cases were run at different parameters as seen in Table 5-2 using the FLUENT FSW model. CFD-Post was then used to process the data and view the shape and size of the MAZ based on the value used to define the iso-viscosity surface; this method has previously been used by Arora et al. [21]to investigate the effect of tool design on the MAZ.

5.3.3 Results of model 1

Four values of viscosity were considered to measure the size of the MAZ at each line; these values were then compared with experimental values. Figure 5-2 a and b shows an example for the shape of the MAZ for case 1 and 4 at same value of iso-viscosity surface (1.5×10^6 Pa s. The Root Mean Square Error (RMSE)) was calculated for each of these values of viscosity as shown in Table 5-3, and it can be seen that a viscosity of 1.5×10^6 Pa s shows a consistently good match with the experimental values for MAZ width across the parameters studied. Additionally, it can be seen that the simulation shows a good agreement with the experimental data in terms of the size of MAZ using this viscosity value. This suggests that the FLUENT FSW model can be considered an appropriate method for predicting the flow behaviour around the unworn and worn tool.
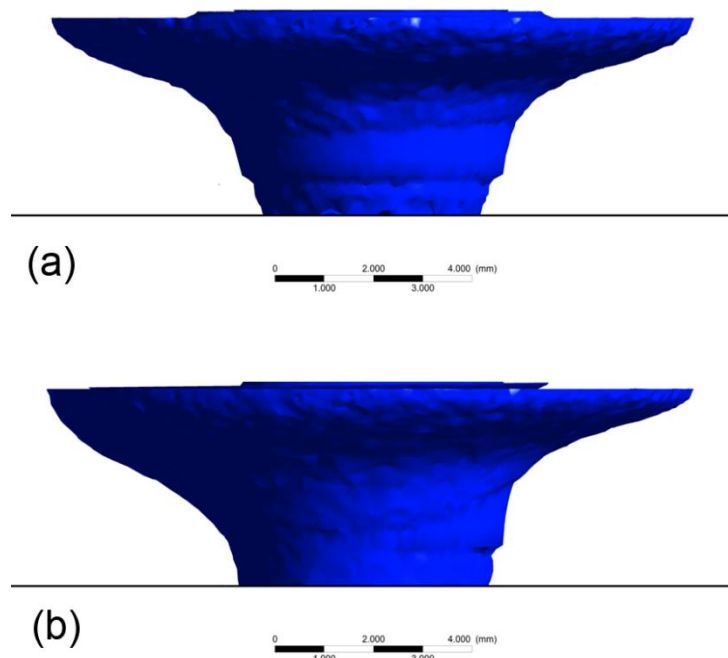
Figure 5-2 Predicated shape of the weld zone (a) case 1 at 1.66 mm s^{-1} and 300 rpm, (b) case 4 at 15 mm s^{-1} and 900 rpm

Table 5-3: MAZ widths and RMSE for different viscosity values for three different tool rotational
speeds

Case	Viscosity [Pa s]	L3 [mm]	L2 [mm]	L1 [mm]	Lr [mm]	RMSE [mm]
1	1×10^6	5.4	5.6	5.3	3.8	1.7
	1.5×10^6	9.5	5.9	5.3	4.7	0.5
	2×10^6	10	6.4	5.4	4.5	0.7
	5×10^6	5.9	5.6	5.3	4.6	1.4
2	1×10^6	9.77	6.06	5.42	4.46	0.9
	1.5×10^6	10.44	6.65	5.48	4.63	0.5
	2×10^6	10.9	7.04	5.53	4.76	0.6
	5×10^6	11.56	8.08	5.93	5.31	1
3	1×10^6	9.5	5.6	5.3	4.5	1.2
	1.5×10^6	10.2	6.6	5.5	4.6	0.7
	2×10^6	1	7.2	5.6	4.9	0.6
	5×10^6	9.3	7	5.9	4.3	0.7
4	1×10^6	10.2	6.4	5.55	4.7	0.5
	1.5×10^6	10.6	7.1	5.6	4.9	0.4
	2×10^6	11.1	7.5	5.8	5.1	0.7
	5×10^6	7.9	5.3	5.2	4.8	1.3

Moreover, a viscosity of 1.5×10^6 Pa s was used to draw a scatter plot shown in Figure
5-3 for the predicated weld zone size at each line then compared with measured values.
It can be seen that good match with the measured values for MAZ width across the
parameters studied was seen using this value of the viscosity.
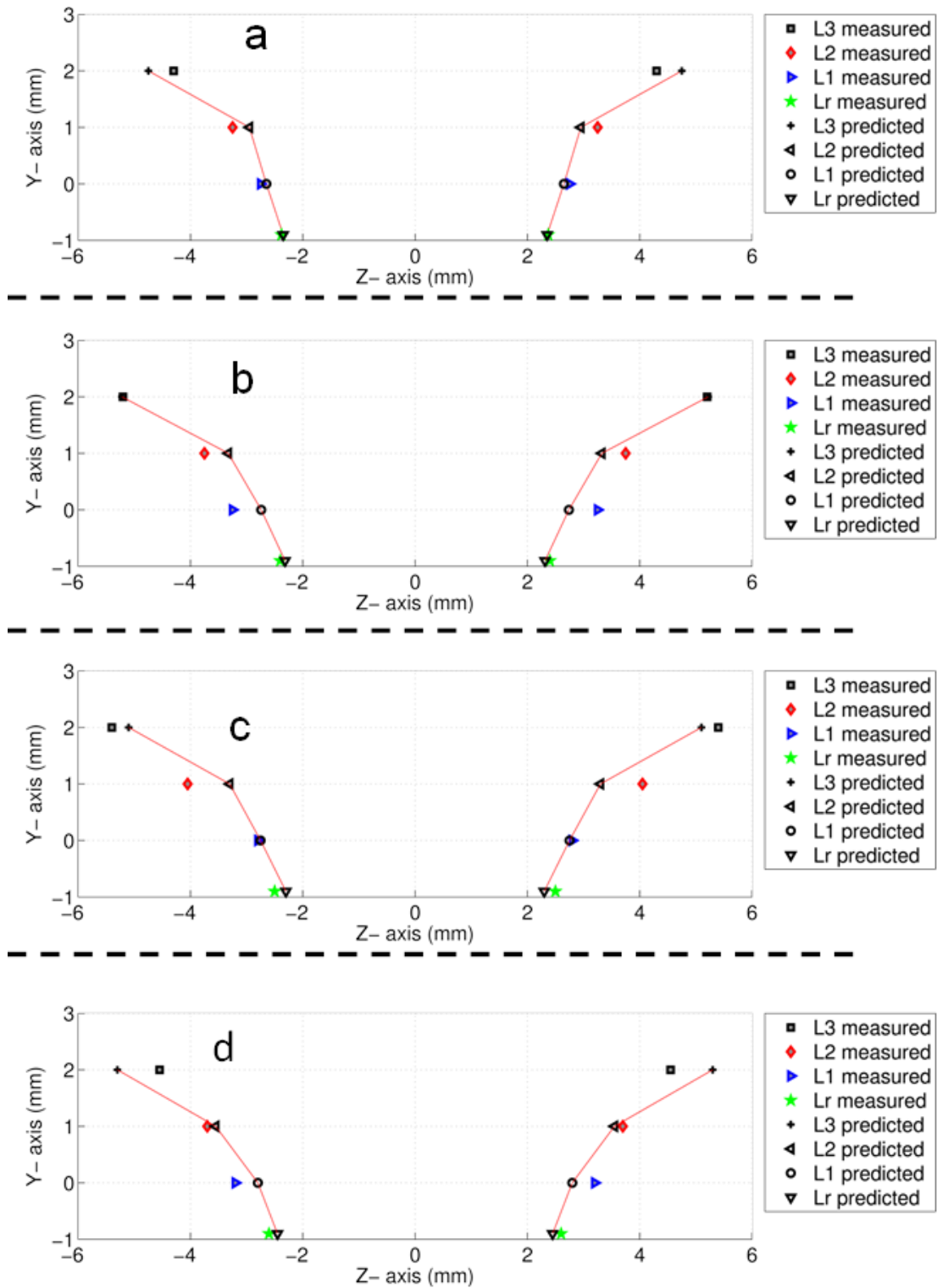
Figure 5-3 Measured and predicted values of the weld zone (in mm) (a) case 1 at 1.66 mm s^{-1} and 300 rpm, (b) case 2 at 1.66 mm s^{-1} and 600 rpm, (c) case 3 at 8.33 mm s^{-1} and 600 rpm and (d) case 4 at 15 mm s^{-1} and 900 rpm; using a viscosity of 1.5×10^6 Pa s

5.4 Comparison of the flow behaviour around unworn and worn tools

5.4.1 Geometry of the model 2

Model 2 was used to conduct a mesh study using a threaded tool and used to compare the flow behaviour of the unworn and worn tools; the geometry of the computational domain of the model 2 was a rectangular cuboid with the dimensions presented in Table 5-4. The unworn tool pin geometry for was a 1/4-20 UNC thread (6.35 major diameter with 12.7 mm pitch) constructed with PTC Creo software. The image of the worn tool was taken from the work of Prado et al. [10] and imported into PTC Creo and the tool geometry was constructed using this to approximately match the shape of the worn tool. Figure 5-4 presents the unworn and worn tool geometries that were used for the study, while the computational domain is shown in Figure 5-5.

Table 5-4: Description of the dimensions of the models.

Dimensions in mm	Model 2
Plate length	260
Plate width	120
Plate thickness	4.8
Pin diameter	6.3
Pin length	4.2
Shoulder diameter	19
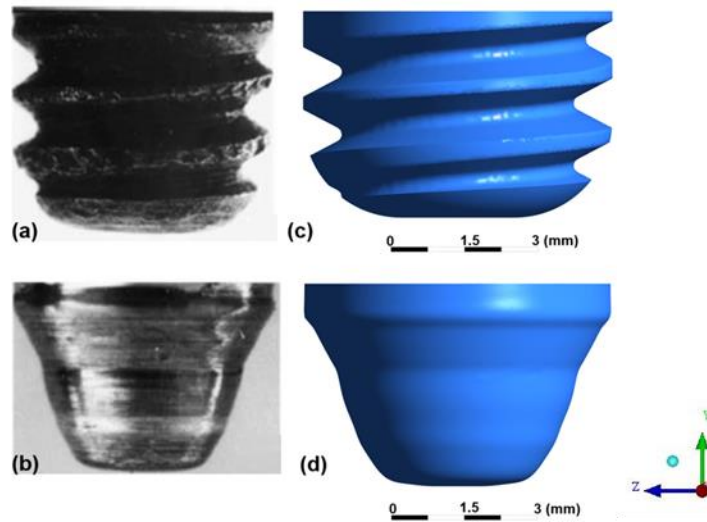
Figure 5-4: Geometry of the tools used for the study [10] (a) unworn and (b) worn and corresponding

solid models used in the numerical simulation (c) unworn and (d) worn
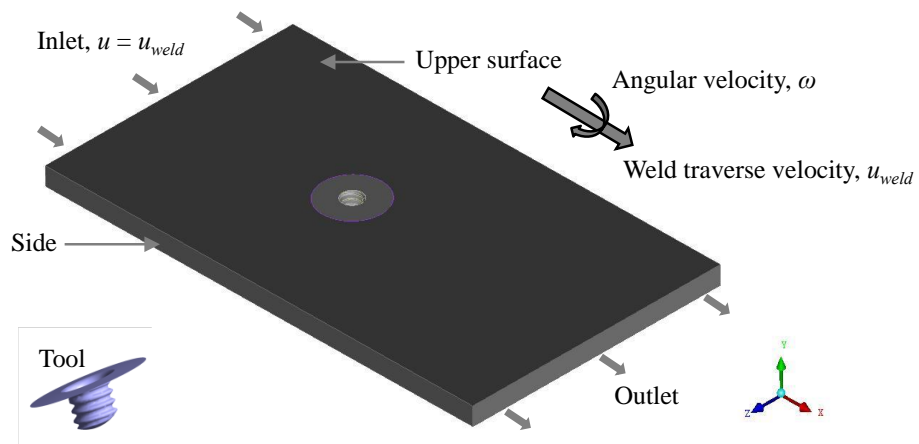
Figure 5-5: Computational domain and boundary conditions

5.4.2 Mesh Study

To demonstrate the potential of the meshing strategy that was presented in chapter 4 and its suitability for the application in complex tool design, an independent mesh study is investigated in this chapter. Here, Model 2 was used with the weld parameters shown in Table 5-5; to achieve this study.

Table 5-5: Mesh study process parameters

Weld Traverse Speed [mm s-1]	Tool Rotation Speed [rpm]	Tool Geometry [-]
1.66	300	Threaded

The generated mesh is entirely the same as that presented in Chapter 4- section 4.6.2, only block 9 in Figure 4-2 which is surrounding the tool is meshed with tetrahedral cells. The cell edge size in that block took values of 0.8 mm, 0.4 mm, 0.2 mm, 0.125 mm and 0.1 mm in order to assess mesh independence.

The study used four prism element prism height of 0.05 mm on the surface of the threaded tool as shown in Figure 5-6. The velocity magnitude at two points (P1 and P2) close to the base of the pin from the converged FLUENT models using the different meshes was used to assess the mesh independence.
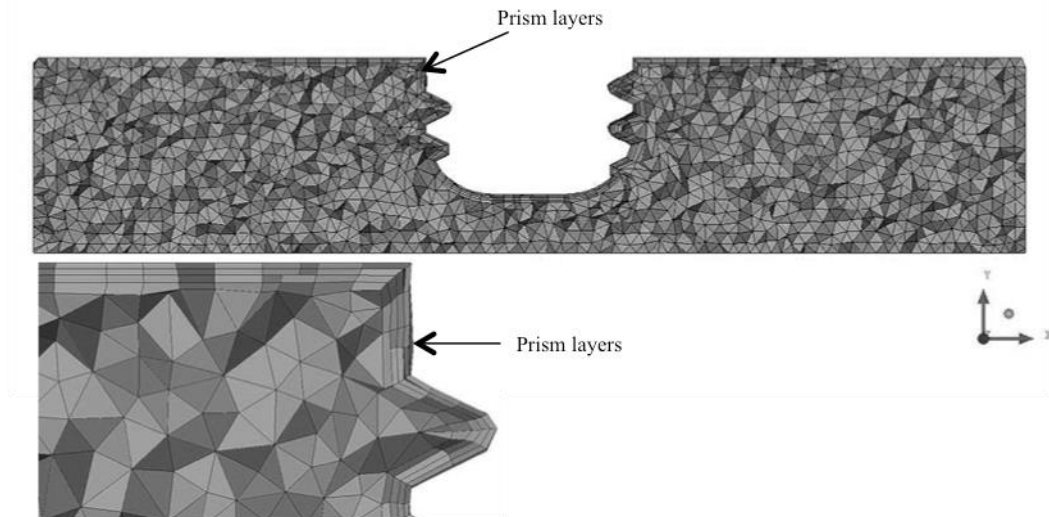
Figure 5-6: Mesh detail with prism layers at the tool surface

Figure 5-7 shows the relationship between 1/cell size and the value of velocity at point 1 and point 2. It is clear that by refining the mesh, the value of the velocity converges to 10 mm s^{-1} for point 1, while, for point 2, it converges to 14 mm s^{-1}. By refining the mesh, the difference in the results between a cell size of 0.125 mm and 0.1 mm is less than 5%; however, computational times for these mesh sizes are greater than 22 hours. In contrast, the results of the mesh including the prism layers show differences compared to the finest mesh of less than 22%, with a computational time of only 6 hours. The mesh including the prism layers also brings a significant improvement over the pure tetrahedral mesh with the equivalent size without increasing the computational time significantly. These models have very complex flow and at the monitoring points chosen, the flow shows a combination of rotation, separation, and incoming flow along in the vertical direction (material flows down from the top surface to underneath the tool) [33]. It is noteworthy that the tetrahedral mesh with a cell size of 0.125 mm had more than 4.5 million cells, while the mesh containing the prism layers with a cell thickness of 0.4 mm had 1.25 million cells, highlighting that mesh with the prism layers is more efficient in terms of computational time and can maintain a reasonable level of accuracy in predicting the velocity near the pin of the tool. The

chosen meshing strategy has given sufficient confidence even when it was used in the complicated flow within complex tool design.
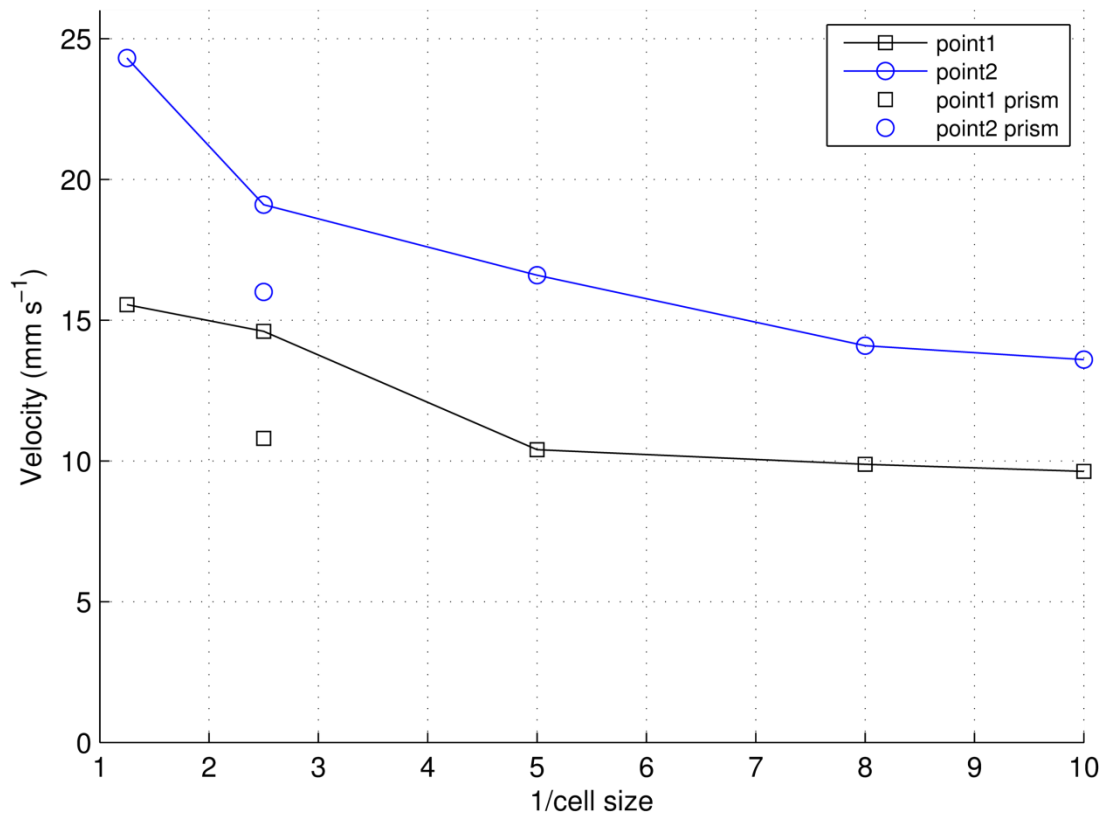
Figure 5-7: Mesh sensitivity study showing the variation in the total velocity at points 1 and 2 against 1/cell size and the effect of the inclusion of the prism layer at the tool surface.

5.4.3 Results of model 2 (Results for the unworn and worn tool)

A comparison of the unworn and worn tool geometries was made using Model 2 and the parameters shown in Table 5-6. A total of four cases were run to enable comparison of the flow behaviour across a range of rotational speeds.

Table 5-6: Process parameters for tool wear comparison

Weld Traverse Speed [mm s-1]	Tool Rotation Speed [rpm]	Tool Geometry [-]
1.66	300 & 600	Threaded unworn & worn

5.4.3.1 Predictions of the size and shape of the Mechanically Affected Zone (MAZ)

The size and shape of the MAZ in FSW are considered important criteria for achieving a good weld joint. The size and shape of the MAZ for the unworn and worn tools were calculated using the FSW CFD model developed in this work by plotting the iso-viscosity surface at a value of 1.5×10^6 Pa s as determined previously; three lines in the y-z plane, on the base of the plate for Lr, while L1 and L2 were located at y = 0.5 mm and 2.1 mm respectively, were used to compare the flow behaviour of the two tools as shown in Figure 5-8.
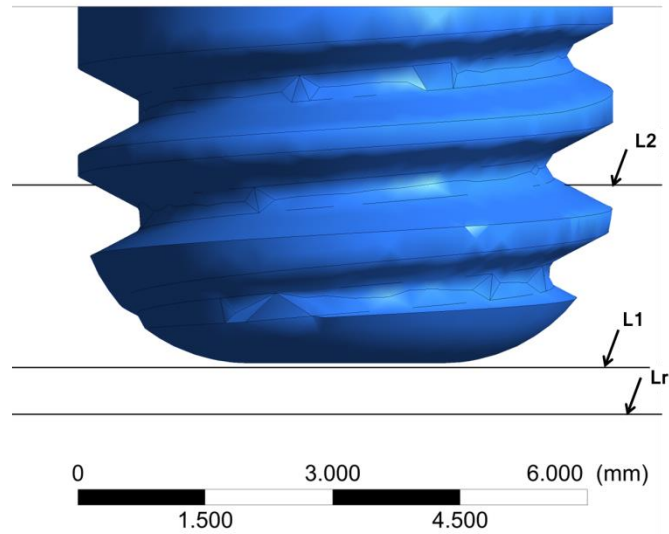
Figure 5-8: Locations used for comparison of MAZ between unworn and worn tool geometries

Figure 5-9 shows the shape of the MAZ for the unworn and worn tools tool at 300 rpm. It can clearly be seen that for the same value of iso-viscosity surface (1.5×10^6 Pa s), the shape of the MAZ for the worn tool (Figure 8b) is not as wide as that for the unworn tool (Figure 8a) and also, it does not reach the bottom of the plate (depicted by the grey line in the figure).
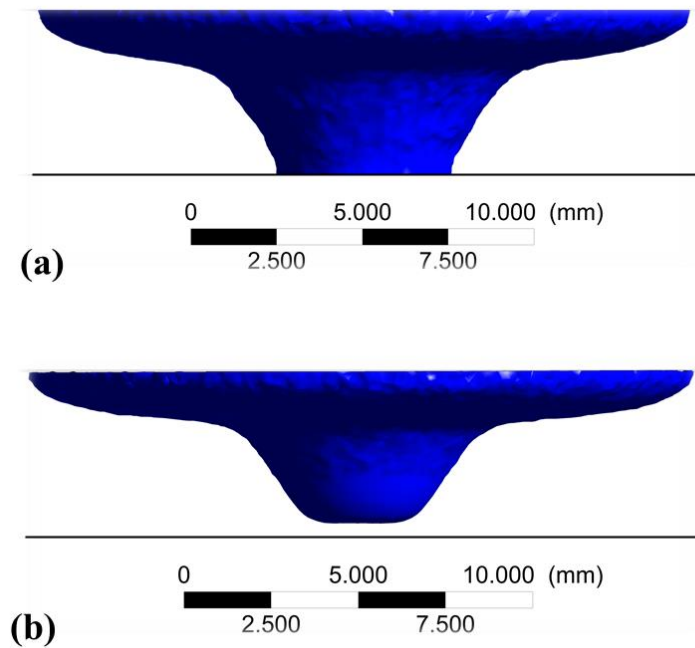
Figure 5-9: Shape of the weld zone at 1.66 mm s^{-1} and 300 rpm (a) unworn, (b) worn tool

Table 5-7 shows the differences in the size of the MAZ at different locations perpendicular to the weld direction. At 300 rpm, the results of the weld zone at L2 and L1 for the unworn tool were slightly larger than the values of the worn tool. At Lr the size of the MAZ for the unworn tool was 5.15 mm while there is no data in the same location for the worn tool at that particular value of the viscosity. This due to the fact that there is no significant plastic deformation at this area (near the weld root) and the value of the viscosity at that region remains above 1.5×10^6 Pa s. At 600 rpm, the results showed that for the unworn case, the size of the MAZ was predicted to be slightly larger than the values from the 300 rpm case for all locations. At L2 the values were 7.72 mm for the unworn tool and 5.72 mm for the worn tool. For L1, the results were also different. Similar to the case at 300 rpm, the size of the L1 at 600 rpm is smaller for the worn tool in comparison to the unworn tool. Again no data is available for Lr from the worn model for the 600 rpm case as the deformation in the weld root does not reach the underside of the plate being welded. The results show that a difference

between the unworn and worn tools can be predicted by the CFD model and seen in the iso-viscosity surface, which is representative of the MAZ. Additionally, Figure 5-10 shows the scatter plot for the data in Table 5-7, it is clear that how the worn tool size was changed and a no date for the root measured value which showed the reduction of the penetration at that region.

Table 5-7 Predictions of the MAZ size [mm] for the unworn and worn tool geometries

	[mm]	Unworn tool at 1.5×10^6 [Pa s]	Worn tool at 1.5×10^6 [Pa s]
300 rpm	L2	7.2	5.35
	L1	5.23	2.65
	Lr	5.15	No data
600 rpm	L2	7.72	5.72
	L1	5.63	2.8
	Lr	5.5	No data
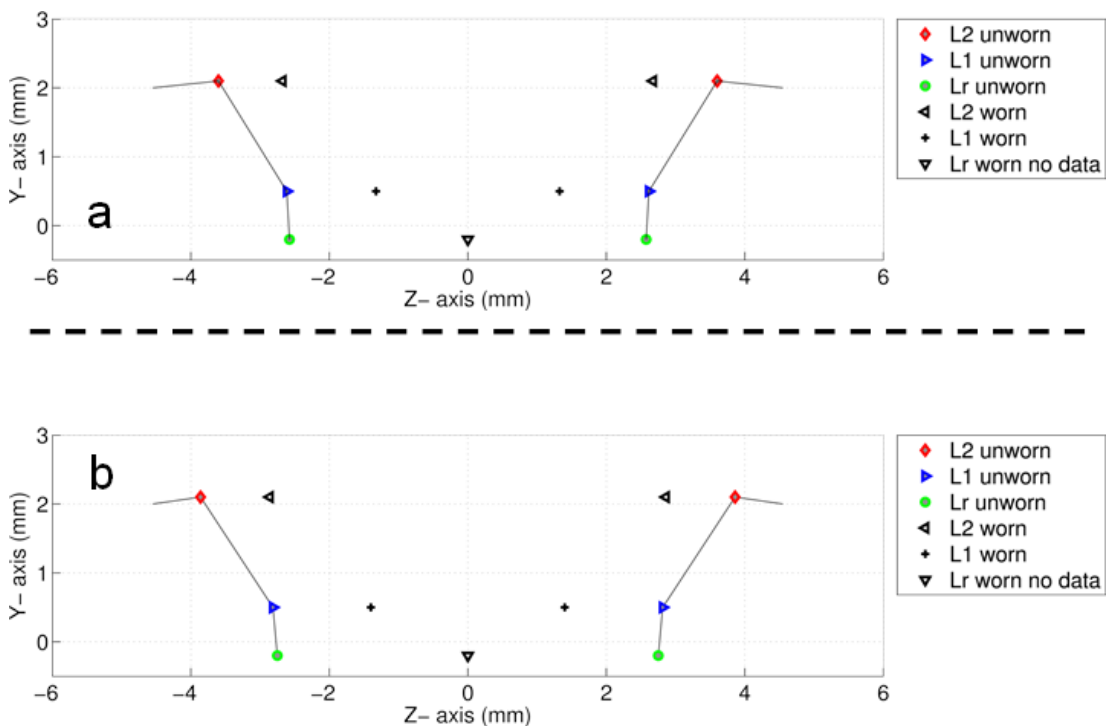
Figure 5-10 Predictions of the MAZ size [mm] for the unworn and worn tool geometries at 1.66 mm s^{-1};(a) 300 rpm and (b) 600 rpm.

5.4.3.2 Predictions of the strain rate distribution

Strain rate is considered one of the important factors in FSW as it can be used to determine the effect of the stirring action; it can also give an indication of the size of the deformation region due to the tool rotation during the process [144]. In this study, L1 and Lr, which are shown in Figure 5-8, were used to examine what happens underneath the pin in the weld root zone. Figure 5-11 shows the strain rate distribution at L1 for the unworn and worn tools; it can be seen that the width of the high strain rate region for the unworn tool is slightly wider than that for the worn tool; however, the results of the worn tool showed that the peak values of the strain rate are larger than those calculated for the unworn tool suggesting that there is a larger stirring action in a smaller area in this case, probably due to localization and softening of the weld material as explained by the study of Chionopoulos et al.[145] and Lorrain et al. [143].
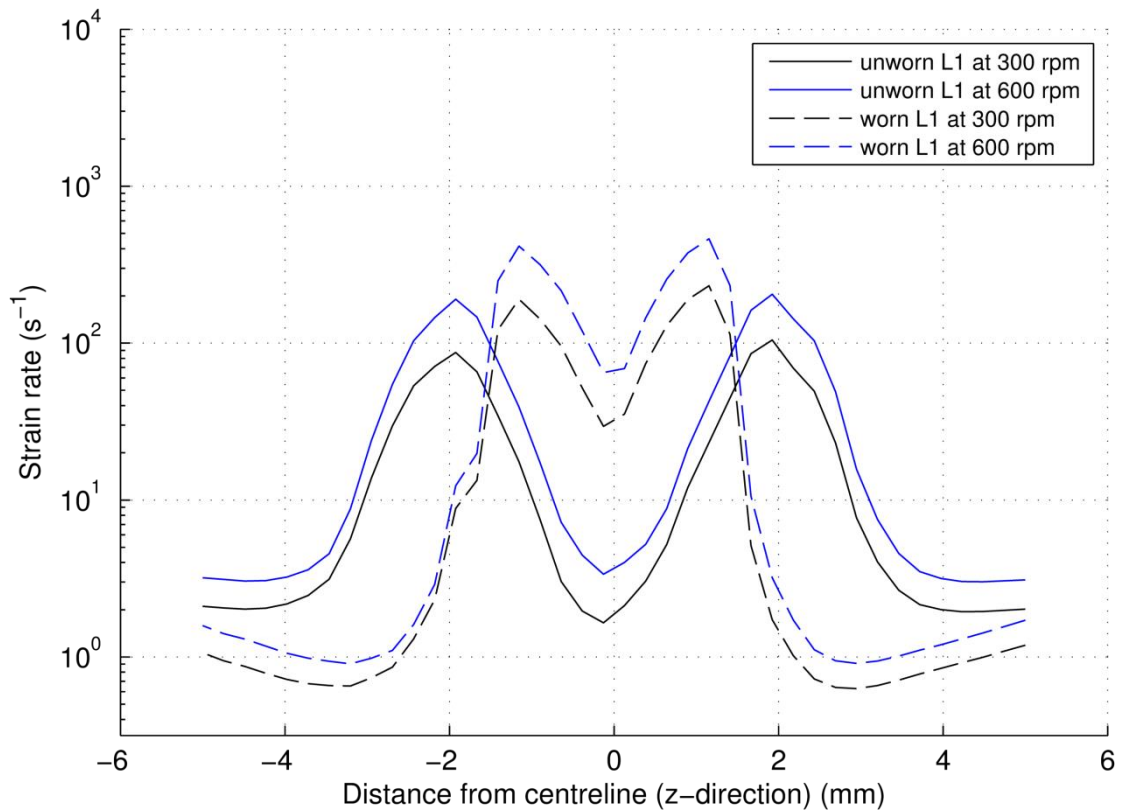
Figure 5-11: Strain rate distribution as a function of the distance from the axis of the tool rotation at

L1

Figure 5-12 shows the strain rate distribution for Lr at 300 and 600 rpm for the unworn and worn tool; the data show that the values of strain rate at this location for the unworn tool are higher than those for the worn tool, with peak values of 50 and 100 s^{-1} at 300 and 600 rpm respectively on both sides of the tool for the unworn tool and values of around 10 s^{-1} for the worn tool. Lower strain rates in this region are characteristic of a lack of stirring action for the worn tool, due to the conical shape, resulting in a narrow MAZ size that could cause improper flow and insufficient metal consolidation in this region [145]. It is also important to note that the rotating layers of the metal flow that form the weld zone strongly depends upon the tool geometry and process parameters [20, 143]. As is shown in this study, a worn tool has a conical shape, which produces lower stirring action near the weld root with a reduction in the MAZ size. This finding

is consistent with those on shape of the weld zone and flow behaviour in the study of

Mishra and Ma [3].
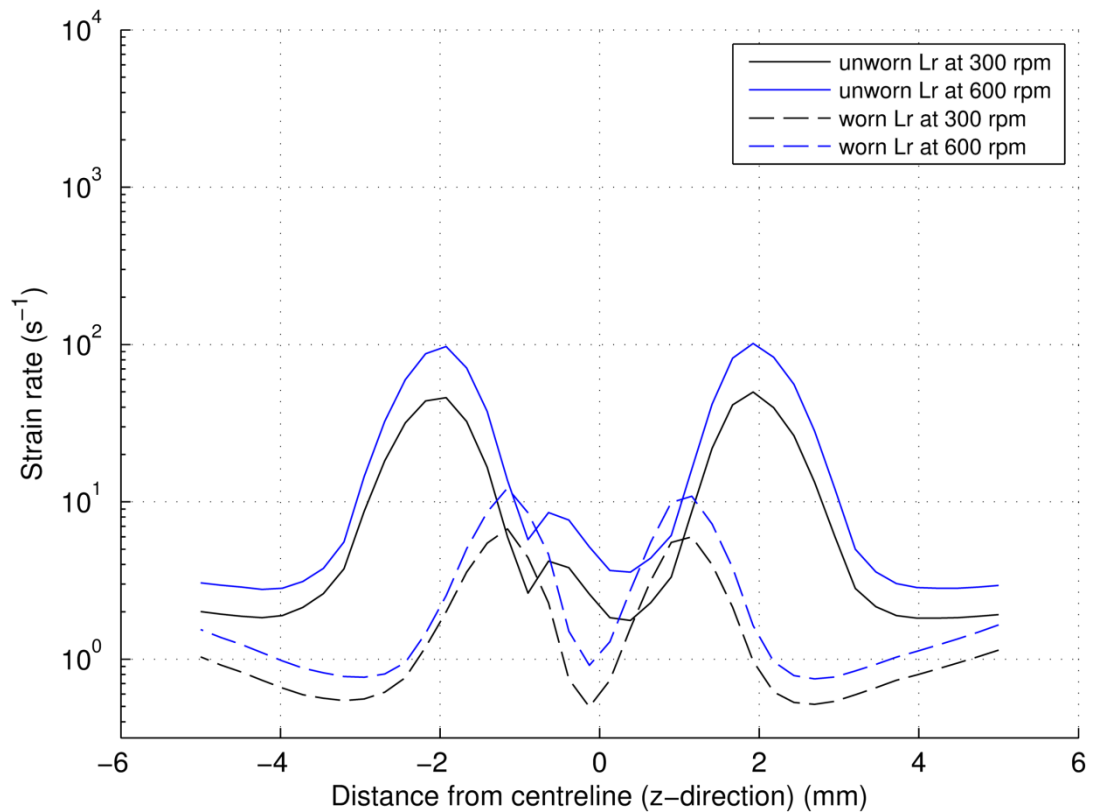
Figure 5-12: Strain rate distribution as a function of the distance from the axis of the tool rotation at Lr

Velocity contours were also examined on the plane parallel to the flow direction on

the (x-z) plane at 0.1 mm underneath the pin for both tools (unworn and worn). From

Figure 5-13 and Figure 5-15 (unworn), it can be seen that the peak velocity magnitude

was 43.6 mm s^{-1} at 300 rpm, while at 600 rpm it was 85.46 mm s^{-1}. For the worn tool,

the velocity was 13.5mm s^{-1} at 300rpm, and at 600 rpm was 24.14 mm s^{-1} as shown in

Figure 5-14 and Figure 5-16. It is clear from a comparison of Figures 11 and 12 that

the area under the pin with a significant velocity gradient is higher for the unworn tool

than that for the worn tool in the same location; as the tool becomes worn, the diameter

of the pin is reduced resulting in a corresponding reduction in flow velocity in the weld

zone, consistent with the study of Ji et al. [24].
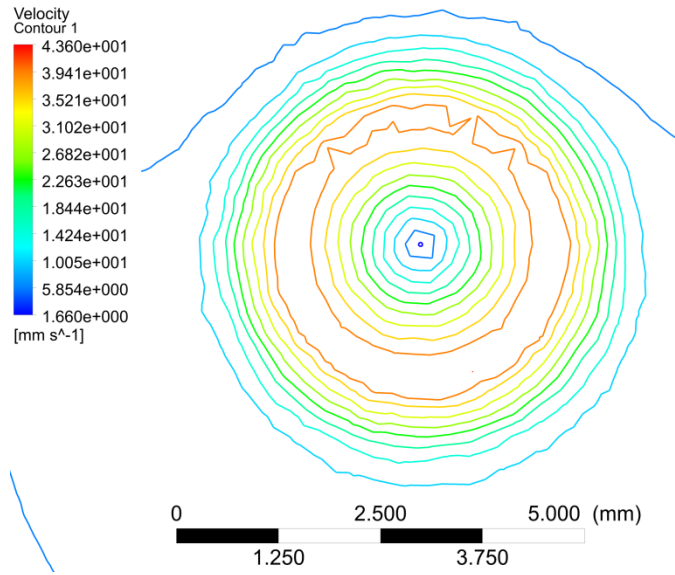
Figure 5-13: Velocity profile at 300 rpm for the unworn tool
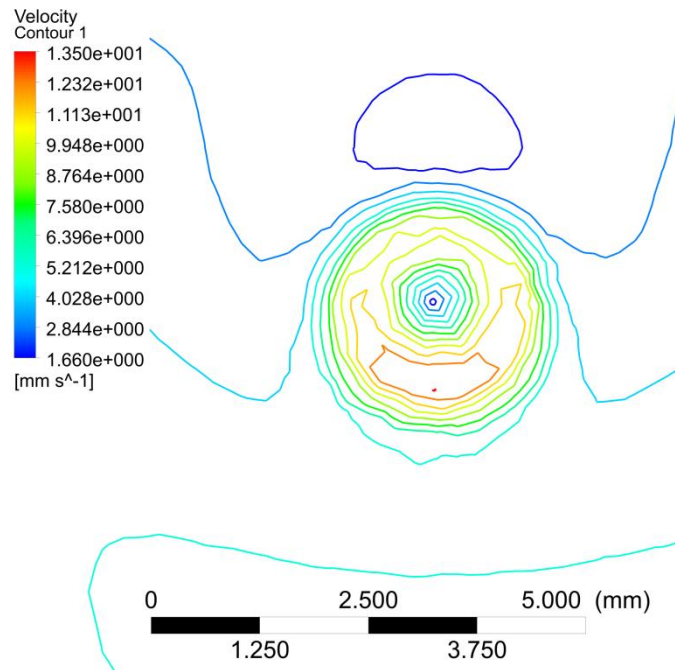
Figure 5-14: Velocity profile at 300 rpm for the worn tool
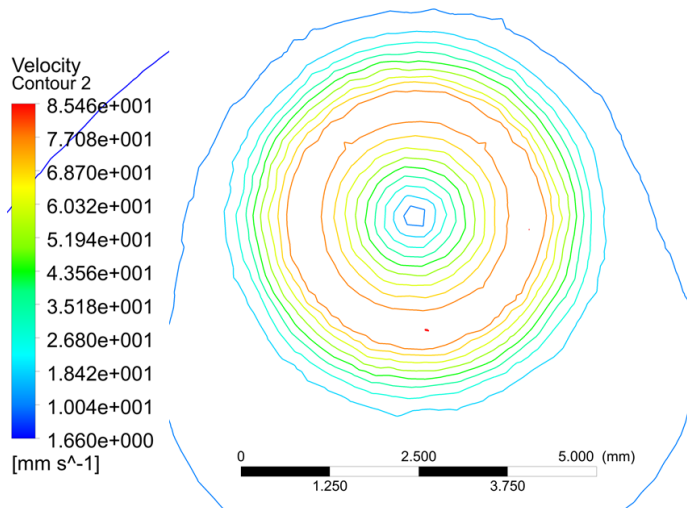
Figure 5-15: Velocity profile at 600 rpm for the unworn tool
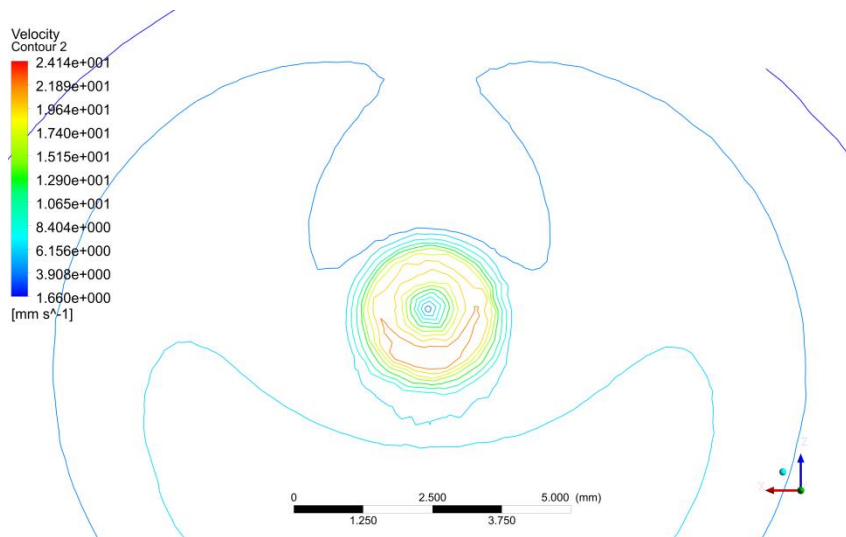
Figure 5-16: Velocity profile at 600 rpm for the worn tool

5.5   Discussion

It is commonly agreed that the formation of the weld zone in FSW is strongly dependent upon the tool geometry and process parameters. From Figure 5-11 and Figure 5-12, it can be seen that the distribution of the strain rate on both sides of the tool seems to be symmetrical as the flow in this region is dominated by the rotation of the tool and the stick-slip condition used on the tool surface. The values of the strain rate at L1 are slightly higher than those at Lr for the unworn tool, and significantly different for the worn tool, showing that higher deformation can be gained from the unworn tool with a more uniform distribution through the depth and a reasonable area of deformation. However, when the tool becomes worn, the deformed region becomes narrower and there is a significant reduction in the stirring action at the bottom surface of the plate, which could lead to a poor weld in this region. This low stirring action could also contribute to a lower temperature underneath the worn tool due to the fact that the tool is the source of heat generation [14], and as the tool becomes worn there is a reduction in the surface area of the tool in contact with the weld material and thus a corresponding reduction in frictional heat generation and also a smaller volume of material being deformed to produce heat through plastic deformation.

It is important to note that the analysis of the MAZ size, velocity profile and strain rate distribution from the model show how the worn tool could affect the joint quality. Although when worn, the tool is still capable of deforming material around it, the volume of material is significantly reduced and flow localization occurs, resulting in a poor level of deformation in the weld root which is likely to lead to poor grain refinement and mixing in this region and a therefore a reduction in weld quality.

5.6 Conclusions

In this chapter, a 3D-CFD model of the FSW process has been developed and used to compare the strain rate distribution and the size of the MAZ for the use of unworn and worn tool geometries at rotational speeds of 300 and 600 rpm. A validation process has been carried out in this study in order to obtain robust results when using the model. Unstructured grids with prism layers were also utilised to produce an optimise mesh quality for CFD modelling of the FSW process.

The key findings of the work can be summarised as follows:

- A tetrahedral mesh takes a long time to solve; however, a hybrid mesh has been shown to be more computationally efficient in achieving an accurate solution for the FSW process and for modelling complex tool geometry.

- Flow in the boundary layer is a crucial issue therefore a grid with a prism layer has been shown to be a powerful technique for solving this issue.

- The results of the FLUENT CFD model showed a good agreement with an error of less than 15 % with the experimental data for the size of the MAZ.

- The predicted size and shape of the MAZ with the worn tool is shorter and about 2.5 mm smaller than that associated with the unworn tool.

- The results of the strain rate and velocity distribution indicate a low stirring action for the worn tool, particularly near the weld root, potentially leading to defective weld joints.

- The results of the shape of the weld zone showed the weld penetration does not reach to the bottom of the plate when tool becomes worn, which could affect the quality of the weld joint.

The contribution of this chapter is clear as the resulting outcomes can be capitalized as guidelines to assess the flow differences between unworn and worn tools, which may be used to give an indication of the weld quality and of tool lifetime. Recent developments in FSW materials have heightened the need for an efficient method that can be used to predict the tool wear in FSW process. Therefore, a methodology for calculating tool wear in FSW based on a CFD model is presented in chapter 6.

Chapter 6 Modelling of tool wear

6.1 Introduction

This chapter focuses on development and validation of a methodology for calculating tool wear in FSW process based on a CFD model. In order to test the robustness of this methodology, considering the specific weld parameters and component geometry, it is necessary to calibrate it with experimental trails. In this chapter, the proposed methodology is presented by predicting the effect of the deformation of the highly viscous flow around the tool on tool wear. The outcome of this chapter are utilized for studying the effect of weld parameters on the prediction of the tool wear presented in chapter 7.

6.2 Experimental tests

In order to determine the tool wear in FSW process and to validate the proposed methodology of the tool wear prediction, a series of welds were carried out on the Transformation Technologies Inc. (now MTI) FSW machine RM2 (FW32) at TWI Yorkshire, which has a force capability of 100 kN in the vertical (z) axis and 45 kN in both x and y horizontal axes, a torque capability of 225 N m, and a geared maximum rotation speed of 200 rpm. The machine has a high concentricity spindle, which enables ceramic and refractory metal FSW tools to be evaluated. The tools used were of tungsten − rhenium − hafnium carbide (WRe-HfC) material with a simple domed profile as shown in Figure 6-1.

The tool was measured before and after use using a Mitutoyo shadowgraph and the degree of wear on the tool recorded.
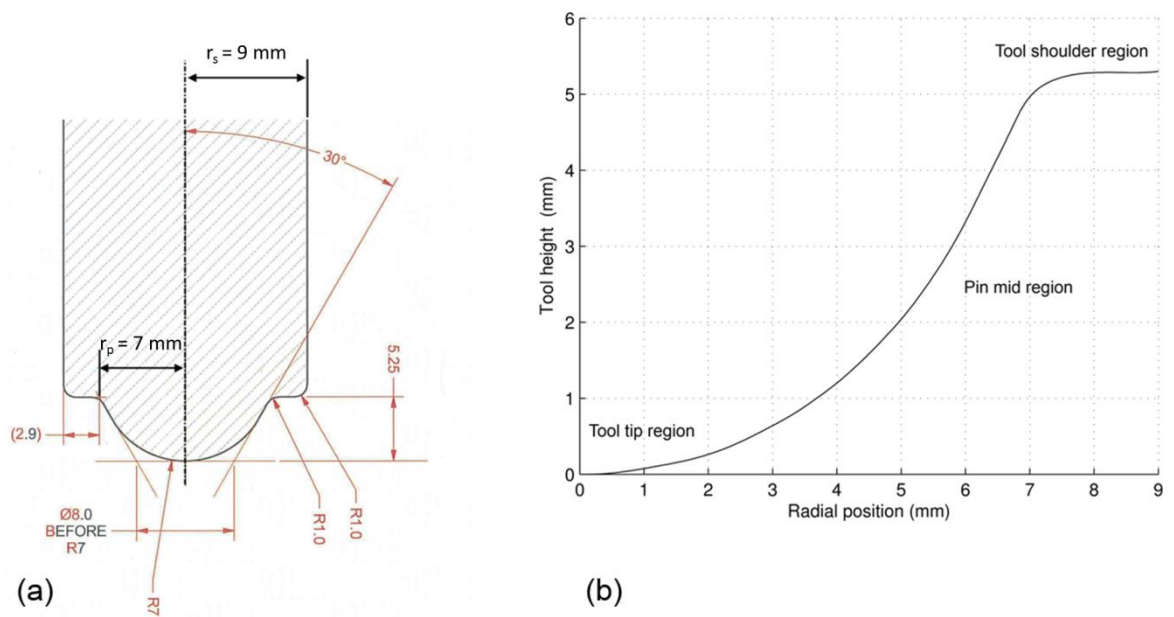
Figure 6-1 Tool geometry used in the study, (a): tool dimensions, (b): tool regions.

Argon gas shielding was used for all the welds to prevent oxidation of both the tool and the weld. The workpiece material was a 6mm thick plate of AISI 304 austenitic stainless steel which was degreased with acetone prior to welding and clamped to the machine bed using standard finger clamps. The tools were plunged directly into the steel plate with no pilot being drilled first to aid entry into the steel. The welds were made at a tool traverse speed of 2.5 mm s^{-1} and a rotation rate of 225 rpm. The provided data was experimental measurements of tool profile that were conducted for the different welding distance.

A total of three cases were considered both experimentally and numerically across a range of welding distances to validate the developed approach. The weld was performed using the parameters shown in Table 6-1.

Table 6-1 Process parameters.

Weld Traverse speed [mm s-1]	Tool Rotation speed [rpm]	Weld distance [mm]
2.5	225	2, 4 and 6 $\times 10^3$

The main purposes of these tests were to measure the wear depth and to determine the

wear coefficient value in order to validate this work.

6.3 Tool wear modelling

In this section, the CFD model that was presented and used in chapter 5 has been updated to match the experimental test in terms of tool design, welded material and process parameters; and the CFD model includes a heat generation model because 304 stainless steel is very sensitive to temperature and strain rate. In this section a tool wear calculation has also been described in order to predict the wear depth and validate the proposed approach.

6.3.1 CFD modelling

6.3.1.1 Model description

In this study, a steady state 3D coupled thermal-flow model of the FSW process was generated using the commercial CFD software FLUENT. This model was used to extract the pressure and velocity values in order to predict the tool wear that occurs during the FSW process. A model was defined based on the modelling methodology that was established in chapter 4 in terms of assumptions, workpiece boundary conditions, solver, convergence and mesh. For this model, the heat generation was implemented through the application of equation 4-10; as described in chapter 4 section 4.3.2.

Regarding the tool boundary condition, a slip-stick condition was implemented on the tool surface by defining the material interface velocity, V_{mat}, as the boundary condition on the tool surface which is related to the tool velocity, V_{tool}, by the contact state variable, δ, defined by equation 6-1. The tool velocity V_{tool} is defined as the velocity components on the surface of the tool (position dependent tool velocity of $\omega\, r$), where the value of r lies in the range $r_p < r < r_s$ [14] ;as described in chapter 4 section 4.3.1.

$$\delta = \frac{V_{mat}}{V_{tool}} \qquad\qquad 6\text{-}1$$

Therefore, V_{mat} is defined as the velocity components for u_{mat} and w_{mat} which are shown in equations 6-2 and 6-3, while $v_{mat} = 0$.

$$u_{mat} = (1 - \delta)(\omega r \sin\theta - u_{weld}) \qquad\qquad 6\text{-}2$$

$$w_{mat} = (1 - \delta)(\omega r \cos\theta) \qquad\qquad 6\text{-}3$$

In this work, a constant value of 0.07 was used for δ; this assumption was made based on the work of Chen et al. [32] when they calculated the value of δ experimentally based on the estimation of the pin travel distance after one revolution and location of the flow front layer which, is a portion of the shear deformation material that left to rotate and then detached next to the pin during the process. This value is included as wear is caused by relative motion between surfaces; therefore, in order to predict tool wear in this case, a relative interface velocity is required, V_{slip}, which can be calculated according to equation 6-4.

$$V_{slip} = V_{tool} - V_{mat} \qquad\qquad 6\text{-}4$$

The geometry of the computational domain of the model was a rectangular cuboid with the dimensions presented in Table 6-2; the tool was a dome shape, as shown in Figure 6-1, while the detail of the computational domain and the boundary conditions is presented in Figure 6-2.

Table 6-2 Description of the dimensions of the model

Dimension	Value [mm]
Plate length	304
Plate width	203.2
Plate thickness	6
weld distance	2, 4 and 6 $\times 10^3$
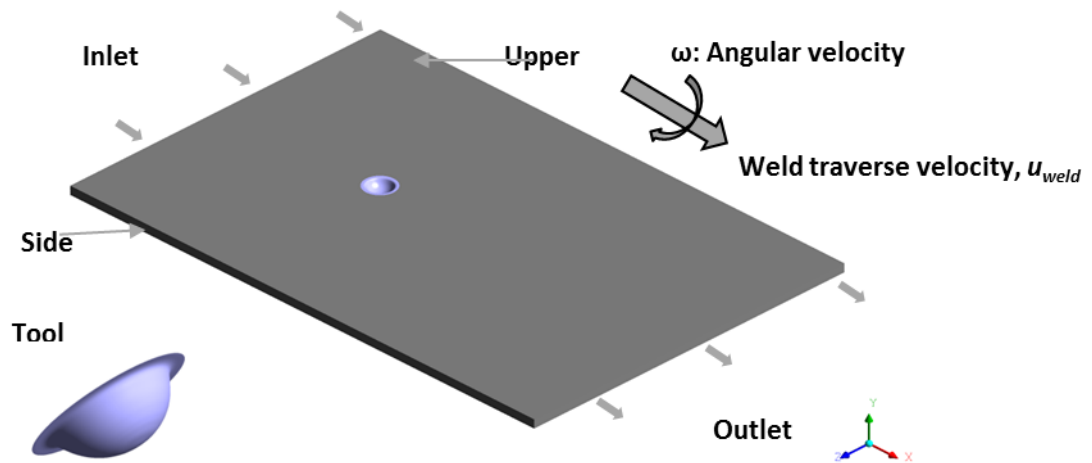
Figure 6-2 Computational domain and boundary conditions used in the study.

The material constants and further relevant properties for 304 stainless steel are shown

in Table 6-3.

Table 6-3 Material properties [8, 146, 147].

Material property	Value (stainless steel 304)
ρ, density	7406 kg m^{-3}
A, material constant	1.62 x10^{16} s^{-1}
α, material constant	0.008 x10^6 Pa $^{-1}$
n, material constant	6.1
Q_e, activation energy	446000 J mol^{-1}
R, gas constant	8.314 (J K^{-1} mol^{-1})
C_P, specific heat at 1273K	610 (J Kg k^{-1})
λ, Thermal conductivity at 1273K	30 (Wm^{-1} K^{-1})

6.3.2 Tool wear methodology

6.3.2.1 Wear model

A model that has been commonly used in the literature to predict wear in many machine parts and sliding wear damage [73, 148] is Archard's Equation [64]:

$$V = k\,W\,S \qquad\qquad 6\text{-}5$$

where V is the total wear volume; k is the dimensional Archard wear coefficient, which is dependent on the material and surface cleanliness; W is the applied load and S is the sliding distance. In many applications it is necessary to determine the local wear depth for a given position, therefore, 6-5 is modified and known as modified the Archard's Equation as shown in equation 4-8 [149]:

$$h = k\,Pt\,V_{slip} \qquad\qquad 6\text{-}6$$

where h is the wear depth and k is the dimensional Archard wear coefficient, while P is the contact pressure , t is the time, and V_{slip} is the relative interface velocity .

Accordingly, tool wear in the FSW process was calculated using the modified Archard equation for a given point on the tool surface; equation 2-8 is thus reformulated in order to calculate wear depth increment for a given point [149]:

$$\Delta h = k\,P\Delta t\,V_{slip} \qquad\qquad 6\text{-}7$$

where Δh and Δt are the wear depth increment and time increment respectively. Using equation 6-7, it is possible to calculate the wear depth increment for a given time increment and for a given point on the FSW tool, based on the pressure and slip velocity, which can be extracted from the CFD model. However, the wear coefficient is not known; to derive a value for the wear coefficient, the procedure that is presented

in Figure 6-3 was used. The values of pressure and slip velocity were extracted from the CFD model, run with the initial tool geometry for the first increment, and then using the experimental tool profile data, an average wear coefficient value of 2.36×10^{-13} mm^3 N^{-1} m^{-1} was calculated using equation 6-7 and fitting using the Least Mean Squared Error (LMSE) optimisation method. This value was then used to perform the wear calculations for subsequent increments. Regarding the wear coefficient value, no data was available for this tool material and for the case of the complicated FSW process. However, literature wear coefficient data [150, 151] available for tungsten carbide on carbon steel and tungsten cobalt coated AISI 304 on silicon nitride using a pin on disc test provides values of 6×10^{-16} mm N- m^{-1} and 2.9×10^{-14} mm N- m^{-1} respectively. It is clear that the predicted value from this study is somewhat higher than that provided in the literature which is attributed to the fact that different case setups and materials are used in FSW is different.
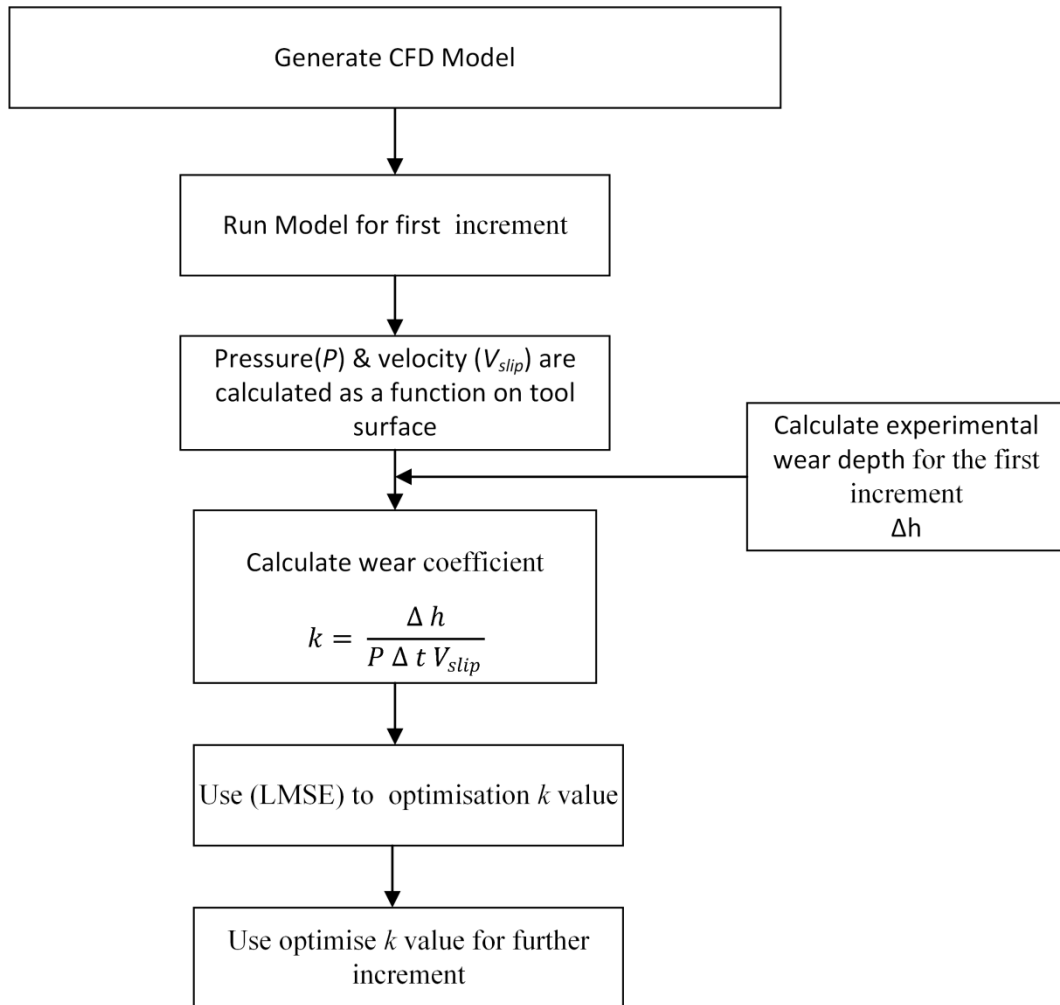
Figure 6-3 Wear coefficient determination diagram

6.3.2.2 Wear modelling procedure

This section describes the methodology that was used to calculate tool wear in the FSW process. The developed approach is presented schematically in Figure 6-4.
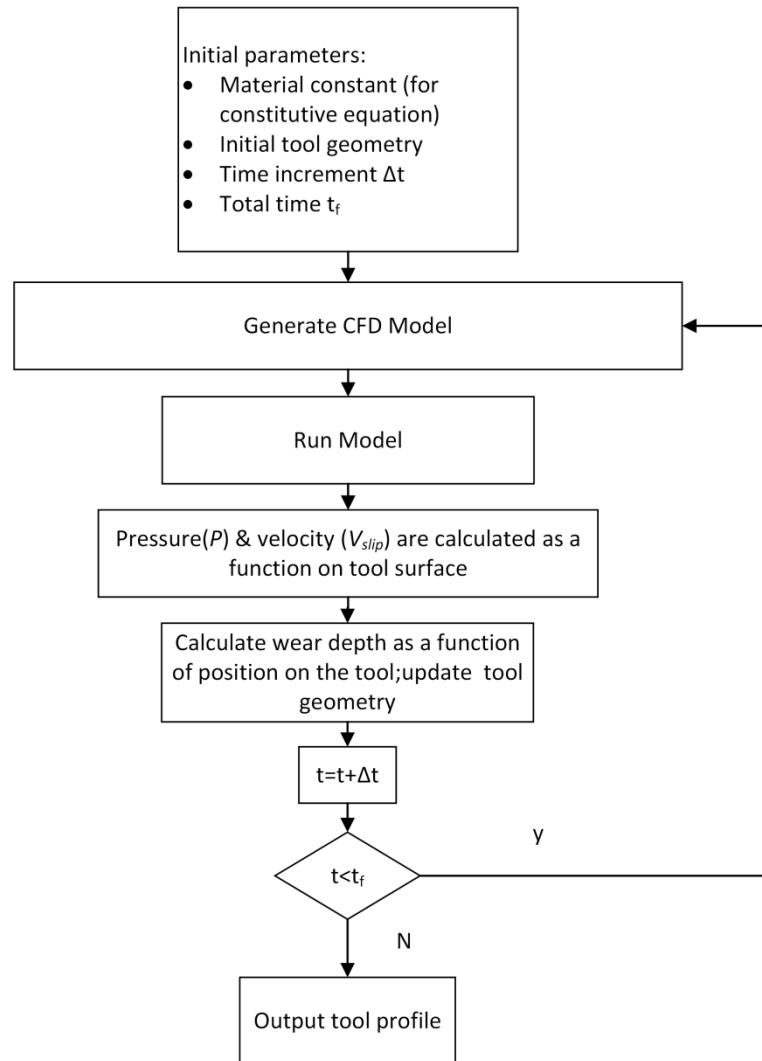
Figure 6-4 Flow diagram of FSW tool wear simulation.

Generally, this approach is based on the CFD model, the details of which were described in the previous section. As can be seen in Figure 6-4, the first step was the determination of the initial parameters required for the calculation of tool wear; these

parameters were material constants related to the CFD model, initial tool geometry, and the time increment. Once the CFD model of the initial geometry (unworn tool) had been generated, the pressure values and the velocity on the tool surface were extracted. After the CFD model had been solved for the parameters stated in Table 6-2, and the convergence criteria were met, a data file was exported giving the position, pressure and velocity of 1250 points from four polylines on the tool surface, as shown in Figure 6-5. A MATLAB script was used to average these data for those polylines to obtain a set of values as a function of tool radial position, representing one tool surface. In this study only positive values of pressure were considered to contribute to the tool wear and therefore any negative value of pressure was made equal to zero before the averaging calculations. The averaged values were then used to calculate the wear depth for each radial position on the tool surface.
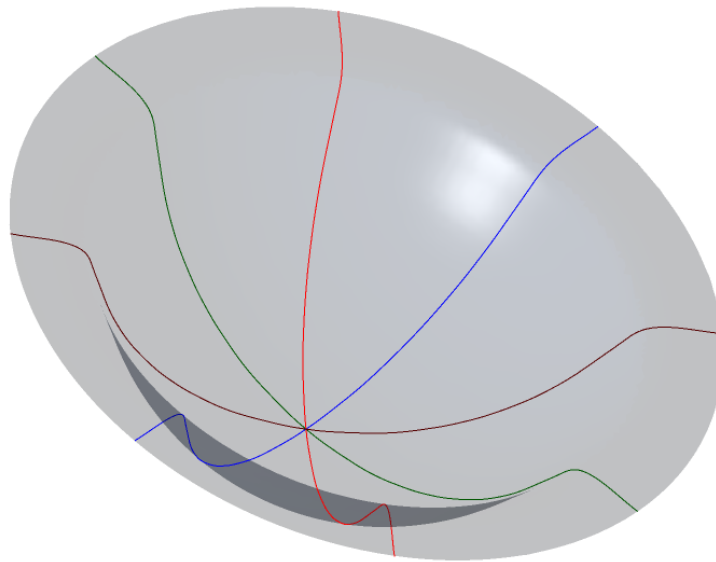
Figure 6-5 Polylines on the tool surface used to obtain the position, pressure and velocity values.

After the tool wear was calculated for a given time increment, the new tool geometry was defined and the mesh was updated in order to run the CFD model for the next time increment to derive the values of pressure and velocity at the tool surface with the revised tool geometry. This process was repeated until $t = t_f$.

It should be noted that in the FSW process, the pressure distribution and the slip velocity are not constant over the tool surface, which leads to different wear rates at different locations on the tool surface. Moreover, in order to validate this work, the top surface of the plate was retained as a reference position for measuring the wear depth. Since the wear at the shoulder is higher than the tip, as the tool position is adjusted to keep the shoulder on the top surface of the plate, the tip intrudes deeper into the plate.

6.4   Results

6.4.1   Computed temperature fields

In this study, three x-z planes were used to plot the predicted temperature contours from the model at three positions through the thickness of the plate; the first plane was on the top surface of the plate, the second plane was at the pin tip, and the third plane was on the bottom surface of the plate. The simulated temperature contours are shown in Figure 6-6. It is evident that the peak temperature is on the top surface at the shoulder edge, and has a value of 1498K.
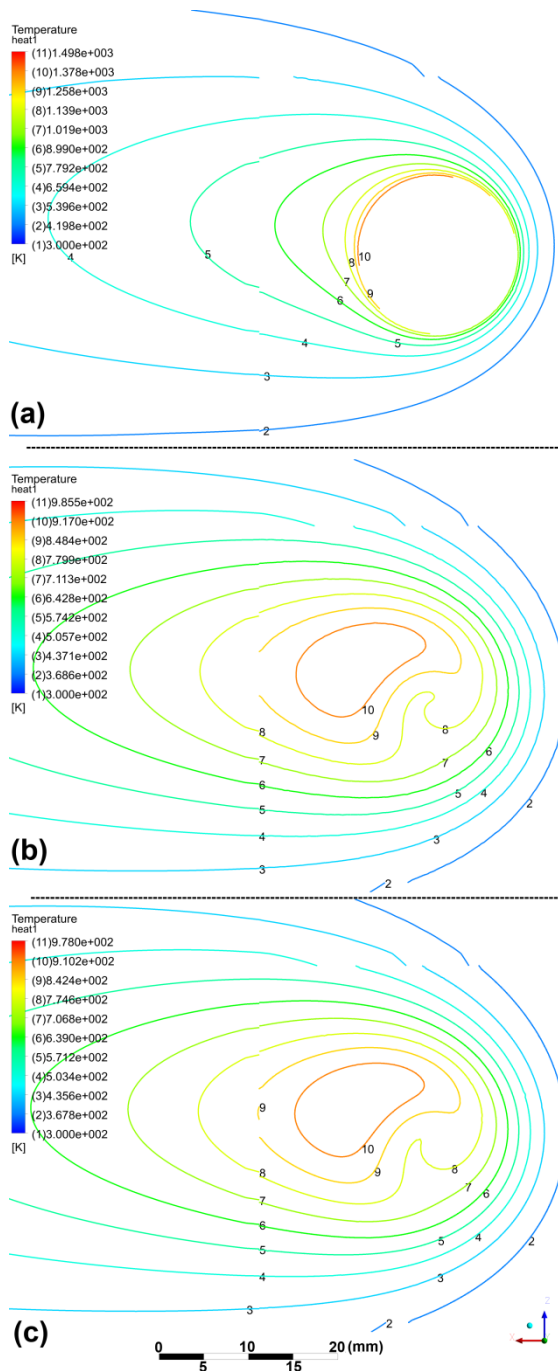
Figure 6-6 Plot of the temperature distribution at 2×10^3 mm weld distance: (a) on the top surface of the plate, (b) on a plane at the pin tip and (c) on the bottom surface of the plate for the initial geometry.

As we go further down the pin Figure 6-6 b, the predicted the temperature reduces by 30% to 985K. On the bottom surface of the plate Figure 6-6 c, the peak temperature during the welding process is 978K. The most important thing which can be observed from these predicted temperature contours is that the melting temperature, T_m, of the

304 stainless steel, which is 1698 K, is not reached; this is consistent with the study by Zhu and Chao [114]. It is also important to note that the temperature distribution is a function of the rotation speed and tool radius, as presented in equation 4-10. Therefore, it should be expected that the temperature is highest at the top surface of the plate where the primary heat source (the shoulder) is situated and decreases through the thickness of the plate. The simulated temperature on the top surface of the plate shows a good agreement with the simulated value by Selvaraj [8], although there are slight differences between that and the current study due to differences in the input parameters, as shown in Table 6-4

Table 6-4 Comparison between predicted peak temperature at shoulder area with Selvaraj work [8]

	Rotation speed (rpm)	shoulder radius mm	Peak temperature at the shoulder(K)
Selvaraj [8]	300	19	1430
Current work	225	18	1498

6.4.2 Material flow behaviour (velocity distribution and Pressure)

To analyse the flow behaviour in the FSW process around the tool, and to develop understanding of the flow patterns for this particular tool design, velocity streamlines were used to examine how the material flows around the tool and to identify the region of plastic deformation near the tool. Streamlines were plotted on two planes: the first plane was a horizontal x-z plane at the top surface of the plate, while the second was an x-y plane parallel to the flow direction on the axis of the pin rotation. The area around the tool was divided into several zones as shown in Figure 6-7b in order to investigate the flow patterns in this tool design.
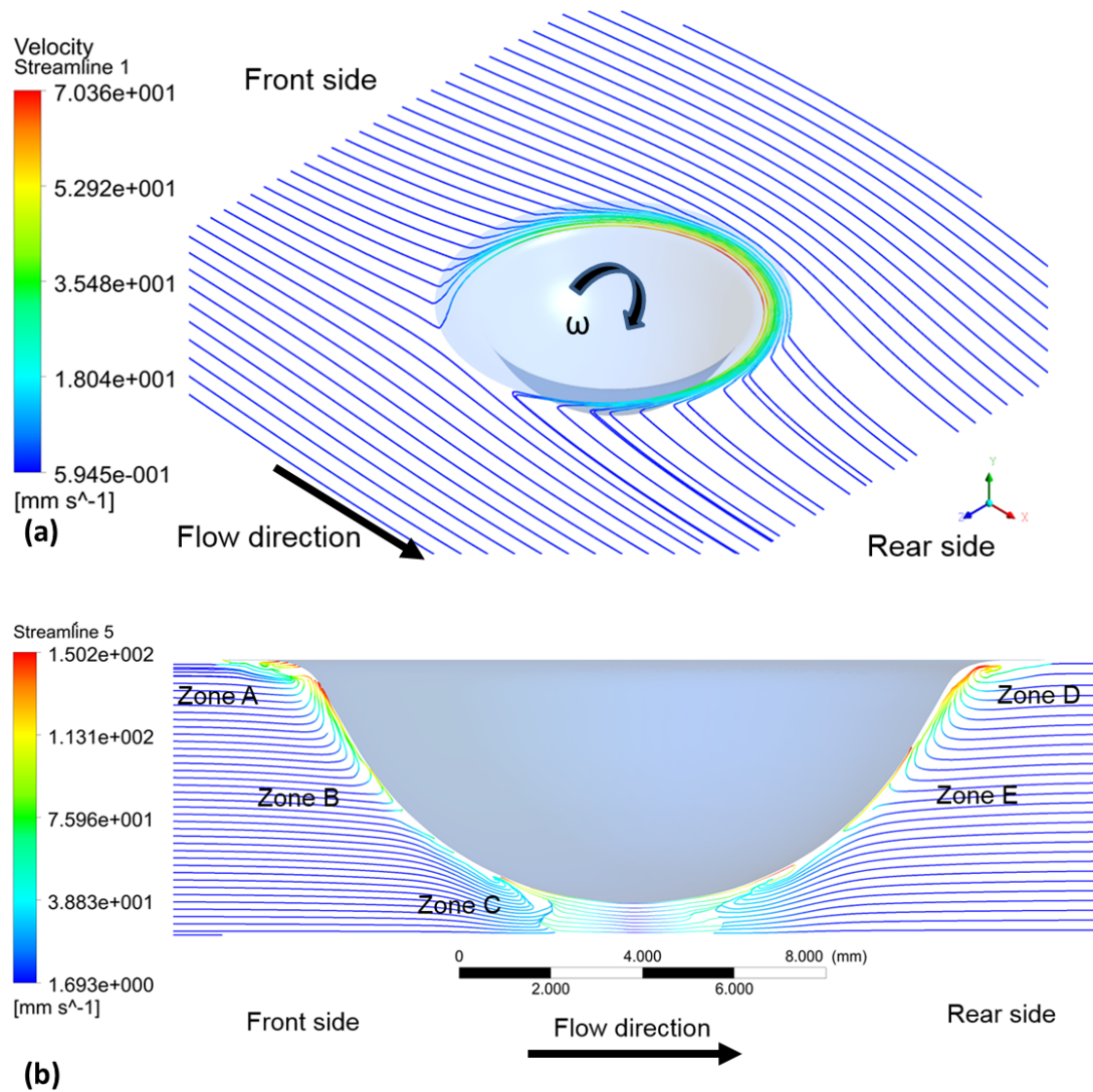
Figure 6-7 Stream-lines in different planes; (a) a horizontal x-z plane at the top surface of the plate, (b) x-y plane parallel to the flow direction for the initial geometry.

Figure 6-7 a shows that the flow of the material near the tool is dominated by the tool rotation; flow of this type is quite commonly reported for the FSW process [22, 52, 152]. It can be seen from the velocity streamlines in Figure 6-7b that in zones A and D, have high deformation due to the presence of high velocity gradient. On the front side of the tool in zones A and C, some material in the shear deformation zone is moved upward, while some parts of the material are pulled down through the thickness of the plate. It is worth mentioning that the results of this behaviour of the flow show a good

agreement with the findings of Colegrove and Shercliff [23] and Grujicic et al. [55]. On the rear side of the tool, in zones D and E, the material is pulled down by the tool rotation, causing separation of the material from the tool surface. The plot of streamlines explains the interaction of the axial flow with the pin; causing a bifurcation of the flow past the pin, which leads to an increase in the pressure at that position as shown in Figure 6-8. This figure shows the contour of the pressure distribution on the tool surface plotted in the x-y plane. The lines visible on tool surface in this figure are the polylines that were created to extract the tool surface data that were used to calculate the wear depth. It this study only positive values of pressure were considered to contribute to the tool wear and therefore any negative value was made equal to zero in the wear calculations.
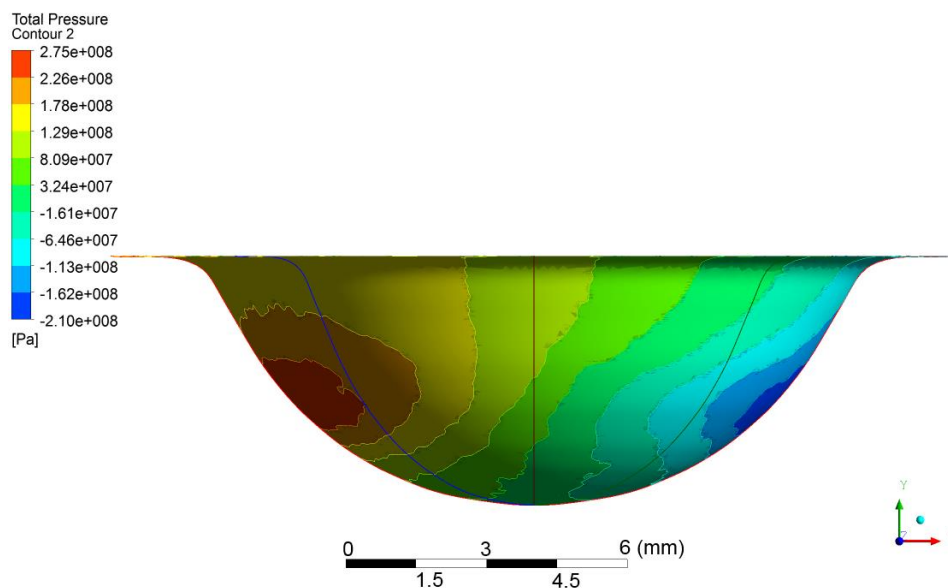
Figure 6-8 Pressure contours on the tool surface in the x-y plane parallel to the flow direction for the initial geometry.
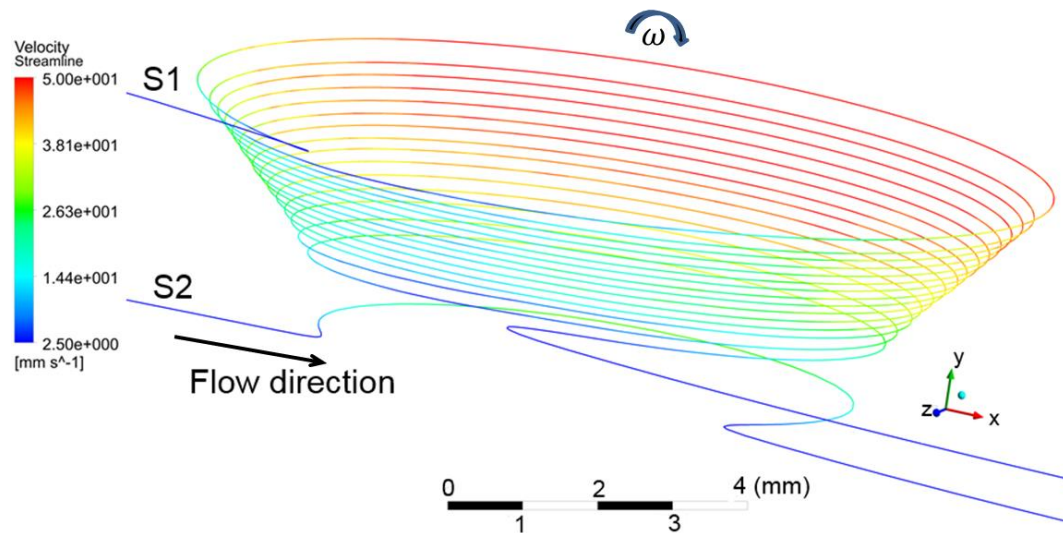
Figure 6-9 Stream-lines plots showing flow separation from the tool surface at 225 rpm and 2.5 mm s^{-1} weld speed. S1: stream line at mid pin zone; vertical position 3 mm, S2: stream line at tool tip zone; vertical position 0 mm.

In Figure 6-9 , the streamline plots are detailed from two initial points to further analyse the flow behaviour. The first point, S1, was located in the pin mid-zone, at a vertical position of 3 mm, while, S2 was located in the tool tip region at a vertical position of 0 mm, where (0,0,0) is at pin tip. Once near the pin, the material from S1 is wrapped around the tool and undergoes more than one rotation around the tool surface before separation occurs, this finding is consistent with Owen [153]. However, at S2 the material flows around the tool without completing a full rotation and then separates. It is possible to determine from Figure 6-9 that near the tool tip region, separation occurs leading to a decreases in pressure in that region as shown in Figure 6-8.

6.4.3 Tool wear prediction

To achieve sufficient confidence in the wear methodology for predicting the tool wear in FSW the approach must be thoroughly validated. The tool profile was measured using a shadowgraph at increments of distance and the incremental wear depth was calculated. Moreover, wear depth for the simulation tool profile cases was predicted as well using the average data of pressure and velocity. The average pressure distribution on the tool surface predicted at different radial positions (see Figure 6-1 which shows the initial tool geometry) used for tool wear calculation is presented in Figure 6-10. The overall trend shows that, near the pin tip (r = 0 to 1 mm) the pressure decreases and then the pressure increases until it reaches the peak value at r = 5.2 mm (tool mid surface). Following the maximum, the pressure decreases and there is no significant change until the shoulder region (r =7 to 8.9 mm).
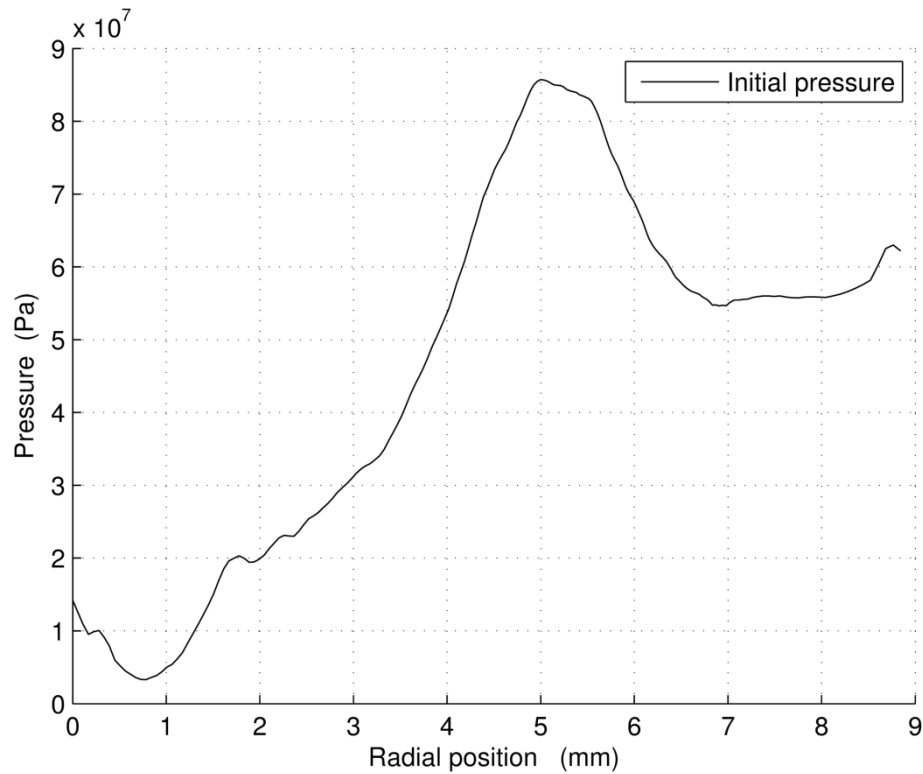
Figure 6-10 Average pressure distributions as a function of position on the tool for the initial

geometry used for wear calculation.

6.4.3.1 Wear depth results

Figure 6-11-a shows the measured and predicated values of the wear depth increment

for the increment of weld distance from 0 to 2×10^3 mm. The data shows that no

significant wear occurs near the pin tip. Overall trends of the experimental and

simulation data show that wear depth increment increases steadily from the pin tip to

the mid pin region, which is shown in Figure 6-1 -b; at close to $r = 5$ mm, the trend is

for the wear depth increment to fall steadily and finally increase at $r = 7.5$ mm. As can

be seen in Figure 6-11, the simulated results show a good agreement with experimental

data from the pin tip to $r \approx 6.5$mm. After this distance, some mismatch can be observed

until the shoulder edge (at $r = 8.9$ mm). This can be attributed to the use of, single-

phase flow and FVM requiring a non-deforming wall to be specified as the top surface

of the plate, which leads to an increase in the pressure in that area.
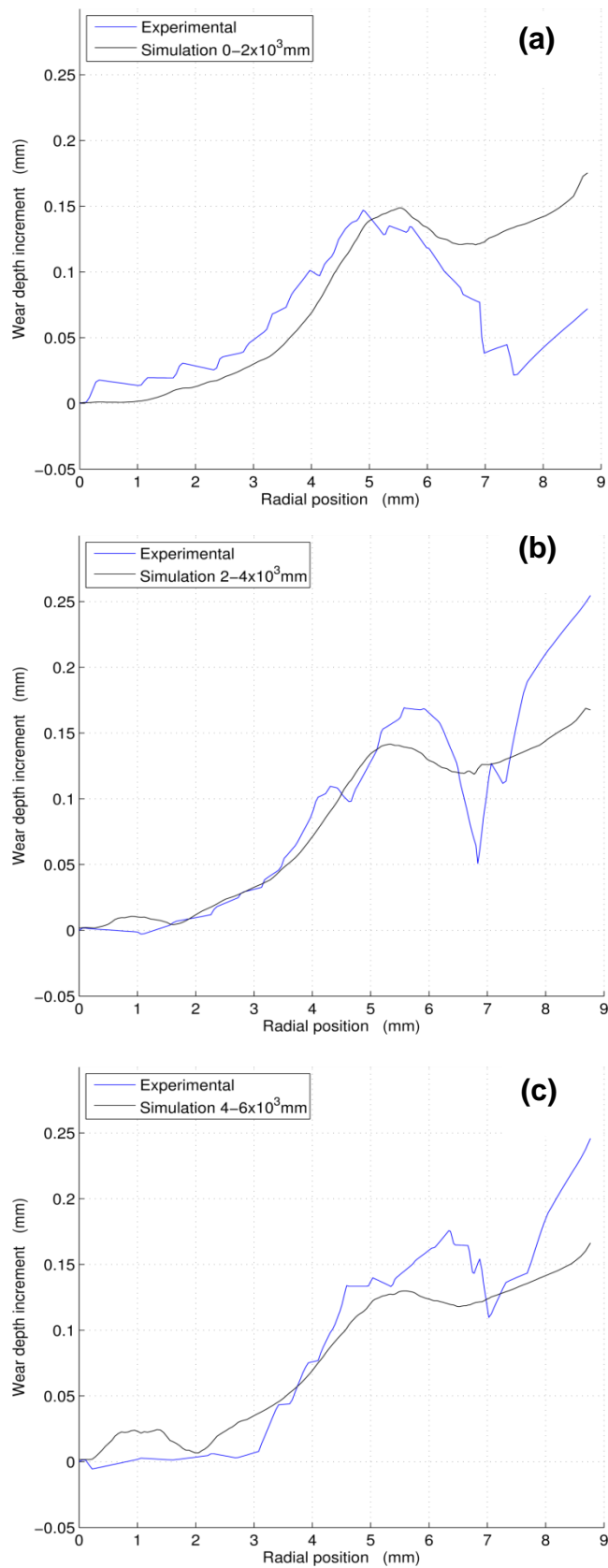
Figure 6-11 Plot of the wear depth along the tool surface after an increment of weld distances of; (a)

0-2×10^3 mm, (b) of 2- 4×10^3 mm, (c) of 4- 6×10^3 mm.

The results of the tool wear for the increment of weld distance from 2 - 4 $\times 10^3$ mm (Figure 6-11-b) showed a similar behaviour to those in Figure 6-11-a. At r = 5 mm, the value of the wear depth increment was 0.13 mm, which is slightly lower than that calculated for the increment in weld distance from 0 - 2$\times 10^3$ mm. The numerically computed results are in good agreement with the general trend behaviour of the experimental results however, some under predicting can be seen near the shoulder area, as in Figure 6-11-a.

A similar trend is seen in Figure 6-11-c as in Figure 6-11-a in terms of wear depth on the tool surface; the graph shows slightly higher wear occurred near the pin tip, which could be because of localized pressure in this region. The reason for this is the short distance between the bottom plate surface and the pin tip, as explained in section 3.2 (wall boundary condition).

Again, good agreement was obtained when comparing the results of the simulated and experimental wear depth increment and, in common with the results presented in Figure 6-11-a and b, mismatching was seen near the shoulder area.

The simulated results for the three increments weld distances showed that the highest material loss occurs in the shoulder area and at the mid pin (r ≈ 5 mm).

There is a greater likelihood of obtaining a high value for wear depth at the shoulder because high plastic deformation occurs within the shoulder region and wear is caused by high pressure and high velocity differences, which occurs in this region. In addition, as shown in Figure 6-7, on the front side, the flow is obstructed by the tool in the mid pin region (stagnation point) and then the material flows upwards or flows down, so there is already a high pressure in this region. For all the weld distances, the peak increment of wear was between 0.13 - 0.15 mm at a radius of 5 mm. Finally, it is

important to conclude that the predicted tool wear results showed a good agreement with the measured values, with a maximum error of less than 19% and average error for the three cases of less than 13%, when compared with the experimental results in the zone located below the shoulder edge and pin root.

6.4.3.2 Tool profile results

Figure 6-12 shows the evolution of the tool geometry at different weld distances; it is evident that very little wear was predicted during welding near the pin tip; however, in other regions on the tool surface, it can be seen that the wear increased as the weld distance increased (due to wear on the shoulder increasing the effective length of the tool). The tool length increased by only 0.5 mm after a weld distance of 6×10^3 mm weld distance. It can be argued that this is due to a combination of the rapidly changing of the flow patterns at dome-shoulder junction and the increased peripheral speed of the tool out towards the edge of the shoulder. On the other hand, no significant change in the tool shape can be observed, even after a weld distance of 6×10^3 mm, which means this tool is able to retain its original dome shape and it can therefore be assumed that the tool was able to continue producing weld under these circumstances.
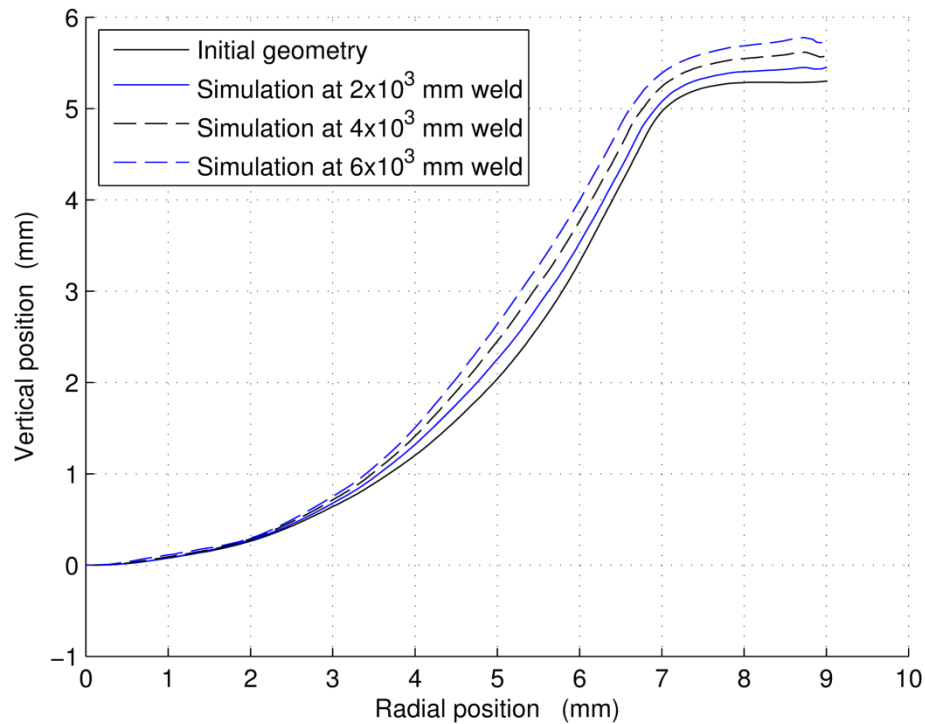
Figure 6-12 Tool profile after different welding distances.

6.5 Discussion

It should be noted that the pressure distribution generated due to material flow during the process causes wear on the tool as concluded by the study of Prado et al. [10] and Ke et al. [154].

Flow of the material near the tool is dominated by the tool rotation. It also demonstrates the circular behaviour of the flow within the tool region. The streamline plots reveal that the material on the front side of the tool near the shoulder is pushed up; on the rear side of the tool it flows down; and at the lower part of the tool the material flows downward on both sides of the tool. These streamline plots can give a good explanation for the flow patterns for this particular tool design. The numerically computed flow patterns are in good agreement with the general findings that have been reported in the literature [20, 31] in terms of the stagnation and separation points, and for the vertical flow motion near the tool surface .

The results of the developed methodology in terms of tool wear show that, for all three increments in weld distance, in the region between r ≈ 0 to 5.5 mm, the wear depth increment increased gradually reaching a peak at ≈ 5.5 mm; thereafter, the increment of wear depth fell until r ≈ 7 mm and then start to increase towards the shoulder edge. A good correlation was obtained with experimental data in terms of wear depth. Clearly, the proposed approach is able to predict tool wear in the FSW process based on the investigation into the effect of the highly viscous flow on the FSW tool.

In all three cases, the tool was worn radially and vertically. To summarise the main finding, this tool design, even when worn, largely retains the original dome design Figure 6-1. The mechanism of the wear for this particular tool in these circumstances is deformation and sliding wear, and this finding is confirmed by previous studies [30, 67, 86].

Furthermore, the inconsistency of the results in some regions can be attributed to the use of a one-phase flow model. Clearly, one of the most important problems with using the FVM is in defining the boundary where the material being welded begins to deform. This boundary is defined as the top surface of the workpiece in this case, by assuming it to be a non-deforming wall [52]; this assumption prevents material flow past the boundary and leads to an increase in the pressure close to that position. Another important factor which causes this pressure distribution in Figure 6-10 may be bulge formation, which has been observed in the literature [155]. Indeed, all these factors cause some difficulties, which leads to the inconsistency in the results produced using this method near the shoulder area.

6.6   Conclusions

In this study, a methodology for calculating tool wear in FSW based on a CFD model has been developed to predict the effect of the deformation of the highly viscous flow around the tool on tool wear. A modified Archard Equation, implemented in MATLAB, was used to calculate the wear on the dome shaped FSW tool. A validation process has been carried out in this study in order to obtain robust results when using this methodology.

The key findings of the work can be summarised as follows:

- The results of the FLUENT CFD model showed a good agreement with the literature data for peak temperature.

- The velocity streamlines indicate that a rapidly changing flow occurs at the shoulder edge, potentially leading to high tool wear in this region.

- The velocity streamlines show the interaction of the axial flow with the pin; causing a bifurcation of the flow past the pin at the mid surface, which leads to an increase in the pressure values at that position.

- The proposed approach is able to predict tool wear associated with high viscous flow around the FSW tool.

- The results of the predicted tool wear showed a good agreement with a maximum error of less than 19% and average error for the three cases less than 13%, when compared with the experimental results at zone located below shoulder edge and pin root.

- The inconsistency in the results near the shoulder can be developed further in terms of including consideration of the loading history at each location on the tool surface and thus calculating geometry independent variable wear coefficient and two phase flow approach.

- From the results it can be concluded that the sliding wear model gives good prediction of the wear rate.

- This modelling approach could be used to improve understanding of the effective limits of tool use for welding, and as a method for calculating tool wear (as a function of tool geometry and basic FSW process parameters) without the need for experimental trials.

Chapter 7 The effect of weld parameters on the prediction of tool wear

7.1 Introduction

In order for the tool wear methodology that was described and validated in Chapter 6 to be a useful method, it is important to investigate this methodology across a wide range of process parameters and to show that the developed approach is able to predict tool wear in FSW processes using different tool designs. Moreover, it has been documented that further investigation is needed to achieve better understanding of the tool wear that occurs in the FSW process [3, 156]. In this chapter, a parametric study was undertaken for two tool designs, a dome and a conical shape, to predict the wear depth in FSW process tools; this includes different rotation speeds and traverse speeds. Comparison is also made between the dome and conical tool designs at a particular radial position; the aim of this comparison is to show the relationship between the weld process parameters and wear depth for both tool designs.

7.2 Model description

Two CFD models were defined based on modelling methodology detailed in Chapter 4; as with the model used in Chapter 6, heat generation was included as 304 stainless steel was the weld material. For both models, a slip-stick condition was implemented on the tool surface (shoulder and pin) through the application of equations 4-5 and 4-6. The dome shape (Figure 7-1) was the same as that investigated in Chapter 6, while

the conical tool design (Figure 7-2) had a 30 degree cone angle, a lower cone radius of 4 mm, and a shoulder radius of 9 mm. A total of nine cases were run using the parameters shown in Table 7-1 and Table 7-2 for each tool design to predict the tool wear using the methodology presented in Chapter 6. It is important to note that, in this chapter, each tool profile was obtained after running the initial geometry for the increment of weld distance from 0 to 2×10^3 mm. Table 7-1 and Table 7-2 include the value of weld pitch, which is calculated by dividing the traverse speed by the tool rotation speed [31] and therefore describes the advancement of the tool per rotation. This term was documented by Seidel and Reynolds [31], who linked the weld pitch with weld energy stated that weld pitch was inversely proportional to the weld energy [7].

Table 7-1 The range of tool rotation speeds at constant weld traverse speed and weld distance

Traverse speed [mm s^{-1}]	Rotation speed [rpm]	Weld pitch [mm rev^{-1}]
2.5	150	1
2.5	225	0.66
2.5	450	0.33
2.5	675	0.22
2.5	900	0.16

Table 7-2 The range of weld traverse speeds at constant tool rotation speeds and weld distance

Traverse speed [mm s^{-1}]	Rotation speed [rpm]	Weld pitch [mm rev^{-1}]
1.25	225	0.33
2.5	225	0.66
3.75	225	1
5	225	1.33
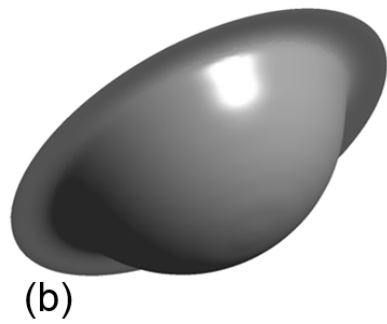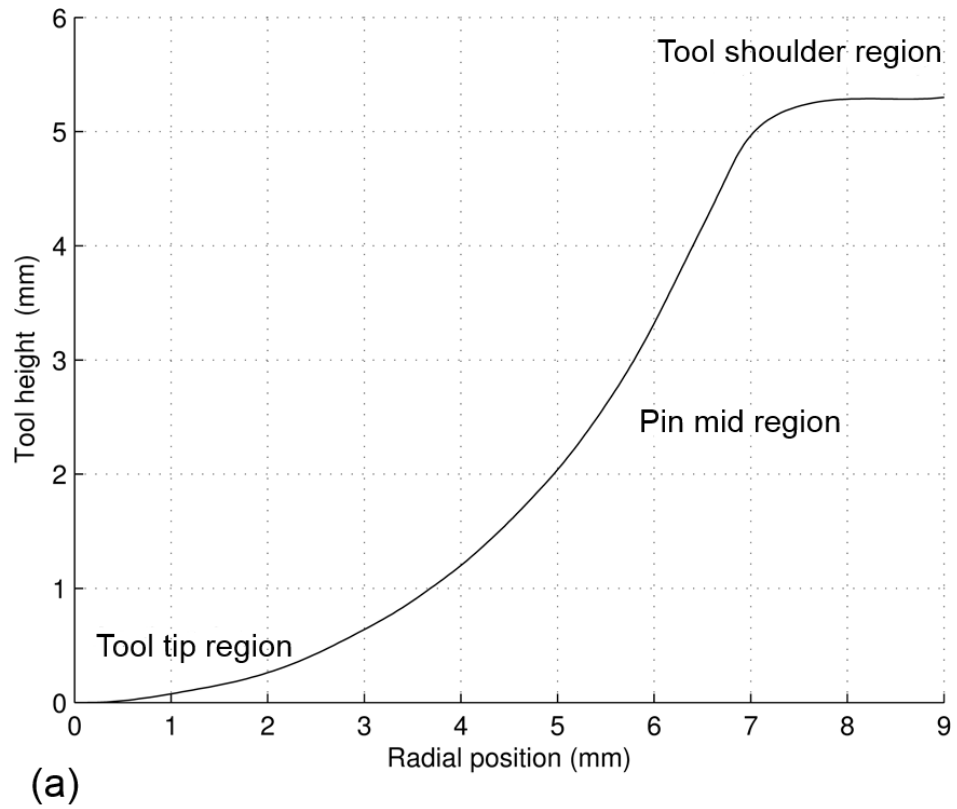
Figure 7-1 Dome tool geometry used in the study: (a) 2D plot shows the tool regions; (b) 3D model
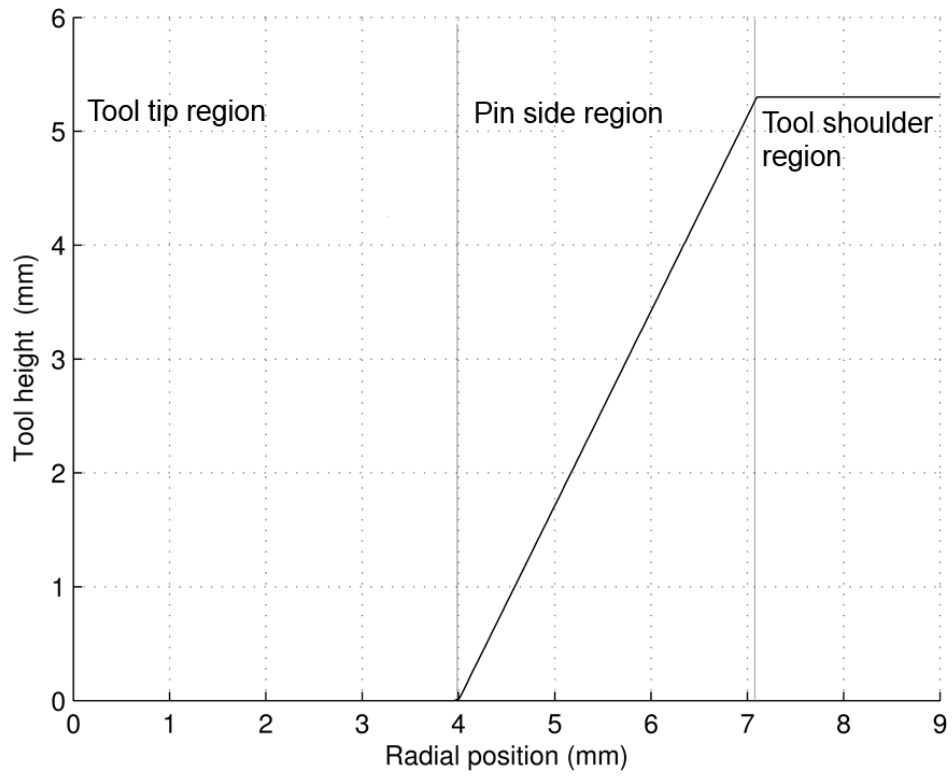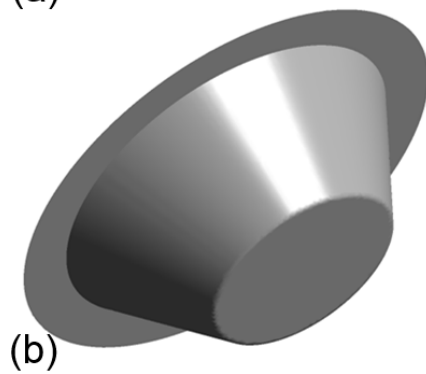
Figure 7-2 Conical tool geometry used in the study: (a) 2D plot shows the tool regions; (b) 3D model

7.3 Results

7.3.1 The dome shaped tool

The flow behaviour was assessed in terms of velocity contours and velocity vectors at different planes around the tool surface in order to determine the region of plastic deformation near the tool. The pressure distribution on the tool surface was also predicted at different radial positions with the initial tool geometry used for the tool wear calculation.

7.3.1.1 Material flow behaviour

In this section, the material flow around the dome tool shape was evaluated in order to gain a better understanding of the flow patterns and to link this profile to the pressure distribution on the tool surface. Therefore, several planes were analysed, as seen in Figure 7-3 and Figure 7-4. Figure 7-3 shows the velocity contours plotted in the y-z plane perpendicular to the flow direction on the axis of the tool rotation. From this figure, it can be seen that the material velocity is highest in the tool shoulder region; this is due to the fact that the peripheral tool speed increases towards the outer edge of the shoulder [24, 48].
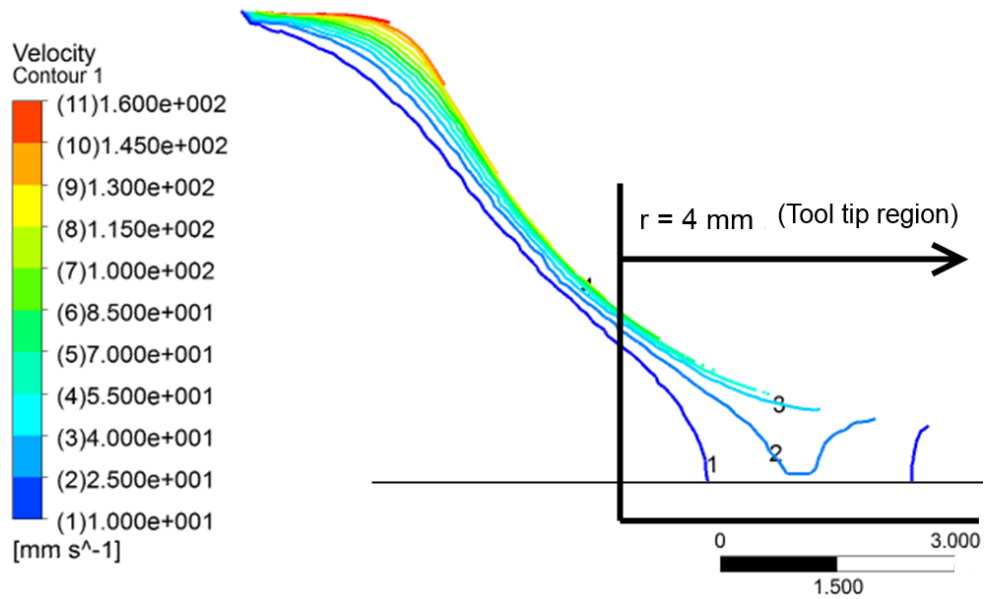
Figure 7-3 Velocity contour for the dome tool design at 225 rpm and 2.5 mm s^{-1} traverse speed for the initial geometry plotted in the y-z plane perpendicular to the flow direction on the axis of the tool rotation (Note: half tool presented)

It can be seen that there is a high velocity gradient near the shoulder, where the highest plastic deformation occurs, and it reduces through the thickness of the plate. Another interesting observation is that the peak velocity magnitude in the tool tip region is 70 mm s^{-1} and that no significant gradient can be seen in the velocity in the region underneath the tool.

In Figure 7-4 a, velocity vectors were plotted in the x-z plane, which is perpendicular to the tool axis at y = 0 mm where (0, 0, 0) is located on the pin tip surface (tool tip region; Figure 7-1 a). It can be seen that the material rotates in the same direction as the tool rotation direction, and that the peak material velocity value is 30 mm s^{-1}. Figure 7-4 b shows the velocity vectors as in Figure 7-4 a; including the tool geometry; a small contact area can be seen near the tool tip region due to the dome-shaped end.
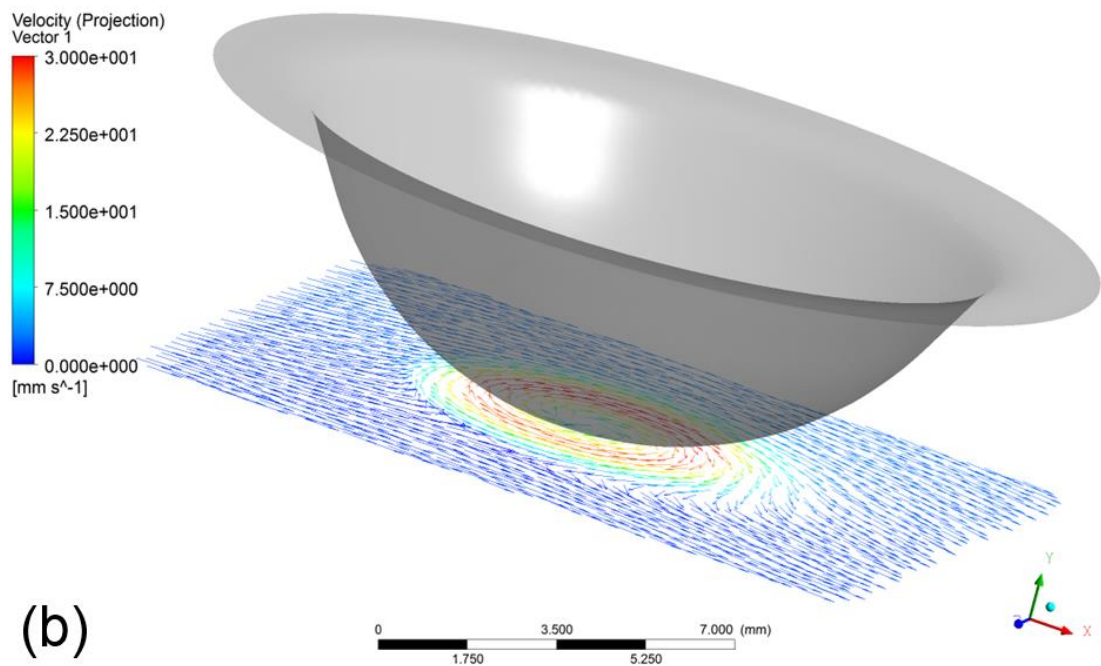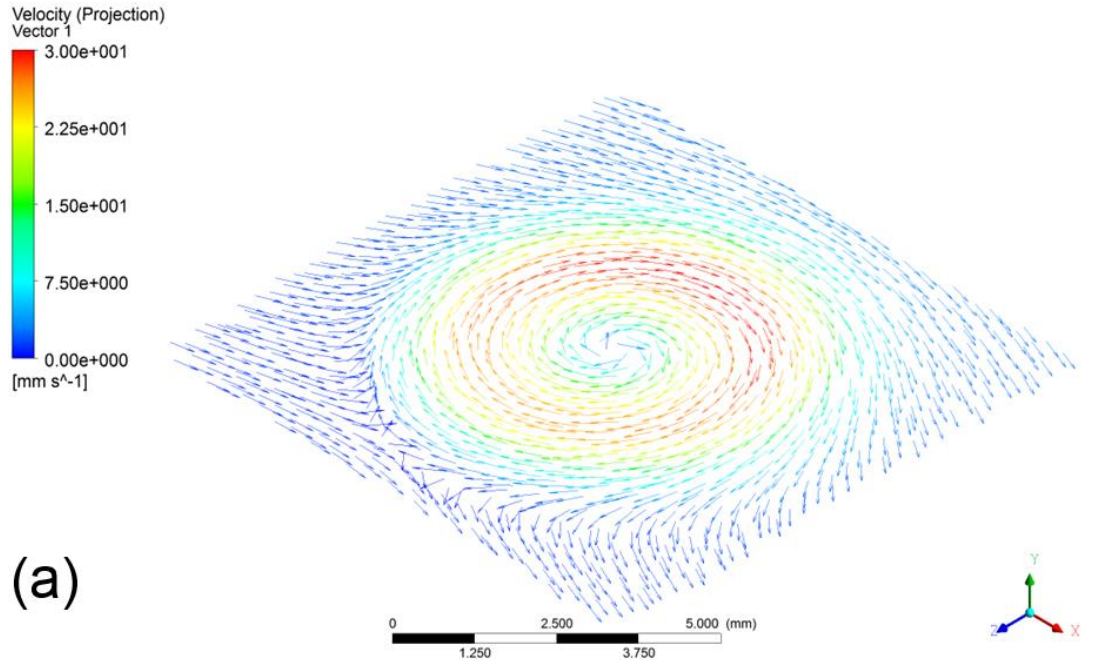
Figure 7-4 Velocity vectors for the dome tool design at 225 rpm and 2.5 mm s^{-1} traverse speed for the initial geometry on the plane at the tool tip: (a) in 3D; (b) on the same plane, including the tool (shows tool contact with the plane of the velocity vectors)

7.3.1.2 Tool wear prediction

As presented and discussed in Chapter 6, tool wear calculations were computed based on equation 6-7, in which pressure and sliding distance are considered variables while the remaining parameters are assumed to be constants.

The average pressure distribution was calculated on the tool surface at different radial positions with the initial tool geometry for the dome tool used for tool wear calculation illustrated in Figure 7-5 using the parameters shown in Table 7-1. The results show that the peak value of the pressure occurred at a radius of 5 mm on the pin mid region, as shown in Figure 7-5. As explained in Chapter 6, Section 6.4.2, the interaction of the axial flow with the pin causes a bifurcation of the flow past the pin, which leads to an increase in the pressure in the pin mid region. The overall trends show that near the tool tip region (for example, r = 0 to 2 mm) the pressure decreased; thereafter, the pressure increased until reaching a peak at r = 5 mm (pin mid region). Following this, the values decreased and there was no significant change until the tool shoulder region (r = 7 to 8.9 mm), except for the case of 150 rpm.
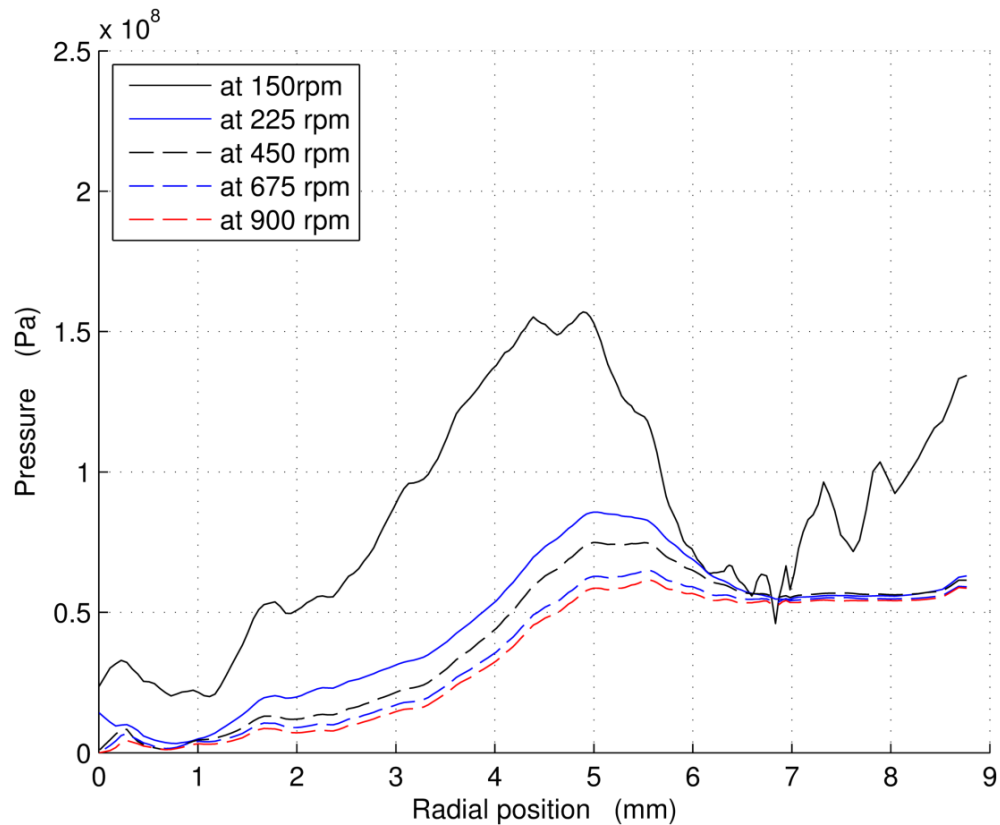
Figure 7-5 Pressure distributions on the dome tool surface for the initial geometry using parameters in

Table 7-1

From Figure 7-5, it can be seen that the calculated pressure trends are similar across a range of rotation speeds and that the pressure decreases with increasing tool rotation speed. This is due to the fact that increasing the tool rotation speed leads to increased tool surface velocity, which in turn causes a drop in the pressure value on the tool surface. It can be argued that the reason for this drop in the pressure is due to the Magnus effect [132] that uses Bernoulli principals. In Magnus effect, the pressure distribution on the any rotating object moving through a fluid is changed. Pressure is decreased on the upper surface and increased on the lower surface and vice versa, causing a positive net lift force according to rotating object direction. Moreover, at r = 5 mm, the peak value of pressure at a tool speed of 900 rpm is calculated to have been reduced to less than 30% of that at 225 rpm, while in the case of 150 rpm, it is reduced

by 160% and the pressure distribution along the tool surface for all cases tends to be uniform.

Here, the study used the parameters presented in Table 7-2 to calculate the pressure distribution on the tool surface. Figure 7-6 shows the average pressure distribution versus the radial position at different traverse speeds with the initial tool geometry; these data were used for the tool wear calculation. The overall trends in Figure 7-6 show the same behaviour as seen in Figure 7-5 in terms of pressure profiles. However, in contrast to Figure 7-5, Figure 7-6 illustrates that pressure distributions on the tool surface increases with increasing traverse speeds. The peak pressure value, which is in the pin mid region of the tool, is increased to a value of 2.75×10^8 Pa, while in the case of rotation speed, it has a value of 1.6×10^8 Pa. Furthermore, the results in Figure 7-6 show that a significant increase in the pressure values at 3.75 and 5 mm s^{-1} traverse speed may be due to the value of the weld pitch of these cases, which is clearly quite high, and this can greatly influence the flow behaviour by causing a reduction in fluidity of the material [157].
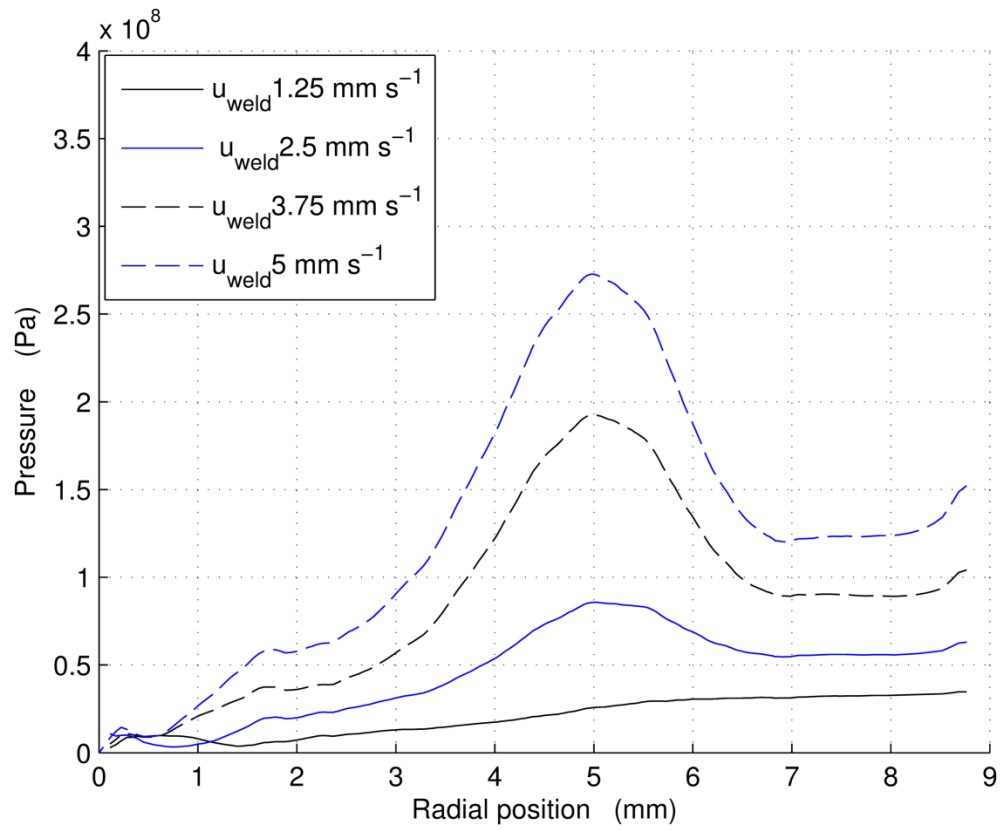
Figure 7-6 Pressure distributions on the dome tool surface for the initial geometry using the

parameters in Table 7-2

7.3.1.2.1 Wear depth results

Figure 7-7 shows the calculated values of the wear depth versus different radial positons at different rotation speeds. The graph reveals that no significant wear occurs near the tool tip region. Overall trends of the predicted data show that wear depth increases steadily from the tool tip to the pin mid region as shown in Figure 7-1 a, at close to r = 5 mm; the trend is for wear depth to fall steadily and finally increase at r = 7.5 mm. As seen in Figure 7-7, wear depth increases with increased rotation speed. It is found that the maximum wear depth is always calculated at the shoulder edge; this can be attributed to fact that there is a greater likelihood of obtaining a high value for wear depth at the shoulder because high velocity gradient occurs within the shoulder region [86]. In addition it can be seen that the trend of 150 rpm does not follow the other trends, probably because of changing in the flow behaviour which requires further investigation.
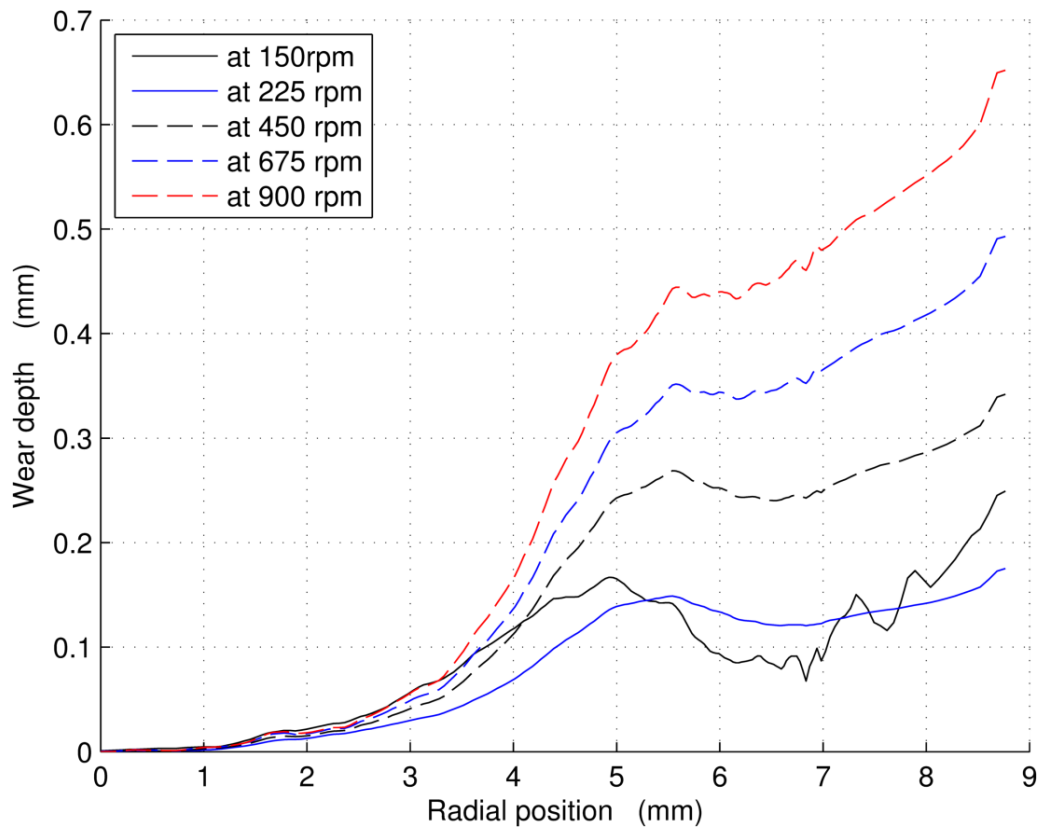
Figure 7-7 Plot of the wear depth along the dome tool surface at a weld distance of 2×10^3 mm using

parameters in Table 7-1

In addition, as explained in Chapter 6, Section 6.4.2, the interaction of the axial flow with the pin causes a bifurcation of the flow past the pin, which leads to an increase in the pressure values at that position. For all rotation speeds, wear was achieved; the peak wear depth value was between 0.18-0.65 mm at the shoulder edge ($r \approx 8.9$ mm). The results reveal that wear depth increases by increasing the tool rotation speed, despite the fact that the pressure plots show the opposite. It is important to observe that at high tool rotation speed sliding distance is more dominant than pressure in the wear calculation equation 6-7.

Wear depth was calculated using the parameters shown in Table 7-2 to investigate the effect of changing traverse speed on tool wear in FSW. The wear depth results in Figure 7-8 show very little wear occurring near the tool tip region, whereas tool wear is significantly higher in the pin mid region, particularly at $r \sim 5.2$ mm. Thereafter,

there is a decrease from 0.45 mm and 0.33 mm for traverse speed 5 mm s^{-1} and 3.75 mm s^{-1} respectively, falling to 0.27 and 0.2 mm for those traverse speeds. Within the shoulder edge (r = 8.9 mm), the trend is for values to increase, though reaching values that are lower than those produced at position 5.2 mm. This behaviour can be attributed to the peripheral speed of the tool towards the outer edge of the shoulder.
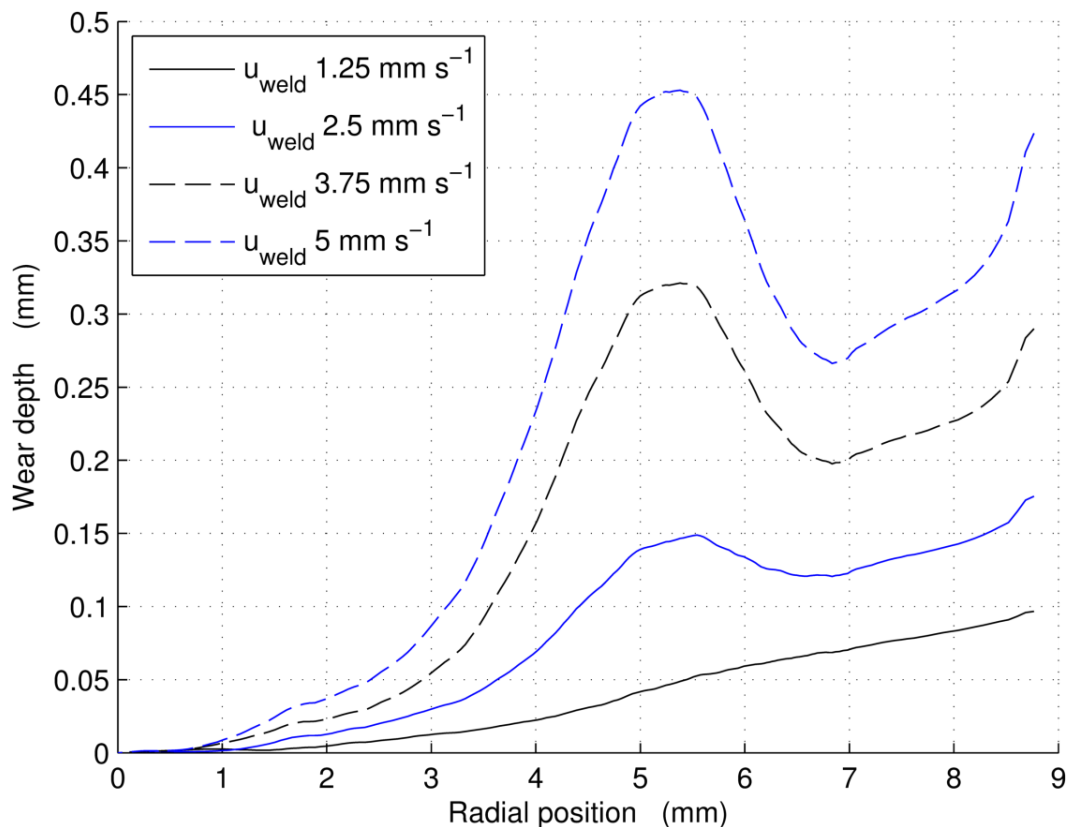
Figure 7-8 Plot of the wear depth along the dome tool surface at a weld distance of 2×10^{3} mm using parameters in Table 7-2

It is clear that for traverse speeds of 1.25 and 2.5 mm s^{-1}, there is a significant change in the wear depth profile in the pin mid region, the junction of the dome and shoulder (r = 7 mm), and the periphery of the shoulder (r = 8.9 mm). However, at traverse speeds of 3.75 and 5 mm s^{-1}, the significant changes in the wear depth profile in the pin mid region are higher than that seen near the shoulder when compared with traverse speeds of 1.25 and 2.5 mm s^{-1}. It is worth noting that the high wear rates along the surface of

the pin are due to the interaction of the axial flow with the pin causing a bifurcation of

the flow past the pin, which leads to an increase in the pressure values at that position.

As presented and discussed in Chapter 6, tool wear calculations were computed based

on equation 6-7, in which wear depth is a function of pressure and sliding distance.

Therefore, in this case the pressure is the dominant factor in the wear calculation. It is

important to note that increasing traverse speeds means the tool is moving quickly and

thus heat does not have time to saturate the local weld area, which leads to a reduction

in the fluidity of the material [157].

7.3.2 The conical shaped tool

As in Section 7.3.1, flow behaviour was examined in terms of velocity contours and velocity vectors at different planes around the tool surface to determine the region of plastic deformation near the tool. The pressure distribution on the tool surface was also computed at different radial positions with the initial tool geometry for this tool design.

7.3.2.1 Material flow behaviour

In the graphs Figure 7-9 and Figure 7-10, the velocity contours and vectors were plotted as in Section 7.3.1.1. In Figure 7-9, it can be seen that the velocity contours for the conical tool tends to be similar to that predicted for the dome tool in the tool shoulder and pin mid regions, in terms of velocity gradient. However, the results of the conical tool show that the velocity gradient is higher than that for the dome tool in the tool tip region, suggesting that there is a greater stirring action caused by the flat surface of the conical tool. This finding is consistent with the flow behaviour at the pin tip described in the study of Fratini et al. [158]. The results also show that in the tool tip region the peak material velocity value is 85 mm s $^{-1}$, which is clearly higher than dome tool design.
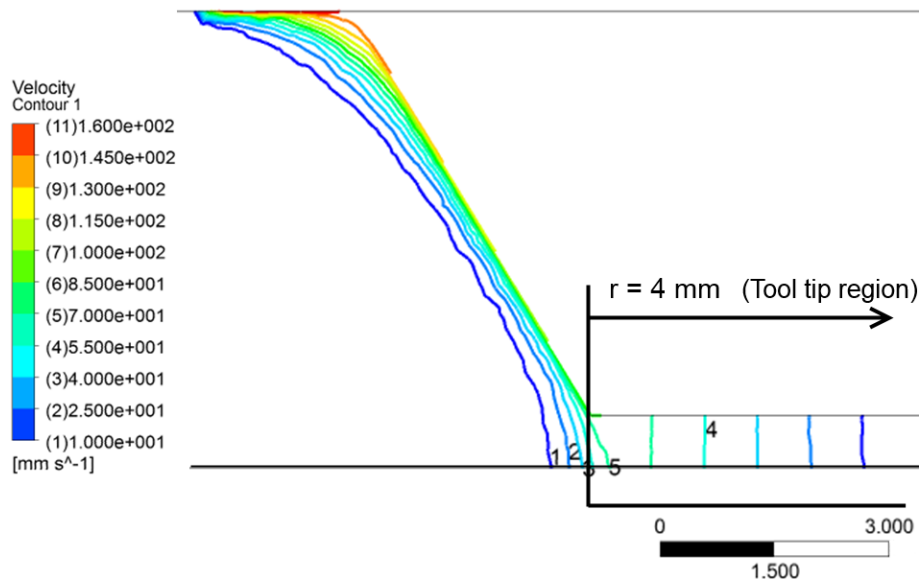
Figure 7-9 Velocity contour for the conical tool design at 225 rpm and 2.5 mm s^{-1} traverse speed for the initial geometry plotted in the y-z plane perpendicular to the flow direction on the axis of the tool rotation (Note: half tool presented).

In Figure 7-10 a, a similar behaviour for the material flow can be seen relative to that in Figure 7-4 a, and the peak material velocity value is 75 mm s^{-1}. Additionally, Figure 7-10 b shows the plane of the velocity vectors with the tool, as described for Figure 7-4, and shows a larger contact area near the tool tip, which is essentially because of the flat tip surface of the conical tool.

When comparing Figure 7-4 and Figure 7-10, the area on the tool tip surface with a significant velocity gradient is higher for the conical tool than for the dome tool in the same location; in the dome tool, the diameter of the pin is reduced, resulting in a corresponding reduction in flow velocity in the weld region.
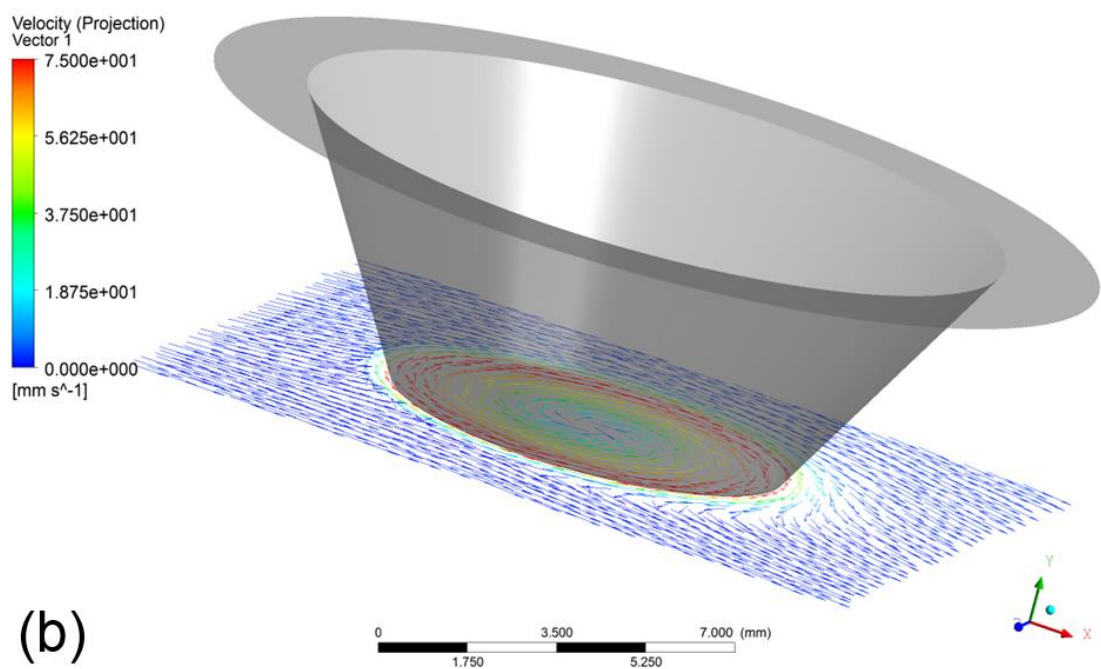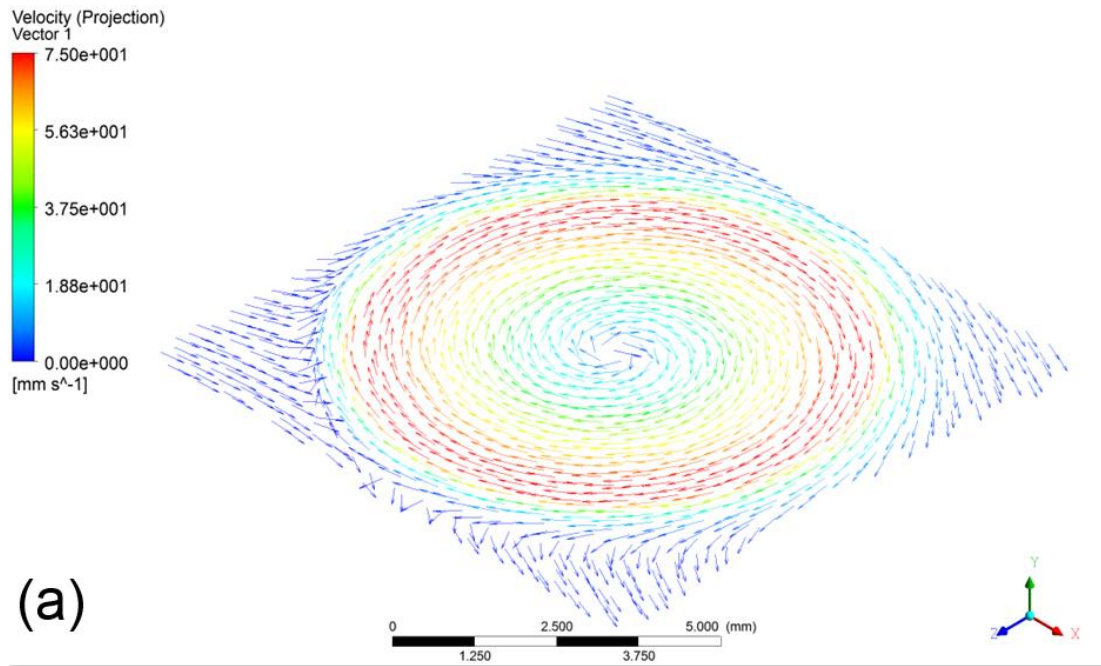
Figure 7-10 Velocity vectors for the conical tool design at 225 rpm and 2.5 mm s^{-1} traverse speed for the initial geometry on the plane at the tool tip: (a) in 3D; (b) on the same plane including the tool (shows tool contact with the plane of the velocity vectors).

7.3.2.2 Tool wear prediction

In this section, the study presents the results of the pressure distribution on the tool surface and calculated the wear depth values of the conical tool design as shown in Figure 7-11 and Figure 7-12 and using the parameters in Table 7-1 and Table 7-2. Figure 7-11 depicts the average pressure distribution on the tool surface calculated at different radial positions with the initial tool geometry employed for the tool wear calculation using the parameters shown in Table 7-1. As can be seen in Figure 7-2, the tool was divided into three regions, which are tool tip, pin side, and tool shoulder regions. In the tool tip region, the pressure profiles in Figure 7-11 are different from that seen in Figure 7-5. The pressure distribution on the tool surface in that region has an irregular behaviour for all rotation speeds. The irregular behaviour of the pressure distribution in the tool tip region can be attributed to the spiral motion of the flow in that region and a high stirring action, as can be seen in Figure 7-9 and Figure 7-10.
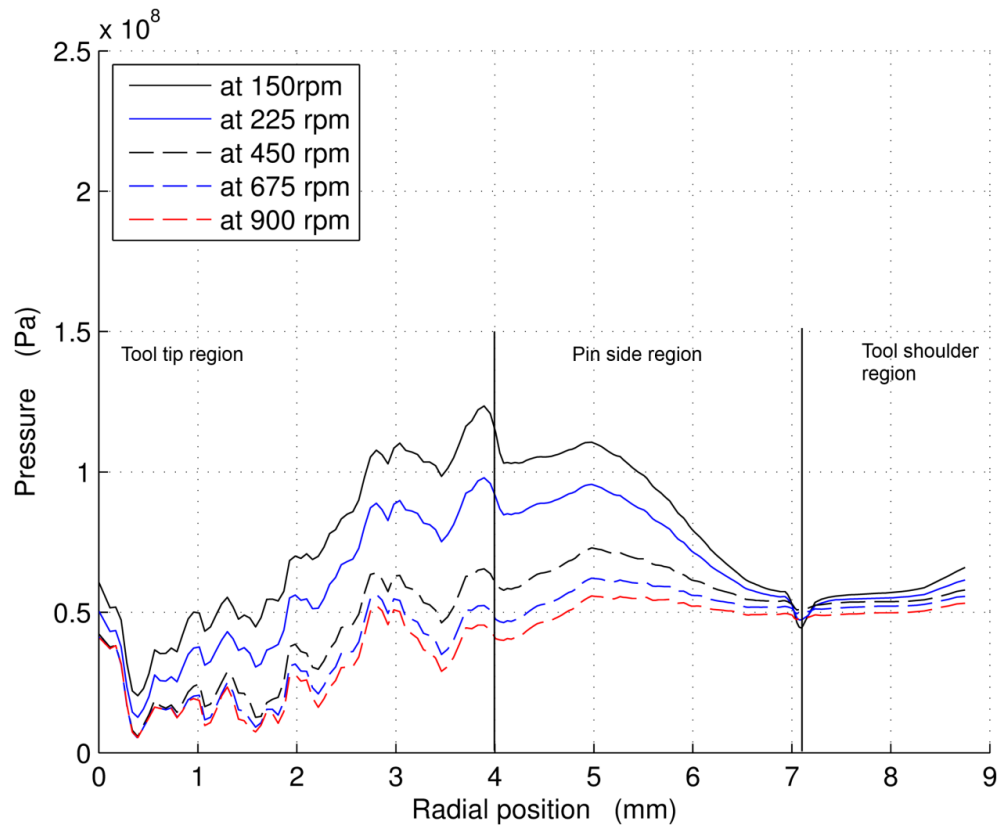
Figure 7-11 Pressure distributions on the conical tool surface for the initial geometry using the

parameters in Table 7-1

Similar trends are seen in Figure 7-12 as in Figure 7-11 in terms of pressure distribution in the tool tip, pin side, and shoulder regions. However, the non-uniform pressure distribution in the tool tip region shown in Figure 7-12 is higher than that predicted in Figure 7-11. It can be seen that for all trends in Figure 7-12 the pressure values were higher than those shown in Figure 7-11. For example, the peak value of pressure in Figure 7-12 at r = 4 mm was 2.5×10^8 Pa, while, in Figure 7-11, it was ~1.2 $\times 10^8$ Pa. It can be concluded that the primary reason for this non-uniform pressure distribution on the tool tip region of the conical tool is a presence of a significant velocity gradient.
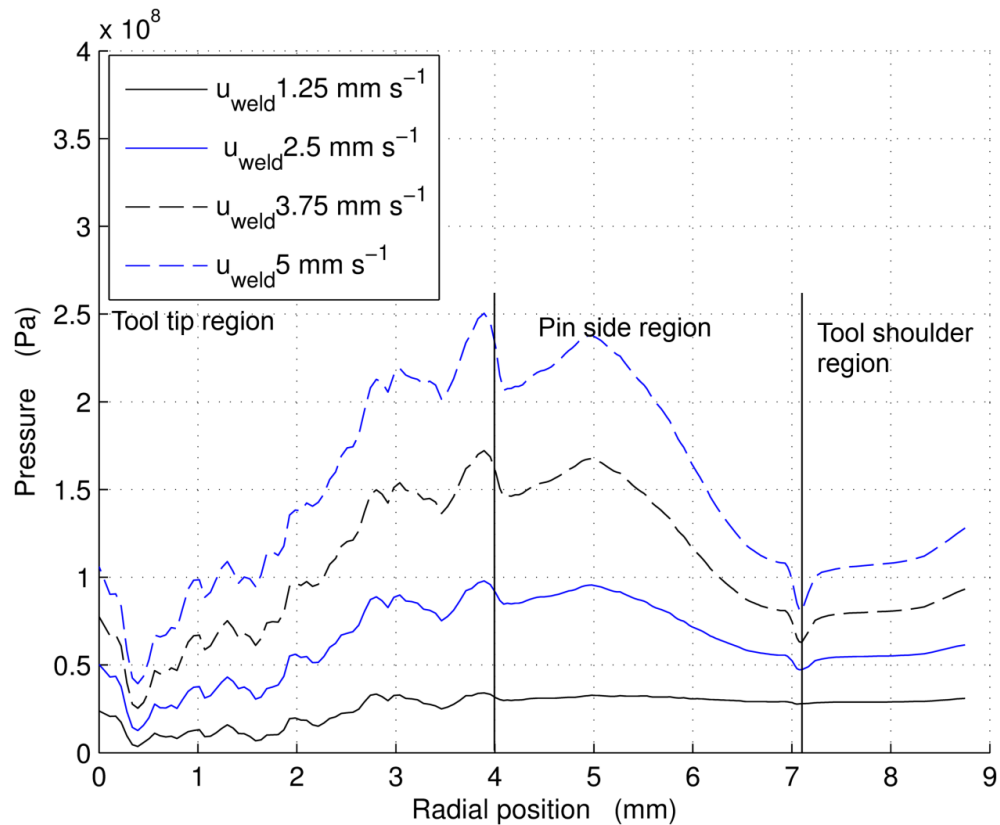
Figure 7-12 Pressure distributions on the conical tool surface for the initial geometry using parameters

in Table 7-2

It is also important to note that the pressure distribution on the tool surface at different

traverse speeds increases with increasing traverse speed. Using this tool design, the

behaviour observed is that an increase in traverse speed causes an increase in pressure,

due to the increasing effect of the axial flow that is obstructed by the tool. As already

noted, pressure has a greater effect on wear than slip speed and thus this increase in

pressure will lead to increased wear.

7.3.2.2.1 Wear depth results

Figure 7-13 shows the calculated values of the wear depth versus radial position at

different rotation speeds. The results reveal that in the tool tip region, irregular

behaviour in terms of wear depth with no significant wear occurs near the tool tip;

however, at r = 3 and 4 mm, which are located just before the tool tip and pin side intersection in this location, the wear depth value reaches ~ 0.2 mm at the highest rotation speed. Furthermore, beyond this region, the wear depth profile appears to be similar to that produced by the dome-shaped tool.
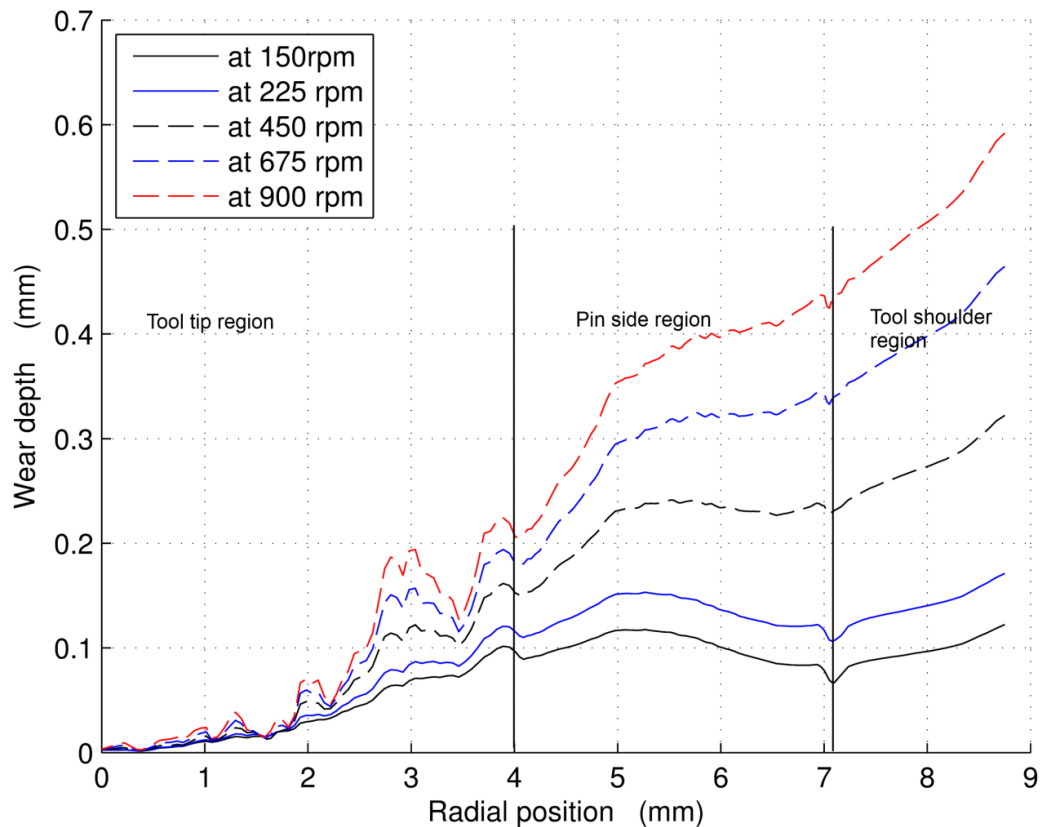
Figure 7-13 Plot of the wear depth along the conical tool surface at a weld distance of 2×10^3 mm using parameters in Table 7-1

It is important to note that wear depth increases by increasing the tool rotation speed, despite the fact that the pressure plots show the opposite. Again here, as explained in Section 7.3.1, with high tool rotation speeds, sliding distance is more dominant than pressure in the wear calculation equation 6-7.

In Figure 7-14, it can be seen that the overall trends in wear depth are similar to those in Figure 7-13, in terms of irregular behaviour in the wear depth values at tool tip, and pin side intersection, and the pin side and tool shoulder intersection, which is due to

the sharp edge causing changes in the flow behaviour of the material being welded in that position. However, a sharp drop in the wear depth values can be seen in Figure 7-14 at those positions; particularly for traverse speeds of 3.75 and 5 mm s^{-1} respectively. At the sharp edge, wear was accelerated by the high flow velocity, causing more tool wear in this region, which is confirmed by the study by Michael [67]. Furthermore, for the traverse speed values of 3.75 and 5 mm s^{-1} at r = 5 mm within the pin's side region, the peak wear depth values shows a sharp increase, which is clearly higher than those seen for the traverse speed values of 1.25 and 2.5 mm s^{-1}. It is especially interesting to mention that, as the traverse speeds increases, the corresponding pressure values at those points increases, which causes an increase in the wear depth. The case of 2.5 mm s^{-1}, 225 rpm appears on both graphs and it can be seen that similar increases in wear rate occur both from increased weld speed and increased rotation rate.
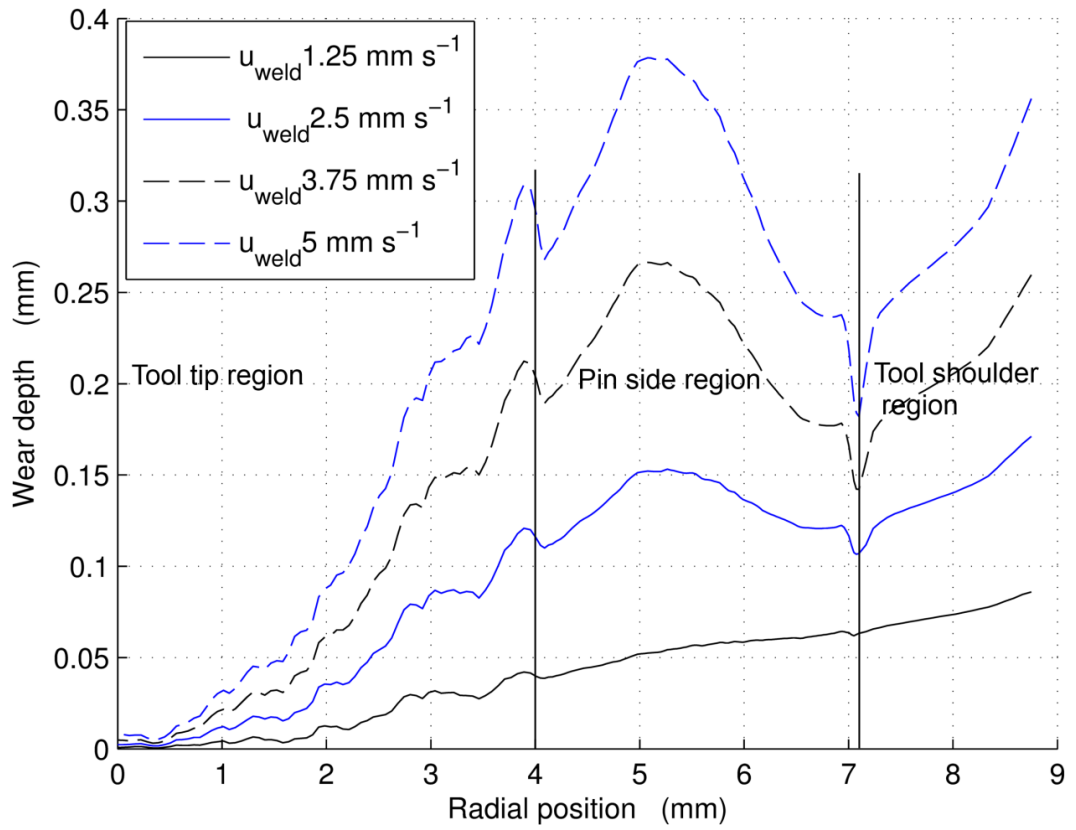
Figure 7-14 Plot of the wear depth along the conical tool surface at a weld distance of 2×10^3 mm using

parameters in Table 7-2

7.3.3 Tool profile results

Figure 7-15 a and b show the evolution of the dome tool geometry using the parametrisation shown in Table 7-1 and Table 7-2. For both graphs, it is evident that very little wear occurred for a welding distance of $2{\times}10^3$ mm near the tool tip region; however, in other regions on the tool surface, it can be seen that wear increased as the rotation speed and traverse speed increased. It is found that much higher wear was predicted throughout the pin mid region of the tool when compared with the tool tip region; this is consistent with the study by Michael [67].

In Figure 7-15 a, it can be seen that the predicted wear at the tool shoulder region is higher than that predicted in Figure 7-15 b. It can be argued that this is due to a combination of radial changing of the flow patterns at the dome-shoulder junction and the increased peripheral speed of the tool out towards the edge of shoulder. By considering both cases in Figure 7-15 a and b, it is found that no significant change in tool shape can be observed, which means that this tool is able to retain its original shape shown in Figure 7-1 under these circumstances.
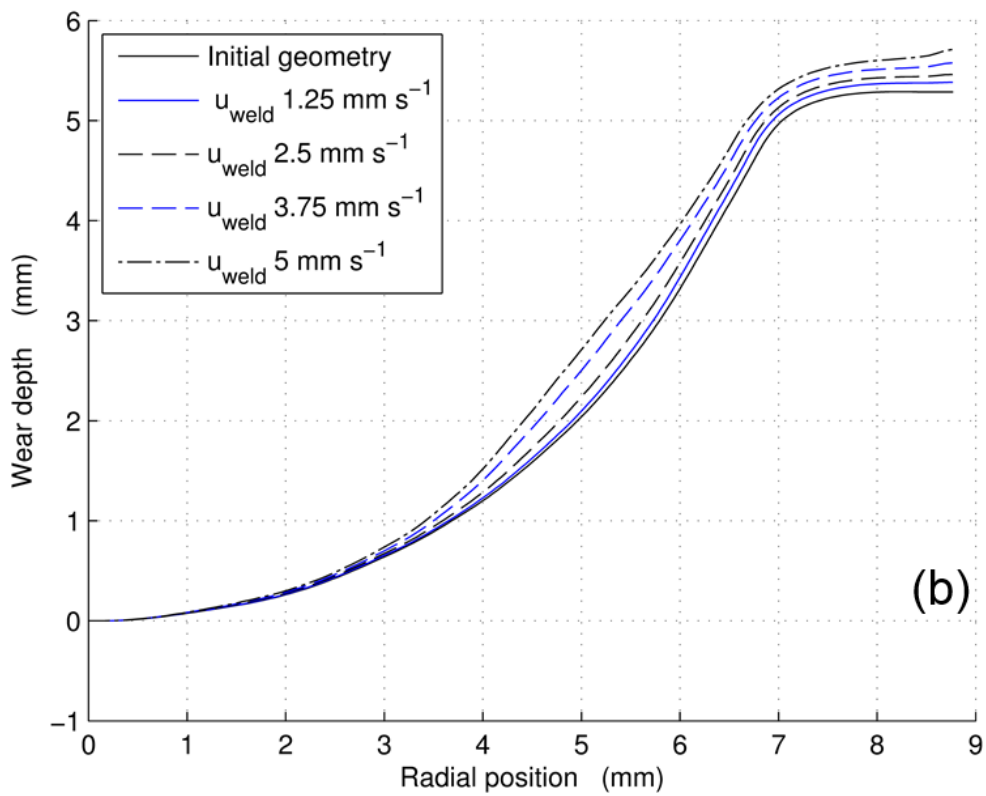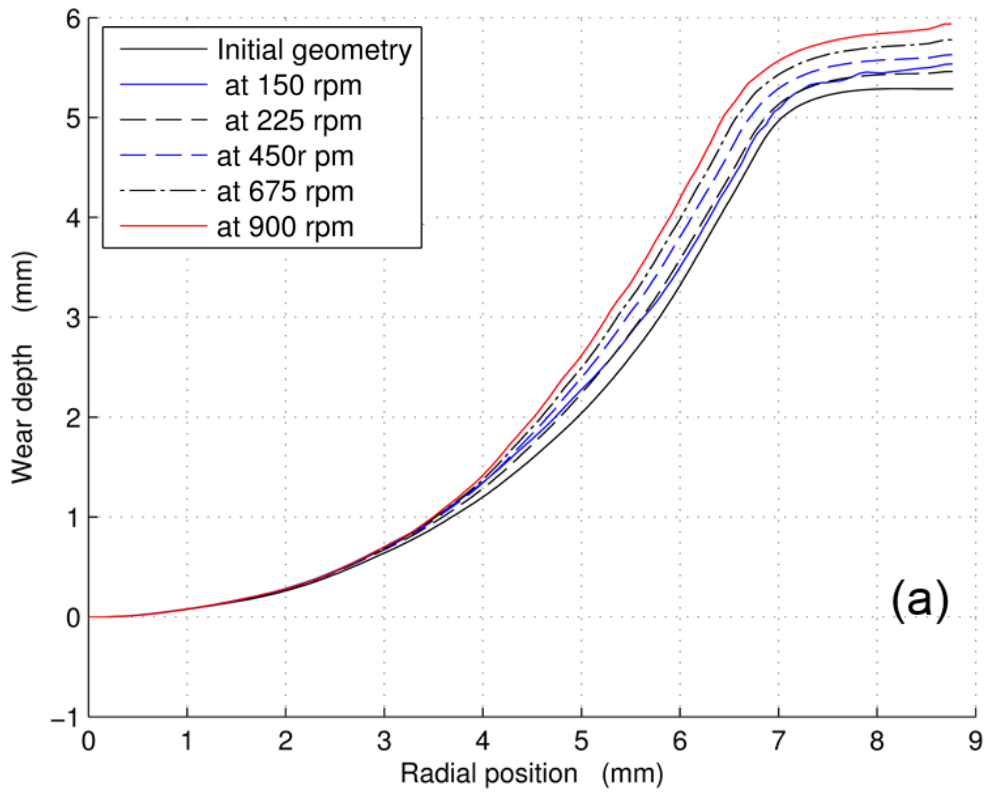
Figure 7-15 Dome tool profile after of 2×10^3 mm weld distance: (a) using parameters in Table 7-1; (b) using parameters in Table 7-2

Figure 7-17 a and b show the evolution of the conical tool geometry using parameters shown in Table 7-1and Table 7-2. For both graphs, Figure 7-17 a and b, the results reveal that in the tool tip region at radial position between 0 to 2.5 mm, very little wear was predicted during the welding, which is similar to what was seen in Figure 7-15. However, at radial position between 2.5 to 4 mm, it is evident that the predicted wear in Figure 7-17 a is different from that predicted in Figure 7-17 b. In Figure 7-17 a, on the periphery of the base of the pin a groove starts to form at the highest rotation speed which is similar to that observed by Siddiquee and Pandey [86] and Michael [67]as shown in Figure 7-16.
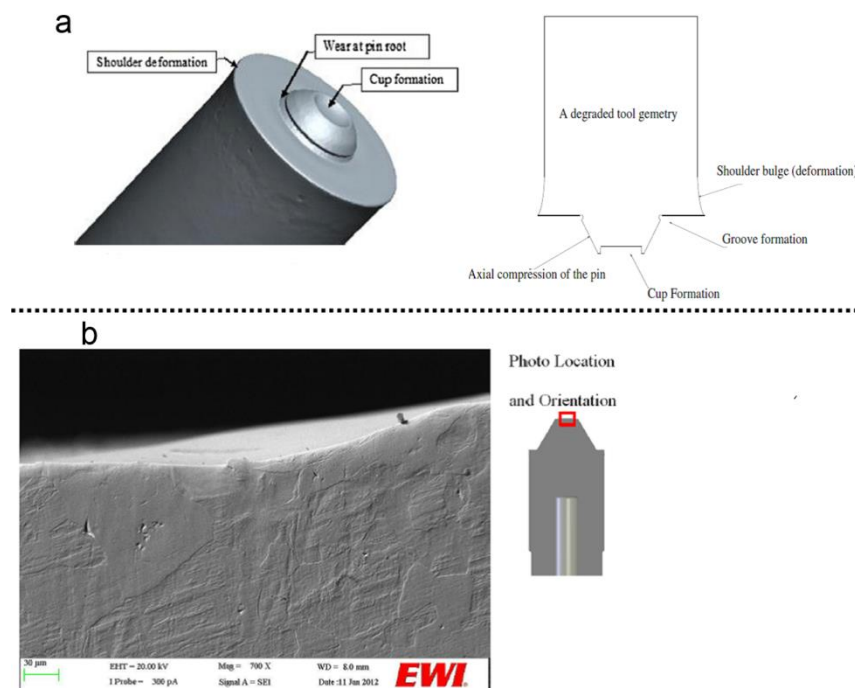
Figure 7-16 Groove formation on the tool surface: (a) observed by Siddiquee and Pandey [86], (b) observed by Michael [67]

At this region, r = 2.5 to 4 mm, wear was accelerated by the high flow velocity that was generated by increasing tool rotation speed, causing more tool wear in this region. This difference in flow can be seen in Figure 7-18 and Figure 7-19, where velocity vectors are presented in the plane perpendicular to the flow direction on the y-z plane

on the axis of conical tool rotation at 225 rpm and 900 rpm, respectively, with constant traverse speed of 2.5 mm s^{-1}. In Figure 7-18 and Figure 7-19, it can be seen that the velocity gradient under the tool tip region is larger for the case of 900 rpm than that for the case of 225 rpm due to increasing rotation speed. Furthermore, beyond this region, the wear depth profile seems to be similar to that produced by the dome-shaped tool (Figure 7-15).
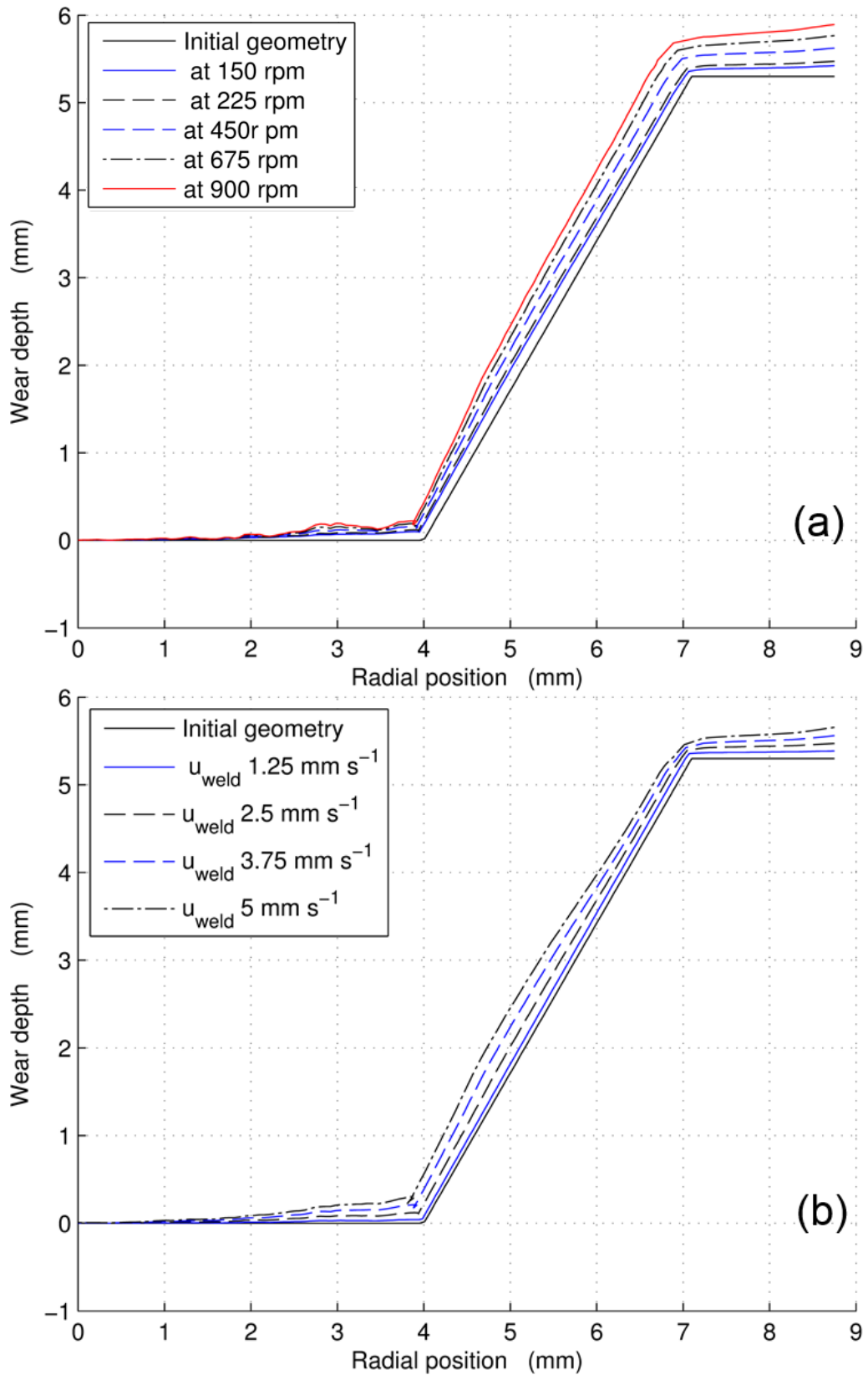
Figure 7-17 Conical tool profile after of 2×10³ mm weld distance (a): using parameters in Table 7-1,

(b): using parameters in Table 7-2
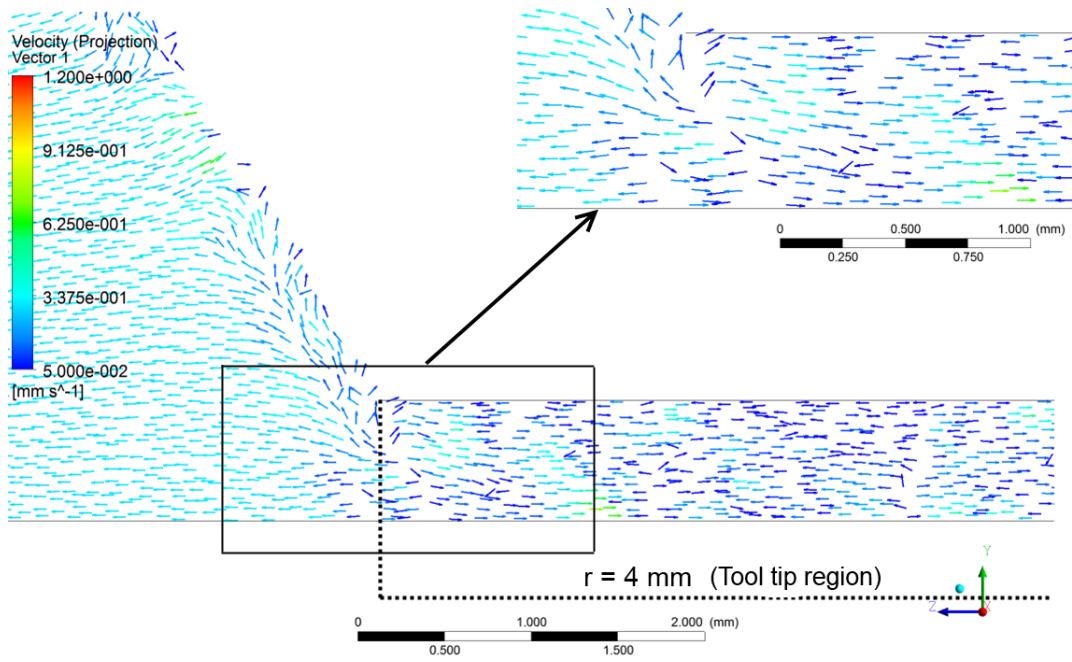
Figure 7-18 Velocity vectors for the conical tool design at 225 rpm and 2.5mm s^{-1} traverse speed for the initial geometry on the y-z plane perpendicular to the flow direction on the axis of the tool rotation (the top right graph is a magnification of the highlighted region).
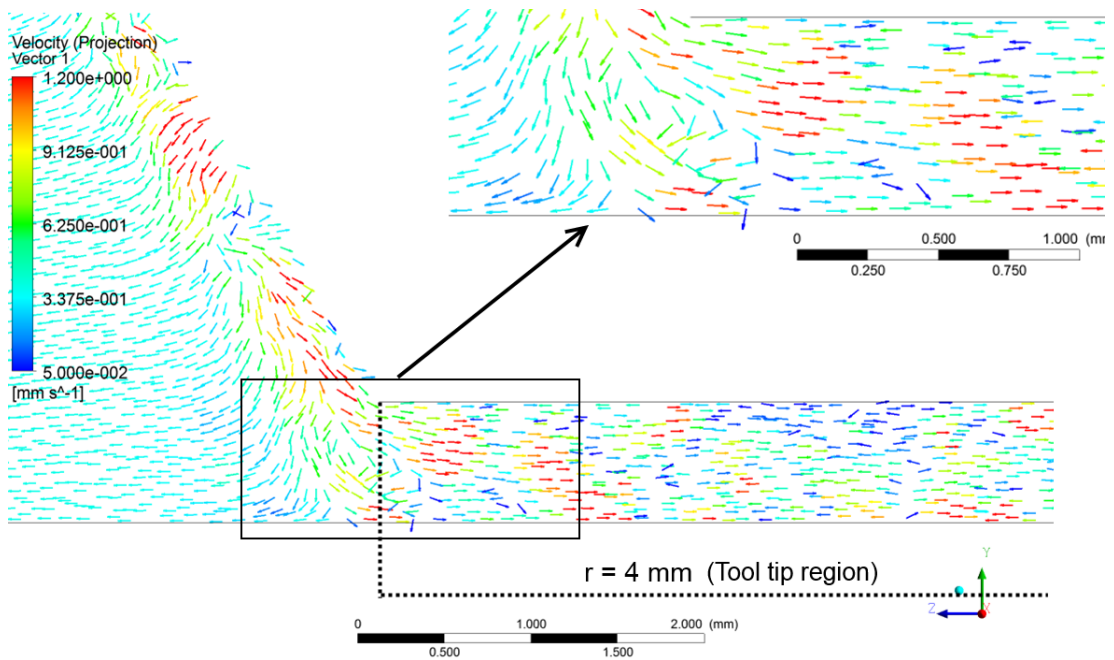
Figure 7-19 Velocity vectors for the conical tool design at 900 rpm and 2.5mm s^{-1} traverse speed for the initial geometry on the y-z plane perpendicular to the flow direction on the axis of the tool rotation (the top right graph is a magnification of the highlighted region).

7.3.4 Wear depth comparison

This subsection presents a comparison between the dome and conical tool designs at a radial position of 5.5 mm. As shown in Figure 7-1 and Figure 7-2, both tools were designed to give identical tangents (30 degree to the radial axis) at a radial position of 5.5 mm. Therefore, wear depth was plotted for both tools at that radial position at different rotation and traverse speeds, as shown in Figure 7-20 and Figure 7-21, respectively.

From the graphs, it can be determined that the highest wear depth occurred at the highest rotation speed and traverse speed, and that at the lowest value of the rotation and traverse speed both tools showed no significant difference in wear depth values.

However, it is especially interesting to note that, at a rotation speed of 450 rpm and above, the dome tool's wear depth tended to be higher than that of the conical tool. Similarly, at a traverse speed of 3.75 and 5 mm s^{-1}, the same behaviour as for the rotation speed was produced; it can be argued that this is due to the pressure values shown in Figure 7-5, Figure 7-6, Figure 7-11, and Figure 7-12. Therefore, at a radial position of 5.5 mm, wear depth for the dome tool design was higher than that predicted for the conical tool design. As shown in Figure 7-2, the conical tool has a sharp edge at the pin-shoulder intersection, which causes a pressure drop in that region with a significantly higher flow than that produced when using the dome tool.
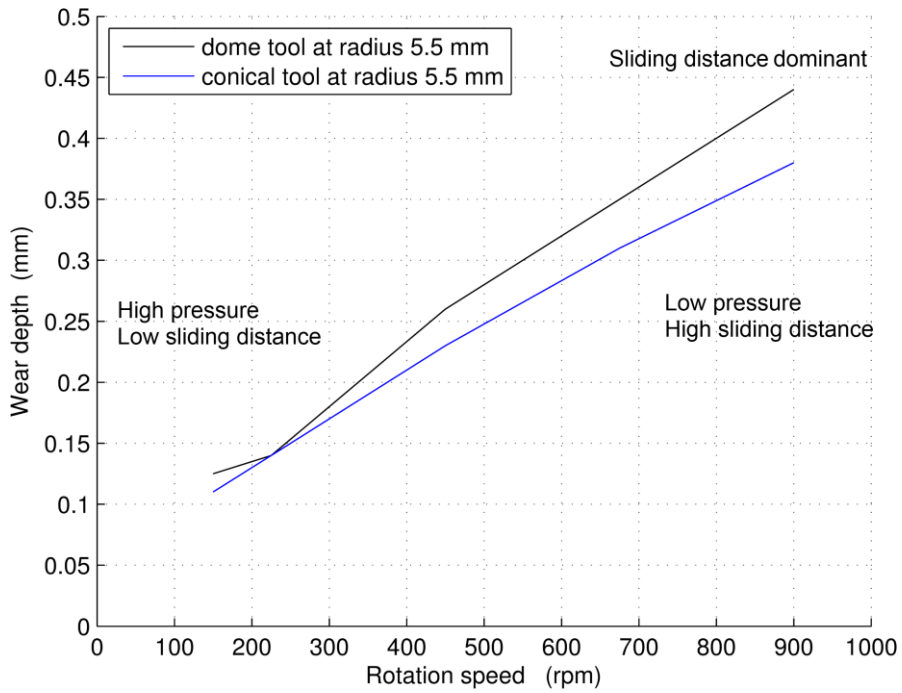
Figure 7-20 Predicted wear depth at radial position 5.5 mm for dome and conical shapes using

different rotation speeds (parameters in Table 7-1)
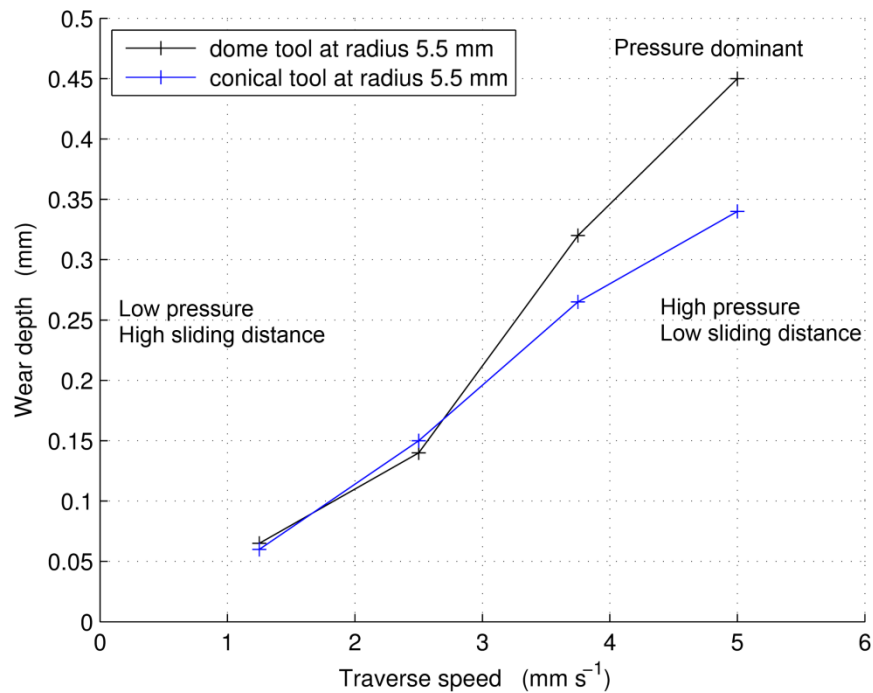
Figure 7-21 Predicted wear depth at radial position 5.5 mm for dome and conical shapes using

different traverse speeds (parameters in Table 7-2)

In Figure 7-22 and Figure 7-23, the calculated wear depth was plotted against weld pitch at a weld distance of 2×10^{3}mm using the parameters in Table 7-1 and Table 7-2. For both figures, Figure 7-22 and Figure 7-23, the data show that wear depth increased as the weld pitch increased when traverse speed is considered. According to what was presented earlier in this chapter, this behaviour can be attributed to the increasing of traverse speed and pressure being more dominant in the wear calculation. In contrast, for the case of rotation speed, wear depth decreased as the weld pitch decreased; it can be argued that this is due to a combination of increasing tool rotation speed and decreasing of traverse speed. It can be concluded that sliding distance is more dominant than pressure in tool wear calculation.

It is especially interesting to note that for a weld pitch value of 0.66, the data presented in Figure 7-22 and Figure 7-23, revealed that there is an intersection between tool rotation speed and traverse speed where the predicted wear depth had a value of 0.14 mm. This value shows that it is possible to obtain a low wear case by controlling the weld parameters for any weld pitch value. Additionally, in order to reduce high wear it is important to control process parameters that can achieve that.
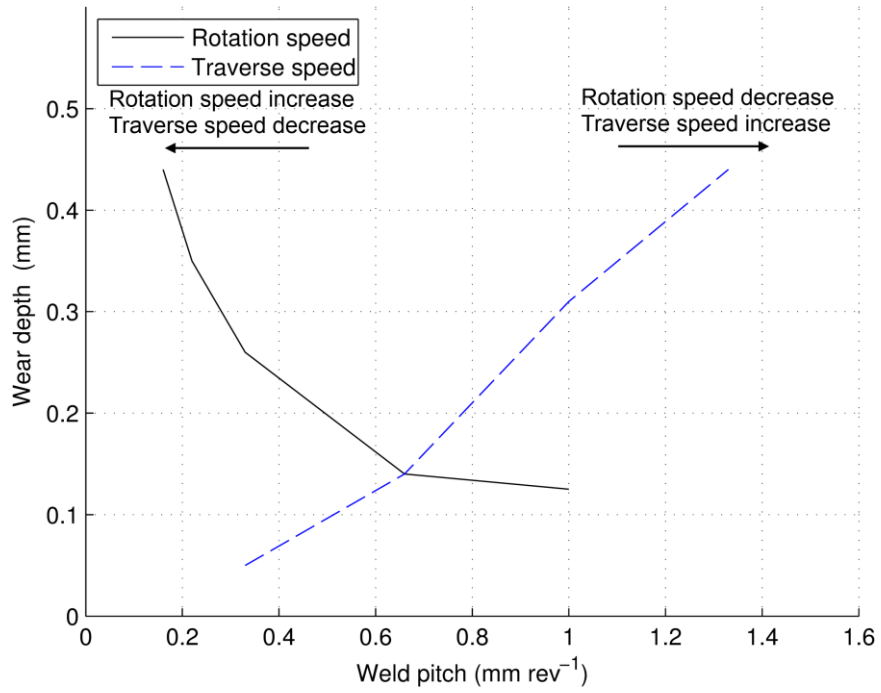
Figure 7-22 Predicted wear depth at radial position of 5.5 mm for dome tool shape using different

weld pitch (Tables 7.1 and 7.2)
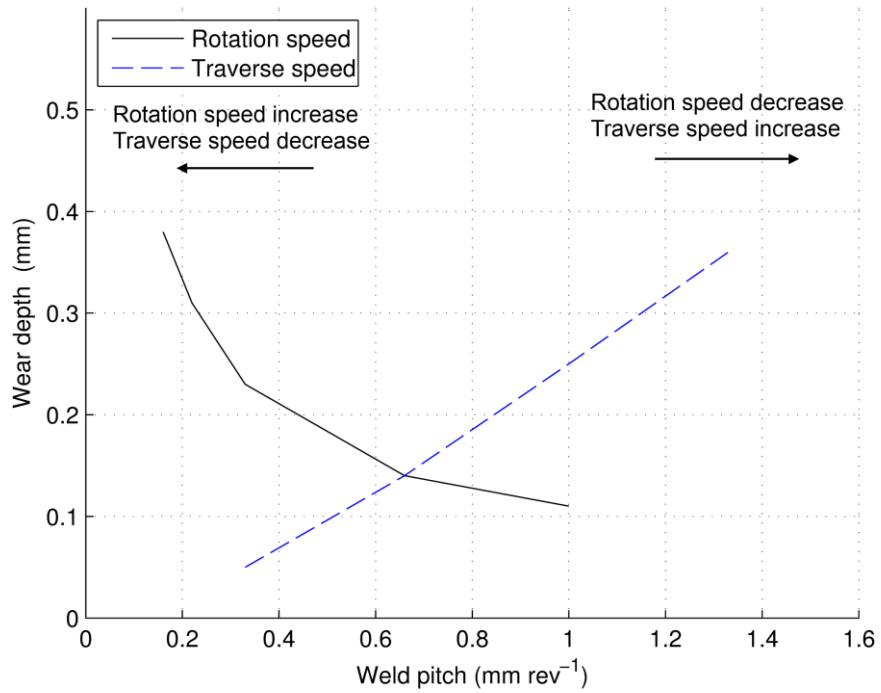
Figure 7-23 Predicted wear depth at radial position of 5.5 mm for conical tool shape using different

weld pitches (Tables 7.1 and 7.2)

7.4 Discussion

It is worth observing that tool wear calculation is related to the weld process parameters, which are rotation speed, traverse speed and sliding distance [86, 156]. From Figure 7-7, Figure 7-8, Figure 7-13, and Figure 7-14, it can be noted that rotation speed and traverse speed have an effect on the wear depth when their values increase. The results show that when increasing rotation speed and keeping traverse speed constant the wear is more influenced by the increase in slip velocity $(V_{slip}$, equation 6-4), whereas, when keeping rotation speed constant and increasing traverse speed pressure is the influencing factor.

The wear depth is similar for the dome and conical tool designs, particularly in the tool shoulder region and pin mid (side) region. With both tool shapes, this study has found very little wear occurring at the tip. Most wear occurs at the junction of the pin and the shoulder and then out into the periphery of the shoulder. This can be attributed to a combination of the rapidly changing flow patterns at the pin and shoulder junction and the increasing peripheral speed of the tool out towards the edge of the shoulder. In contrast, in the tool tip region, the wear depth is different for the dome and conical tool designs, where the results reveal that the conical tool has a greater area of contact with the flowing material than the dome design; therefore, wear is more likely to occur. This finding is consistent with studies by Siddiquee and Pandey [86] and Zhang et al. [156].

For both tool shapes, increasing the rotation rate of the tool increases the heat input into the system [137], and the results show a corresponding rise in wear rates. This is probably due to an increase in the velocity gradient of the viscous flow near the tool surface which cause a reduction in the material viscosity and accelerated wear under these conditions. In this case, the flow of the highly deformed material that flows

parallel or perpendicular to the tool axis causes physical tool wear in FSW; this finding has been further confirmed by Prado et al. [10], Gan et al. [78], and Siddiquee and Pandey [86].

By increasing the traverse speed of the weld, the results show a corresponding rise in wear rates. This can be attributed to the fact that the tool is moving quickly and thus heat does not have time to saturate the local weld area [85, 159]. This results in the case in which the velocity gradient is less in the weld region and higher pressure on the tool surface is increased.

The tools used in this study can be compared in terms of the velocity gradient and wear where it can be concluded that using a conical tool with a wider tip can produce a higher velocity gradient than the dome tool. This can result in enhancement with regards to the stirring action when using low rotation speed thus producing a good weld particularly in the weld root region. On other hand, the study showed that wear was accelerated by the high flow velocity that was generated by conical tool with a wider tip, causing more tool wear in the tool tip region. In contrast, low wear can occur when using the domed end shape tool particularly in the tool tip region potentially leading to better tool life.

7.5 Conclusion

In this chapter, a parametric study has been undertaken in order to investigate the methodology described in Chapter 6 and show that it is able to predict the tool wear in FSW when using different tool designs and process parameters. This can be achieved by firstly, using the developed CFD model in Chapter 5 in order to determine the appropriate criteria for the weld zone in terms of the size / shape of the deformation zone, (MAZ), and weld penetration using iso-viscosity plot. Secondly, calculating tool wear under certain process parameters, then determining whether the tool is able to produce a defect free weld under particular parametrises based on the weld zone criteria.

From this parametric study, some findings can be summarised as shown below:

- For both tool designs, pressure decreases with increasing tool rotation speed, while the opposite behaviour was reported for the traverse speed.

- The result of the velocity contours showed that velocity gradient at the pin tip region for the dome tool was less than that for the conical tool.

- The flow region under the dome tool is smaller than that of the conical tool.

- For both tool designs, wear depth increases with increasing tool rotation speed and traverse speed.

- From the study, it is possible to obtain low wear by controlling the process parameters.

- A conical tool with a wider tip can produce higher velocity gradient than the dome tool, while the dome tool has lower wear near the tool tip region.

- From the results, it can be concluded that this approach is able to predict tool wear for different process parameters and tool designs.

Chapter 8 Conclusions and future work

8.1 Conclusions

This thesis has presented the results of a developed numerical approach that can be used to predict tool wear associated with high viscous flow around FSW tools and to assess flow pattern differences in FSW with worn tools

This project was undertaken to develop a 3D-CFD model of the FSW process and to validate it according to the fundamentals of fluid mechanics. The author has conducted an intensive mesh independent study in order to produce a meshing strategy that can provide an appropriate solution for the FSW process and to model complex tool geometry in terms of rate of convergence and capturing for the flow features. The major findings of this study were that a tetrahedral mesh takes a long time to solve; however, a hybrid mesh has been shown to be more computationally efficient in achieving a better solution for the FSW process and for modelling complex tool geometry. Also, flow in the boundary layer is a crucial issue; however, a grid with a prism layer has been shown to be a powerful technique for solving this issue.

A validation process has been carried out in this project in terms of the mechanically affected zone (MAZ) shape and size. An important conclusion drawn from this process is that the developed model results showed a good agreement with an error of less than 15% with the experimental data for the size of the MAZ.

A novel methodology for calculating tool wear associated with high viscous flow around the FSW tool was presented in this project. The most obvious finding to emerge from this research is that the results of the predicted tool wear showed a good

agreement with a maximum error of less than 19% and average error for the three cases of less than 13%, when compared with the experimental results in the zone located below the shoulder edge and pin root. Thus, this modelling approach could be used to improve understanding of the effective limits of tool use for welding, and as a method for calculating tool wear (as a function of tool geometry and basic FSW process parameters) without the need for experimental trials.

It has been also shown that a 3D-CFD model of the FSW process can be used to assess in detail the differences in flow behaviour, MAZ size and strain rate distribution around the tool for both unworn and worn geometries. This study has shown that there are significant differences in flow behaviour around and under the tool when it is worn; the outcome of this could be used to determine the quality of the weld joint.

Finally, in the last chapter of this thesis, a parametric study was undertaken for two tool designs - a dome and a conical shape - to predict the wear depth in the FSW process tool; this included different rotation speeds and traverse speeds. This study has found that, generally, the wear depth is different for the dome and conical tool designs in the pin tip zone, where the results reveal that the conical tool has a greater area of contact with the flowing material than the dome design; therefore, the formation of a grove was predicted in this region. It was also shown that for both tool designs, wear depth increased with increasing the rotation speed and traverse speed. Preliminary investigation in terms of weld pitch showed that it is possible to determine the weld pitch value that can give lower wear. From the results, it can be concluded that this approach is able to predict tool wear for different process parameters and tool designs.

8.2 Future work

In this current project, achievements have been made to produce a useful tool for modelling the FSW process and predicting tool wear in the FSW process, based on a CFD-FLUENT package. The outcome of this project shows the ability to predict and interpret the behaviour of the flow when using specific weld parameters and component geometry without the need for experimental trials. However, some challenges have arisen which need further work in future.

As shown in chapter 6, there was inconsistency in the results near the shoulder region and it was argued that this was due to the use of a one-phase flow model. Therefore, more work is needed to use the Volume of Fluid Method (VOF) to model two-phase flow. This suggestion would be a worthwhile study in order to allow the material flow past the top surface of the plate, leading to a decrease in the pressure close to that position.

As presented in this research, the developed methodology successfully predicted the tool wear in the FSW, but was unable to predict the tool failure. Therefore, additional further developments for this methodology should include a couple solvers (CFD based model and solid mechanics based model) in order to predict the tool failure and tool wear.

In this study wear coefficient value of the FSW tool was predicted numerically. Further experimental investigation is needed to determine this value; this investigation will help to provide robust results for tool wear prediction.

Other further actions planned by the author is to develop the model to be able to predict tool wear using complex tools geometry such as threads and trivex tool design.

A further extension of this research would be analysis the flow behaviour after each weld increment in order to determine the appropriate weld joint in terms of stirring

action and complete weld through the plate thickness. This will give an indication for the weld quality and how long the tool can achieve acceptable weld.

It is believed that the improvement in the developed methodology in terms of repeated jobs (multiple weld increments) and involves less user interaction, requires automating workflow, this can be achieved by using batch system. The outcomes of this this will enhance the understanding of the effect limit of tool use for welding.

Moving forward, further development for tool wear methodology may follow which considers tool surface temperature during tool wear calculations. These suggestions may enhance this approach to provide a useful tool to model the entire FSW process and usefully predict tool wear.

Follow-on work could focus on developing the current methodology to predict the tool wear in metal matrix composite (MMCs) and incorporation of particle size for dispersed MMCs of tool wear.

References

1.   P. Sinha, S. Muthukumaran, and S. Mukherjee, *Analysis of first mode of metal transfer in friction stir welded plates by image processing technique.* Journal of Materials Processing Technology, 2008. **197**(1): p. 17-21.
2.   M. Sued, D. Pons, J. Lavroff, and E. Wong, *Design features for bobbin friction stir welding tools: Development of a conceptual model linking the underlying physics to the production process.* Materials & Design, 2014. **54**: p. 632-643.
3.   R. S. Mishra and Z. Ma, *Friction stir welding and processing.* Materials Science and Engineering: R: Reports, 2005. **50**(1): p. 1-78.
4.   N. McPherson, A. Galloway, S. Cater, and M. Osman. *A comparison between single sided and double sided friction stir welded 8mm thick DH36 steel plate.* in *Trends in Welding Research 2012: Proceedings of the 9th International Conference.* , 2013. ASM International.
5.   D. Lohwasser and Z. Chen, *Friction stir welding: From basics to applications*, 2009: Elsevier.
6.   A. Toumpis, A. Galloway, L. Molter, and H. Polezhayeva, *Systematic investigation of the fatigue performance of a friction stir welded low alloy steel.* Materials & Design, 2015. **80**: p. 116-128.
7.   Y. J. Chao, X. Qi, and W. Tang, *Heat transfer in friction stir welding— experimental and numerical studies.* Journal of manufacturing science and engineering, 2003. **125**(1): p. 138-145.
8.   M. Selvaraj, *A temperature dependent slip factor based thermal model for friction stir welding of stainless steel.* Sadhana, 2013. **38**(6): p. 1393-1405.
9.   W. Thomas, P. Threadgill, and E. Nicholas, *Feasibility of friction stir welding steel.* Science and Technology of Welding & Joining, 1999. **4**(6): p. 365-372.
10.   R. Prado, L. Murr, K. Soto, and J. McClure, *Self-optimization in tool wear for friction-stir welding of Al 6061+ 20% Al$_2$ O$_3$ MMC.* Materials Science and Engineering: A, 2003. **349**(1): p. 156-165.
11.   D. Choi, C. Lee, B. Ahn, J. Choi, Y. Yeon, K. Song, H. Park, Y. Kim, C. Yoo, and S. Jung, *Frictional wear evaluation of WC–Co alloy tool in friction stir spot welding of low carbon steel plates.* International Journal of Refractory Metals and Hard Materials, 2009. **27**(6): p. 931-936.
12.   H. Bhadeshia and T. DebRoy, *Critical assessment: friction stir welding of steels.* Science and Technology of Welding & Joining, 2009. **14**(3): p. 193-196.
13.   P. A. Colegrove and H. R. Shercliff, *3-Dimensional CFD modelling of flow round a threaded friction stir welding tool profile.* Journal of Materials Processing Technology, 2005. **169**(2): p. 320-327.
14.   H. Schmidt, J. Hattel, and J. Wert, *An analytical model for the heat generation in friction stir welding.* Modelling and Simulation in Materials Science and Engineering, 2004. **12**(1): p. 143.
15.   D. M. Neto and P. Neto, *Numerical modeling of friction stir welding process: a literature review.* The International Journal of Advanced Manufacturing Technology, 2013. **65**(1-4): p. 115-126.
16.   X. He, F. Gu, and A. Ball, *A review of numerical analysis of friction stir welding.* Progress in Materials Science, 2014. **65**: p. 1-66.

---

17.   D. Kim, H. Badarinarayan, J. H. Kim, C. Kim, K. Okamoto, R. Wagoner, and K. Chung, *Numerical simulation of friction stir butt welding process for AA5083-H18 sheets.* European Journal of Mechanics-A/Solids, 2010. **29**(2): p. 204-215.

18.   K. Sugiyama, S. Ii, S. Takeuchi, S. Takagi, and Y. Matsumoto, *A full Eulerian finite difference approach for solving fluid–structure coupling problems.* Journal of Computational Physics, 2011. **230**(3): p. 596-627.

19.   M. Song and R. Kovacevic, *Numerical and experimental study of the heat transfer process in friction stir welding.* Proceedings of the Institution of Mechanical Engineers, Part B: Journal of Engineering Manufacture, 2003. **217**(1): p. 73-85.

20.   R. Nandan, G. Roy, T. Lienert, and T. Debroy, *Three-Dimensional heat and material flow during friction stir welding of mild steel.* Acta Materialia, 2007. **55**(3): p. 883-895.

21.   A. Arora, R. Nandan, A. Reynolds, and T. DebRoy, *Torque, power requirement and stir zone geometry in friction stir welding through modeling and experiments.* Scripta Materialia, 2009. **60**(1): p. 13-16.

22.   A. Hasan, C. Bennett, and P. Shipway, *A numerical comparison of the flow behaviour in Friction Stir Welding (FSW) using unworn and worn tool geometries.* Materials & Design, 2015. **87**: p. 1037-1046.

23.   P. Colegrove and H. Shercliff, *Development of Trivex friction stir welding tool Part 2–three-dimensional flow modelling.* Science and Technology of Welding & Joining, 2004. **9**(4): p. 352-361.

24.   S. Ji, Y. Jin, Y. Yue, L. Zhang, and Z. Lv, *The effect of tool geometry on material flow behavior of friction stir welding of titanium alloy.* Engineering Review, 2013. **33**(2): p. 107-113.

25.   H. Zhang, Z. Zhang, and J. Chen, *3D modeling of material flow in friction stir welding under different process parameters.* Journal of materials processing technology, 2007. **183**(1): p. 62-70.

26.   V. Soundararajan, S. Zekovic, and R. Kovacevic, *Thermo-mechanical model with adaptive boundary conditions for friction stir welding of Al 6061.* International Journal of Machine Tools and Manufacture, 2005. **45**(14): p. 1577-1587.

27.   S. Sadeghi, M. A. Najafabadi, Y. Javadi, and M. Mohammadisefat, *Using ultrasonic waves and finite element method to evaluate through-thickness residual stresses distribution in the friction stir welding of aluminum plates.* Materials & Design, 2013. **52**: p. 870-880.

28.   J. Zhang, Y. Shen, B. Li, H. Xu, X. Yao, B. Kuang, and J. Gao, *Numerical simulation and experimental investigation on friction stir welding of 6061-T6 aluminum alloy.* Materials & Design, 2014. **60**: p. 94-101.

29.   S. Aljoaba, O. Dillon, M. Khraisheh, and I. Jawahir, *Modeling the Effects of Coolant Application in Friction Stir Processing on Material Microstructure Using 3D CFD Analysis.* Journal of Materials Engineering and Performance, 2012. **21**(7): p. 1141-1150.

30.   B. T. Thompson, *Tool Degradation Characterization in the Friction Stir Welding of Hard Metals*, 2010, The Ohio State University.

31.   T. Seidel and A. Reynolds, *Visualization of the material flow in AA2195 friction-stir welds using a marker insert technique.* Metallurgical and Materials Transactions A, 2001. **32**(11): p. 2879-2884.

32. Z. Chen, T. Pasang, and Y. Qi, *Shear flow and formation of Nugget zone during friction stir welding of aluminium alloy 5083-O.* Materials Science and Engineering: A, 2008. **474**(1): p. 312-316.

33. M. Guerra, C. Schmidt, J. McClure, L. Murr, and A. Nunes, *Flow patterns during friction stir welding.* Materials Characterization, 2002. **49**(2): p. 95-101.

34. C. Leitãoa, R. Leala, D. M. Rodriguesa, P. Vilaçac, and A. Loureiroa, *Material flow in friction stir welding.* Microscopy and Microanalysis, 2008. **14**: p. 87-90.

35. M. M. Attallah and H. G. Salem, *Friction stir welding parameters: a tool for controlling abnormal grain growth during subsequent heat treatment.* Materials Science and Engineering: A, 2005. **391**(1): p. 51-59.

36. C. G. Rhodes, M. W. Mahoney, W. H. Bingel, R. A. Spurling, and C. C. Bampton, *Effects of friction stir welding on microstructure of 7075 aluminum.* Scripta Materialia, 1997. **36**: p. 69-75.

37. Z. Ma, R. Mishra, and M. Mahoney, *Superplastic deformation behaviour of friction stir processed 7075Al alloy.* Acta Materialia, 2002. **50**(17): p. 4419-4430.

38. Y. S. Sato, H. Kokawa, M. Enomoto, and S. Jogan, *Microstructural evolution of 6063 aluminum during friction-stir welding.* Metallurgical and Materials Transactions A, 1999. **30**(9): p. 2429-2437.

39. T. Lienert, W. Stellwag Jr, B. Grimmett, and R. Warke, *Friction stir welding studies on mild steel.* WELDING JOURNAL-NEW YORK-, 2003. **82**(1): p. 1.

40. P. V. Kumar, G. M. Reddy, and K. S. Rao, *Microstructure, mechanical and corrosion behavior of high strength AA7075 aluminium alloy friction stir welds–Effect of post weld heat treatment.* Defence Technology, 2015. **11**(4): p. 362-369.

41. K. Colligan, *Material flow behavior during friction stir welding of aluminum.* WELDING JOURNAL-NEW YORK-, 1999. **78**: p. 229.

42. Y. Li, L. Murr, and J. McClure, *Flow visualization and residual microstructures associated with the friction-stir welding of 2024 aluminum to 6061 aluminum.* Materials Science and Engineering: A, 1999. **271**(1): p. 213-223.

43. T. Dickerson, H. R. Shercliff, and H. Schmidt. *A weld marker technique for flow visualization in friction stir welding.* in *International symposium on friction stir welding.* 2003.

44. B. Liechty and B. Webb, *The use of plasticine as an analog to explore material flow in friction stir welding.* Journal of materials processing technology, 2007. **184**(1): p. 240-250.

45. C. Hamilton, S. Dymek, and M. Blicharski, *A model of material flow during friction stir welding.* Materials characterization, 2008. **59**(9): p. 1206-1214.

46. A. P. Reynolds, Z. Khandkar, T. Long, W. Tang, and J. Khan. *Utility of relatively simple models for understanding process parameter effects on FSW.* in *Materials Science Forum.* 2003. Trans Tech Publ.

47. P. Colegrove and H. Shercliff, *Two-dimensional CFD modelling of flow round profiled FSW tooling.* Science and Technology of Welding & Joining, 2004. **9**(6): p. 483-492.

48. S. Aljoaba, I. Jawahir, O. Dillon, M. Ali, and M. Khraisheh, *Modeling of friction stir processing using 3D CFD analysis.* International Journal of Material Forming, 2009. **2**: p. 315-318.

49.   H. Zhang, Z. Zhang, and J. Chen, *The finite element simulation of the friction stir welding process.* Materials Science and Engineering: A, 2005. **403**(1): p. 340-348.

50.   X. D. a. S. Xu, *Solid mechanics simulation of friction stir welding process.* Society of Manufacturing Engineers, , 2001. **Volume XXIX**: p. pp. 631-638.

51.   G. Buffa, J. Hua, R. Shivpuri, and L. Fratini, *Design of the friction stir welding tool using the continuum based FEM model.* Materials Science and Engineering: A, 2006. **419**(1): p. 381-388.

52.   P. A. Colegrove, H. R. Shercliff, and R. Zettler, *A Model for Predicting the Heat Generation and Temperature in Friction Stir Welding from the Material Properties.* Science and Technology of Welding & Joining, Volume 12, Number 4, May 2007, pp. 284-297, 2007. **12**: p. 284-297.

53.   S. Guerdoux and L. Fourment, *A 3D numerical simulation of different phases of friction stir welding.* Modelling and simulation in materials science and engineering, 2009. **17**(7): p. 075001.

54.   D. Santiago, S. Urquiza, G. Lombera, and L. Vedia, *3D modeling of material flow and temperature in Friction Stir Welding.* Welding and Inspection, 2009. **14**(3): p. 248-256.

55.   M. Grujicic, G. Arakere, B. Pandurangan, J. Ochterbeck, C. Yen, B. Cheeseman, A. Reynolds, and M. Sutton, *Computational Analysis of Material Flow During Friction Stir Welding of AA5059 Aluminum Alloys.* Journal of Materials Engineering and Performance, 2012. **21**: p. 1824-1840.

56.   D. Jacquin, B. De Meester, A. Simar, D. Deloison, F. Montheillet, and C. Desrayaud, *A simple Eulerian thermomechanical modeling of friction stir welding.* Journal of materials processing technology, 2011. **211**(1): p. 57-65.

57.   P. Heurtier, M. Jones, C. Desrayaud, J. H. Driver, F. Montheillet, and D. Allehaux, *Mechanical and thermal modelling of friction stir welding.* Journal of materials processing technology, 2006. **171**(3): p. 348-357.

58.   W. Pan, D. Li, A. M. Tartakovsky, S. Ahzi, M. Khraisheh, and M. Khaleel, *A new smoothed particle hydrodynamics non-Newtonian model for friction stir welding: Process modeling and simulation of microstructure evolution in a magnesium alloy.* International Journal of Plasticity, 2013.

59.   B. Darras, M. Khraisheh, F. Abu-Farha, and M. Omar, *Friction stir processing of commercial AZ31 magnesium alloy.* Journal of materials processing technology, 2007. **191**(1): p. 77-81.

60.   A. J. C. Crespo, *Application of the smoothed particle hydrodynamics model SPHysics to free surface hydrodynamics.* Universidade de Vigo, 2008.

61.   G. Buffa, J. Hua, R. Shivpuri, and L. Fratini, *A continuum based fem model for friction stir welding—model development.* Materials Science and Engineering: A, 2006. **419**(1): p. 389-396.

62.   T. Özel and A. Nadgir, *Prediction of flank wear by using back propagation neural network modeling when cutting hardened H-13 steel with chamfered and honed CBN tools.* International Journal of Machine Tools and Manufacture, 2002. **42**(2): p. 287-297.

63.   P. Sahoo, *Engineering tribology* 2005: PHI Learning Pvt. Ltd.

64.   R. Gohar and H. Rahnejat, *Fundamentals of tribology* 2008: World Scientific Publishing Company Incorporated.

65.   B. Li, *A review of tool wear estimation using theoretical analysis and numerical simulation technologies.* International Journal of Refractory Metals and Hard Materials, 2012. **35**: p. 143-151.

66. D. Contorno, M. Faga, L. Fratini, L. Settineri, and G. Gautier di Confiengo, *Wear Analysis During Friction Stir Processing of A359+ 20% SiC MMC.* Key Engineering Materials, 2009. **410**: p. 235-244.

67. E. Michael, *The Effects of Tool Texture on Tool Wear in Friction Stir Welding of X-70 Steel*, 2012, Ohio State University.

68. E. Mahmoud, M. Takahashi, T. Shibayanagi, and K. Ikeuchi, *Effect of friction stir processing tool probe on fabrication of SiC particle reinforced composite on aluminium surface.* Science and Technology of Welding & Joining, 2009. **14**(5): p. 413-425.

69. E. Y. T. Adesta, M. Al Hazza, M. Riza, and D. Agusman, *Tool life estimation model based on simulated flank wear during high speed hard turning.* European Journal of Scientific Research, 2010. **39**(2): p. 265-278.

70. D. S. H. Eskelinen. *Lecture 4 Wear Phenomena.* [cited 2015 22/09/2015]; Available from: https://noppa.lut.fi/noppa/opintojakso/bk50a2200/.../wear_phenomena.p.

71. E. Rabinowicz, *Friction and wear of materials.* 1965.

72. T. J. Prater, *Predictive process modeling of tool wear in friction stir welding of metal matrix composites*, 2012.

73. J. Ding, S. Leen, and I. McColl, *The effect of slip regime on fretting wear-induced stress evolution.* International journal of fatigue, 2004. **26**(5): p. 521-531.

74. K. Ersoy-Nürnberg, G. Nürnberg, M. Golle, and H. Hoffmann, *Simulation of wear on sheet metal forming tools—An energy approach.* Wear, 2008. **265**(11): p. 1801-1807.

75. M. Akkök, B. Acar, and E. Açmaz, *Experimental analysis and wear modeling for mechanical components of a typical rail launcher.* Wear, 2013. **306**(1): p. 1-9.

76. A. Cruzado, M. Urchegui, and X. Gómez, *Finite element modeling and experimental validation of fretting wear scars in thin steel wires.* Wear, 2012. **289**: p. 26-38.

77. T. Thepsonthi and T. Özel, *3-D finite element process simulation of micro-end milling Ti-6Al-4V titanium alloy: Experimental validations on chip flow and tool wear.* Journal of materials processing technology, 2015. **221**: p. 128-145.

78. W. Gan, Z. Li, and S. Khurana, *Tool materials selection for friction stir welding of L80 steel.* Science and Technology of Welding and Joining, 2007. **12**(7): p. 610-613.

79. T. J. Prater, A. M. Strauss, G. E. Cook, B. T. Gibson, and C. D. Cox, *A phenomenological model for tool wear in friction stir welding of metal matrix composites.* Metallurgical and Materials Transactions A, 2013. **44**(8): p. 3757-3764.

80. A. Nunes, E. Bernstein, and J. McClure. *A rotating plug model for friction stir welding.* in *81st American Welding Society Annual Convention*. 2000.

81. D. Shindo, A. Rivera, and L. Murr, *Shape optimization for tool wear in the friction-stir welding of cast AI359-20% SiC MMC.* Journal of Materials Science, 2002. **37**(23): p. 4999-5005.

82. T. Prater and A. Strauss, *Statistical modelling and prediction of wear in Friction Stir welding of a metal matrix composite (AL 359/SIC/20P).* Journal of Manufacturing Technology Research, 2010. **2**: p. 1-13.

83. P. Tracie, B. Gibson, C. Chase, E. C. George, and M. S. Alvin, *Effect of particle size on tool wear in Friction Stir welding of Al 6061 with silicon*

---

carbide reinforcement. Journal of Manufacturing Technology Research, 2014. **6**(3/4): p. 125-142.

84. G. Buffa, L. Fratini, F. Micari, and L. Settineri, *On the Choice of Tool Material in Friction Stir Welding of Titanium Alloys.* Proceedings of NAMRI/SME, 2012. **40**.

85. T. Miyazawa, Y. Iwamoto, T. Maruko, and H. Fujii, *Friction stir welding of 304 stainless steel using Ir based alloy tool.* Science and Technology of Welding and Joining, 2012. **17**(3): p. 207-212.

86. A. N. Siddiquee and S. Pandey, *Experimental investigation on deformation and wear of WC tool during friction stir welding (FSW) of stainless steel.* The International Journal of Advanced Manufacturing Technology, 2014. **73**(1-4): p. 479-486.

87. J. Wang, J. Su, R. S. Mishra, R. Xu, and J. A. Baumann, *Tool wear mechanisms in friction stir welding of Ti–6Al–4V alloy.* Wear, 2014. **321**: p. 25-32.

88. J. Andersson, A. Almqvist, and R. Larsson, *Numerical simulation of a wear experiment.* Wear, 2011. **271**(11): p. 2947-2952.

89. R. Prado, L. Murr, D. Shindo, and K. Soto, *Tool wear in the friction-stir welding of aluminum alloy 6061+ 20% Al_2O_3: a preliminary study.* Scripta materialia, 2001. **45**(1): p. 75-80.

90. R. Rai, A. De, H. Bhadeshia, and T. DebRoy, *Review: friction stir welding tools.* Science and Technology of Welding & Joining, 2011. **16**(4): p. 325-342.

91. S. H. C. Park, Y. S. Sato, H. Kokawa, K. Okamoto, S. Hirano, and M. Inagaki, *Boride formation induced by pcBN tool wear in friction-stir-welded stainless steels.* Metallurgical and Materials Transactions A, 2009. **40**(3): p. 625-636.

92. P. Kundu, I. Cohenra, and D. Dowling, *FLUID MECHANICS*, ed. Fifth, 2012, USA: Academic Press is an imprint of Elsevier. 919.

93. J. Wendt, *Computational fluid dynamics: an introduction*2008: Springer Science & Business Media.

94. R. Löhner, *Applied computational fluid dynamics techniques: an introduction based on finite element methods*, ed. 2nd, 2008: Wiley.

95. A. A. Draad, G. Kuiken, and F. Nieuwstadt, *Laminar–turbulent transition in pipe flow for Newtonian and non-Newtonian fluids.* Journal of Fluid Mechanics, 1998. **377**: p. 267-312.

96. B. Noack, *On the flow around a circular cylinder. Part II: Turbulent regime.* ZAMM -Journal of Applied Mathematics and Mechanics/Zeitschrift für Angewandte Mathematik und Mechanik, 1999. **79**(S1): p. 227-230.

97. M. J. McPherson, *Introduction of fluid mechanics*, in *Subsurface Ventilation and Environmental Engineering*, 1993, Springer. p. 15-49.

98. H. K. Versteeg and W. Malalasekera, *An introduction to computational fluid dynamics: the finite volume method*, 2007: Prentice Hall.

99. A. Arora, *Thermomechanical conditions and stresses on the friction stir welding tool*, 2011, The Pennsylvania State University.

100. H. Atharifar, D. Lin, and R. Kovacevic, *Numerical and experimental investigations on the loads carried by the tool during friction stir welding.* Journal of Materials Engineering and Performance, 2009. **18**(4): p. 339-350.

101. C. T. Shaw, *Using computational fluid dynamics*. Vol. 325. 1992: Prentice Hall Hemel Hempstead, England.

102. A. R. ANSYS®, *Release 14.0, ANSYS Fluent User's Guide*, 2011, ANSYS, Inc.

103. T. Sheppard and A. Jackson, *Constitutive Equations for Use in Prediction of Flow Stress During Extrusion of Aluminium Alloys.* Materials Science and Technology, 1997. **13**(3): p. 203-209.

104. T. Sheppard and D. Wright, *Determination of Flow Stress. Pt. 1. Constitutive Equation for Aluminum Alloys at Elevated Temperatures.* Met. Technol., 1979. **6**(6): p. 215-223.

105. R. Nandan, G. Roy, and T. DebRoy, *Numerical simulation of three-dimensional heat transfer and plastic flow during friction stir welding.* Metallurgical and Materials Transactions A, 2006. **37**(4): p. 1247-1259.

106. B. M. Darras, *Experimental and analytical study of friction stir processing*, in *Mechanical Engineering*2005, UNIVERSITY OF KENTUCKY

107. A. R. ANSYS®, *Release 14.0, ANSYS FLUENT UDF Manual*, 2011, ANSYS, Inc. .

108. M. M. Zdravkovich, *Flow around circular cylinders: applications*. Vol. 2. 2003: Oxford University Press on Demand.

109. Z. Deng, M. R. Lovell, and K. A. Tagavi, *Influence of Material Properties and Forming Velocity on the Interfacial Slip Characteristics of Cross Wedge Rolling.* Journal of Manufacturing Science and Engineering, 2001. **123**(4): p. 647-653.

110. A. Belyakov, H. Miura, and T. Sakai, *Dynamic recrystallization under warm deformation of a 304 type austenitic stainless steel.* Materials Science and Engineering: A, 1998. **255**(1): p. 139-147.

111. B. C. Liechty, *Material Flow Behavior in Friction Stir Welding.* 2008.

112. C. Hamilton, S. Dymek, and A. Sommers, *A thermal model of friction stir welding in aluminum alloys.* International Journal of Machine Tools and Manufacture, 2008. **48**(10): p. 1120-1130.

113. R. Nandan, G. Roy, T. Lienert, and T. DebRoy, *Numerical modelling of 3D plastic flow and heat transfer during friction stir welding of stainless steel.* Science and Technology of Welding & Joining, 2006. **11**(5): p. 526-537.

114. X. Zhu and Y. Chao, *Numerical simulation of transient temperature and residual stresses in friction stir welding of 304L stainless steel.* Journal of materials processing technology, 2004. **146**(2): p. 263-272.

115. Y. J. Chao and X. Qi, *Thermal and thermo-mechanical modeling of friction stir welding of aluminum alloy 6061-T6.* Journal of materials processing and manufacturing science, 1998. **7**(2): p. 215-233.

116. S. Daftardar, *Laser Assisted Friction Stir Welding: Finite Volume Method and Metaheuristic Optimization*, 2009, Louisiana State University

117. G. Duan and B. Chen, *Stability and accuracy analysis for viscous flow simulation by the moving particle semi-implicit method.* Fluid Dynamics Research, 2013. **45**(3): p. 035501.

118. M. W. Bern and P. E. Plassmann, *Mesh generation*1997: Pennsylvania State University, Department of Computer Science and Engineering, College of Engineering.

119. R. Biswas and R. C. Strawn, *Tetrahedral and hexahedral mesh adaptation for CFD problems.* Applied Numerical Mathematics, 1998. **26**(1): p. 135-151.

120. Milovan Peric and Stephen Ferguson. *The advantage of polyhedral meshes*. [cited 2014 06/02]; Available from: http://www.plmmarketplace.com/upload/Temp/The_Advantage_of_polyhedral.pdf.

121. I. C. U. Manual, *ANSYS ICEM CFD 14 – User Manual*2011: ANSYS, Inc.

122. A. F. Ansys, *14.0 Theory Guide.* ANSYS inc, 2011: p. 390-1.
123. T. Zitzmann, M. Cook, P. Pfrommer, S. Rees, and L. Marjanovic. *Simulation of steady-state natural convection using CFD*. in *Proc. of the 9th International IBPSA Conference Building Simulation 2005*. 2005. Montréal: IBPSA.
124. S. Mittal and B. Kumar, *Flow past a rotating cylinder.* Journal of Fluid Mechanics, 2003. **476**(4): p. 303-334.
125. P. M. Knupp. *Remarks on mesh quality*. in *45th AIAA Aerospace Sciences Meeting and Exhibit*. 2007.
126. D. Mavriplis, *Unstructured grid techniques.* Annual Review of Fluid Mechanics, 1997. **29**(1): p. 473-514.
127. M. Harris, *Flow feature aligned mesh generation and adaptation*, 2013, University of Sheffield.
128. D. Stojković, M. Breuer, and F. Durst, *Effect of high rotation rates on the laminar flow around a circular cylinder.* Physics of Fluids (1994-present), 2002. **14**(9): p. 3160-3178.
129. S. Mittal and B. Kumar, *Flow past a rotating cylinder.* Journal of Fluid Mechanics, 2003. **476**: p. 303-334.
130. S. Champmartin, A. Ambari, and N. Roussel, *Flow around a confined rotating cylinder at small Reynolds number.* Physics of Fluids (1994-present), 2007. **19**(10): p. 103101.
131. M. Zdravkovich, *Flow Around Circular Cylinder: A Comprehensive Guide Through Flow Phenomena, Experiments, Applications, Mathematical Models, and Computer Simulations, Vol. 1*, 1997, Oxford University Press, New York.
132. S. Carstensen, X. Mandviwalla, L. Vita, and U. S. Paulsen. *Lift of a Rotating Circular Cylinder in Unsteady Flows*. in *The Twenty-second International Offshore and Polar Engineering Conference*. 2012. International Society of Offshore and Polar Engineers.
133. a. T. K. Masami Sato and M. D. A. Corporation, *A fundamental study of the flow past a circular cylinder using Abaqus/CFD*, in *2012 SIMULIA Community Conference*2012.
134. J.-H. Cho, S. Kang, H. Han, and K. Oh, *Modeling friction stir welding process of aluminum alloys.* Metals and Materials International, 2008. **14**(2): p. 247-258.
135. P. A. Colegrove and H. R. Shercliff, *Development of Trivex friction stir welding tool, Part 1 – two-dimensional flow modelling and experimental validation* Science and Technology of Welding and Joining 2004, 2004. **Vol. 9**: p. 345.
136. R. Naidu, *Friction stir welding: Thermal effects of a parametric study on butt and lap welds*, 2006, Wichita State University.
137. H. B. Schmidt and J. H. Hattel, *Thermal modelling of friction stir welding.* Scripta Materialia, 2008. **58**(5): p. 332-337.
138. T. Pinter and M. El Mehtedi, *Constitutive Equations for Hot Extrusion of AA6005A, AA6063 and AA7020 Alloys.* Key Engineering Materials, 2012. **491**: p. 43-50.
139. Ø. Frigaard, Ø. Grong, and O. Midling, *A process model for friction stir welding of age hardening aluminum alloys.* Metallurgical and Materials Transactions A, 2001. **32**(5): p. 1189-1200.
140. W. Kim, C. Kang, and B. Kim, *The effect of the solid fraction on rheological behavior of wrought aluminum alloys in incremental compression experiments*

---

with a closed die. Materials Science and Engineering: A, 2007. **447**(1): p. 1-10.

141. R. Nandan, *Computational modeling of heat transfer and visco-plastic flow in Friction Stir Weld*, in *Materials Science and Engineering*, 2008, The Pennsylvania State University: USA. p. 198.

142. H. Nassar and M. Khraisheh, *Simulation of Material Flow and Heat Evolution in Friction Stir Processing Incorporating Melting.* Journal of Engineering Materials and Technology, 2012. **134**(4): p. 041006.

143. O. Lorrain, V. Favier, H. Zahrouni, and D. Lawrjaniec, *Understanding the material flow path of friction ftir welding process using unthreaded tools.* Journal of Materials Processing Technology, 2010. **210**(4): p. 603-609.

144. H. Pashazadeh, J. Teimournezhad, and A. Masoumi, *Numerical investigation on the mechanical, thermal, metallurgical and material flow characteristics in friction stir welding of copper sheets with experimental verification.* Materials & Design, 2014. **55**: p. 619-632.

145. S. Chionopoulos, C. Sarafoglou, D. Pantelis, and V. Papazoglou. *Effect of tool pin and welding parameters on friction stir welded (FSW) marine aluminum alloys.* in *Proceedings of the 3rd International Conference on Manufacturing Engineering (ICMEN).* 2008.

146. K. E. Tello, A. P. Gerlich, and P. F. Mendez, *Constants for hot deformation constitutive models for recent experimental data.* Science and Technology of Welding & Joining, 2010. **15**(3): p. 260-266.

147. C. Nkhoma and R. Kasanalowe, *Hot Working Characteristics of AISI 321 in Comparison to AISI 304 Austenitic Stainless Steels*, 2014.

148. I. Fuerstner, *Advanced Knowledge Application in Practice* November, 2010: Sciyo. 378.

149. I. McColl, J. Ding, and S. Leen, *Finite element simulation and experimental validation of fretting wear.* Wear, 2004. **256**(11): p. 1114-1127.

150. L. Yang, *Determination of the wear coefficient of tungsten carbide by a turning operation.* Wear, 2001. **250**(1-12): p. 366-375.

151. J. Avelar-Batista, E. Spain, J. Housden, G. Fuentes, R. Rebolé, R. Rodriguez, F. Montalá, L. Carreras, and T. Tate, *Characterisation of Pristine and Recoated electron beam evaporation plasma-assisted physical vapour deposition Cr–N coatings on AISI M2 steel and WC–Co substrates.* Thin Solid Films, 2005. **491**(1): p. 177-183.

152. H. Su, C. S. Wu, M. Bachmann, and M. Rethmeier, *Numerical modeling for the effect of pin profiles on thermal and material flow characteristics in friction stir welding.* Materials & Design, 2015. **77**: p. 114-125.

153. C. B. Owen, *Two dimensional friction stir welding model with experimental validation*, in *Department of Mechanical Engineering*, 2006, Brigham Young University. p. 129.

154. L. Ke, L. Xing, and J. Indacochea, *Material flow patterns and cavity model in friction-stir welding of aluminum alloys.* Metallurgical and Materials Transactions B, 2004. **35**(1): p. 153-160.

155. D. P. Fairchild, S. J. Ford, A. Kumar, N. E. Nissley, N. E. Biery, and M. L. Macia, *Butt weld and method of making using fusion and friction stir welding*, 2011, Google Patents.

156. Y. Zhang, X. Cao, S. Larose, and P. Wanjara, *Review of tools for friction stir welding and processing.* Canadian Metallurgical Quarterly, 2012. **51**(3): p. 250-261.

157. P. Cavaliere, A. Squillace, and F. Panella, *Effect of welding parameters on mechanical and microstructural properties of AA6082 joints produced by friction stir welding.* Journal of materials processing technology, 2008. **200**(1): p. 364-372.

158. L. Fratini, G. Buffa, F. Micari, and R. Shivpuri, *On the material flow in FSW of T-joints: Influence of geometrical and tecnological parameters.* The International Journal of Advanced Manufacturing Technology, 2009. **44**(5-6): p. 570-578.

159. H. Liu, H. Fujii, M. Maeda, and K. Nogi, *Tensile properties and fracture locations of friction-stir-welded joints of 2017-T351 aluminum alloy.* Journal of materials processing technology, 2003. **142**(3): p. 692-696.

160. I. M. C. Rjucsh K. Kundu *Fluid Mechanics, Second Edition*2002, USA: Elsevier Science.

161. J. B. Patel, B. Gotawala, and K. Bhatt, *Modelling of FSW Tools and Simulation of Viscosity & Flow Stress during Friction Stir Welding of Aluminum Alloy AA6061.*

Appendices

User Define Function

Appendix 1

1. Material viscosity

1.1.Isothermal model

```c
# include <udf.h>
int counter=0;

DEFINE_PROPERTY(U_Visc,c,t)
{
real Temp, Visc, str, A, alfa, n, Q, Z, stress, R,
asinh_input, asinh_output, Visc_limit;

A = 1.62E16; /* Material constant 304 ss*/
alfa = 0.008E-6;
n = 6.1;
Q = 446000;
R = 8.314; /* Specific gas constant */
Temp = 1189; /*0.7Tm*T_melting is 1698K*/
Visc_limit = 7.e8;
str = C_STRAIN_RATE_MAG(c,t);
Z = str*exp(Q/(R*Temp));
asinh_input = pow(Z/A,1/n);
asinh_output = log(asinh_input + sqrt(asinh_input *
asinh_input + 1));
stress = (1/alfa)*asinh_output;
Visc = stress/(3*str);
if ( (Visc > Visc_limit) || (str == 0) )
{
    Visc = Visc_limit;
}


if(counter<=20)
 {counter++;
 CX_Message("Strain= %E(1/s) Viscosity =%E PaS\n", str, Visc);
/* CX_Message("Strain*1e6= %E\n", str*1e6); */
 }

 return Visc;
```

```
}
```

1.2. Thermal model

```c
# include <udf.h>
int counter=0;

DEFINE_PROPERTY(U_Visc,c,t)
{
real Temp, Visc, str, A, alfa, n, Q, Z, stress, R,
asinh_input, asinh_output, Visc_limit;

A = 1.62E16; /* Material constant 304 ss*/
alfa = 0.008E-6;
n = 6.1;
Q = 446000;
R = 8.314; /* Specific gas constant */
Temp = C_T(c,t); /*0.7Tm*/
Visc_limit = 7.e8;
str = C_STRAIN_RATE_MAG(c,t);
Z = str*exp(Q/(R*Temp));
asinh_input = pow(Z/A,1/n);
asinh_output = log(asinh_input + sqrt(asinh_input *
asinh_input + 1));
stress = (1/alfa)*asinh_output;
Visc = stress/(3*str);
if ( (Visc > Visc_limit) || (str == 0) )
{
    Visc = Visc_limit;
}


if(counter<=20)
 {counter++;
 CX_Message("Strain= %E(1/s) Viscosity =%E PaS\n", str, Visc);
/* CX_Message("Strain*1e6= %E\n", str*1e6); */
 }


 return Visc;

}
```

Appendix 2

1. Tool velocity

```c
/* Tool velcity in u-direction*/
#include <udf.h>
#include <math.h>
#include <stdio.h>
#include <stdlib.h>
int debugCounterp=0;
DEFINE_PROFILE(udeltau_2,t,i)


{
real x[ND_ND], A[ND_ND], c[ND_ND], rcal[ND_ND]; /* this will
hold the position vector */
real omega, omega_dot, r_shoulder,tau_yeld, shear_t;
face_t f;
real theta;
real r, u_delta, x1, z1, x_vel, z_vel, delta, delta_dot,u1;
real rpin=0.004;
omega = 23.561; /*rad per sec */
omega_dot = 41.8879; /*rad per sec */
r_shoulder = 0.002; /* meter */
delta_dot = 4.;
delta = 0.07;
u1 = 0.0025; /* meter */
/* get radial position
c[0] = 0.;
c[1] = 0.;
c[2] = 0.;
*/

begin_f_loop(f,t)
{
    F_CENTROID(x,f,t); /*Get the centroid positions into x */
    x1 = x[0] ;
    z1 = x[2] ;

    /*
     NV_VV(rcal,=,x,-,c);
    r = NV_MAG(rcal);
    */

  r=pow(x1*x1+z1*z1,0.5);

    /*
    if (r<=r_shoulder && r>=rpin )
    */
```

```
        theta=atan2(z1,x1) ;
        /*

        delta = 0.2+0.6*(1-exp(-
(delta_dot)*(omega/omega_dot)*(r/r_shoulder)));
        */

        u_delta = (1-delta)*(-omega*r*sin(theta)-u1);

        F_PROFILE(f,t,i)= u_delta;


 }
end_f_loop(f,t)

}



/* Tool velcity in w-direction*/
#include <udf.h>
#include <math.h>
#include <stdio.h>
#include <stdlib.h>

DEFINE_PROFILE(wdeltap,t,i)

{
real x[ND_ND], A[ND_ND], c[ND_ND], rcal[ND_ND]; /* this will
hold the position vector */
real omega, omega_dot, r_shoulder,tau_yeld, shear_t;
face_t f;
real r, w_delta, x1, z1, x_vel, z_vel, delta, delta_dot,u1;
real theta;
real rpin=0.004;
omega = 23.561; /*rad per sec */
omega_dot = 41.8879; /*rad per sec */
r_shoulder = 0.002; /* meter */
delta_dot = 4.;
delta = 0.07;
u1 = 0.0025; /* meter */
/* get radial position
al7020aa
c[0] = 0.;
c[1] = 0.;
c[2] = 0.;
*/

begin_f_loop(f,t)
```

```
{
    F_CENTROID(x,f,t);
    x1 = x[0] ;
    z1 = x[2] ;
    /*
  NV_VV(rcal,=,x,-,c);
    r = NV_MAG(rcal);
    */
    r=pow(x1*x1+z1*z1,0.5);
    /*

    if (r<=r_shoulder && r>=rpin )
    */
        theta=atan2(z1,x1) ;
        /*

        delta = 0.2+0.6*(1-exp(-
(delta_dot)*(omega/omega_dot)*(r/r_shoulder)));
        */

        w_delta = (1-delta)*(omega*r*cos(theta));

         F_PROFILE(f,t,i)= w_delta;

}
end_f_loop(f,t)

}
```

Appendix 3

1. Heat generation

```c
#include "udf.h"

real x[ND_ND], A[ND_ND], c[ND_ND], rcal[ND_ND], Atotal[ND_ND];
/* this will hold the position vector */
face_t f;
real r, q, qt, y;

DEFINE_PROFILE(heatfx,t,i)
{

int abst;
Atotal[0]=0;
Atotal[1]= 0;
Atotal[2]=0;
c[0]=0;
c[1]= 0.0053;
c[2]=0;
qt=0;
begin_f_loop(f,t)
{
    F_CENTROID(x,f,t);
    NV_VV(rcal,=,x,-,c);
    r=NV_MAG(rcal);
    if(r<0.00900787&&r>0)
    {
        q=(3*2272*r)/(2*3.14*(pow(0.00900787,3))); /*//w/m2*/
        F_PROFILE(f,t,i)=q;
        F_AREA(A,f,t);
        qt=qt+q*NV_MAG(A);
        /*printf("qAreas=%f%f%f%f\n",q,A[0],A[1],A[2]); */
        NV_VV(Atotal,=,Atotal,+,A);
    }
    else
    {
        F_PROFILE(f,t,i)=-30*(F_T(f,t)-298);/*//w/m2*/
        y=F_T(f,t);
    }
}
end_f_loop(f,t)
    /*printf("\nQtdiff=%f\n",qt); */
}
```

Appendix 4

1. UDF Validation

Since the nature of the problem solved in this thesis requires some extra capability on top of the standard CFD functions, in the form of material constitutive equations and user defined boundary conditions, these were formulated and implemented in the commercial software (ANSYS-Fluent) as User Defined Functions (UDF), as outlined in chapter 3, and explained in this appendix.

2. Couette flow

The flow between two parallel plates, separated by a distance H, is known as a Couette flow. It is considered a simple, exact solution for the Navier-Stokes (N-S) equations. This simple shear flow has been widely used to investigate the flow behaviour for plastic deformation, tribology, lubricants, and food processing [160] and is shown schematically in Figure 24.

We present the Navier-Stokes N-S equation for incompressible flow and then we will obtain the exact solution of this equation by assuming the specific boundary condition which makes the solution close to reality. The equation below represents the N-S equation:

$$\left(\rho \, \frac{d_v}{d_t} + \rho \, \boldsymbol{v}. \nabla \boldsymbol{v} = -\nabla p + \mu \, \nabla^2 \, \boldsymbol{v} \right) \tag{1}$$

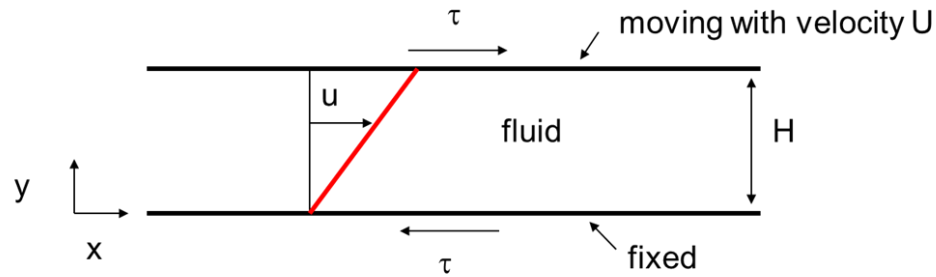$\boldsymbol{v}$ = velocity field vector, *(u,v,w)*

Figure 24 Couette flow schematic

Where, t is the time, p is the pressure, μ is the dynamic viscosity and τ is the shear stress, H is the distance between two plates.

Let us assume the flow moves in the x-direction with constant velocity U, while the opposite wall will be considered to have a no-slip boundary condition, which means the velocity of the fluid at the wall is zero and the velocity compounds for v, w equal to zero. The z-plane will be assumed to have symmetry (no gradient) and the fluid has a constant value of density. So, the flow is uni-directional with a steady state and there is no pressure gradient, which means $v = u$ only. This assumption will lead to $\frac{d_v}{d_t} = 0$, $\rho\, v = 0$, and $\nabla p = 0$. The fact that $v, \nabla v$ are orthogonal can also be neglected, so they equals zero. That will lead to velocity in the x-direction only with a gradient in the y-direction. Now we can write the governing equation in this form:

$$u(y) = \frac{U}{H} \times y \tag{2}$$

To validate the results of the strain rate and viscosity which are computed by FLUENT, they will be compared with the analytical solution of the Couette flow for the Navier-Stokes equation.

3. Simulation the couette flow model.

The Simulation of the couette flow model is presented in this section. The results of this simulation are compared with analytical solution in terms of velocity profile and strain rate to validate the UDF.

4. FLUENT domain and boundary conditions

A 3D laminar fluid flow model with a 0.001 m cubic shape has been implemented in ANSYS FLUENT 14 as shown in Figure 25. The study considers one side of the geometry as a moving wall with translation velocity u_x in the x-direction, while the opposite side was specified as a fixed wall with a no-slip boundary condition. The upper and lower boundaries of the domain were specified as a symmetry boundary condition. The remaining boundaries were assigned an outlet pressure boundary condition.
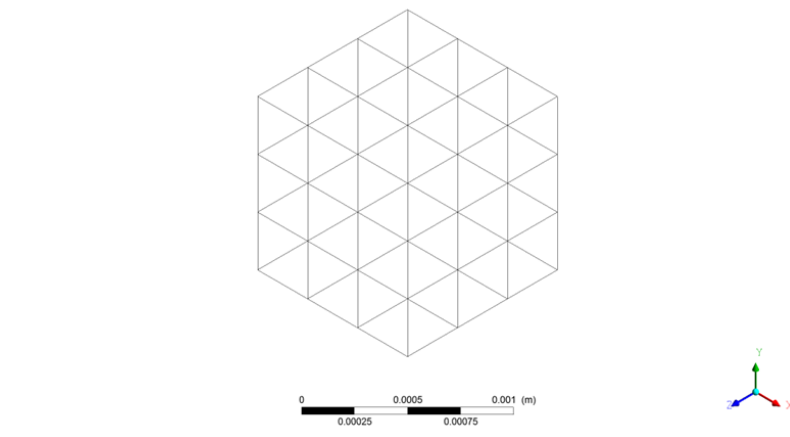

Figure 25 A3Dimensional model

The fluid used in the simulation was an Al AA6061 – T6 alloy, the properties of which are shown in the table 4-2, and material viscosity was calculated through the UDF (User Defined Function) as a function of the strain rate and flow stress [105].

5. Validation preliminary results

The velocity profile along the x-direction is calculated using the Couette flow model. The results of the analytical and FLUENT solution are shown in Figure 26. It is clear that the velocity profile is directly proportional to the x-distance from the wall. The FLUENT results showed good agreement with the analytical solution.
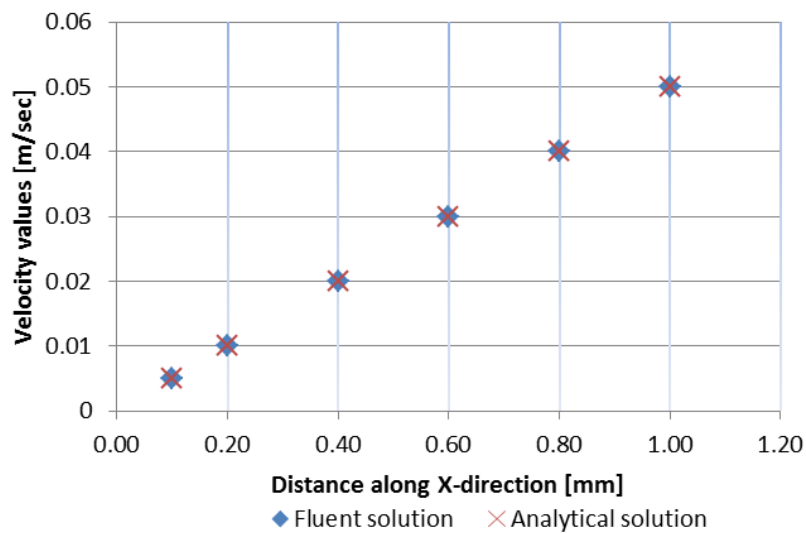

Figure 26 Velocity profile along x- direction at velocity 0.05 m/sec

To make sure that the values of the viscosity that were computed by the UDF are accurate, the strain rate was calculated from FLUENT and was then compared with the analytical solution of the couette flow. The strain rate and viscosity values at temperatures of 673, 748, and 800 K are presented in Table (1).

Table 1 Compare strain rate values

Velocity [m/sec]	Fluent values of strain rate [1 s^{-1}]	Analytical values of strain rate from velocity field [1 s^{-1}]	Fluent viscosity values at 673K [Kg m.s $^{-1}$]	Fluent viscosity values at 748K [Kg m.s $^{-1}$]	Fluent viscosity values at 800K [Kg m.s $^{-1}$]
0.05	50	50	8.4×10^5	7.11×10^5	6.35×10^5
0.075	75	75	7.60×10^5	6.16×10^5	5.33×10^5
0.1	100	100	5.80×10^5	4.73×10^5	4.10×10^5
0.25	250	250	2.46×10^5	2.03×10^5	1.78×10^5

From Table 4, the data of the strain rate which were computed by FLUENT and the analytical solution seemed to be identical. As explained in the constitutive equation the material viscosity is a function of the effective strain rate and the flow stress, and therefore the values of the material viscosity which were computed by FLUENT through the UDF code can be considered valid because they are verified by the values of the effective strain rate.

6. Plastic deformation limit

The UDF code which is presented in Appendix 1 shows that the condition is set in the code: the maximum limit of the material viscosity (the limit of the plastic deformation) a viscosity limit is applied in order to avoid computational difficulties (viscosity tending to infinity at zero strain rate). When the value of viscosity reaches more than 7.1×11 Pa s, which is a critical value, no significant plastic flow occurs, this value was assumed according to the work of Patel et al. [161]. In Figure 27, the implementation of the plastic deformation limit by comparing the analytical solution and the FLUENT solution using UDF. It can be seen that the UDF sets the plastic deformation limit of the viscosity value at the lower value of the strain rate. According to this figure it can be said that this code is valid in applying the critical viscosity value.
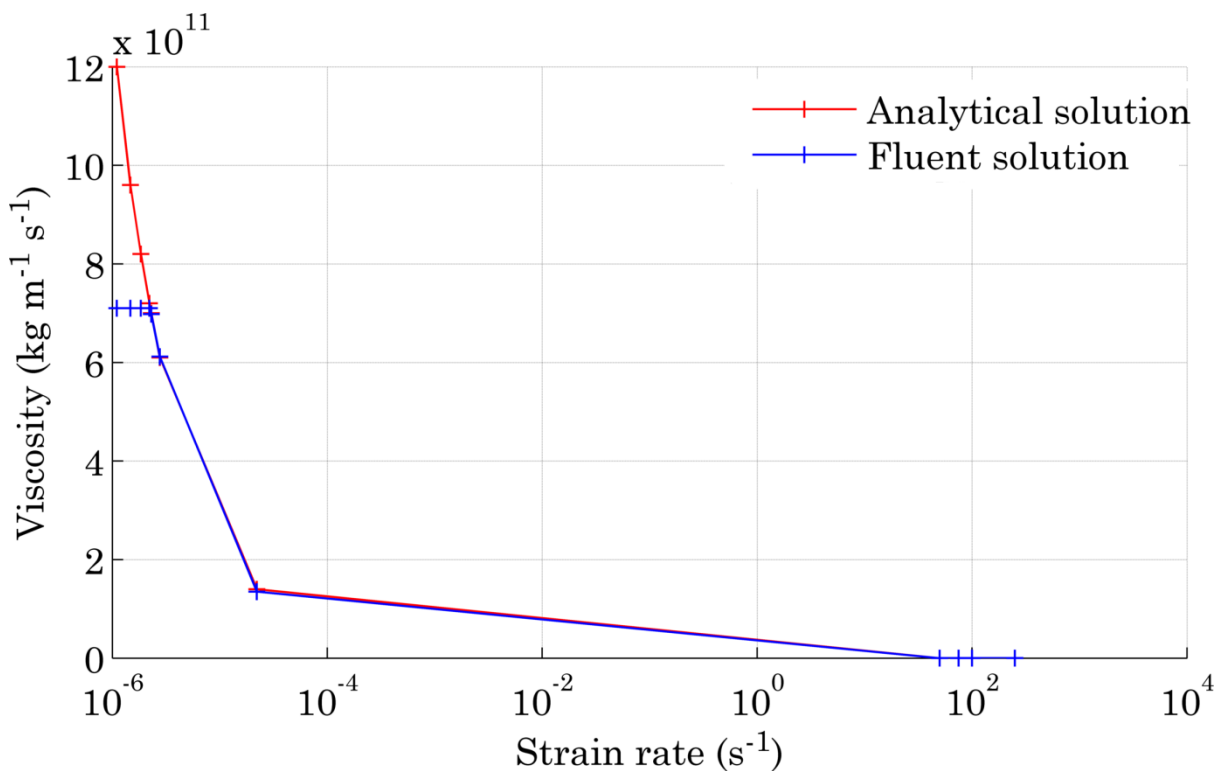

Figure 27 Indicate plastic deformation limit